

CONSOLIDATED UNDRAINED-TRIAxIAL BEHAVIOR  
OF A SAND-BENTONITE MIXTURE  
AT ELEVATED TEMPERATURE

by

BRIAN E. LINGNAU

A Thesis  
Submitted to the Faculty of Graduate Studies  
in Partial Fulfillment of the Requirements for the Degree of  
DOCTOR OF PHILOSOPHY

Department of Civil Engineering  
University of Manitoba  
Winnipeg, Manitoba

© Copyright June 1993.



National Library  
of Canada

Acquisitions and  
Bibliographic Services Branch

395 Wellington Street  
Ottawa, Ontario  
K1A 0N4

Bibliothèque nationale  
du Canada

Direction des acquisitions et  
des services bibliographiques

395, rue Wellington  
Ottawa (Ontario)  
K1A 0N4

*Your file* *Votre référence*

*Our file* *Notre référence*

The author has granted an irrevocable non-exclusive licence allowing the National Library of Canada to reproduce, loan, distribute or sell copies of his/her thesis by any means and in any form or format, making this thesis available to interested persons.

The author retains ownership of the copyright in his/her thesis. Neither the thesis nor substantial extracts from it may be printed or otherwise reproduced without his/her permission.

L'auteur a accordé une licence irrévocable et non exclusive permettant à la Bibliothèque nationale du Canada de reproduire, prêter, distribuer ou vendre des copies de sa thèse de quelque manière et sous quelque forme que ce soit pour mettre des exemplaires de cette thèse à la disposition des personnes intéressées.

L'auteur conserve la propriété du droit d'auteur qui protège sa thèse. Ni la thèse ni des extraits substantiels de celle-ci ne doivent être imprimés ou autrement reproduits sans son autorisation.

ISBN 0-315-86144-4

Name: \_\_\_\_\_  
 Dissertation Abstracts International is arranged by broad, general subject categories. Please select the one subject which most nearly describes the content of your dissertation. Enter the corresponding four-digit code in the spaces provided.

0428 U·M·I  
 SUBJECT CODE

SCIENCES AND ENGINEERING (GEOTECHNOLOGY)  
 SUBJECT TERM

**Subject Categories**

**THE HUMANITIES AND SOCIAL SCIENCES**

**COMMUNICATIONS AND THE ARTS**

Architecture ..... 0729  
 Art History ..... 0377  
 Cinema ..... 0900  
 Dance ..... 0378  
 Fine Arts ..... 0357  
 Information Science ..... 0723  
 Journalism ..... 0391  
 Library Science ..... 0399  
 Mass Communications ..... 0708  
 Music ..... 0413  
 Speech Communication ..... 0459  
 Theater ..... 0465

**EDUCATION**

General ..... 0515  
 Administration ..... 0514  
 Adult and Continuing ..... 0516  
 Agricultural ..... 0517  
 Art ..... 0273  
 Bilingual and Multicultural ..... 0282  
 Business ..... 0688  
 Community College ..... 0275  
 Curriculum and Instruction ..... 0727  
 Early Childhood ..... 0518  
 Elementary ..... 0524  
 Finance ..... 0277  
 Guidance and Counseling ..... 0519  
 Health ..... 0680  
 Higher ..... 0745  
 History of ..... 0520  
 Home Economics ..... 0278  
 Industrial ..... 0521  
 Language and Literature ..... 0279  
 Mathematics ..... 0280  
 Music ..... 0522  
 Philosophy of ..... 0998  
 Physical ..... 0523

Psychology ..... 0525  
 Reading ..... 0535  
 Religious ..... 0527  
 Sciences ..... 0714  
 Secondary ..... 0533  
 Social Sciences ..... 0534  
 Sociology of ..... 0340  
 Special ..... 0529  
 Teacher Training ..... 0530  
 Technology ..... 0710  
 Tests and Measurements ..... 0288  
 Vocational ..... 0747

**LANGUAGE, LITERATURE AND LINGUISTICS**

Language  
 General ..... 0679  
 Ancient ..... 0289  
 Linguistics ..... 0290  
 Modern ..... 0291  
 Literature  
 General ..... 0401  
 Classical ..... 0294  
 Comparative ..... 0295  
 Medieval ..... 0297  
 Modern ..... 0298  
 African ..... 0316  
 American ..... 0591  
 Asian ..... 0305  
 Canadian (English) ..... 0352  
 Canadian (French) ..... 0355  
 English ..... 0593  
 Germanic ..... 0311  
 Latin American ..... 0312  
 Middle Eastern ..... 0315  
 Romance ..... 0313  
 Slavic and East European ..... 0314

**PHILOSOPHY, RELIGION AND THEOLOGY**

Philosophy ..... 0422  
 Religion  
 General ..... 0318  
 Biblical Studies ..... 0321  
 Clergy ..... 0319  
 History of ..... 0320  
 Philosophy of ..... 0322  
 Theology ..... 0469

**SOCIAL SCIENCES**

American Studies ..... 0323  
 Anthropology  
 Archaeology ..... 0324  
 Cultural ..... 0326  
 Physical ..... 0327  
 Business Administration  
 General ..... 0310  
 Accounting ..... 0272  
 Banking ..... 0770  
 Management ..... 0454  
 Marketing ..... 0338  
 Canadian Studies ..... 0385  
 Economics  
 General ..... 0501  
 Agricultural ..... 0503  
 Commerce-Business ..... 0505  
 Finance ..... 0508  
 History ..... 0509  
 Labor ..... 0510  
 Theory ..... 0511  
 Folklore ..... 0358  
 Geography ..... 0366  
 Gerontology ..... 0351  
 History  
 General ..... 0578

Ancient ..... 0579  
 Medieval ..... 0581  
 Modern ..... 0582  
 Black ..... 0328  
 African ..... 0331  
 Asia, Australia and Oceania ..... 0332  
 Canadian ..... 0334  
 European ..... 0335  
 Latin American ..... 0336  
 Middle Eastern ..... 0333  
 United States ..... 0337  
 History of Science ..... 0585  
 Law ..... 0398  
 Political Science  
 General ..... 0615  
 International Law and Relations ..... 0616  
 Public Administration ..... 0617  
 Recreation ..... 0814  
 Social Work ..... 0452  
 Sociology  
 General ..... 0626  
 Criminology and Penology ..... 0627  
 Demography ..... 0938  
 Ethnic and Racial Studies ..... 0631  
 Individual and Family Studies ..... 0628  
 Industrial and Labor Relations ..... 0629  
 Public and Social Welfare ..... 0630  
 Social Structure and Development ..... 0700  
 Theory and Methods ..... 0344  
 Transportation ..... 0709  
 Urban and Regional Planning ..... 0999  
 Women's Studies ..... 0453

**THE SCIENCES AND ENGINEERING**

**BIOLOGICAL SCIENCES**

Agriculture  
 General ..... 0473  
 Agronomy ..... 0285  
 Animal Culture and Nutrition ..... 0475  
 Animal Pathology ..... 0476  
 Food Science and Technology ..... 0359  
 Forestry and Wildlife ..... 0478  
 Plant Culture ..... 0479  
 Plant Pathology ..... 0480  
 Plant Physiology ..... 0817  
 Range Management ..... 0777  
 Wood Technology ..... 0746  
 Biology  
 General ..... 0306  
 Anatomy ..... 0287  
 Biostatistics ..... 0308  
 Botany ..... 0309  
 Cell ..... 0379  
 Ecology ..... 0329  
 Entomology ..... 0353  
 Genetics ..... 0369  
 Limnology ..... 0793  
 Microbiology ..... 0410  
 Molecular ..... 0307  
 Neuroscience ..... 0317  
 Oceanography ..... 0416  
 Physiology ..... 0433  
 Radiation ..... 0821  
 Veterinary Science ..... 0778  
 Zoology ..... 0472  
 Biophysics  
 General ..... 0786  
 Medical ..... 0760

**EARTH SCIENCES**

Biogeochemistry ..... 0425  
 Geochemistry ..... 0996

Geodesy ..... 0370  
 Geology ..... 0372  
 Geophysics ..... 0373  
 Hydrology ..... 0388  
 Mineralogy ..... 0411  
 Paleobotany ..... 0345  
 Paleocology ..... 0426  
 Paleontology ..... 0418  
 Paleozoology ..... 0985  
 Palynology ..... 0427  
 Physical Geography ..... 0368  
 Physical Oceanography ..... 0415

**HEALTH AND ENVIRONMENTAL SCIENCES**

Environmental Sciences ..... 0768  
 Health Sciences  
 General ..... 0566  
 Audiology ..... 0300  
 Chemotherapy ..... 0992  
 Dentistry ..... 0567  
 Education ..... 0350  
 Hospital Management ..... 0769  
 Human Development ..... 0758  
 Immunology ..... 0982  
 Medicine and Surgery ..... 0564  
 Mental Health ..... 0347  
 Nursing ..... 0569  
 Nutrition ..... 0570  
 Obstetrics and Gynecology ..... 0380  
 Occupational Health and Therapy ..... 0354  
 Ophthalmology ..... 0381  
 Pathology ..... 0571  
 Pharmacology ..... 0419  
 Pharmacy ..... 0572  
 Physical Therapy ..... 0382  
 Public Health ..... 0573  
 Radiology ..... 0574  
 Recreation ..... 0575

Speech Pathology ..... 0460  
 Toxicology ..... 0383  
 Home Economics ..... 0386

**PHYSICAL SCIENCES**

**Pure Sciences**

Chemistry  
 General ..... 0485  
 Agricultural ..... 0749  
 Analytical ..... 0486  
 Biochemistry ..... 0487  
 Inorganic ..... 0488  
 Nuclear ..... 0738  
 Organic ..... 0490  
 Pharmaceutical ..... 0491  
 Physical ..... 0494  
 Polymer ..... 0495  
 Radiation ..... 0754  
 Mathematics ..... 0405  
 Physics  
 General ..... 0605  
 Acoustics ..... 0986  
 Astronomy and Astrophysics ..... 0606  
 Atmospheric Science ..... 0608  
 Atomic ..... 0748  
 Electronics and Electricity ..... 0607  
 Elementary Particles and High Energy ..... 0798  
 Fluid and Plasma ..... 0759  
 Molecular ..... 0609  
 Nuclear ..... 0610  
 Optics ..... 0752  
 Radiation ..... 0756  
 Solid State ..... 0611  
 Statistics ..... 0463  
 Applied Sciences  
 Applied Mechanics ..... 0346  
 Computer Science ..... 0984

Engineering  
 General ..... 0537  
 Aerospace ..... 0538  
 Agricultural ..... 0539  
 Automotive ..... 0540  
 Biomedical ..... 0541  
 Chemical ..... 0542  
 Civil ..... 0543  
 Electronics and Electrical ..... 0544  
 Heat and Thermodynamics ..... 0348  
 Hydraulic ..... 0545  
 Industrial ..... 0546  
 Marine ..... 0547  
 Materials Science ..... 0794  
 Mechanical ..... 0548  
 Metallurgy ..... 0743  
 Mining ..... 0551  
 Nuclear ..... 0552  
 Packaging ..... 0549  
 Petroleum ..... 0765  
 Sanitary and Municipal ..... 0554  
 System Science ..... 0790  
 Geotechnology ..... 0428  
 Operations Research ..... 0796  
 Plastics Technology ..... 0795  
 Textile Technology ..... 0994

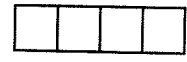
**PSYCHOLOGY**

General ..... 0621  
 Behavioral ..... 0384  
 Clinical ..... 0622  
 Developmental ..... 0620  
 Experimental ..... 0623  
 Industrial ..... 0624  
 Personality ..... 0625  
 Physiological ..... 0989  
 Psychobiology ..... 0349  
 Psychometrics ..... 0632  
 Social ..... 0451



Nom \_\_\_\_\_

Dissertation Abstracts International est organisé en catégories de sujets. Veuillez s.v.p. choisir le sujet qui décrit le mieux votre thèse et inscrivez le code numérique approprié dans l'espace réservé ci-dessous.



U·M·I

CODE DE SUJET

SUJET

Catégories par sujets

**HUMANITÉS ET SCIENCES SOCIALES**

**COMMUNICATIONS ET LES ARTS**

Architecture	0729
Beaux-arts	0357
Bibliothéconomie	0399
Cinéma	0900
Communication verbale	0459
Communications	0708
Danse	0378
Histoire de l'art	0377
Journalisme	0391
Musique	0413
Sciences de l'information	0723
Théâtre	0465

**ÉDUCATION**

Généralités	515
Administration	0514
Art	0273
Collèges communautaires	0275
Commerce	0688
Economie domestique	0278
Education permanente	0516
Education préscolaire	0518
Education sanitaire	0680
Enseignement agricole	0517
Enseignement bilingue et multiculturel	0282
Enseignement industriel	0521
Enseignement primaire	0524
Enseignement professionnel	0747
Enseignement religieux	0527
Enseignement secondaire	0533
Enseignement spécial	0529
Enseignement supérieur	0745
Evaluation	0288
Finances	0277
Formation des enseignants	0530
Histoire de l'éducation	0520
Langues et littérature	0279

Lecture	0535
Mathématiques	0280
Musique	0522
Orientation et consultation	0519
Philosophie de l'éducation	0998
Physique	0523
Programmes d'études et enseignement	0727
Psychologie	0525
Sciences	0714
Sciences sociales	0534
Sociologie de l'éducation	0340
Technologie	0710

**LANGUE, LITTÉRATURE ET LINGUISTIQUE**

Langues	
Généralités	0679
Anciennes	0289
Linguistique	0290
Modernes	0291
Littérature	
Généralités	0401
Anciennes	0294
Comparée	0295
Médiévale	0297
Moderne	0298
Africaine	0316
Américaine	0591
Anglaise	0593
Asiatique	0305
Canadienne (Anglaise)	0352
Canadienne (Française)	0355
Germanique	0311
Latino-américaine	0312
Moyen-orientale	0315
Romane	0313
Slave et est-européenne	0314

**PHILOSOPHIE, RELIGION ET THEOLOGIE**

Philosophie	0422
Religion	
Généralités	0318
Clergé	0319
Etudes bibliques	0321
Histoire des religions	0320
Philosophie de la religion	0322
Théologie	0469

**SCIENCES SOCIALES**

Anthropologie	
Archéologie	0324
Culturelle	0326
Physique	0327
Droit	0398
Economie	
Généralités	0501
Commerce-Affaires	0505
Economie agricole	0503
Economie du travail	0510
Finances	0508
Histoire	0509
Théorie	0511
Études américaines	0323
Études canadiennes	0385
Études féministes	0453
Folklore	0358
Géographie	0366
Gérontologie	0351
Gestion des affaires	
Généralités	0310
Administration	0454
Banques	0770
Comptabilité	0272
Marketing	0338
Histoire	
Histoire générale	0578

Ancienne	0579
Médiévale	0581
Moderne	0582
Histoire des noirs	0328
Africaine	0331
Canadienne	0334
Etats-Unis	0337
Européenne	0335
Moyen-orientale	0333
Latino-américaine	0336
Asie, Australie et Océanie	0332
Histoire des sciences	0585
Loisirs	0814
Planification urbaine et régionale	0999
Science politique	
Généralités	0615
Administration publique	0617
Droit et relations internationales	0616
Sociologie	
Généralités	0626
Aide et bien-être social	0630
Criminologie et établissements pénitentiaires	0627
Démographie	0938
Études de l'individu et de la famille	0628
Études des relations interethniques et des relations raciales	0631
Structure et développement social	0700
Théorie et méthodes	0344
Travail et relations industrielles	0629
Transports	0709
Travail social	0452

**SCIENCES ET INGÉNIERIE**

**SCIENCES BIOLOGIQUES**

Agriculture	
Généralités	0473
Agronomie	0285
Alimentation et technologie alimentaire	0359
Culture	0479
Élevage et alimentation	0475
Exploitation des péturages	0777
Pathologie animale	0476
Pathologie végétale	0480
Physiologie végétale	0817
Sylviculture et faune	0478
Technologie du bois	0746
Biologie	
Généralités	0306
Anatomie	0287
Biologie (Statistiques)	0308
Biologie moléculaire	0307
Botanique	0309
Cellule	0379
Ecologie	0329
Entomologie	0353
Génétique	0369
Limnologie	0793
Microbiologie	0410
Neurologie	0317
Océanographie	0416
Physiologie	0433
Radiation	0821
Science vétérinaire	0778
Zoologie	0472
Biophysique	
Généralités	0786
Médicale	0760

Géologie	0372
Géophysique	0373
Hydrologie	0388
Minéralogie	0411
Océanographie physique	0415
Paléobotanique	0345
Paléocologie	0426
Paléontologie	0418
Paléozoologie	0985
Palynologie	0427

**SCIENCES DE LA SANTÉ ET DE L'ENVIRONNEMENT**

Economie domestique	0386
Sciences de l'environnement	0768
Sciences de la santé	
Généralités	0566
Administration des hôpitaux	0769
Alimentation et nutrition	0570
Audiologie	0300
Chimiothérapie	0992
Dentisterie	0567
Développement humain	0758
Enseignement	0350
Immunologie	0982
Loisirs	0575
Médecine du travail et thérapie	0354
Médecine et chirurgie	0564
Obstétrique et gynécologie	0380
Ophtalmologie	0381
Orthophonie	0460
Pathologie	0571
Pharmacie	0572
Pharmacologie	0419
Physiothérapie	0382
Radiologie	0574
Santé mentale	0347
Santé publique	0573
Soins infirmiers	0569
Toxicologie	0383

**SCIENCES PHYSIQUES**

**Sciences Pures**

Chimie	
Généralités	0485
Biochimie	487
Chimie agricole	0749
Chimie analytique	0486
Chimie minérale	0488
Chimie nucléaire	0738
Chimie organique	0490
Chimie pharmaceutique	0491
Physique	0494
Polymères	0495
Radiation	0754
Mathématiques	0405
Physique	
Généralités	0605
Acoustique	0986
Astronomie et astrophysique	0606
Electronique et électricité	0607
Fluides et plasma	0759
Météorologie	0608
Optique	0752
Particules (Physique nucléaire)	0798
Physique atomique	0748
Physique de l'état solide	0611
Physique moléculaire	0609
Physique nucléaire	0610
Radiation	0756
Statistiques	0463

**Sciences Appliqués Et Technologie**

Informatique	0984
Ingénierie	
Généralités	0537
Agriculture	0539
Automobile	0540

Biomédicale	0541
Chaleur et thermodynamique	0348
Conditionnement (Emballage)	0549
Génie aérospatial	0538
Génie chimique	0542
Génie civil	0543
Génie électronique et électrique	0544
Génie industriel	0546
Génie mécanique	0548
Génie nucléaire	0552
Ingénierie des systèmes	0790
Mécanique navale	0547
Métallurgie	0743
Science des matériaux	0794
Technique du pétrole	0765
Technique minière	0551
Techniques sanitaires et municipales	0554
Technologie hydraulique	0545
Mécanique appliquée	0346
Géotechnologie	0428
Matériaux plastiques (Technologie)	0795
Recherche opérationnelle	0796
Textiles et tissus (Technologie)	0794

**PSYCHOLOGIE**

Généralités	0621
Personnalité	0625
Psychobiologie	0349
Psychologie clinique	0622
Psychologie du comportement	0384
Psychologie du développement	0620
Psychologie expérimentale	0623
Psychologie industrielle	0624
Psychologie physiologique	0989
Psychologie sociale	0451
Psychométrie	0632



**CONSOLIDATED UNDRAINED-TRIAxIAL BEHAVIOR  
OF A SAND-BENTONITE MIXTURE AT  
ELEVATED TEMPERATURE**

**BY**

**BRIAN E. LINGNAU**

A Thesis submitted to the Faculty of Graduate Studies of the University of Manitoba in partial fulfillment of the requirements for the degree of

**DOCTOR OF PHILOSOPHY**

© 1993

Permission has been granted to the LIBRARY OF THE UNIVERSITY OF MANITOBA to lend or sell copies of this thesis, to the NATIONAL LIBRARY OF CANADA to microfilm this thesis and to lend or sell copies of the film, and UNIVERSITY MICROFILMS to publish an abstract of this thesis.

The author reserves other publications rights, and neither the thesis nor extensive extracts from it may be printed or otherwise reproduced without the author's permission.

## ABSTRACT

This thesis is primarily experimental and describes the first triaxial equipment and procedures used at the University of Manitoba for testing a dense sand/clay mixture (buffer) at temperatures of 26°C, 65°C and 100°C.

Three hypotheses are posed in this thesis: (1) buffer responds to elevated temperature in a way similar to lower plasticity clays; (2) a simple macroscopic model can be used to describe the compression and shear response of buffer to temperature; and (3) the concept of effective stress applies to buffer at elevated temperature. The first two hypotheses are proved in this thesis. The third hypothesis has been discussed by another researcher (Yarechewski 1993).

A simple isothermal (pseudo-elastic) macroscopic model of material behavior at elevated temperatures is developed. A more complex thermo-elasto-plastic model is also developed and calibrated. Validation of the models is beyond the scope of this thesis. Reference to 'a model' is intended to mean a generic qualitative model with elements specific to buffer. These elements are discussed quantitatively and are: isothermal curved critical state (CS) envelopes; isothermal Hvorslev surfaces; isothermal yield loci; isothermal hardening laws; and multiple nested state boundary surfaces (SBS). A new pore pressure parameter  $n^*$  which describes anisotropy is developed based on the classical parameters A and B. A method has been developed for determining the yield stresses during undrained shear from pore pressure response. A volumetric thermal expansion coefficient,  $\beta_{st}$ , for the soil skeleton is calculated using concepts from Mitchell (1977), Agar (1984) and Kosar (1989).

Buffer undergoes thermo-plastic straining (compression) during heating and shows anisotropic elastic behavior in shear at elevated temperature. Peak shear strength from individual tests at elevated temperature is lower than at room temperature, yet the peak shear strength envelope at elevated temperature is higher

than at room temperature. The critical state strength envelope in  $q, p'$ -space is curved. This curvature, particularly at low mean effective stresses is greater at elevated temperatures and this indicates a linkage to  $\kappa$ -lines in  $V, \ln(p')$ -compression space which have slopes dependent on temperature. The yield locus of buffer 'shrinks' during drained heating. The pseudo-elastic moduli are greater at elevated temperature than at room temperature. Hardening laws applicable to buffer use separate parallel lines in semi-logarithmic compression space for each temperature. Buffer pore water undergoes thermal expansion and the soil skeleton undergoes thermal compression resulting in expulsion of water from the specimens.

## ACKNOWLEDGEMENTS

I gratefully acknowledge the support of my advisor, Dr. James Graham, throughout my research program. His continuous encouragement, understanding and friendship kept me going when I felt like giving up. He guided me through technical difficulties as a true professional, taught me important research skills, and gave generously of his time.

Many people at the University of Manitoba, too numerous to mention, helped bring this work to completion through friendship and technical assistance. I would like to thank fellow students F. Saadat, A.W-L Wan, K. Osiowy, P. Lach, J.-H. Yin, R. Kenyon, B. Carter, Y. Yuang, R. Chin, D. Yarechewski, N. Tanaka, T. Crilly for their friendship and good humour. N. Lindsay, and I. Trestrail provided office assistance. E. Lemke, N. Piamsalee and M. Green provided technical assistance. Professor Stimpson was a source of inspiration and moral support.

The staff of AECL, Pinawa participated in helpful discussions. In particular, stimulating challenges came from conversations with B. Kjartanson, D. Dixon, and M. Gray.

Financial support was provided by a research contract from AECL, Pinawa and Dr. Graham, U of M Teaching Assistantships, and the ENGAP tutoring program.

Many people from my church took an interest in my progress. I especially thank R. Fullerton, A. Schlick, and F. Saadat for their close friendship. My roommates often furnished me with a fresh perspective.

Last of all I would like to thank my family for their thoughtful support which they expressed in many ways. In particular, I want to express my love and thanks to my mother, Gwendolyn, my siblings Derek, David, Daniel, Barbara, and their families.



## TABLE OF CONTENTS

<i>Title Page</i>	
<i>Approval Form</i>	
<i>Abstract</i>	i
<i>Acknowledgements</i>	iii
<i>Table of Contents</i>	iv
<i>List of Figures</i>	xi
<i>List of Tables</i>	xxv
<i>List of Symbols and Abbreviations</i>	xxiii
1.0 INTRODUCTION	1
1.1 General	1
1.2 Hypotheses	3
1.3 Objectives and Proposed Methodology	3
1.4 Organization of Thesis	4
2.0 LITERATURE REVIEW	8
2.1 Introduction	8
2.2 Properties of Active Clay-water Systems at Elevated Temperature	10
2.2.1 Mineralogy and Hydrothermal Stability	10
2.2.2 Fabric and Structure	12
2.2.3 Index and Material Properties	14
2.2.4 Strength	15
2.2.5 Volume Change	19
2.2.6 OCR and Yield Locus (YL)	21
2.2.7 Measured Swelling Pressure	23
2.2.8 Applicability of Effective Stress at Elevated Temperature	24

		v
	2.2.9 Creep	26
	2.2.10 Hydraulic Conductivity	26
2.3	Thermo-Mechanical Models	27
	2.3.1 Thermo-Elastic (TE)	29
	2.3.1.1 Theory	30
	2.3.1.2 Laboratory Tests and Model Calibrations	31
	2.3.1.3 Model Predictions	32
	2.3.2 Thermo-Elasto-Plastic Models	34
	2.3.2.1 Theory	34
	2.3.2.2 Laboratory Tests and Model Calibrations	36
	2.3.2.3 Model Predictions	37
2.4	Synthesis of Literature	38
2.5	Review of Buffer Research	41
2.6	Temperature Effects on Buffer Behavior	42
3.0	EXPERIMENTAL EQUIPMENT: Hardware, Compliance, and Calibration	44
	3.1 Introduction	44
	3.2 Equipment: Triaxial Apparatus	45
	3.2.1 Ambient Temperature	45
	3.2.2 HITEP Apparatus	46
	3.2.3 Double-walled Apparatus	49
	3.2.4 Membrane Diffusion/Leakage Apparatuses	50
	3.3 Ancilliary Equipment and Calibrations	51
	3.3.1 LVDT	51
	3.3.2 Load Cells (LC)	52
	3.3.3 Pressure Transducers (PT)	54
	3.3.4 Thermocouples (TC)	56
	3.3.5 Resistance Thermal Devices (RTD)	56

3.3.6	Volume Change Devices: VCT, DPT, Burettes	57
3.3.7	Lateral Strain Gauge (LSG)	58
3.3.8	Temperature Control, Heaters and Insulation	59
3.3.9	Automatic Pressure Control System (PCS)	60
3.3.10	Load Frame	61
3.3.11	Compaction Mold/Frame	61
3.4	Data Acquisition (D/A)	61
3.5	Membranes	63
3.5.1	Selection	63
3.5.2	Manufacture	64
3.5.3	Compliance: Extension Tests/Rubber Dummy Tests	65
3.5.4	Diffusion	69
3.5.5	Strength: Test Results and Temperature Effects	69
3.6	System Compliance	70
3.6.1	Triaxial Cell	70
3.6.1.1	Pressure	70
3.6.1.2	Temperature	71
3.6.2	Controller and System Thermal Inertia	71
3.6.3	Side Drainage	71
3.6.3.1	Pressure Effects on Efficiency	71
3.6.3.2	Specimen Confinement	72
3.6.4	Compaction Frame/Mold	72
3.6.5	HITEP Leakage	72
3.6.6	Burette-Water System: Pressure-Volume-Time Response	73
3.6.7	Thermal Stability of Components	73
3.6.8	Room Temperature Response of the HITEP System	74

4.0	TEST PROCEDURES AND BUFFER PREPARATION	75
4.1	Introduction	75
4.2	Test Materials	75
4.3	Specimen Preparation	76
4.3.1	Specimen Compaction	76
4.3.2	Specimen Drainage	78
4.3.3	Specimen Installation	80
4.3.3.1	Ambient Temperature Tests	80
4.3.3.2	HITEP Tests	82
4.4	Consolidation	83
4.5	Heating Procedure	84
4.6	Undrained, Drained Shear	85
4.7	Post-Test Procedure	85
5.0	TEST RESULTS	87
5.1	Introduction	87
5.2	Planning of the test program	87
5.3	Test Results	90
5.3.1	Forming Specimens	90
5.3.2	Consolidation	92
5.3.3	Undrained Shear Tests	99
5.3.4	Drained Shear Tests	110
5.3.5	Buffer Mass Loss Tests (BML)	113
5.3.6	Apparatus Leakage and Membrane Diffusion	116
5.3.7	Membrane/Side Drain Restraint	120
5.4	Preliminary Discussion of Results	121
5.4.1	Failure Patterns in Buffer Specimens	122

6.0	FACTORS AFFECTING INTERPRETATION OF DATA	129
6.1	Introduction	129
6.2	Final Moisture Content of Buffer	130
6.2.1	Average Moisture Content	130
6.2.2	Mass Loss	131
6.2.3	Drying Gradients	136
6.3	Thermal Volume Change	137
6.3.1	Method 1: Pore Water and System Compliance	140
6.3.1.1	Back Calculation	140
6.3.1.2	Forward Calculation	143
6.3.2	Method 2: Pore Water, Pore Void, and System Compliance	146
6.3.2.1	Forward Calculation	146
6.3.3	Method 3: Skeletal Thermal Volume Change	147
6.3.3.1	$\beta_{st}$ (mechanical+thermal compression)	147
6.3.3.2	$\beta_{st}$ (thermal compression)	152
6.3.4	Discussion of Thermal Expansion Calculations	154
6.4	Membrane Diffusion	157
6.4.1	Theory and Calculations	158
6.4.2	Measured Diffusion	160
6.5	Side Drain Restraint and Membrane Modulus	164
6.5.1	Side Drain Restraint	164
6.5.2	Membrane Modulus	164

7.0	SYNTHESIS OF DATA	166
7.1	Introduction	166
7.2	Pore Pressure Parameters	166
7.2.1	Definition of Parameters	166
7.2.2	Graphical and Physical interpretation	167
7.2.3	Pore Pressure Equation (Curve Fit Model)	171
7.2.4	Pore Pressure Equation (Pseudo-Elastic Model)	175
7.2.5	Pore Pressure Parameter $n^*$	177
7.2.6	Discussion	178
7.3	Critical State Data	179
7.3.1	Buffer	179
7.3.2	Synthesis of Other Research	181
7.4	Discussion of Critical State Results	185
8.0	MODELING AND DISCUSSION	186
8.1	Introduction	186
8.2	Isothermal Pseudo-Elastic Model	186
8.2.1	Isothermal Pseudo-Elastic Moduli (First Loading)	187
8.2.2	Isothermal Elastic Moduli (Unload/Reload)	197
8.3	Isothermal-Elasto-Plastic Model	199
8.3.1	Curved CS Envelope	200
8.3.2	Isothermal Curved CS Envelopes	203
8.3.3	Isothermal Peak Strength and Hvorslev Surfaces	212
8.3.4	Isothermal Yield Loci	215
8.3.5	Isothermal Hardening Laws	219
8.3.6	State Boundary Surfaces	222
8.4	Concluding Remarks	226

9.0	REVIEW, CONCLUSIONS, AND SUGGESTED RESEARCH	227
9.1	Discussion	227
9.2	Conclusions	230
9.3	Suggested Research	234
10.0	REFERENCES	236
	FIGURES:	247
	APPENDICES:	422
A	Membrane Corrections	422
B	Moisture Content Data	427
C	Compaction Data	429
D	Membrane Types	431
E	Leakage and Diffusion Tests	433
F	Thermal Expansion Coefficients	438
G	Thermal Expansion Calculations	445
H	Diffusion in Polymers	451

## LIST OF FIGURES

	Page	
FIGURE 2.1	Structure of montmorillonite: (a) schematic representation; (b) molecular interpretation; (c) charge distribution. (after Mitchell 1976)	249
FIGURE 2.2	Bentonite clay autoclaved at 150°C for 0.3 years: (a) general view displaying the microstructural pattern (b) close view of smectite folds and titania inclusion (after Pusch and Güven 1990)	250
FIGURE 2.3	Schematic image of the microstructure of Na bentonite clay. Upper: dense clay with larger voids (A), smaller pores (B), interlamellar space in stacks (C), and interface of adjacent stacks (D). Lower: expanded, soft clay gel. (after Pusch and Güven 1990)	251
FIGURE 2.4	Scanning electron micrographs of buffer: (a) isothermal reference buffer material (b) after exposure to steam. (after Oscarson and Dixon 1990a)	252
FIGURE 2.5	Atterberg limits of high plasticity clay as a function of temperature: (a) plastic limit; and (b) liquid limit. (after Youssef and El Ramli 1961)	253
FIGURE 2.6	Relation between liquid limit $w_L$ and plasticity index $I_p$ for: (a) different temperatures (after Youssef and El Ramli 1961); (b) typical soils: 1, gumbo clays; 2, glacial clays; 3, clay (Venezuela); 4, organic silt and clay; 5, organic clay; 6, kaolin; 7, organic silt and clay; 8, micaceous sandy silt; 9, kaolin-type clays (after Casagrande, 1947); (c) Norwegian marine clays (data from Bjerrum, 1954, 1967).	254
FIGURE 2.7	Deformation response of four marine clays to a temperature cycle of 25°C-50°C-25°C. C1: Deep water 4000m, $w_L = 113$ , CH. C2: Deep water 4000m, $w_L = 93$ , CH. C4: Shallow water 400m, $w_L = 56$ , CH. M1: Deep water 4000m, $w_L = 45$ , ML, Carbonates = 59% (after Demars and Charles 1982)	255
FIGURE 2.8	Drained triaxial compression tests on Pontida silty clay at room and high temperature at confining stress of 0.5 MPa (OCR = 5.0); 1 at 23°C, 2 at 98°C: (a) deviatoric stress versus axial strain; and (b) volumetric strain versus axial strain. (after Hueckel and Baldi 1990)	256



- FIGURE 2.9 Drained triaxial compression tests on Pontida silty clay at room and high temperature at confining stress of 0.2MPa (OCR = 12.5); 1 at 23°C, 2 at 95°C: (a) deviatoric stress versus axial strain; and (b) volumetric strain versus axial strain. (after Hueckel and Baldi 1990) 257
- FIGURE 2.10 Failure stresses in the triaxial tests. Notice the different scales of the axes.  
 X temperature = 22°C  
 ⊗ temperature = 60°C  
 — failure envelope  
 - - Mohr-Coulomb failure envelope  
 (after Börgesson *et al.* 1990) 258
- FIGURE 2.11 Pontida silty clay. Undrained heating test: (a) pore pressure generation (b) effective stress path. 259
- FIGURE 2.12 Oedometer tests on high plastic sensitive marine clays: (a) incremental load tests where the temperature was increased at 40, 50, 60, and 80 kPa, respectively (b) constant rate of strain tests with varying temperature. Clay from Bäckebo. (after Tidfors and Sällfors 1989) 260
- FIGURE 2.13 Effects of temperature variations on saturated illite: (a) on height (b) on volume change (c) on isotropic consolidation (after Mitchell 1976) 261
- FIGURE 2.14 Oedometer tests on clay: (a) 'identical undisturbed' samples of high plastic marine clay at different temperatures (b) preconsolidation pressure evaluated from primary compression, 1 day and 7 days of loading. (after Eriksson 1989) 262
- FIGURE 2.15 Schematic of the yield surface sensitivity to temperature. (after Hueckel and Pellegrini 1991) 263
- FIGURE 2.16 Yield locus response to drained heating at constant  $p'$ : (a)  $q$ - $p'$  stress space interpretation (b)  $V$ - $\log p'$  space, thermomechanical cycle on Pontida silty clay (after Hueckel and Baldi 1990) (c) yield locus interpretation using concepts of plastic volumetric hardening and thermal (elastic) softening 264
- FIGURE 2.17 Triaxial drained compression of normally consolidated specimens of Pontida silty clay 1: at room temperature, 2: at room temperature up to  $q = 1.2$  MPa, followed by Heating up to 100°C and then by further triaxial compression at high temperature-arrows indicate onset and end of heating: (a) stress deviator versus axial strain; (b) volumetric strain versus axial strain; and (c) thermoplastic strain increment vector during heating-vector  $n$  shows plastic strain rate at room temperature in triaxial loading at this stress state. 265

- FIGURE 2.18 Thermomechanical drained loading cycle on Pontida clay: (a) temperature versus effective mean normal stress; (b) temperature versus volumetric strain; and (c) isotropic effective stress versus volumetric strain. (after Hueckel and Baldi 1990). 266
- FIGURE 2.19 Interpretation of thermal strains: (a) classical elastic and plastic strains; (b) volumetric strain versus temperature at constant isotropic effective stress. Drained test: (1) at 2.0 MPa on Pontida clay; and (2) at 6 MPa on Boom clay. (after Hueckel and Baldi 1990) 267
- FIGURE 2.20 Initial yield surfaces for pure aluminum at elevated temperature. (after Phillips 1968) 268
- FIGURE 2.21 Effect of temperature on the undrained strength of kaolinite in unconfined compression. (after Sherif and Burrous 1969) 269
- FIGURE 2.22 Stress paths used in high temperature high pressure triaxial testing of Athabasca oil sand. (after Agar 1984) 270
- FIGURE 2.23 Cam clay representation of yield surface: (a) room temperature; (b) at variable thermoplastic volumetric strain,  $\epsilon_v^{tp}$ , and variable temperature,  $\Delta T$ ; and (c) at constant  $\epsilon_v^{tp}$  and variable  $\Delta T$  (thermoelastic process). (after Hueckel and Baldi 1990) 271
- FIGURE 2.24 Two stress paths and theoretical response at room temperature and at 90°C, according to an associative flow rule. (after Hueckel and Baldi 1990) 272
- FIGURE 2.25 Triaxial tests on Pontida clay: (a) volumetric strain during heating under constant isotropic effective stress conditions, calculated from measured axial strain; (b) volumetric skeleton strain-comparison between measured strain and the free-water prediction. (after Hueckel and Baldi 1990) 273
- FIGURE 2.26 Thermomechanical cycle of loading on overconsolidated Boom clay: (a) strain variation with temperature and pressure loading (inset); (b) stress-strain response. (after Baldi *et al.* 1987) 274
- FIGURE 2.27 Numerical simulation of drained triaxial tests until failure, from Borsetto *et al.* (1987): (a) stress difference versus axial strain; and (b) volumetric versus axial strain. (after Hueckel and Baldi 1990) 275
- FIGURE 3.1 Ambient temperature, high pressure triaxial apparatus 276
- FIGURE 3.2 Schematic diagram of High Temperature, high Pressure (HITEP) cell 277

FIGURE 3.3	High Temperature, high Pressure (HITEP) triaxial cell: (a) with and without insulating jacket; (b) with sleeve lifted.	278
FIGURE 3.4	Schematic diagram of Temperature Control System (TCS) for HITEP cell	279
FIGURE 3.5	The complete HITEP apparatus: (a) temperature controllers and data acquisition system; (b) loading frame (background) and pressure control system (foreground)	280
FIGURE 3.6	Buffer specimen before consolidation. Lateral strain gauge and RTD shown.	281
FIGURE 3.7	Leakage apparatus in HITEP cell	282
FIGURE 3.8	Schematic diagram of membrane diffusion cell	283
FIGURE 3.9	Membrane diffusion apparatus	284
FIGURE 3.10	LVDT calibration at 26°C and 36°C	285
FIGURE 3.11	Pressure dependency of a load cell in HITEP test T1221: (a) load versus elapsed time; (b) pressure versus elapsed time	286
FIGURE 3.12	Temperature dependency of a load cell: (a) output versus applied load at different temperatures; (b) repeatability of output versus applied load at 100°C	287
FIGURE 3.13	Pressure transducer calibrations: (a) effect of elevated temperature; (b) effect of continuous use	288
FIGURE 3.14	RTD calibrations compared to a digital thermometer (D.THER)	289
FIGURE 3.15	Volume change measurement: (a) system response including DPT, burette, fittings, water and data acquisition; (b) DPT signal conversion (Amps to Volts); (c) system response simplified	290
FIGURE 3.16	Lateral Strain Gauge (LSG): (a) isometric view; (b) plan view	291
FIGURE 3.17	Calibration of the Lateral Strain Gauge (LSG)	292
FIGURE 3.18	Schematic diagram of the Pressure Control System (PCS)	293
FIGURE 3.19	Specimen forming apparatus	294
FIGURE 3.20	Specimen compaction mold (foreground) and compaction frame (background)	295

FIGURE 3.21	Improved split mold for forming membranes under pressure and vacuum	296
FIGURE 3.22	Rubber dummy tests: (a) effect of confining pressure; (b) effect of test procedure.	297
FIGURE 3.23	Basic drainage conditions for buffer	298
FIGURE 3.24	Pressure-volume-time response of the back-pressure burettes	299
FIGURE 4.1	Sieve analysis of blended sand used in buffer specimens. (after Dixon and Woodcock 1986)	300
FIGURE 5.1	Bulging of compacted buffer specimens following removal from split mold	301
FIGURE 5.2	Consolidation results from CIU(TXC) test T1221: (a) volumetric strain versus elapsed time; (b) pressure versus elapsed time; and (c) temperature versus elapsed time	302
FIGURE 5.3	Consolidation results from CIU(TXC) test T1220: (a) volumetric strain versus elapsed time; (b) pressure versus elapsed time; and (c) temperature versus elapsed time	303
FIGURE 5.4	Consolidation results from CIU(TXC) test T1222: (a) volumetric strain versus elapsed time; (b) pressure versus elapsed time; and (c) temperature versus elapsed time	304
FIGURE 5.5	Consolidation results from CIU(TXC) test T1222: (a) lateral strain gauge readings versus elapsed time; and (b) temperature vs. elapsed time	305
FIGURE 5.6	Consolidation results from CIU(TXC) test T1225: (a) volumetric strain versus elapsed time; (b) pressure versus elapsed time; and (c) temperature versus elapsed time	306
FIGURE 5.7	Consolidation results from CIU(TXC) test T1233: (a) volumetric strain versus elapsed time; (b) pressure versus elapsed time; and (c) temperature versus elapsed time	307
FIGURE 5.8	Consolidation results from CIU(TXC) test T1235: (a) volumetric strain versus elapsed time; (b) pressure versus elapsed time; and (c) temperature versus elapsed time	308
FIGURE 5.9	Consolidation results from CIU(TXC) test T1227: (a) volumetric strain versus elapsed time; (b) pressure versus elapsed time; and (c) temperature versus elapsed time	309

- FIGURE 5.10 Consolidation results from CIU(TXC) test T1229: (a) volumetric strain versus elapsed time; (b) pressure versus elapsed time; and (c) temperature versus elapsed time 310
- FIGURE 5.11 Consolidation results from CIU(TXC) test T1229: (a) lateral strain gauge readings versus elapsed time; and (b) temperature versus elapsed time 311
- FIGURE 5.12 Summary of triaxial isotropic consolidation results 312
- FIGURE 5.13 Undrained shear results from CIU(TXC) test T1221: (a) deviator stress versus axial strain; (b) pore pressure change versus axial strain; and (c) temperature versus axial strain 313
- FIGURE 5.14 Undrained shear results from CIU(TXC) test T1221: (a) pressure versus axial strain and (b) deviator stress versus mean effective stress 314
- FIGURE 5.15 Undrained shear results from CIU(TXC) test T1211: (a) deviator stress versus axial strain; (b) pore pressure change versus axial strain; and (c) temperature versus axial strain 315
- FIGURE 5.16 Undrained shear results from CIU(TXC) test T1233: (a) deviator stress versus axial strain; (b) pore pressure change versus axial strain; and (c) temperature versus axial strain 316
- FIGURE 5.17 Photographs of specimen T1219: (a) before consolidation; (b) after undrained triaxial shear, CIU. 317
- FIGURE 5.18 Photographs of specimen T1229: (a) before consolidation; (b) after undrained triaxial shear, CIU. 318
- FIGURE 5.19 Photographs of specimens after undrained triaxial shear, CIU: (a) T1209; (b) T1236 319
- FIGURE 5.20 Comparison of results from CIU(TXC) tests,  $\sigma'_{cons} = 0.6$  MPa: (a)  $q$  versus  $\epsilon_1$  (b)  $\Delta u$  versus  $\epsilon_1$  and (c)  $\Delta u$  versus  $\Delta p$  320
- FIGURE 5.21 Comparison of results from CIU(TXC) tests,  $\sigma'_{cons} = 0.6$  MPa: (a)  $\sigma_3$  versus  $\epsilon_1$ ; and (b)  $T$  versus  $\epsilon_1$  321
- FIGURE 5.22 Comparison of results from CIU(TXC) tests,  $\sigma'_{cons} = 0.6$  MPa:  $q$  versus  $p'$  322

FIGURE 5.23	Comparison of results from CIÚ(TXC) tests, $\sigma'_{cons} = 1.6$ MPa: (a) $q$ versus $\epsilon_1$ ; (b) $\Delta u$ versus $\epsilon_1$ ; and (c) $\Delta u$ versus $\Delta p$	323
FIGURE 5.24	Comparison of results from CIÚ(TXC) tests, $\sigma'_{cons} = 1.6$ MPa: (a) $\sigma_3$ versus $\epsilon_1$ ; and (b) $T$ versus $\epsilon_1$	324
FIGURE 5.25	Comparison of results from CIÚ(TXC) tests, $\sigma'_{cons} = 1.6$ MPa: $q$ versus $p'$	325
FIGURE 5.26	Comparison of results from CIÚ(TXC) tests, $\sigma'_{cons} = 3.0$ MPa: (a) $q$ versus $\epsilon_1$ ; (b) $\Delta u$ versus $\epsilon_1$ ; and (c) $\Delta u$ versus $\Delta p$	326
FIGURE 5.27	Comparison of results from CIÚ(TXC) tests, $\sigma'_{cons} = 3.0$ MPa: (a) $\sigma_3$ versus $\epsilon_1$ ; and (b) $T$ versus $\epsilon_1$	327
FIGURE 5.28	Comparison of results from CIÚ(TXC) tests, $\sigma'_{cons} = 3.0$ MPa: $q$ versus $p'$	328
FIGURE 5.29	Summary of stress paths from tests at 26°C	329
FIGURE 5.30	Summary of stress paths from tests at 65°C	330
FIGURE 5.31	Summary of stress paths from tests at 65°C	331
FIGURE 5.32	Summary of stress paths from tests at 100°C	332
FIGURE 5.33	Summary of Peak and End-of-Test strength results 26°C	333
FIGURE 5.34	Summary of Peak and End-of-Test strength results 65°C	334
FIGURE 5.35	Summary of Peak and End-of-Test strength results at 100°C	335
FIGURE 5.36	Comparison of strength envelopes at 26°C, 65°C, and 100°C: (a) Peak; (b) End-of-Test	336
FIGURE 5.37	Summary of critical state lines in $V_c$ versus $\log(p')$ space	337
FIGURE 5.38	Summary of critical state lines and normal consolidation lines in $V_c$ versus $\log(p')$ space	338
FIGURE 5.39	Summary of values of $m = \Delta u/\Delta p$	339

FIGURE 5.40	Drained shear results from CID(TXC) test T1204: (a) deviator stress versus axial strain; (b) pore pressure change versus axial strain; and (c) volumetric strain versus axial strain	340
FIGURE 5.41	Drained shear results from CID(TXC) test T1204: (a) deviator stress versus mean effective stress; and (b) pressure versus axial strain	341
FIGURE 5.42	Effect of silicone oil contamination on the measurement of dry mass of compacted buffer at 110°C	342
FIGURE 5.43	Consolidation results for T1222: (a) volume versus time; (b) pressure versus time; and (c) temperature versus time	343
FIGURE 5.44	Leakage rate in test Leak#1	344
FIGURE 5.45	Diffusion and leakage tests on silicone and latex membranes using different cell fluids. (a) results of diffusion tests on silicone membranes at 26°C, 65°C and 100°C using the diffusion apparatus; and (b) leakage test results for membranes in triaxial cells	345
FIGURE 5.46	Swelling of silicone rubber immersed in silicone oil at 110°C: (a) change in weight of test sample (b) change in circumference	346
FIGURE 5.47	Undrained shear results from CIU(TXC) test TRDC9 (triaxial rubber dummy compression test 9): (a) deviator stress versus axial strain; and (b) pore pressure change versus axial strain	347
FIGURE 5.48	Undrained shear results from CIU(TXC) test TRDC9 (triaxial rubber dummy compression test 9): deviator stress versus mean effective stress	348
FIGURE 5.49	Undrained shear results from CIU(TXC) test TRDC9 (triaxial rubber dummy compression test 9): (a) calculated lateral strain versus measured lateral strain; and (b) Poisson's ratio versus axial strain	349
FIGURE 5.50	Undrained shear results from CIU(TXC) test TRDC2 (triaxial rubber dummy compression test 2): (a) deviator stress versus axial strain; and (b) deviator stress versus mean effective stress	350
FIGURE 5.51	Undrained shear results from CIU(TXC) test TRDC2 (triaxial rubber dummy compression test 2): (a) calculated lateral strain versus measured lateral strain; and (b) Poisson's ratio versus axial strain	351

FIGURE 5.52	Definition of isotropic overconsolidation ratio, $R$ using modified Cam clay: (a) deviator stress versus mean effective stress; (b) clay specific volume versus mean effective stress (log scale); and (c) pore pressure parameter, $a_f$ versus $R$	352
FIGURE 5.53	Failure modes in selected test specimens	353
FIGURE 6.1	Division of buffer specimens for final moisture content determination	354
FIGURE 6.2	Drying curves for natural soils (After Lambe, 1951)	355
FIGURE 6.3	Change in final clay specific volume, $\Delta V_{cf}$ due to correction for oil contamination (Entire buffer specimen): $\Delta V_{cf}$ versus temperature, $T$ ( $^{\circ}\text{C}$ )	356
FIGURE 6.4	Clay specific volume, $V_c$ versus mean effective stress, $p'$ for uncorrected data	357
FIGURE 6.5	Clay specific volume, $V_c$ versus mean effective stress, $p'$ for corrected data	358
FIGURE 6.6	Schematic illustrating different types of water in clay	359
FIGURE 6.7	Back calculation of final specific volume at $26^{\circ}\text{C}$ , $V_{CF}^{26}$ , using measured final specific volumes at elevated temperatures, $V_{CF}^{65}$ [meas], and $V_{CF}^{100}$ [meas]	360
FIGURE 6.8	Forward calculation of final specific volume at $26^{\circ}\text{C}$ , $V_{CF}^{26}$ , using measured initial specific volume of buffer specimens, measured volume changes at elevated temperatures, and thermal expansion coefficients for bulk water.	361
FIGURE 6.9	Prediction of final specific volume at elevated temperatures, $V_{CF}^{100}$ [Predicted] and $V_{CF}^{65}$ [Predicted] using final specific volume measured at room temperature, $V_{CF}^{26}$ [Meas], and thermal expansion calculations for pore water and soil voids.	362
FIGURE 6.10	Data from thermal expansion tests on Na-bentonite showing: (a) percent expansion, and (b) difference between % expansion of porewater and % expansion of bulk water with temperature (after Baldi <i>et al</i> 1991)	363
FIGURE 6.11	Effects of pressure on the specific volume of bulk water (after Eisenberg and Kauzmann 1969). Note: Specific volume of bulk water is defined as the reciprocal of density.	364



FIGURE 6.12	Pressure dependency of $\beta_w$ at (a) 100°C; and (b) 65°C	365
FIGURE 6.13	Coefficient of volume change for thermo-mechanically induced particle rearrangement (skeletal changes)	366
FIGURE 6.14	Calculation of $\beta_{st}$ (a) using $V_{co}$ , $\epsilon_v$ , $\beta_w$ and $\beta_s$ (Forward); (b) using $V_{cf}$ , $\beta_w$ and $\beta_s$ (Backward)	367
FIGURE 6.15	Thermo-mechanical strains for buffer consolidation (path 1-2-3), Inset: Definition of thermo-elastic strain (from Heat-Cool cycle)	368
FIGURE 6.16	Comparison of measured and predicted diffusion rates across a silicone membrane.	369
FIGURE 6.17	Regression of peak and end-of-test data where full length side drainage strips were used.	370
FIGURE 7.1	Definition of pore pressure parameters: (a) $m_Y = \Delta u / \Delta p$ (b) $n_f = -\Delta p' / \Delta q$	371
FIGURE 7.2	Pore pressure parameter $m$ versus consolidation pressure $p'_{Cons}$ for buffer at 26°C, 65°C, and 100°C.	372
FIGURE 7.3	Pore pressure parameter $m$ versus volumetric strain, $\epsilon_v$ , for buffer at 26°C, 65°C, and 100°C.	373
FIGURE 7.4	Stress changes in a Heavily OverConsolidated (H-OC) specimen: (a) $\Delta p'$ values (b) $\Delta u$ values	374
FIGURE 7.5	Pore pressure parameter ' $n_Y$ ' versus consolidation pressure $p'_{Cons}$ for buffer at 26°C, 65°C, and 100°C.	375
FIGURE 7.6	Pore pressure parameter ' $n_f$ ' versus consolidation pressure $p'_{Cons}$ for buffer at 26°C, 65°C, and 100°C.	376
FIGURE 7.7	Pore pressure parameter ' $A_f$ ' versus consolidation pressure $p'_{Cons}$ for buffer at 26°C, 65°C, and 100°C.	377
FIGURE 7.8	Pore pressure parameter ' $A_f$ ' versus volumetric strain, $\epsilon_v$ , for buffer at 26°C, 65°C, and 100°C.	378
FIGURE 7.9	Pore pressure parameter ' $A_{EOT}$ ' versus consolidation pressure $p'_{Cons}$ for buffer at 26°C, 65°C, and 100°C.	379

FIGURE 7.10	Comparison of pore pressure parameters $A_f$ and $A_{EOT}$	380
FIGURE 7.11	Pore pressure parameter ' $A_{EOT}$ ' versus volumetric strain, $\epsilon_v$ , for buffer at 26°C, 65°C, and 100°C.	381
FIGURE 7.12	Definition of isotropic overconsolidation ratio ' $n_p$ ' and parameter ' $r$ '.	382
FIGURE 7.13	Definition of pore pressure parameter $n^* = A_f - m/3$ : (a) referenced to line in q-p' space; and (b) referenced to line $m = 1$ in $\Delta u - \Delta p$ space.	383
FIGURE 7.14	Critical state behavior of pacific illite at elevated temperature: (a) in the q-p' effective stress plane; (b) in the V-log(p') compression plane (After Green 1984)	384
FIGURE 7.15	Power law fit to critical state data for pacific illite (After Green 1984)	385
FIGURE 7.16	Stress paths of CIU(TXC) tests on pacific illite at 4°C, 40°C, 100°C, and 200°C (After Green 1984)	386
FIGURE 8.1	Graphical method for obtaining the secant shear modulus, $G_{50}$ , from CIU(TXC) tests	387
FIGURE 8.2	Normalized shear modulus, $G_{50}/p'_{cons}$ , versus consolidation pressure, $p'_{cons}$ for dense buffer at 26°C, 65°C and 100°C	388
FIGURE 8.3	Normalized shear modulus, $G_{50}/p'_{cons}$ , versus temperature, T, for dense buffer at different consolidation pressures.	389
FIGURE 8.4	Normalized shear modulus, $G_{50}/p'_{cons}$ , versus log of consolidation pressure, $p'_{cons}$ for dense buffer at 26°C, 65°C and 100°C	390
FIGURE 8.5	Comparison of Poisson's ratio, $\nu$ , for T1205, and rubber specimen, TRDC9: (a) $\epsilon_3$ [Meas] versus $\epsilon_3$ [Calc]; (b) Poisson's ratio, $\nu$ , versus axial strain, $\epsilon_1$	391

- FIGURE 8.6 Modified method for calculating Poisson's ratio,  $\nu$ , at low axial strains,  $\epsilon_1$ : 392  
 (a) deviator stress,  $q$ , versus axial strain,  $\epsilon_1$ ;  
 (b) Poisson's ratio,  $\nu$ , versus axial strain,  $\epsilon_1$ .
- FIGURE 8.7 Method of calculating elastic secant modulus,  $G^e$ , from buffer specimen T1228 for unloading and reloading 393
- FIGURE 8.8 State Boundary Surface (SBS) viewed in  $V_\lambda$  space: 394  
 (a) CSL and Yield Loci in  $q$ - $p'$  stress space;  
 (b) Definition of  $V_\lambda$ ; SBS is viewed as a section A-A in the direction of the arrow;  
 (c) appearance of SBS and paths of conventional drained and undrained triaxial compression tests in  $V_\lambda$  space (after Wood 1990)
- FIGURE 8.9 Description of SBS: 395  
 (a) with curved CSL in  $q$ - $p'$  stress space;  
 (b) linear CSL in  $V_c$ - $\ln(p')$  compression space;  
 (c) CSL in  $q/p'$ - $V_\lambda$  space.
- FIGURE 8.10 Comparison of CSL predicted from Equation 8.24 and average critical state data point  $CS_1$  in normalized  $q/p'$ - $V_\lambda$  space. 396
- FIGURE 8.11 Comparison of CSL's at 26°C, 65°C, and 100°C predicted from Equation 8.24 and average critical state data points  $CS_1$ ,  $CS_2$ , and  $CS_3$  in normalized  $q/p'$ - $V_\lambda$  space. 397
- FIGURE 8.12 Average stress paths for 26°C, 65°C and 100°C buffer data in  $q/p'$ - $V_\lambda$  space. Average data points are shown for End-Of-Consolidation (EOC), Yield (Y), Peak (P), and Critical State (CS) 398
- FIGURE 8.13 Critical State data at 26°C, 65°C and 100°C shown in  $q/p'$ - $V_\lambda$  space. 399
- FIGURE 8.14 Description of SBS using normalization to equivalent pressure: 400  
 (a) definition of equivalent pressure,  $p'_e$ ;  
 (b) SBS in  $q/p'_e$  -  $p'/p'_e$  stress space
- FIGURE 8.15 Average data points for EOC, Yield, Peak and Critical State in  $V_\lambda$  space normalized to the 26°C NCL from the current program 401

- FIGURE 8.16 Critical state data for 26°C, 65°C and 100°C in  $V_\lambda$  space normalized to the 26°C NCL from the current program 402
- FIGURE 8.17 Critical state data for 26°C, 65°C and 100°C in q-p' stress space normalized to the 26°C NCL from the current program 403
- FIGURE 8.18 State Boundary Surfaces for 26°C, 65°C, and 100°C interpreted from q-p' stress space normalized to 26°C swelling equilibrium line (SEL). 404
- FIGURE 8.19 Examples of peak strength behavior for specimens at the same effective stress: 405  
 (a) at  $p' = 3.0$  MPa;  
 (b) at  $p' = 0.6$  MPa
- FIGURE 8.20 Hvorslev surfaces interpreted from 26°C, 65°C and 100°C data plotted in q-p' stress space normalized to the 26°C SEL 406
- FIGURE 8.21 Peak strength data at 26°C, 65°C and 100°C plotted in  $V_\lambda$  space and normalized to the 26°C NCL. The Hvorslev surfaces are also shown. 407
- FIGURE 8.22 Yield data (early) and rupture data in q,p'-space. The solid yield locus is the original "first" early locus. The dashed yield locus is the "second" rupture locus 408
- FIGURE 8.23 Average yield data at 26°C, 65°C, and 100°C plotted in q-p' stress space normalized to equivalent pressure from the 26°C SEL. Early yield loci are interpreted for each temperature. 409
- FIGURE 8.24 Yield loci and stress paths for averaged data at 26°C, 65°C, and 100°C in q-p' stress space normalized to equivalent pressure from the 26°C NCL. 410
- FIGURE 8.25 Yield data from 65°C specimens plotted in q-p' stress space normalized to equivalent pressure from the 26°C NCL. 411
- FIGURE 8.26 Stress paths for 100°C specimens plotted in q-p' stress space normalized to equivalent pressure from the 26°C NCL. 412
- FIGURE 8.27 Examples of mean effective stress-volumetric strain behavior due to drained heating and loading: 413  
 (a) For a normally consolidated specimen (NC)  
 (b) overconsolidated specimen (OC).
- FIGURE 8.28 Examples of mean effective stress-volumetric strain behavior due to undrained heating: 414  
 (a) for a NC specimen  
 (b) for an OC specimen

- FIGURE 8.29 Cam-clay type representation of Yield surface: 415  
 (a) Room temperature;  
 (b) at Variable  $\epsilon_v^{ip}$  and  $\Delta T$ ;  
 (c) at constant  $\epsilon_v^{ip}$  and variable  $\Delta T$   
 (after Hueckel and Baldi 1990)
- FIGURE 8.30 Stress paths for randomly selected tests plotted in q-p' stress space normalized to equivalent pressures for each temperature. A single surface is produced for the SBS. 416
- FIGURE 8.31 Representation of SBS: 417  
 (a) constant volume sections in q-p' stress space normalized to equivalent pressures from the 26°C NCL;  
 (b) constant volume sections in normalized compression space
- FIGURE 8.32 Average data points for EOC, Yield, Peak and CS in q/p'- $V_\lambda$  space normalized to NCL's for each temperature. 418
- FIGURE 8.33 Average data points for EOC, Yield, Peak and CS in q/p'- $V_\lambda$  space normalized to SEL's for each temperature 419
- FIGURE 8.34 Hardening laws and SEL's lines in compression space 420
- FIGURE 8.35 Interpretation of swelling equilibrium pressures (SEP's) at elevated temperature: 421  
 (a) from hardening laws at elevated temperature and 26°C SEL;  
 (b) at compaction specific volume

## LIST OF TABLES

	Page	
Table 3.1:	LVDT temperature dependency	52
Table 3.2:	Summary of pressure transducer calibrations	55
Table 3.3:	Details of membrane materials that have been investigated	64
Table 3.4:	Membrane corrections: example calculations. Extension modulus, $E_m$ , from ASTM D4767-88 on 1 cm. wide band of membrane. Membranes are 1.25 mm thick.	67
Table 3.5:	Summary of membrane/side drain compliance tests using rubber dummy specimens. All tests at 26°C for loading condition only. Single membranes only.	68
Table 3.6:	Manufacturer's specifications of room temperature properties of candidate materials.	70
Table 4.1:	Statistical data for specimen preparation	78
Table 5.1:	Summary of test schedule for the HITEP Apparatus	89
Table 5.2:	Summary of drained shear test results at peak deviator stress.	111
Table 5.3:	Summary of normalized drained shear test results at peak deviator stress	112
Table 5.4:	Summary of drained shear test results at end-of-test	112
Table 5.5:	Summary of normalized drained shear test results at end-of-test	113
Table 5.6:	Summary of membrane diffusion/leakage Results from a low pressure triaxial cell at 1.0 MPa effective stress using full size membrane.	116
Table 5.7:	Summary of membrane diffusion/leakage results from diffusion apparatus at 0.6 MPa, 3.0 MPa, 9.0 MPa effective stress. Membrane diffusion area is 1/20 of triaxial membranes.	119
Table 6.1:	Clay specific volume of buffer with and without correction for oil contamination.	134
Table 6.2:	Final clay specific volume of buffer corrected for thermal expansion of bulk water and apparatus water (drain line, porous stone, and transducer housing).	141

Table 6.3:	Calculation of thermal expansion coefficient, $\beta_{st}$ , for 65°C and 100°C	151
Table 6.4:	Summary of thermal expansion coefficients for buffer (average values)	153
Table 6.5:	Diffusion rates (tangent) of silicone oil and water across silicone membranes (Yarechewski unpublished). The system is oil-membrane -water. One membrane (polydimethylsiloxane) 1.2 mm thick was used for all the results reported. The nominal surface area of the membrane was 178 cm <sup>2</sup> .	161
Table 6.6:	Comparison of Young's modulus for buffer, membranes and rubber dummy specimens	165
Table 7.1:	Comparison of values for $n_f$ and $a_f$	174
Table 7.2:	Values of $n_f$ for isotropic and anisotropic elastic soils (after Oswell 1990)	176
Table 7.3:	Summary of critical state differentials	180
Table 8.1:	Undrained secant modulus, $G_{50}$ , from $CI\bar{U}(TXC)$ tests on buffer at 26°C, 65°C, and 100°C. Poisson's ratio, $\nu_p$ , at peak deviator stress shown for tests with Lateral Strain Gauge (LSG) readings	189
Table 8.2	Statistical analysis of shear (secant) modulus, $G_{50}$ , and Young's modulus, $E_{50}$ , at 50% of peak deviator stress, $q_{50}$ , for buffer at 26°C, 65°C, and 100°C. All tests averaged together.	191
Table 8.3	Statistical analysis of shear (secant) modulus, $G_{50}$ and Young's modulus $E_{50}$ at 50% of peak deviator stress for buffer program at 26°C, 65°C, and 100°C.	191
Table 8.4	Poisson' ratio, $\nu$ , at 50% of peak deviator stress, $q_{50}$ , and peak deviator stress, $q_p$ . Selected results are shown for the prototype lateral strain gauge (LSG#1). All results are shown for the modified version (LSG #2).	195

Table 8.5	Average values of Poisson's ratio, $\nu$ , for deviatoric stress ranges: $0.25-0.50q_p$ , $0.25-0.75q_p$ , and $0.25-1.0q_p$ .	196
Table 8.6	Plastic bulk modulus, $K^P$ , for dense buffer at $26^\circ\text{C}$ , $65^\circ\text{C}$ , and $100^\circ\text{C}$ and 1.0 MPa effective stress calculated from equation [8.14]. A $\lambda$ -value of 0.121 is assumed for each temperature	197
Table 8.7	Isotropic elastic moduli from isothermal unload/reload buffer data at $26^\circ\text{C}$ and $100^\circ\text{C}$	199
Table 8.8	Calculation of $M$ and $\kappa$ at $26^\circ\text{C}$ , $65^\circ\text{C}$ , and $100^\circ\text{C}$ for specific volume of 2.252 ( $\gamma_d = 1.67 \text{ Mg/m}^3$ and $w_o = 22.75 \%$ ). Assume: (1) $\kappa$ is constant with stress level (2) the buffer is normally consolidated and (3) that the NCL and CSL coincide in $V-\ln(p')$ compression space.	206



## LIST OF SYMBOLS

- (superscript) indicates line segment
- ' Indicates effective stress
- a Classical pore pressure parameter A; new notation by Wood (1990)
- A Area
- A Area of membrane
- A Classical pore pressure parameter =  $\Delta u / \Delta \sigma_1$  (Skempton 1954)
- AECL Atomic Energy Canada Ltd.
- b Classical pore pressure parameter B; new notation by Wood (1990)
- B Classical pore pressure parameter =  $\Delta u / \Delta \sigma_3$  (Skempton 1954)
- BP Back Pressure =  $u_b$
- c' Effective cohesion
- cons (subscript) 'consolidation'
- C Concentration of diffusing substance (g diffusant/ml polymer)
- CIŪ(TXC) Consolidated Isotropic Undrained (TriaXial Compression test):  
(Bar indicates pore pressure measurement)
- CID(TXC) Consolidated Isotropic Drained (TriaXial Compression test)
- CS Critical State
- CP Cell Pressure =  $\sigma_{3c}$
- CSL Critical State Line
- d Indicates increment
- dp/dx Water vapour pressure gradient across the membrane;
- D Diffusion coefficient ( $\text{cm}^2/\text{sec}$ )
- $D_{10}$  Particle diameter for which 10% passes through a given sieve mesh
- $D_{85}$  Particle diameter for which 85% passes through a given sieve mesh
- DA Data Acquisition
- DW Distilled Water
- DW Double-Walled cell
- DPT Differential Pressure Transmitter
- e Void ratio
- $e_c$  Clay void ratio =  $2.037 \cdot e$
- e (superscript) 'elastic'

E	Young's modulus
$E_{50}$	Pseudo-elastic (first loading) undrained secant shear modulus at 50% of peak deviatoric stress
EOC	End-Of-Consolidation
EOT	End-Of-Test
EIU	Elastic Isotropic Undrained
EAU	Elastic Anisotropic Undrained
f	(subscript) 'failure state'
F	Rate of diffusion (flow rate) per unit area
FC	Factory Calibration
FS	Full Scale
G	Shear modulus
$G_{50}$	Pseudo-elastic (first loading) undrained secant shear modulus at 50% of peak deviatoric stress
$G^*$	Modified shear modulus (Graham and Houlsby 1983)
$G_s$	Specific gravity of soil solids
$G_U$	Undrained shear modulus
$G'$	Drained shear modulus
$G^c$	Elastic shear modulus
HITEP	High TEMperature, high Pressure
$I_L$	Liquidity index = $(w_o - w_L)/I_P$
$I_P$	Plasticity index = $w_L - w_P$
J	Cross coupling modulus
$J^*$	Modified cross coupling modulus (Graham and Houlsby 1983)
K	Bulk modulus
$K^*$	Modified bulk modulus (Graham and Houlsby 1983)
$K'$	Drained bulk modulus
$K^P$	Plastic bulk modulus
LC	Load Cell
LSG	Lateral Strain Gauge
LVDT	Linear Variable Displacement Transducer
L-OC	Lightly OverConsolidated
m	Pore pressure parameter = $\Delta u/\Delta p$
$m_v$	Coefficient of compressibility for one-dimensional compression
M	Slope of the critical state line = $q/p'$

MD	Membrane Diffusion
MDAL	Membrane Diffusion AnaLysis
n	Pore pressure parameter = $-\Delta p'/\Delta q$
$n_p$	Isotropic overconsolidation ratio = $p'_c/p'_i$
$n^*$	Pore pressure parameter = $A - m/3$
N	Intercept of $\lambda$ -line with ordinate axis at $p' = 1$ kPa
NC	Normally Consolidated
NCL	Normal Consolidation Line
NMR	Nuclear Magnetic Resonance
o	(subscript) 'initial state'
OB-ML1	Oil/Buffer Mass Loss test 1
OC	OverConsolidated
OCR	OverConsolidation Ratio = $\sigma'_c/\sigma'_i = \sigma'_{zc}/\sigma'_{zo}$
H-OC	Heavily OverConsolidated
p	Driving vapour pressure (cm Hg)
p	Mean stress = $(\sigma_1 + \sigma_2 + \sigma_3)/3$
$p'_c$	Preconsolidation pressure
$p'_e$	Equivalent effective mean stress
$(p'_e)^{cons, 26^\circ C}$	Equivalent mean effective stress with respect to the 26°C normal consolidation line (NCL)
$(p'_e)^{SEL, 26^\circ C}$	Equivalent mean effective stress with respect to the 26°C swelling equilibrium line (SEL)
$p'_i$	Initial mean effective stress
$p'_s$	Mean effective swelling pressure
p	(superscript) 'plastic'
P	(subscript) 'peak state'
$P_r$	Permeability $\left[ \frac{\text{cc gas (STP) cm (thick)}}{\text{cm}^2(\text{memb}) \cdot \text{sec} \cdot \text{cm Hg} (\Delta p)} \right]$
PT	Pressure Transducer
PCS	Automatic Pressure Control System
PWP	Pore Water Pressure = u
q	Deviator stress = $(\sigma_1 - \sigma_3)$
$q_{50}$	50% peak deviatoric stress

- Q Flow rate of vapour (ml/day) for silicone rubber and water vapour as diffusant,  $= 75P_r \cdot \frac{dp}{dx} \cdot A$ ; The constant 75 is used to convert units of cm Hg. to units of atm.
- r Separation of the CSL and NCL along an URL  $= p'_o/p'_{cs}$
- R Isotropic overconsolidation ratio  $= p'_c/p'_o$
- R<sup>2</sup> Regression coefficient
- RTD Resistance Thermal Device
- RTP Room Temperature and Pressure
- RTV Bulk curing silicone rubber
- sp (superscript) 'stress dependent plastic'
- se (superscript) 'stress dependent elastic'
- s' Abscissa axis in triaxial stress space  $= (\sigma'_1 + \sigma'_3)/2$
- S Degree of saturation (%)
- S Solubility coefficient of the membrane with diffusant (ml(RTP)/ml·cm Hg),
- SD Standard Deviation
- SBS State Boundary Surface
- SEL Swelling Equilibrium Line
- SEP Swelling Equilibrium Pressure
- SM1-1 Silicone Membrane test 1; stage 1
- SML3 Silicone Membrane Leakage test 3
- SCSSS Standard Canadian Shield Saline Solution
- SEM Scanning Electron Micrograph
- STP Standard Temperature and Pressure
- t Time
- t (superscript) time
- t' Ordinate axis in triaxial stress space  $= (\sigma'_1 - \sigma'_3)/2$
- Te (superscript) 'temperature dependent elastic'
- Tp (superscript) 'temperature dependent plastic'
- T Temperature (°C)
- T (superscript) temperature (°C)
- T<sub>TR</sub> Temperature of transducer housing
- TC ThermoCouple
- TCS Temperature Control System

TEP	Thermo-Elasto-Plastic
THE	Thermo-HyperElastic
THO	Thermo-HypOelastic
THERM	Thermistor
TRDC9	Triaxial Rubber Dummy Compression test number 9
u	Pore water pressure
u <sub>b</sub>	Back pressure
u <sub>f</sub>	Pore water pressure at failure = $(u_{top} + u_{bot})/2$
u <sub>top</sub>	Pore water pressure at the top of a specimen
u <sub>bot</sub>	Pore water pressure at the bottom of a specimen
URL	Unload-Reload Line
V	Specific volume of soil in total
V	Volume
V <sub>c</sub>	Clay specific volume = $1 + e_c$
V <sub>s</sub>	Volume of soil solids
V <sub>t</sub>	Total volume of soil = $V_s + V_w$
V <sub>w</sub>	Volume of water
V <sub>w</sub> <sup>BS</sup>	Volume of water in buffer specimen
V <sub>w</sub> <sup>PS</sup>	Volume of water in porous stone
V <sub>co</sub>	Clay specific volume at the beginning of a test
V <sub>cf</sub>	Clay specific volume at the end of a test
$(V_{\lambda}^{cons})^{26^{\circ}C}$	Specific volume normalized to the 26°C normal consolidation line
V <sub>cf</sub>	Final clay specific volume (EOT)
V <sub>cf</sub> <sup>OC</sup>	Final clay specific volume corrected for oil contamination
V <sub>cf</sub> <sup>TA</sup>	Final clay specific volume corrected for thermal expansion of water in the test apparatus
V <sub>cf</sub> <sup>TB</sup>	Final clay specific volume corrected for thermal expansion of bulk water
V <sub>cf</sub> <sup>CTE</sup>	Final clay specific volume corrected for thermal expansion
VDC	Volts Direct Current
VAC	Volts Alternating Current
w <sub>L</sub>	Atterberg limit (liquid limit)
w <sub>P</sub>	Atterberg limit (plastic limit)
x	Space coordinate measured normal to the section

XRD	X-Ray Diffraction
Y	(subscript) 'yield state'
YL	Yield Locus
$\alpha$	Linear coefficient of thermal expansion
$\alpha$	Anisotropy parameter (Graham and Houlsby 1983)
$\beta_s$	Thermal expansion coefficient for mineral solids (1/°C)
$\beta_w$	Thermal expansion coefficient for water (1/°C)
$\beta_w^{65}$	Volumetric coefficient of thermal expansion for water from room temperature to 65°C
$\beta_{cw}$	Thermal expansion coefficient for pore water (1/°C)
$\beta_{st}$	Thermal expansion coefficient for mineral skeleton (1/°C)
$\partial$	Indicates differential
$\delta$	Indicates small finite change in value
$\Delta$	Indicates large finite change in value
$\Delta p$	Change in mean stress
$\Delta u$	Change in pore water pressure
$\Delta T_{max}^{trans}$	Maximum differential temperature across the length of a specimen under transient thermal conditions
$\Delta T_{max}^{ss}$	Maximum differential temperature across the length of a specimen under steady state conditions
$\Delta V_w$	Change in volume of water
$\Delta V_{app}$	Change in volume of apparatus
$(\Delta V_{app})\Delta T$	Change in volume of apparatus due to thermal expansion
$\Delta V_{cf}^{OC}$	Correction to final clay specific volume for oil contamination
$\Delta V_{cf}^{TA}$	Correction to final clay specific volume for thermal expansion of soil and water using a forward calculation
$\Delta V_{cf}^{TB}$	Correction to final clay specific volume for thermal expansion of soil and water using a forward calculation
$\Delta V_w^{65} [Calc]$	Calculated change in volume of water at 65°C
$\Delta V_w^{TR} [Calc]$	Calculated change in volume of water in transducer housing
$\Delta V_{DR}$	Volume of fluid drained

$(\Delta V_d)_{\Delta T}$	Volume of fluid drained due to thermal expansion
$\epsilon_p$	Volumetric strain = $\epsilon_v$
$\epsilon_v$	Volumetric strain = $(\epsilon_1 + \epsilon_2 + \epsilon_3)$
$\epsilon_v$	Total volumetric strain = $(\epsilon_v^{Te} + \epsilon_v^{Tp} + \epsilon_v^{sc} + \epsilon_v^{sp})$
$\epsilon_v^C$	Corrected volumetric strain
$\epsilon_v^{65}$ [Meas]	Measured volumetric strain at 65°C
$\epsilon_v^{TA}$	Volumetric strain due to thermal expansion
$\epsilon_1$	Major principal strain
$\epsilon_2$	Intermediate principal strain
$\epsilon_3$	Minor principal strain
$\epsilon_s$	Shear strain = $2(\epsilon_1 - \epsilon_3)/3$
$\epsilon_s$	Shear strain = $\epsilon_s$
$\dot{\epsilon}_1^q$	Rate of axial strain (in relation to time)
$\gamma$	Density ( $Mg/m^3$ )
$\gamma_c$	Density of clay fraction ( $Mg/m^3$ )
$\gamma_d$	Dry density ( $Mg/m^3$ )
$\gamma_s$	Density of mineral solids ( $Mg/m^3$ )
$\gamma_t$	Density of soil in total ( $Mg/m^3$ )
$\gamma_w$	Density of water ( $Mg/m^3$ )
$\Gamma$	Intercept of $\kappa$ -line with ordinate axis at $p' = 1$ kPa
$\lambda$	Slope of normal compression line in log space = $\Delta V/\ln(p'_1-p'_2)$
$\lambda_c$	Slope of compression line for clay fraction in $V_c, \ln(p')$ -space
$\Lambda$	Hardening parameter = $(\lambda-\kappa)/\lambda$
$\kappa$	Slope of elastic compression line in log space = $\Delta V/\ln(p'_1-p'_2)$
$\sigma'_{cons}$	Effective consolidation pressure = $CP - BP = \sigma'_3$
$\sigma_1$	Major principal stress
$\sigma_2$	Intermediate principal stress
$\sigma_3$	Minor principal stress
$\sigma_z$	Stress at depth z
$\eta$	Slope of a line in q-p' stress space at current stress state = $q/p'$
$\phi'$	Effective angle of friction
$\nu$	Poisson's ratio
$\nu_{50}$	Poisson's ratio at 50% of peak deviatoric stress

## CHAPTER 1 INTRODUCTION

### 1.1 General

International research on the thermal behavior of active materials used to contain nuclear waste is currently active in six nations. Canada is studying processed Na-montmorillonite; Belgium, natural 'Boom' clay (montmorillonite-illite); Sweden, processed Ca-/Na-montmorillonite; Italy, natural 'Pasquasia' (illite) and 'Pontida' silty clay (kaolinite); Japan, processed Ca-/Na-montmorillonite and natural 'Otay' marine clay (montmorillonite); and France, processed Ca-montmorillonite. The following major international research facilities are involved: AECL-Research, Pinawa, Canada; ISMES, Bergamo, Italy; Clay Technology AB, Lund, Sweden; Duke University, Durham, NC, U.S.A.; CEA/ANDRA, Fontenay-Aux-Roses, France; SCK/CEN, Mol, Belgium; and Power Reactor and Nuclear Fuel Development Corporation, Tokai-mura, Japan. Research participants in the Canadian program include: Ontario Hydro, University of Manitoba, Carleton University, McGill University, and University of Alberta.

The Canadian Nuclear Fuel Waste Management Program (CNFWMP) will make use of a multi-barrier system to prevent the escape of radionuclides to the biosphere. The system is being engineered to withstand, for instance, the potential effects of container temperature, groundwater pressure, and chemistry. The proposal for long term disposal of radioactive waste in underground vaults has been discussed by Bird and Cameron (1982). A clay/sand mixture called 'Reference Buffer Material' (RBM) or 'buffer' will be placed around the nuclear waste containers to act as one barrier in the system.

'Buffer' comprises an engineered mixture (50:50 by weight) of processed natural Na-montmorillonite, (sold as Avonseal bentonite by Avonlea Mineral Industries, Regina) and a well graded silica sand from Quebec. This mixture was



developed and 'defined' at the Whiteshell Nuclear Research Establishment of Atomic Energy of Canada Ltd. (AECL) (Dixon and Gray 1985, Dixon and Woodcock 1986). The reference dry density is  $1.67 \text{ Mg/m}^3$ . The dry density corresponds to an ASTM Modified Proctor Dry Density of 95%. In the laboratory studies, specimens are compacted at a water content of approximately 21% to achieve near saturation.

There are many demands placed on the performance of buffer. Among other requirements, it must have sufficient strength and creep resistance to support the weight of the waste containers, be capable of resisting potentially high hydraulic pressures from the groundwater, maintain a low permeability to water, vapor, and diffusion of ions under a design maximum operating temperature of  $100^\circ\text{C}$ , and resist hydrothermal chemical alteration for the life of the facility. The buffer should also be 'self-healing' so that any cracks or fissures that form will close in the repository environment. The major concerns are shrinkage of the buffer due to thermal drying, hydraulic fracture, generation of gas pressure from potential container corrosion, and re-saturation of the buffer. It is not yet clear when these processes would become active relative to each other or how they would interact.

Research by Canadian participants with Pinawa on the effects of temperature on buffer behavior has involved hydrothermal stability (Bird 1982), thermal properties (Radhakrishna 1982), thermal conductivity (Xu *et al.* 1990), hydraulic conductivity (Dixon *et al.* 1987, Oscarson *et al.* 1990), swelling pressure (Oscarson *et al.* 1988), longevity (Oscarson *et al.* 1988, 1990, Oscarson and Dixon 1989, 1990), self-healing properties (Radhakrishna *et al.* 1989), coupled heat and mass flow (Mohamed *et al.* 1990), phenomenological parameters for unsaturated flow (Yong and Xu 1988), diffusion parameters (Mohamed *et al.* 1990), and laboratory model simulations at Ontario Hydro and Carleton University. In addition, the first in a series of in-situ full scale model heater simulation tests is underway at the Underground

Research Laboratory (URL) at Lac du Bonnet, Manitoba.

Research at the University of Manitoba has provided strength and compressibility data and models (Wan 1987, Saadat 1989), an associated elasto-plastic model (Oswell 1991), and time dependent hypoelastic and elasto-plastic models (Yin 1990). This research was all performed at ambient (room) temperature. This thesis focuses on testing of buffer at elevated temperatures and pressures to provide information needed by the AECL program. A simple macroscopic model is developed for strength and deformation of the material.

## 1.2 Hypotheses

The literature review presented in Chapter 2 and previous work on the buffer at room temperature suggests the following hypotheses: (1) buffer responds to elevated temperature in a way similar to lower plasticity clays; (2) the concept of effective stress applies to buffer at elevated temperature; and (3) a simple macroscopic model can be used to describe the compression and shear response of buffer to temperature. The first and third of these hypotheses will be studied in this thesis. The second has received attention in a concurrent MSc. program by Yarechewski (1993).

## 1.3 Objectives and Proposed Methodology

The motivation for this research comes from the need to ensure the mechanical-thermal stability of the buffer. To do so it is necessary to characterize the strength and compressibility of buffer at high temperatures (100°C) and high pressures (10 MPa). The purpose of this research, in part, is to develop a thermo-mechanical model applicable to buffer. In fact, two models are discussed.

It was necessary to design, construct and commission a new high temperature-high pressure triaxial testing facility, and design a test program to

obtain the parameters needed for the buffer model.

The approach taken in this first program is one of simplicity in the design of the test facility, test program, and material models. The nature of the research is primarily experimental.

This thesis focuses mainly on the technical aspects of equipment development and on the test results that have been obtained. It also includes a section on preparing fairly simple models for describing the material behavior. Numerical modeling of the container, buffer, and rock system was not within the scope of this work.

#### **1.4 Organization of Thesis**

The thesis consists of nine chapters.

**Chapter 1:** Introduction

**Chapter 2:** Since this is the first research conducted on buffer at elevated temperature at the University of Manitoba, a general literature review was undertaken to provide background information regarding the effects of elevated temperature on strength, compressibility, swelling behavior, hydraulic conductivity, plasticity, creep, and pore pressure generation of the three principal clay mineralogies: kaolinite, illite and montmorillonite. A synthesis of this literature is presented in Chapter 2. Current thermo-mechanical models for clays are discussed with reference to theory, testing and model predictions. The chapter concludes with a review of buffer research as it relates to the current program.

**Chapter 3:** The experimental equipment, compliance tests, and calibration are discussed in detail. Four types of test apparatus are described. Three of these were modified or built specifically for this program under the author's direction. The apparatus of most interest involves a new high temperature, high pressure (HITEP) triaxial cell with its ancillary equipment. Three of these were designed

and built at the University of Manitoba for this program. No previous facility of this type existed at the university, and perhaps only four or five worldwide. Sample calibrations with temperature are presented for eight types of instruments used with the HITEP apparatus.

Technology was also developed for in-house production of special temperature and pressure resistant membranes used in the triaxial test program. A new lateral strain gage was designed and built for one triaxial apparatus. In addition a temperature control feedback system, and automatic pressure control system were commissioned. Use of geotextile side drains was pioneered in this test program (Oswell *et al.* 1991). Innovative use of differential pressure transmitters (DPT) allowed precision automatic volume change recording (Oswell *et al.* 1989).

**Chapter 4:** This chapter discusses specimen preparation, installation, heating method, and specimen removal. Where applicable, ASTM standards were adhered to. In some instances new procedures were developed because no standards are available for elevated temperature testing. These were refined as experience was obtained.

**Chapter 5:** The test program is outlined in tabular form, and results from the triaxial consolidation and shear testing are given. The test procedures and operator influence in the current program is calibrated against previous buffer research at ambient temperature by duplicating several earlier tests. A subsidiary study of buffer mass loss due to cell fluid contamination is investigated.

A preliminary discussion of results from the program shows that no severe changes in buffer behavior are caused by 100°C temperatures. However, measurable changes in volume, pore pressures, stiffness, and strength are seen. Buffer behaves like a less plastic material at elevated temperature.

Brittle/ductile behavior is discussed in relation to strain softening and bulging failures in specimens.

**Chapter 6:** This chapter discusses potential sources of error in the analysis of the

data. It shows that contamination of buffer with cell fluid does not significantly affect the final water contents. Sources of error in water content due to drying gradients are minimized. Diffusion of fluids across the membranes is measured and a comparison with calculated theoretical values shows limited agreement. The rate of diffusion is compared to the criterion chosen to define end-of-consolidation.

Pore pressure parameters are developed to account for thermal expansion of the buffer constituents.

Corrections for thermal expansion of water in the drainage lines and porous stones are examined. Coefficients of thermal expansion for the pore water, system compliance, and soil skeleton are suggested.

The influence of membrane stiffness and side drainage strips on specimen restraint are discussed.

**Chapter 7:** This chapter synthesizes buffer behavior with reference to pore pressures and critical state strength. Graphical techniques are used to develop two pore pressure equations based on classical pore pressure parameters A and B. A new pore pressure parameter  $n^*$  is discussed. Critical state data from the current program of testing and other research (Green 1984) are synthesized and compared. Results for Pacific illite from Green's thesis (1984) are plotted in  $q-V-\ln p'$  space.

**Chapter 8:** Here, test results are synthesized to form elements of two macroscopic models: (1) an isothermal pseudo-elastic model with temperature dependent bulk and shear moduli; and (2) an isothermal elasto-plastic model. These are not complete models. The observed thermal and mechanical behavior of buffer used to develop elements of each model are compared to behavior of other clays at elevated temperature. It is shown that volume change parameters are independent of back pressure at elevated temperature. A temperature-dependent hardening law is developed as part of an isothermal elasto-plastic model.

Peak and critical state behavior at elevated temperature is investigated. Criteria are defined for choosing the Normal Consolidation Line (NCL) and Critical State Line (CSL), and for determining if critical state has been reached.

Phenomenological behavior that was seen in the other clays discussed in Chapter 2 (for example, thermal softening and volume reduction) is also observed in buffer. The strength of buffer increases at elevated temperature, although it also becomes a little more brittle.

**Chapter 9:** The thesis finishes with conclusions, recommendations for further work, and a single set of combined references.

Figures are included at the end of Chapter 9, after the 'List of References'. Data are included in brief summary tables within the text of each chapter. Selected data are included in the Appendices.

## CHAPTER 2 LITERATURE REVIEW

### 2.1 Introduction

Chapter 1 presented three hypotheses in relation to dense buffer. They can be briefly restated as: (1) buffer responds to elevated temperature in a way similar to lower plasticity clays; (2) the concept of effective stress applies to buffer at elevated temperature; and (3) a simple macroscopic thermo-mechanical model can be used to describe the compression and shear response of buffer to temperature.

This chapter describes the background to each hypothesis. The behavior of buffer in response to temperature changes is compared to that of low plasticity clays. This comparison has been made because a literature review revealed very little information regarding the effects of elevated temperature on the compressive and shear behavior of active clays. No information was available on sand-clay mixtures like buffer. Since this is the first thesis on the influence of elevated temperatures on the stress-strain behavior of clay-sand mixtures, an extensive literature search formed a significant part of the project.

A large body of literature in the soil sciences and soil physics discusses the microstructural behavior of active clays. Direct information pertaining to temperature effects on the structure and moisture changes in montmorillonites is available, but there is no information on the mechanical properties being sought in this thesis. The approach taken here is to discuss the physical and chemical properties and existing thermodynamic theories in relation to the effects of temperature on interparticle stresses. This provides an indirect theoretical link between temperature and effective stress in active clays.

Three classes of thermomechanical models are discussed in general terms in the following sections. Emphasis is placed on the first class of models which

includes thermo-elastic and thermo-elasto-plastic models. The thermo-elastic model is attractive because it is theoretically simple and requires only one or two soil parameters which are easily obtained from a small number of simple triaxial tests. However, its use is probably limited to small strains. The thermo-elasto-plastic model is attractive because it captures many aspects of soil behavior, is more fundamentally correct than other classes of models, and has good predictive capabilities for larger strains. The remaining two classes of models are considered less important, and will be given less attention.

The implications of the models for this research program will be addressed in the following text. Models developed for non-buffer materials will be discussed first, followed by models for buffer.

The principal focus of this research is experimental. An ongoing review of current technology was undertaken during this program to design, build, then improve an efficient, reliable, and economic test facility. The type of soil model being examined determined the types of tests performed and influenced the design of the experimental equipment. Indeed, the model, the design of the test program, and design of the equipment were almost inseparable at times. For this reason, an incremental approach to equipment design and commissioning was taken. Individual components were developed, and new ones added, when the technology was proven reliable.

Little or no information was available in the literature for the design of high temperature soil testing equipment and for soil testing techniques. As a result, innovation was required in much of the design and construction of the test facility and test program. The pertinent literature is referenced in Chapters 3 and 4.



## 2.2 Properties of Active Clay-water Systems at Elevated Temperature

### 2.2.1 Mineralogy and Hydrothermal Stability

In order to understand and interpret the volume change and shear strength of clays at different temperatures it is necessary to appreciate how the mineralogy affects the microstructure, fabric, macrostructure and chemistry. This research is primarily related to Na-montmorillonite, a member of the smectite mineral group.

Smectites are generally highly expansive minerals with a structure similar to pyrophyllite and hydrous mica. Figure 2.1 (a) is a schematic drawing of the structure. Montmorillonite particles, or flakes, consist of a sheet of octahedrally bonded alumina ions called 'gibbsite' (G) sandwiched between two sheets of tetrahedrally bonded silica ions. Oxygen or hydroxyl groups bond to the alumina and silica ions and hydrogen bonds hold the three sheets together. Figure 2.1 (b) shows the atomic structure of a flake and a separate silica sheet. The mineral flakes are weakly attracted to each other by Van der Waals forces. The charge distribution of dehydrated montmorillonite (pyrophyllite) is shown in Figure 2.1 (c). Water is adsorbed to the surface of the mineral flakes in layers 9 Å thick. A comprehensive description of the mineralogy, atomic structure and bonding is given by Grim (1953), Mitchell (1976) and Gillott (1987).

Recent X-ray diffraction (XRD) studies support the evidence for three hydrate (water) layers, 9 Å thick, in Na saturated montmorillonite. Pusch (1991) suggests that these hydrate layers exist within the flakes, that is, between the tetrahedral and octahedral sheets. (The first hydrate layer is the thinnest and most strongly adsorbed). However, proton Nuclear Magnetic Resonance (NMR) suggests that one or two hydrate layers exist in Na-montmorillonite at 20% water content and dry densities of 1.6 Mg/m<sup>3</sup> (Pusch 1991). There is still controversy in the literature regarding the structure, density, viscosity and chemistry of adsorbed water (Frenkel 1946, Ravina and Low 1972, Low 1976, 1979, Derjaguin *et al.* 1983,

Israelachvili and Pashlay 1983, Oliphant and Low 1983). Thermal expansion of water in clay gels has received considerable attention (Grim 1953, Clementz and Low 1976, Ruiz and Low 1976, Low 1979, and Derjaguin *et al.* 1983). Skinner (1966) provides thermal expansion coefficients for various minerals. McKinstry (1965) examined thermal expansion coefficients for clay minerals in the two major axes.

Aluminum di-octahedral smectites (montmorillonite) are by far the most common in nature and they are often found in bentonites. The term 'bentonite' describes a high plasticity, swelling clay (rock) while montmorillonite is a mineral (Mitchell 1976, Güven 1990). Montmorillonites are subdivided into several varieties according to their type, locality, or special chemistry, for example: (1) Wyoming-type montmorillonite, (2) Otoy-type montmorillonite, and (3) Fe-rich montmorillonite. Each of these may display different physical properties and thermal stabilities due to chemical, morphological, and textural difference (Güven, 1990).

Montmorillonite is gradually converted to illite with elevated temperature. Güven (1990) synthesized the literature of experimental studies on hydrothermal reactions of aluminous smectites and found that reaction factors such as pore fluid chemistry including its pH and  $E_H$  (redox potential), the interlayer cations and temperature control the reaction kinetics. The role of the interlayer cation is paramount, while temperature is secondary, especially below 100°C. Güven (1990) calculated the time required for conversion of K-smectite to illite: one million years at 50°C, 20,000 years at 100°C; and 99 days at 393°C, provided pH and Eh conditions in the pore water remain within moderate regimes. Non-expandable 'illite' layers formed in the 250-400°C range can be re-expanded upon saturation with  $Na^+$ .

Natural alteration of bentonite often occurs by percolating hydrothermal solutions in the 80-200°C range over millions of years. These illite/smectite

materials maintain 50% expandabilities and illite morphologies (Inoue *et al.* 1987, 1988).

### 2.2.2 Fabric and Structure

To characterize properties such as strength, permeability, compressibility, and deformation modulus of fine grained materials, especially active clays, it is necessary to understand both the structure and fabric of the clay. Macroscopic features, such as stratification, fissuring, voids and inhomogeneities, may be determinative in an analysis of stability, settlement, or seepage (Rowe 1972).

The term 'fabric' refers to the arrangement of particles, particle groups, and pore spaces in a soil. The term 'structure' is given the broader meaning of the combined effects of fabric, composition, and interparticle forces (Mitchell 1976). Emphasis in this research is placed on a qualitative understanding of microstructure and fabric and quantitative understanding of macrostructure. Microstructure refers to structure quantified at a microscopic scale.

Dense active clays like the bentonite in buffer typically have aggregated (face-to-face) particles and flocculated (edge-to-edge, edge-to-face) particles at the microscopic scale and form macroscopic peds or blocks depending on the method of compaction and water content (Wan 1987)

Montmorillonite particles appear as thin platelets, or large, flexible films. The particles occur in aggregates with various textures: foliated aggregates of thin films, compact aggregates of platelets, mossy flocks and fine granular (globular) agglomerates (Güven 1990).

Pusch and Güven (1990) aged dense Na-bentonite from Wyoming ( $2.0 \text{ Mg/m}^3$ ) in distilled water for about 3 months at  $150^\circ\text{C}$  and  $200^\circ\text{C}$ . No mineralogical or chemical changes were observed in the smectite particles, but subtle changes in the microstructure were noticed. A network of thin, branch-like, smectite layers

surrounded small and large elongated pores. With increasing temperature, the branches appeared more compact and pores became larger. Micrographs in Figure 2.2 show the microstructure. A schematic diagram of the fabric is given in Figure 2.3. This behavior would explain the decreased swelling pressure and increased hydraulic conductivity of dense partly saturated Na-bentonite heated in a closed system (Oscarson and Dixon 1990a). Micrographs of the unheated and heated bentonite are given in Figure 2.4. Only slight differences in fabric are noticeable, like the network described by Pusch and Güven (1990).

Pressure during consolidation induces preferred orientation of fabric elements. Electron microscope studies show that voids are already anisotropic and preferentially aligned at right angles to the direction of applied pressure at 0.01 MPa in consolidated kaolin (McConnachie 1974). As the pressure is increased the voids decrease in size and breadth, but without any increase in the degree of horizontal alignment of the voids.

Clay density plays an important role in the types and structure of clay-water systems, and is therefore also a governing factor in the response of clays to elevated temperature. Here, clay-water is used in a general sense regardless of type or structure, and includes all water contained in clay.

It is apparent that three types of water exist in active clays: (1) free water in large pores; (2) interlamellar (bound) water consisting of Stern (surface) water and diffuse layer water between the flakes; and (3) structural (intralamellar) water in the crystal structure of the mineral flakes.

Pusch *et al.* (1991) estimates that 10% of the total water volume in Na-montmorillonite is interlamellar (between mineral flakes) at a clay bulk density,  $\gamma_d$ , of 1.22 Mg/m<sup>3</sup>, but 96% of the total water volume is interlamellar at  $\gamma_d$  of 1.67 Mg/m<sup>3</sup>. The interlamellar water is an ordered medium often known as the Diffuse Double Layer (DDL), through which interparticle forces are established and

transferred. It contains non-associated molecules in a relatively free state (dynamic adsorption phase). There does not appear to be agreement on the density of interlamellar water, but recent studies indicate density may oscillate between  $1.0 \text{ Mg/m}^3$  and  $1.05 \text{ Mg/m}^3$  depending on distance from the mineral particles.

Kay and Low (1975) suggest that DDL water in montmorillonite is ordered, even in systems with a high water content, for example 3% clay in a suspension. They propose (1) a 'mixture' model of open structure polymer molecules and (2) a 'continuum' model of oriented individual water molecules. The mixture model refers to random collection of molecules of different sizes and shapes. Both models would experience expansion or contraction, and structural rearrangement or relaxation, when temperature or pressure is changed. Relaxation in the mixture model results in bond breakage and less order, but results only in bending of bonds in the continuum model.

In summary, it is reasonable to assume that heating of active clay minerals, such as Na-montmorillonite leads to bending, breaking, and formation of water-clay, water-water interatomic bonds (Kay and Low 1975), expulsion of water from interlamellar spaces to micropore spaces (Pusch and Güven 1990), and bending of larger clay particles (Murayama 1969). These processes may lead to accumulation of potential energy in bent atomic bonds and deformed clay particles, which would help explain the observed partial reversibility of thermal deformation, volume change and changes in strength of clays upon heating and subsequent cooling (Mitchell 1969, 1976, Green 1984, Hueckel and Baldi 1990).

### 2.2.3 Index and Material Properties

Clay soils are less plastic at elevated temperature. Youssef and Ramli (1961) showed that the Atterberg limits and Plasticity Index of a medium plasticity clayey silt were lower at elevated temperature ( $35^\circ\text{C}$ ) than at room temperature.

Their results are given in Figure 2.5(a) and Figure 2.5(b). Laguros (1969) showed similar findings for montmorillonite and illite. Work by Chandrasekharan *et al* (1969) also supports this finding. The change in plasticity in medium plastic clay is due entirely to the change in the viscosity of water (Youssef and Ramli 1961). Soft clays experience a larger decrease in plasticity than stiff clays.

Increased temperatures move the data points for clay on Casagrande's chart parallel to the A-line in the direction of decreasing liquid limit as shown in Figure 2.6 (a). A variety of natural clay soils are shown in Figure 2.6 (b) for comparison. Figure 2.6 (c) shows the effects of leaching on the plasticity of clay. The effect is similar to that of temperature.

High plasticity clays experience a larger decrease in plasticity than medium plasticity clays at elevated temperature ( Laguros 1969). Buffer would likely show a much larger change in plasticity than Laguros' montmorillonitic sample ( $\Delta I_p = -30\%$ ) because (1) buffer is tested over a larger temperature range ( $\Delta T = 75^\circ\text{C}$  compared to  $34^\circ\text{C}$  in Laguros' tests); and (2) buffer has a higher liquid limit (260%). Such tests have not been carried out on buffer.

Heating-cooling cycles of  $25^\circ\text{C}$  in normally consolidated (low to high plasticity) clays produced unique permanent reduction in volume, independent of effective stress, and related directly to plasticity; with a larger reduction being observed for higher plasticity (Demars and Charles 1981). This is shown in Figure 2.7.

#### 2.2.4 Strength

The first part of this section will discuss peak strength and the second part will discuss critical state strength behavior. Generally, in engineering materials, rock, and shale, elevated temperatures enhance ductility or reduce brittleness (Heuze 1983). This is not always true of soils due to the volume

changes and shear stresses caused by temperature changes. Hueckel and Baldi (1990) observed increased ductility and decreased dilative behavior at elevated temperature for Pontida silty clay as shown in Figure 2.8. A more pronounced effect occurs at high overconsolidation ratio (OCR) as shown in Figure 2.9. OCR is the ratio of past highest stress to present stress.

Strength and effective stress levels in undrained tests decrease with increasing temperature when the water content and fabric are held constant during heating (for example, Mitchell 1969, Sherif and Burrous 1969, Murayama 1969). In contrast, effective stresses increase under drained conditions (Mitchell 1976). An increase in temperature affects undrained compressive strength similar to an increase in moisture content, independent of the initial moisture content (Sherif and Burrous 1969).

In contrast with some of the previous findings, Green (1984) found higher undrained peak strength and stiffness with increasing temperature, and considerable post peak softening. However, she consolidated her specimens at elevated temperature and this resulted in lower void ratios compared to room temperature specimens. After temperature and pore pressure equilibrium was established, she failed the specimens at constant temperature in undrained shear. Her observed 'brittle' behavior seems contradictory to more recent work (Hueckel and Baldi 1990, Baldi *et al.* 1988). There are three reasons in addition to the volume changes mentioned previously: (1) she tested at effective stresses an order of magnitude lower than others; (2) she tested at high temperatures (200°C) which may produce mineralogical changes; and (3) she tested a cemented natural marine clay. Similar findings to Green's were reported by Noble and Demirel (1969) and Williams (1984). Laguros (1969) showed increased strength, but he compacted his specimens at elevated temperature.

Drained peak strength at elevated temperature is stress level dependent.

Figure 2.9 shows a large change in peak strength of a low plasticity kaolinitic clay (Pontida clay) at elevated temperature and with an OCR of 12.5. Figure 2.8 shows only a slight change in peak strength with an OCR of 5.0.

The undrained triaxial shear strength of Ca-montmorillonite increased slightly (10%) with temperature from 22°C to 60°C at effective stresses of 0.2 MPa to 8.0 MPa (Börgesson *et al.* 1990). Figure 2.10 shows a curved failure envelope in  $q$ - $p'$  stress space. The angle of friction decreased with increasing density, but increased with increasing temperature.

Critical state ('large strain' or 'end-of-test' failure) strength of Pontida clay is shown in Figures 2.8 and 2.9. It can be seen that the strength of Pontida clay is unchanged by temperatures of 95°C. That is, the  $q/p'$  ratio at critical state is unchanged by temperature ( $q = \sigma_1 - \sigma_3$ ;  $p' = (\sigma_1 + 2\sigma_3)/3$ ). Boom clay, on the other hand, had a 20% increase in  $q/p'$  at elevated temperature (Hueckel and Pellegrini 1989). This may be because Boom clay contains smectite and has more adsorbed water than Pontida clay. Adsorbed water in smectites is susceptible to loss of its special structure due to heating starting at 70°C (Khitrov and Pugin 1966, Derjaguin *et al.* 1986, Pusch and Güven 1988, Pusch *et al.* 1991). Green (1984) also shows that critical state strength is virtually independent of temperature. Her data has been replotted in Chapter 8. In  $q$ - $p'$  space the slope of her CS line increased slightly up to 100°C, then decreased at 200°C.

Hueckel and Pellegrini (1991) showed that undrained heating of Boom clay at constant  $q$  can lead to failure. Curve 'a' of Figure 2.11 shows a heated test compared to a reference unheated test, curve 'b'. Thermal failure in saturated clays of low porosity is associated with pore pressure build-up and thermoplastic compressive strain in the skeleton. At low porosity, the skeletons of NC and OC clays behave differently. In normally consolidated (NC) clays, volumetric strains



are much larger than in overconsolidated (OC) clays, and mostly irreversible and compressive. In OC clays thermally induced volumetric strains are either expansive or compressive depending on the OCR, and mostly reversible.

Thermomechanical failure may be essentially a mechanical phenomenon (Hueckel and Pellegrini 1991) because it occurs when the effective stresses reach critical state. For a given total stress path, the level of pore pressure leading to failure is independent of temperature, but depends on the initial stress conditions and friction angle. On the other hand, the temperature required to produce failure depends on the elastic bulk modulus, the individual thermal expansion coefficients of clay and water, temperature dependence of the yield locus (discussed in section 2.2.6), initial stress state, friction angle, and OCR. Cohesion in montmorillonite showed a stronger correlation with dielectric constant than friction angle (Sridharan *et al.* 1979).

Plastic deformation, leading to failure, occurred at 60 to 90°C in undrained tests on Boom clay, Pasquasia clay and remolded Pontida silty clay (Hueckel and Pellegrini 1989).

Green (1984) performed undrained shear tests on specimens which were subjected to a heating/partial cooling consolidation cycle. These were called 'thermally rebounded' specimens. These specimens showed much smaller increases in pore pressures during undrained shear than monotonically heated specimens with the same shear test temperature (Green 1984).

Increased temperatures may produce weakening through decreased water viscosity, but corresponding increases in density offset this. Therefore, heating causes drained strengths and stiffnesses to increase.

### 2.2.5 Volume Change

To characterize the strength of active clays it is also necessary to know how density and volume changes respond to temperature changes.

Heat causes compressive volumetric strains in clays (Tidfors and Sällfors 1989). Results from a sensitive, high-plasticity marine clay tested in incremental load oedometer tests are shown in Figure 2.12 (a). Constant rate of strain tests on the same clay are shown in Figure 2.12 (b). Thermally induced volumetric strains are smaller in OC clays than NC clays. Figure 2.13 (a) shows this behavior for illite. Compressive reversible strains occur on heating OC clays; compressive irreversible strains occur in NC clay. Drained triaxial consolidation tests on illite show significant permanent volume decreases during initial temperature increases (Mitchell 1969). Temperature increase under drained constant effective stress conditions, followed by cooling, has an effect similar to overconsolidation (Plum and Esrig 1969, Demars and Charles 1981).

Kaolite, illite, and montmorillonite all show similar temperature dependence in their  $\lambda$  and  $\kappa$  lines respectively, the slopes of the normally consolidated and overconsolidated regions of behavior in plots of  $V$  versus  $\ln p'$ . The slopes all remain approximately constant, but the lines shift toward decreasing void ratio with increased temperature from 2°C to 36°C (Laguros 1969). Mitchell's results for illite confirm this behavior in Figure 2.13 (b). Similarly, the compression index,  $C_c$ , at high confining stress is unchanged with temperature (Plum and Esrig 1969, Campanella and Mitchell 1968). Demars and Charles (1981) used higher pressures, temperatures and OCR values than the former authors. In doing so, they showed that permanent volume reduction caused by temperature cycles of 25°C is independent of confining stress in NC illite, but dependent on soil type and plasticity. In OC soil, the permanent volume change is pressure and temperature dependent. Some clays such as the high plasticity sulphide rich marine

clay tested by Eriksson (1989) show temperature dependence of  $\kappa$ . Figure 2.14 (a) shows that the value of  $\kappa$  increases with elevated temperature for this clay.

The coefficient of consolidation is unchanged except for kaolinite which shows decreased  $C_v$  with increased temperature.

Temperature effects can be as important as pore fluid chemistry in the compressive behavior of smectite at temperatures of 100°C for typical test durations of 30 days. For example, an order of magnitude increase in temperature from 2°C to 20°C produces a 10% compression in montmorillonite at 22% moisture content (Laguros 1969). Interpreting results from Mesri and Olson (1971), an order of magnitude increase in pore fluid salinity from  $10^{-1}$ N causes about 10% compression in Na-montmorillonite at an equivalent starting moisture content. The effects of chemical and temperature changes on compression become very important in Na-montmorillonite at high moisture contents.

Heating followed by cooling causes a combination of plastic and elastic volumetric strains, (Mitchell 1976, Eriksson 1989, Tidfors and Sällfors 1989). This is shown in Figure 2.13 (b). Demars and Charles (1988) subjected a high-plasticity marine clay to 25°C temperature cycles. In NC clay there was a permanent decrease in void ratio independent of effective confining stress. Overconsolidated clay had changes in void ratio that were stress level dependent.

Thermal volume change in the pore water results from thermal expansion of the bulk water and the release of interlamellar water (Claesson *et al.* 1986, Derjaguin 1987, Pusch and Güven 1990). In low porosity clays, the thermal expansion of adsorbed water is smaller than that of bulk water (Baldi *et al.* 1988). However, as clay density increases, the thermal expansion of adsorbed water approaches that of bulk water. For example, the thermal expansion of pore water in Na-bentonite heated to 100°C, at a dry density of  $1.09 \text{ Mg/m}^3$ , is 91% of bulk water

(Dixon 1991). A useful approximation may be to assume that all water in dense active clays has the thermal expansion coefficient of bulk water.

Attempts have been made to predict volume changes, swelling pressure, and particle spacings in active clays due to physical, chemical and thermal gradients using variations of diffuse double layer (DDL) theory (Van Olphen 1963, Mesri and Olsen 1971, Yong and Warkentin, 1975, Mitchell 1976, Low 1980, Sridharan and Jayadeva 1982, Oliphant and Low 1983, Viani *et al.* 1983, Dixon *et al.* 1987, Barbour and Fredlund 1989). While most claim accurate predictions for material characterization of gels and low density soils (sols), the findings are less convincing for dense clays. The main difficulties regarding temperature predictions are (1) temperature is implicit in the governing equations; and (2) properties such as the dielectric constant of water are temperature dependent, and are unknown at the clay-water interface. Moreover, there is no reason to expect DDL theory to apply to dense clays because most of the water is likely contained in the Stern layer rather than in the adsorbed layers. Diffusion theory may provide a more rational approach since low porosity clays such as the buffer behave more like semi-permeable membranes.

#### 2.2.6 OCR and Yield Locus (YL)

The preconsolidation pressure in isothermal tests of active clays decreases with increasing temperature (Eriksson 1989). This is shown in Figure 2.14 (a). There is a noticeable similarity to the effect of time shown in Figure 2.14 (b). In a similar way, Hueckel and Pellegrini (1991b) showed that undrained heating at constant  $q$  implies thermal softening, or shrinkage of the yield locus (YL). The yield locus is sensitive to temperature variations as shown in Figure 2.15.

Drained heating at constant  $p'$  does not change the size of the yield locus in  $q$ - $p'$  stress space (Figure 2.16 (a)). However, plastic volumetric strains occur

during the heating. Results from Hueckel and Baldi (1990) have been replotted in Figure 2.16 (b). They interpreted this as plastic volumetric hardening simultaneous with thermal (elastic) softening. A graphical simplification is given for the first time in Figure 2.16 (c). In  $V-\ln p'$  space, thermal softening is interpreted as shrinkage of the YL relative to the stress-strain state at room temperature. At elevated temperature the clay behaves NC even though it is OC relative to room temperature state.

The peak and failure strengths appear to be unaffected by drained heating of this clay in the plotting used in Figure 2.17 (a). This would appear consistent with a constant YL. Plastic strain increments during heating at constant  $q$  are mostly volumetric as shown in Figure 2.17 (c). As in the Cam clay model, the direction of the strain increment vector at elevated temperature indicates whether strain hardening or softening will occur under mechanical loading (Hueckel *et al.* 1987a, 1987b). However, this does not imply that the associated flow rule is necessarily the same at low and high temperature (Hueckel and Baldi 1990). It will be shown later that the behavior of buffer is more complex than suggested by this model.

No plastic strain increment is produced during cooling, but the yield surface expands and the stress point remains fixed in the interior of an elastic domain. Figure 2.16 (b) shows heating BC followed by cooling CD. After cooling, loading produces elastic deformation, DE until the expanded yield surface is reached, and thereafter plastic deformation, EF (Hueckel *et al.* 1987).

Hueckel and Baldi (1990) investigated the evolution of a yield surface using an elaborate loading temperature cycle on Pontida clay, Figure 2.18 (a). The results of their test are shown in Figure 2.18 (b) and (c). This confirms previous observations. None of this work has been done on high plasticity clay like that studied in the present investigation.

Clay content and water content govern the effect a temperature change will have on a clay. The liquid limit can be used to estimate the magnitude of the effect which is higher for higher liquid limits.

Temperature produces effects analogous to pressure because drained heating produces plastic volumetric compressive strains with smaller elastic components as shown in Figure 2.19 (a) and (b).

Observation of the phenomenon of shrinking yield surfaces with increased temperature is not new. Figure 2.20 (after Phillips 1970) shows a 30% reduction in shear stress of pure aluminum tubes subjected to tension and torsion when isothermal stress probe tests are compared at 70°F (21°C) and 227°C (108°C). Elliptical yield loci in  $s_{11}$ - $s_{12}$  stress space are apparent. The initial condition is tensile loading at room temperature without torsion.

There is experimental data that supports the concept of parallelism between the hardening law ( $\lambda$ -line) in  $V$ - $\ln p'$  space and the peak shear strength locus (Sherif and Burrous 1969). This is shown in Figure 2.21.

### 2.2.7 Measured Swelling pressure

Until recently, very little testing on the effects of temperature on swelling pressure of clays has been done. Yong *et al.* (1969) showed that for saturated systems, increased temperature resulted in slightly increased water contents for the same swelling pressure. Aylmore *et al.* (1969) showed an 80% reduction in water content after preheating of illite clays.

The general consensus regarding the effects of temperatures on buffer and active clays is that swelling pressures may be reduced by as much as an order of magnitude (Güven 1990, Pusch and Güven 1990, Atebek *et al.* 1990, Oscarson *et al.* 1990). Apparently, Stern water is predominant in dense smectite even at 100°C and governs the hydraulic conductivity, swelling pressure, shear strength, and

compressive behavior of the clay. Pore fluid salinity and cation valence have little effect on swelling pressure in active clay at 100°C (Dixon *et al.* 1987, Oscarson and Dixon 1988).

At high effective stress corresponding to high density the effects of elevated temperature, plasticity, osmotic and swelling pressure on the mechanical behavior of clays is less pronounced and in general all clays behave in a similar manner.

### 2.2.8 Applicability of Effective Stress at Elevated Temperature

A modified version of the principle of effective stress is applicable to buffer and Winnipeg clay at room temperature (Oswell 1991). The concept states that the compressibility and strength of buffer can be described by examining the tensor difference (that is the effective stress) between total applied stress and pore water pressures measured on external pressure transducers. This modified effective stress concept cannot be proven explicitly because it is not possible to measure all the parameters with current technology. However, Graham *et al.* (AECL 1990) used 6 corollaries to the classical effective stress postulate to test its validity implicitly. Similar corollaries can be stated for elevated temperatures.

There is still controversy regarding the true form and function of interparticle contacts in active clays. The effects of temperature on these contacts even in dense clays is speculative at best. However, there are experimental and modeling results that support applicability of the effective stress principle at elevated temperature. For example, Green (1984) predicted volume changes in triaxial specimens which were consolidated using (1) isotropic stress and (2) heat, separately and simultaneously. Pore pressure changes in illite accompanying temperature changes under undrained conditions can be predicted reasonably well using the concept of effective stress (Campanella and Mitchell,

1968). This thesis will use Oswell's results as a basis for adopting the applicability of the effective stress concept under conditions of constant specific volume, temperature and pore fluid chemistry.

The effect of elevated temperature on measured pore pressures in clays is well known. Under undrained conditions kaolinite, illite, and montmorillonite all experience increases in pore pressures with increased temperature (Bailey 1965, Campanella and Mitchell 1968, Sherif and Burrous 1969, Plum and Esrig 1969, Green 1984, Hueckel and Pellegrini 1987). Temperature cycling of remolded normally consolidated illite during undrained conditions produces a repeatable hysteretic response after 4 cycles. This is similar to stress cycling which is achieved after 5 cycles (Plum and Esrig 1969). Plum and Esrig (1969) showed that the thermally induced pore pressures are predictable from the results of room temperature triaxial consolidation results.

The net change in effective stress after temperature cycles under undrained isotropic stress conditions may be stress history dependent. Plum and Esrig (1969) tested remolded normally consolidated Neufeld clay (low plasticity hydrous mica chlorite) at constant total stress and found a net decrease in effective stress. Hueckel and Pellegrini (1990) found a similar result for overconsolidated Pasquasia clay. Their test was run with constant deviator stress. On the other hand, Mitchell (1976) found that the effective stress in saturated illite increased.

Mitchell (1976) developed a pore pressure-temperature parameter,  $F = (\Delta u / \Delta T) / \sigma'$ , which accounts for porosity, compressibility and thermal expansion of the fluids, solids and soil skeleton. For several clays, he calculated similar  $F$  values, from  $0.013 \text{ } ^\circ\text{C}^{-1}$  to  $0.018 \text{ } ^\circ\text{C}^{-1}$ . These clays included remolded kaolinite, illite, natural clay, high plasticity clay, normally consolidated and overconsolidated clays. These clays were subjected to similar temperature changes (from  $16^\circ\text{C}$  to  $23^\circ\text{C}$ ), but were tested at different effective stresses, from 0.1 MPa



to 0.65 MPa.

### 2.2.9 Creep

As mentioned earlier, temperature appears to be analogous to time effects on clay behavior. Comparing Figure 2.14(a) with the classical time line of Bjerrum (1967) in Figure 2.14(b), the similarity can be seen. Increasing temperature shifts the compression lines downward to lower specific volumes.

Secondary compression rates in illite are only slightly affected by heating, but are significantly decreased by cooling (Plum and Esrig 1969).

### 2.2.10 Hydraulic Conductivity

Hydraulic conductivity of compacted clays and sand/clay mixtures depends on clay type, density, ionic concentration in the water, hydraulic gradient, temperature and sand content (Oscarson *et al.* 1990). In kaolinites and illites, free water dominates the pore space and hydraulic conductivity depends mainly on density and temperature, possibly through the temperature dependence of the viscosity of water. In bentonites, the ratio of bound water to free water governs the hydraulic conductivity. In low density bentonites ( $\gamma_d < 1.2 \text{ Mg/m}^3$ ), there is appreciable free water, and hydraulic conductivity depends on pore fluid salinity, hydraulic gradient, temperature, and density. In high density bentonite ( $\gamma_d > 1.2 \text{ Mg/m}^3$ ) the hydraulic conductivity is independent of all variables except temperature. In this thesis, high density buffer has a dry density of  $1.67 \text{ Mg/m}^3$  or greater.

Osmotic theory (together with Darcy's Law, Fick's Law, and Fourier's Law) has been used by Cheung *et al.* (1986) to compare hydraulic conductivity and diffusion coefficients of buffer at different hydraulic gradients and temperatures with measured values. Predictions were within an order of magnitude of measured

values for buffer dry densities between 0.34 and 1.75 Mg/m<sup>3</sup> and for hydraulic gradients greater than 400. At low density, increasing the temperature from 25°C to 100°C increases K by a factor of 3.5. At high density, the corresponding factor of change is approximately 3.0 (Dixon *et al.* 1987).

### 2.3 Thermo-Mechanical Models

Several thermomechanical models of soil behavior have been published recently. Three classes of models have been identified in the literature: (1) calibrated theoretical models supported by experimental verification; (2) theoretical models; and (3) rheological (phenomenological) models. (Calibration means that the models have been fitted and validated by comparisons with laboratory data). The models may be further defined as coupled or uncoupled temperature-stress-strain models. The following models have been developed in the last 20 years: (1) a fully coupled thermo-elastic theoretical model (Booker and Savvidou 1985, Booker and Smith 1989, Nowinski 1978); (2) a calibrated coupled thermo-hypoelastic hyperbolic model (Agar 1984, Agar *et al.* 1986, 1987); (3) a calibrated thermo-elasto-plastic model (Green 1984, Wan *et al.* 1991); (4) a calibrated coupled thermo-elasto-plastic model (Hueckel and Baldi 1990, Hueckel and Borsetto 1990, Hueckel *et al.* 1987a,b, Mitchell 1969, ); (5) a rheological thermo-viscoelastic model (Murayama 1969); (6) a rheological thermo-viscoplastic model (Mitchell and Campanella 1963, Eriksson 1989); and (7) a poro-thermo-elastic model (Nowinski 1978, Booker and Savvidou 1985). Theoretical models exist for the last three models; they are of limited usefulness to the current research because they typically describe only one or two aspects of the soil behavior well. Their shortcomings will be addressed later in this chapter.

The first four models are more fundamental, and are of interest to this research program. They were researched using materials different from the active

buffer in the present study. The applications and calibrations of the models with laboratory data will be discussed in the sections that follow. Verification of the models requires an independent suite of tests along different stress paths from those used for calibration (Graham and Houlsby 1983).

In general, the term "coupling" implies the interaction of any of several important relations. In this thesis thermal coupling is defined (in principle) by thermodynamic laws relating the mutual influences of temperature, stress and strain. Semi-coupling is used in some models for simplicity, for instance by assuming that stress induced temperature changes are negligible compared to temperature induced stress changes (Nowinski 1978).

In classical thermodynamics, heat transfer occurs in steady and non-steady state systems by way of three basic mechanisms: (1) convection, (2) conduction, and (3) radiation (Kovalenko 1969). This thesis is most concerned with the end results of heating, that is steady state (isothermal) conditions. Conduction and convection are the primary mechanisms for temperature changes in the models presented. Thermodynamics will be discussed only in a general way in relation to the following models. Thermoelasticity is founded on thermodynamics to help derive important relations without the use of heuristic hypotheses. The theory of thermodynamics comprises a body of general laws governing the transformation of energy, in particular heat and work.

There are many ways of introducing temperature effects into an elasto-plastic model for instance. However, there is no single fundamental model with a specific number of unique elements that has been accepted like the Cam clay model described by Roscoe and Burland (1968) and Schofield and Wroth (1968) for elastic-plastic behavior at ambient temperature.

Practical applications of the theory of thermo-elasto-plasticity in relation to small deformations are discussed by Lee (1974) and Lee and Germaine

(1974).

### 2.3.1 Thermo-Elastic (TE)

The development of thermo-elastic models has typically been on a case-by-case basis to handle specific geotechnical problems. Each model has assumptions, strengths and weaknesses based on the type of problem being modelled. A simple theoretical model with general applicability to practical geotechnical problems is lacking.

Thermoelasticity is a branch of applied mechanics concerned with the effects of heat on the deformation and stresses in solid bodies which are considered to be elastic. It is an extension of the conventional theory of isothermal elasticity to processes in which deformation and stresses are produced not by mechanical forces alone, but by temperature variations as well (Nowinski 1978). Thermo-elastic processes are not totally reversible. The deformations caused by heat are recoverable through cooling, but the heat is non-recoverable due to dissipation of energy.

Although there is a coupling between temperature and deformation, heat does not always produce stress. A uniform temperature field does not produce stress in a body. Thermoelasticity differs from elasticity for which there is no deformation without stress. A non-uniform temperature field generally will cause development of stresses within a body.

In general, mechanical properties such as Young's modulus, Poisson's ratio, the elongation at rupture, the stress at the proportional limit (in metals), thermal conductivity, and coefficient of expansion change with temperature. For the thermomechanical properties to be approximately constant, the temperature increase should not exceed 150°C to 200°C (Lee and Germaine 1974).

Clearly, properties also change with position in non-homogeneous and anisotropic bodies. Unless otherwise stated, this thesis will assume isotropic homogeneous continua.

### 2.3.1.1 Theory

Agar (1984) developed a thermo-elastic model to aid analysis of ground heating problems arising from thermally enhanced recovery of heavy hydrocarbons from oil sand. He used an uncoupled thermo-elastic theory and heat consolidation theory to develop an incremental numerical procedure for estimating the pattern and magnitude of stresses and deformations resulting from in-situ heating and fluid injection.

A hyperbolic elastic incremental model was fitted to the envelope of strengths. Heat consolidation involved simultaneous thermal pore pressure generation and dissipation, and was solved numerically using a non-rigorous approach with heat transfer coupled with consolidation. Total stresses were assumed constant.

Pore water pressure response to undrained heating was a factor in reducing effective stress and available shear strength during rapid heating because of the low effective permeability of oil sand at in-situ temperatures. It was assumed that the classical Terzaghi effective stress relation holds true. The sum of the thermal expansion and mechanical compression of the components of oil sand was equated to the sum of the thermal expansion, effective stress compressibility, and dilatancy of the mineral grain matrix.

Booker and Savvidou (1985) developed an analytical solution for the fundamental problem of a point heat source buried deep in a saturated clay (simulating a container of waste nuclear fuel in a deep clay host medium). The model assumed that the soil is a poro-thermoelastic continuum. Changes to the

density of the soil due to thermal expansion were neglected in developing the equations of equilibrium. Standard strain-displacement relations were used. Volume changes of the soil skeleton and water due to pressure were neglected and Darcy's Law is assumed valid. The mechanical contributions to the energy balance are small compared to thermal contributions and were therefore neglected. Fourier's law of heat conduction was used, and the soil was assumed homogeneous. An approximate solution to the problem of a cylindrical heat source was found by integrating the solution for a point source over the cylindrical volume. In other work Booker developed a linear theory of thermal consolidation to solve the problem of consolidation around a spherical heat source in a fully coupled (displacement, pore pressure, temperature) saturated thermoelastic soil (Booker and Smith 1989).

Britto *et al.* (1989) used a the finite element program 'HOT CRISP' to model thermomechanical behavior of clay in centrifuge tests in which a hot canister (90°C) was buried in kaolin.

Semi-coupled theories have been developed by McTigue (1985) and Booker and Savvidou (1985). The former used coupling of strain, pressure and temperature in the void occupancy equation, but neglected such coupling in the energy balance equation. A similar theory was used by the latter authors for porous elastic solid with incompressible constituents.

### 2.3.1.2 Laboratory Tests and Model Calibrations

Agar used 1-dimensional and triaxial compression and permeability tests on oil sand at temperatures to 300°C and pressures to 30 MPa. Shear strength was determined using 6 stress paths (Figure 2.22) at mean effective stresses of 4 MPa to 8 MPa. The undrained compressibility of water, bitumen and solids,  $\beta_v$ , was determined from isotropic triaxial compression tests. This parameter was approximately constant from 20°C to 200°C for  $p'$  from 4 MPa to 18 MPa. The thermal

expansion coefficient,  $\alpha_u$ , of the water, bitumen and solids was determined from pressure-volume-temperature tests. The parameters  $\beta_u$  and  $\alpha_u$  were used to derive an expression for the thermal pore pressure parameter,  $B_T$ . Agar developed a drained compressibility parameter  $\beta_s = f(\Delta u, \Delta \sigma)$  using oedometer and isotropic (TX) compression tests and found no temperature effects on the values of  $m_v$  and  $C_c$ . Undrained and drained thermal expansion coefficients were determined from oedometer tests.

Britto *et al.* (1989) used triaxial, oedometer, and physical test results for Speswhite kaolin from other researchers to obtain mechanical properties, in-situ state parameters, permeability and thermal properties

Work by Tidfors and Sällfors (1989) testing sensitive marine clays using conventional incremental oedometer tests and constant rate of strains clearly show that the preconsolidation pressure decreases with increasing temperature. Although a specific type of constitutive soil model is not explicitly discussed results are presented which can be interpreted in the form of thermo-hypoelasticity. Figure 2.12 (b) shows CRS test results. Compression lines are parallel in the elastic range ( $\kappa$ -lines). However, testing by other researchers seems to indicate that the slope may be temperature level dependent (Eriksson 1989, Demars and Charles 1981). Figure 2.12 (a) shows a summary of test results for incremental load tests, where the temperature was increased at 40, 50, 60 and 80 kPa.

### 2.3.1.3 Model Predictions

Agar's predictions of stresses, strains, and temperatures in the field are made, but apparently not verified with field measurements. Agar's model was not truly verified in its complete form, rather individual components were apparently fitted to data from several test types. From Agar's work, it is apparent that the

validity of using his uncoupled approach depends on the thermal loading and degree of restraint on thermal strains. Drained heating provided a reasonable lower bound solution. However, assumption of an undrained condition during heating doesn't necessarily provide an upper bound solution for stress and deformations. Effective stresses may reduce due to pore pressures spreading during transient consolidation in low permeability materials upon heating.

Results of 1-dimensional heat consolidation analysis yielded the following conclusions: (1) solutions are sensitive to the size of time steps due to non-linear variation of the coefficient of consolidation; (2) pore pressure changes generated during transient heating are small for oil sand without fines; (3) the permeability decreased 2 to 3 times with addition to 10 to 20% fines. Generated pore water pressures are about 50% of the effective stress. The rate of pore water migration and dissipation is reduced, and therefore the shear strength decreases are proportional to pore pressure increases; (4) heat transfer by convection has little influence on predicted temperature and pore pressure distributions when drainage is towards heat source.

Some of the limitations of this analysis are as follows. Stress redistribution following yield or failure cannot be modeled using a linear thermoelastic solution. Non-recoverable deformation cannot be modeled. Paradoxical results have been observed, for example, predicted stress changes and deformations decrease with time.

Centrifuge tests by Britto *et al.* (1989) indicate that for NC clay, the transient behavior due to the temperature field can be reasonably well predicted using the HOT CRISP model. The temperature distribution was fairly well predicted. Cam clay underpredicted the measured pore water pressures, but were within an order of magnitude. The elastic model predicted even lower pore water pressures. For OC clay, both of Britto's models grossly underpredicted pore pressures. In centrifuge



tests, cracks that were observed fanned out horizontally from the heater. This may have been caused by penetration of the heater into the clay, and compounded by transient heat effects.

Booker and Savvidou (1985) used their model to conduct a parametric study without reference to any particular soil type. They found that pore water pressure only reaches a small fraction of the value it would achieve if consolidation did not occur. The stresses undergo only small compressive changes.

### 2.3.2 Thermo-Elasto-Plastic Models

All of the models in the following discussion are mathematically complex and require numerical solutions, usually finite element formulations, for their implementation.

#### 2.3.2.1 Theory

Hueckel and Borsetto (1990) developed a thermo-plastic version of the critical state model used in Cam clay to describe plastic behavior of soils and shales due to drained heating and loading under constant elevated temperature. These models are illustrated in Figure 2.23 (a) and (b). In the thermo-plastic theory, the yield surface becomes temperature dependent. It shrinks during heating (thermal softening) and expands during cooling when the stress state is elastic, as shown in Figure 2.23 (b) and (c). The theoretical shear stresses and strains at elevated temperature and different OCR are shown in Figure 2.24. The temperature dependency of peak stress, strains, yield loci, and plastic strain increments agrees in principle with the observed behavior discussed in previous sections. Failure strength is independent of temperature.

At constant  $p'$  stress state, thermal softening may be entirely compensated by plastic strain hardening leading to thermal consolidation. Loading and

unloading criteria determine whether the soil response is thermo-elastic or thermo-plastic. Stress increments inside the current yield surface are admissible plastic processes if temperature is increasing. Stress increments at the softening side of the YL may lead to plastic expansive strains during cooling. It is clear that this model is supported by test results for kaolinite, illite and montmorillonite discussed in the previous section on soil properties.

Hueckel and Pellegrini (1991b) developed a similar model to the one just described. However, it was for modeling the undrained failure of low porosity saturated clay due to development of advanced irreversible strains during heating at constant total stress. Boom clay and Pasquasia clay were tested

Wan *et al.* (1991) developed a non-associative thermo-elasto-plastic constitutive model for Alberta oil sands under triaxial stress conditions and elevated temperature. The model is uncoupled in that thermo-plasticity is not used. A Ramberg-Osgood function with a secant hardening parameter,  $H$ , is used to describe a hardening/softening law. The Matsuoka-Nakai failure criterion is used. The plastic potential,  $G$ , is given the same shape as the yield function,  $F$ , based on Rowe's stress dilatancy equation. Temperature dependent material properties are used.

Green (1984) developed a finite element model, HITCON, which sums thermo-plastic strains from a phenomenological creep model with thermo-elastic strains from unloading. Primary consolidation is calculated using an axisymmetric finite element program. Mineral grains were assumed incompressible, and elastic strains were assumed if the current stress level was less than the preconsolidation pressure. Temperature increases caused pore pressure increases and were assumed to produce elastic volumetric deformations of the soil and water. However, these were insignificant compared to plastic strains (Houston *et al.* 1985).

### 2.3.2.2 Laboratory Tests and Model Calibrations

To calibrate Hueckel and Borsetto's model, Hueckel and Baldi (1990) performed heating and cooling tests at constant isotropic stress under drained triaxial conditions. They also used undrained triaxial tests at constant deviator stress. Results from a thermomechanical cycle of isotropic loading, including heating-cooling, shows plastic deformation (Figure 2.16 (b)). Higher temperatures and lower OCR tend to produce more compressive behavior (Figure 2.25). Thermo-elastic strain recovery is proportional to OCR, and generally smaller than thermo-plastic strains of NC soil. In shear, the deviatoric stress at a given axial strain is lower at elevated temperature and thermal ductilization occurs (Figure 2.9). The soils failed under undrained heating at  $q/p'$  ratios equal to the room temperature values in the case of Pontida clay, and 20% higher than room temperature values in the case of Boom Clay.

Baldi *et al.* (1988) used triaxial tests with ramped temperatures and pressures to calibrate a model similar to the one by Hueckel and Borsetto. The test results are shown in Figure 2.26. Clearly, thermomechanical behavior in the OC state is thermo-elastic and in the NC state it is thermo-plastic. It is also apparent that thermal strains depend on both temperature and effective stress. Clays are dilatant at low values of isotropic stress, and compressive at high values of stress. Higher temperatures add to the compressive tendencies. At intermediate effective stresses, the thermal strains may be dilatant at low temperatures, and compressive at higher temperatures.

Wan *et al.* (1991) used approximately 4 drained triaxial tests for calibrating the model in addition to triaxial, oedometer, permeability and physical tests performed earlier by Agar (1984).

Six different types of test were used in Green's model: (1) mechanical consolidation (primary, secondary); (2) thermal consolidation after primary

mechanical consolidation; (3) combined mechanical and thermal consolidation; (4) undrained compressive strength after consolidation; (5) undrained creep at constant deviator stress ratio; and (6) permeability before and after thermal consolidation

Clearly, Hueckel has used the most sophisticated modeling and calibration of all the models examined. He has tested four different clays for calibration using complex loading paths and developed three, or possibly four constitutive models. However, he has not performed as many tests as Green.

### 2.3.2.3 Model Predictions

Hueckel and Baldi (1990) performed a numerical simulation of soil failure in a drained triaxial test as shown in Figure 2.27(a) and (b). Clearly the trends of stress and strain are approximately the same as Hueckel's test results shown earlier, although there is difficulty in modeling the transition from elastic to plastic behavior. This is not a fault of the thermal model *per se*, but rather a limitation of all classical incremental elasto-plastic models. The prediction shows reduced peak shear strength at elevated temperature. Green's undrained tests on Pacific illite and smectite show greater strength and brittle behavior at elevated temperature. This may be due to higher density at elevated temperature and is consistent with data produced by Noble and Demirel (1969) and Williams (1984). Unfortunately, Hueckel has not published test data for CIU triaxial tests at elevated temperature. It is difficult to draw comparisons between his model and data from the literature. Figure 2.27(b) shows more positive volumetric strains at end-of-test conditions for higher temperatures. This apparently conflicts with the dilative behavior expected from increased density, produced by elevated temperature. However, because this is a drained test, additional thermal volumetric compression may dominate any shear induced dilation. His model shows approximately the same volumetric strain at peak strength for different

temperatures, but this is not consistent with the observed behavior of Pontida clay.

Hueckel and Pellegrini used their model to show that thermomechanical failure can occur when effective stresses are brought to critical state by expansion of pore water and thermoplastic compression of the skeleton. The response is stable-plastic if the rate of pore water pressure build-up is less than the thermal degradation of the skeleton. In this case, plastic volumetric compression is generated to slow down the thermal degradation of the skeleton and keep the effective stress at the YL. Effective stresses were slightly overpredicted by the model.

Wan *et al.* (1991) captured the essential material behavior of oil sand, including strain softening with dilation at low confining stresses and temperatures; and work hardening at high confining pressures and temperatures.

Green's model gave good predictions of water content for field heating of a probe in a simulated in-situ test at 3.0 and 7.0 cm radius, but values at other radii are not given. The general trend of vane shear strengths were correctly modelled, but the magnitudes were significantly underpredicted. However, vane shear tests on high plasticity soils tend in any case to overpredict triaxial shear strengths (Graham *et al.* 1984). On the other hand, it is likely that Green's model will give poor overall predictions of  $q$  and  $u$  at different radii because she has assumed that the primary consolidation parameters are constant with temperature and this is incorrect. The measured pore pressures were significantly overpredicted.

#### 2.4 Synthesis of Literature

High effective stress tends to subdue the effects of temperature, mineralogy, pore fluid, cation concentration and valence and cementation on soil behavior.

Clay, oil sand, and metals have broad similarities in their response to temperature, but the detailed differences in kinematic hardening, and volume change behavior preclude a universal thermomechanical model applicable to all three materials.

The strength and volume change behavior of clay is governed more by mechanical response than by direct thermal expansion effects, and is consistent with ideas in the Cam clay family of models. Clays generally experience decreases in peak strength at elevated temperature for a given void ratio with a possible exception for Pacific Illite tested under marine conditions, and Ca-montmorillonite. Pacific illite shows large post peak softening at elevated temperature. Clays undergo plastic deformation under drained heating. Failure of clay under undrained heating is caused by pore pressure generation and plastic skeletal deformation. The large-strain failure strength (critical state) of clays is virtually unchanged, with the exception of smectitic Boom clay which experienced a 20% increase.

Clay experiences thermal softening (shrinking yield locus) during drained heating which is compensated by plastic strain hardening at constant effective stress. This is reflected in preconsolidation pressures decreasing with increases in temperature. Metals also experience shrinking yield loci. This implies a reduced strength and is consistent with observed behavior for metals and clays. Active clays and metals behave in a ductile, yet OC manner at elevated temperature. Temperature cycles leave clay in an overconsolidated state; the volume is less and effective preconsolidation stresses are higher.

Thermal strains at 100°C are generally less than mechanical strains for the range of stresses normally encountered in testing. When considering volume changes temperature is broadly analogous with Bjerrum's time lines of delayed compression. The slope of virgin consolidation lines remains constant with temperature, but the

lines shift towards lower specific volumes. The slopes of  $\kappa$ -lines appear to change with temperature. Temperature also has an effect on volume change that is analogous to pressure; it produces both elastic and plastic strains. Thermal consolidation may be analogous to osmotic consolidation.

Elevated temperatures cause high plasticity clays to behave more like medium or low plasticity clays at ambient temperatures. The Casagrande classification is unchanged at moderately high temperatures but the points move downward parallel to the A-line. The higher the plasticity, the larger the change in behavior.

Elevated temperatures decrease the swelling pressure of active clays and increase hydraulic conductivity.

Buffer appears to behave like other active clays at ambient temperature (Graham *et al.* 1989). The response of buffer permeability and swelling pressure to high temperatures is similar to other active clays. The effective stress concept appears to apply to buffer with respect to permeability and swelling pressure. However, DDL theory does not apply to dense buffer or dense active clays.

Thermo-elasto-plastic modeling is superior to thermo-elasticity, because it captures more aspects of material behavior. Elasto-plasticity provides the most rational framework on which to build an elevated temperature model for soils.

The advantages of the elasto-plastic model are as follows: it is applicable to large strain behavior; it incorporates recoverable (elastic) and non-recoverable (plastic) deformation; path dependence is modeled; it is not limited to one density like hypoelasticity; it describes the transition from elastic to plastic behavior in a fundamental way (incremental yielding); it describes failure and shear dilatancy;(hypoelasticity does not); and it models stress level dependency. Temperature effects can be handled in an uncoupled approach using temperature dependent material constants such as stiffness moduli and angle of friction, and qualitatively can be understood using osmotic theory of interparticle pressure.

Temperature effects can also be modelled in a coupled thermoplastic framework or a more complex coupled thermo-hydraulic-mechanical framework.

Alternative approaches such as hyperelastic and hypoelastic models require extensive calibration. They can be seen as approximate relations at best and empirical in nature. Poro-thermo-elastic models serve to describe specific soil types well, but can not be considered as general models.

Thermo-elasto-plastic models are more fundamentally based and general. They must be calibrated and verified using extensive testing, but model more aspects of mechanical behavior than other models. Elasto-plastic models are good for predicting strains in drained tests and pore pressures in undrained tests, but the main limitation is in accurate prediction of shear strains (Wroth and Houlsby, 1985). Linear elastic models have been avoided because clays typically exhibit highly non-linear stress-strain behavior.

## 2.5 Review of Buffer Research

The current program builds on the results obtained by Sun (1986), Wan (1987), Saadat (1989), Graham *et al.* (1989), Yin (1990), and Oswell (1991) on buffer at ambient temperature and low to high pressures. This work was carried out at the University of Manitoba.

The previous research focused on high pressure (up to 10 MPa) testing of buffer at ambient temperature only. Three constant temperature (isothermal) models have been developed using buffer data: (1) hyperelastic (Sun 1986, Saadat 1989); (2) hypoelastic (Yin 1990, Saadat 1989); and (3) elasto-plastic (Saadat 1989, Oswell 1991).

Swelling potential and shear behavior of buffer are influenced by soil fabric structure (Wan 1987). Fabric is largely determined by the molding water content; for instance, a different material structure is created at 25% than at 35%



water content.

Compacted buffer has a strong tendency to expand at stresses lower than its swelling pressure (Saadat 1989). The strength of the buffer is dominated by the bentonite ( $\phi'=14^\circ$ ) and strain softening behavior is observed in long duration tests. A three-modulus anisotropic hyperelastic model was proposed for early stages of loading and permits coupling of mean pressures with shear strains, and deviator stresses with volume strains. A three-function hypoelastic model was developed to describe straining to failure. An elastic-plastic model accounted for non-reversibility, non-linearity and dilatancy in the plastic range. In addition to these predictive models, a generalized critical state specific volume-pressure relationship at equilibrium was developed which accounted for influence of compaction water content and time on the fabric.

Yin (1990) developed models to describe (1) time independent stress-strain behavior in general stress states; (2) time dependent stress-strain behavior in 1-D straining; and (3) time dependent stress-strain behavior in triaxial stress states. A three modulus hypoelasticity model for time independent behavior was calibrated using conventional triaxial tests on buffer, Paris clay, and medium dense Wuhan sand (Yin *et al.* 1989).

Oswell (1991) examined the applicability of the effective stress concept and yielding behavior of low density and high density buffer. He also described new relationships for yielding, hardening law, flow rule and failure.

None of this work involved the testing at elevated temperatures that forms the principal contribution of this thesis.

## 2.6 Temperature Effects on Buffer Behavior

Oscarson *et al.* (1990) showed that heating unsaturated buffer at 200°C with two different pore fluids, distilled water and 1.4 molar saline solution, produced

no changes in mineralogy over a 7 day heating period. It is possible that different behavior could result with saturated buffer, but steam probably has a more significant effect than water. Comparing Figure 2.4(a) and (b) there is no obvious difference in fabric and structure between heated and unheated montmorillonite.

Montmorillonite maintains its Stern water layer even at an oven temperature of 110°C (Pusch 1990). Therefore when reducing data to determine the clay specific volume,  $V_c$ , we are not normalizing buffer behavior to clay minerals only, but to the clay plus Stern water. This also means that any observed changes in behavior must be due to the presence of either diffuse or free water. It is not clear what effect the Stern water has on the flow of water under pressure, thermal and chemical gradients. In fact, buffer may behave like a semi-impermeable membrane at high density in which diffusion governs. It may be appropriate to use diffusion theory to describe swelling behavior in terms of flow rates instead of the pressure-particle spacing relationships used by Viani *et al.* (1983) for montmorillonites gels.

## CHAPTER 3 EXPERIMENTAL EQUIPMENT

### 3.1 Introduction

Triaxial cells were used exclusively in the testing of buffer in this thesis research. Five sets of apparatus were built, and four were used in the current program. Apparatus #1 was Saadat's prototype triaxial cell (1989), capable of testing up to 10 MPa pressure. Saadat's cell was used to test buffer at ambient temperatures. Later, a second group of three cells consisting of special high temperature, high pressure (HITEP) TX cells were built under the direction of the author for the current thesis research. Two of these three cells, Apparatus #2 and Apparatus #3, were used in the current program to perform 22 of 36 triaxial tests. The third cell (Apparatus #4) was used in a concurrent MSc. program by Yarechewski. The cells were capable of testing at 10 MPa total pressure, with 9 MPa back pressure and temperatures up to 100°C. The author procured the materials and directed construction of these apparatuses and commissioned them for buffer testing. This involved considerable calibration of the triaxial cells and ancillary equipment for temperature, pressure and chemical attack. Modifications to the apparatuses were incorporated to resolve difficulties and meet the needs of the test program, when buffer parameters became better known. Apparatus #5 was an aluminum double-walled cell and 'Haake' refrigeration bath, modified for elevated temperatures. Only 2 tests were performed with this apparatus, after which the HITEP equipment was available.

Eight types of measuring instruments were required for testing buffer in the HITEP apparatus. Each instrument was procured and calibrated to meet the appropriate temperature and pressure requirements.

The author also designed a split mold for static compaction of the buffer

specimens as an improvement over the previous hollow cylinder extrusion method used by Saadat (1989). Further work involved construction of the static compaction frame.

Special attention was paid to the membranes used to confine the buffer specimens. The latex membranes used previously proved to be unsuitable at elevated temperature. Instead, RTV silicone rubber was used. The author developed the technology to produce these in the laboratory. This involved an extensive material selection process until material compatible with the system components could be found. The rubber was tested for temperature stability, compliance, strength, and diffusion of cell fluid and buffer pore fluid. Two triaxial apparatuses were assembled and modified for testing leakage and diffusion of membranes

More details of this extensive equipment development program are given in following sections. Acronyms are used throughout the thesis to abbreviate names of devices, processes and variables. A list of acronyms is given at the beginning of the thesis.

## **3.2 Equipment: Triaxial Cells**

### **3.2.1 Ambient Temperature**

Apparatus #1 was used to perform 12 triaxial tests at ambient temperature. Figure 3.1 shows Saadat's prototype cell, loading frame, and data acquisition system. The main departure from his equipment was the use of geotextile side drains and Whatman #54 filter paper at the ends of the specimens instead of Whatman #1 filter paper. The other equipment is described in detail by Saadat (1989) and will not be discussed further.

Two tests were run to determine axial and radial deformation of the cell

itself at pressures up to 11.7 MPa. Axial deformation was 0.5 mm and radial deformation was 1.0 mm (mid height) at 10 MPa.

### 3.2.2 HITEP Apparatus

The prototype high temperature high pressure (HITEP) cell is shown schematically, not to scale, in Figure 3.2. The total height of the cell is 800 mm, the sleeve diameter is 265 mm and wall thickness is 200 mm. The cell was designed to withstand 10 MPa pressure at 100°C using the ASME 1977 Boiler and Pressure Vessel Code, Section VIII (Revised, update). The cell is designed with a factor of safety of 4.0 for incompressible fluids only, not gases. A nickel-plated mild steel cell, instead of aluminum or stainless steel, was chosen to keep material costs reasonable. This required a relatively thick cell wall and therefore a heavy cell. As a result, a small hoist had to be installed in the laboratory to lift the cell components during assembly.

The main features of the HITEP cell are: (1) a removable top mounted sleeve; (2) internal load cell; and (3) pressure transducers mounted on the cell base. The separate sleeve allows installation and removal of buffer specimens without disturbance of the instrumentation. The internal load cell avoids the problem of piston friction associated with an external load cell. The pressure transducers and control valves were placed on the cell base as close as possible to the buffer specimen to measure pore pressures. This arrangement eliminates the need for a separate control board with transducers and control valves.

A special cell fluid was required instead of water to avoid electrical short circuiting of the internal instrumentation in the load cell and to avoid cell corrosion. Silicone oil was chosen for its viscosity (500 cP) , its low electrical

conductivity (dielectric strength = 138 kV/cm), temperature stability (flashpoint 500°C), non-flammability, low compressibility (1% at 10 MPa), inertness, and non-toxicity. The oil was purchased from CSL Silicones Inc., Guelph, Ontario. The oil is costly (approximately \$5/litre) and must be recovered and filtered and de-watered after each test.

Mineral oils were not compatible with silicone membranes and valve seals, vegetable oils did not possess suitable temperature stability, and kerosene and liquid paraffin attack latex rubber. Leroueil *et al.* (1988) recommend against using glycerin for cell fluid because it has a high affinity for water and can suck significant quantities of pore water through membranes. They have successfully used silicone oil at Laval University for over 10 years.

The main disadvantage of silicone oil for this program is its low thermal conductivity  $3.6 \times 10^{-4}$  cal/cm·s·°C). Heat transfer is relatively slow compared to metals and thermal gradients as much as 5°C can be set up in the fluid from the top to bottom of the cell. These readings were obtained from instrumentation early in the program. Fortunately, convection helps reduce the thermal gradients.

An extensive material selection program was undertaken to find membranes compatible with the silicone oil cell fluid and capable of testing up to 100°C. Silicone rubber was chosen over latex, EPDM, heat shrink tubing, teflon, polyethylene, and polyurethane. A slight reaction occurs with the silicone oil, but Agar (1984) used the same combination successfully up to 300°C and 8.0 MPa for short periods of time.

Extensive specimen instrumentation was provided for each HITEP apparatus as shown in Figure 3.2. Up to nine channels of data were recorded for each HITEP cell. Typical measurements on the specimens included: axial load; axial deformation;

lateral deformation; cell pressure; back pressure; volume change; absolute temperature; differential temperature from top to bottom of the specimens; and room temperature. A third transducer was used in one apparatus to measure pore pressures at the bottom of the specimen, separate from back pressure applied at the top during consolidation. Drainage was closed during shear and the third transducer allowed independent measurement of pore pressures at the top and bottom of the specimens. Details of the instrumentation will be discussed in following sections.

Figure 3.3 shows the HITEP cell. The steel sleeve has been removed to show the inside of the cell. Heat treated alloy steel tie rods were required to meet the load requirements of the pressure vessel code while making use of the same diameter as Saadat's design. Mild steel pedestals and top caps were replaced with stainless steel to reduce corrosion.

A key component of the design was the seals. Viton O-rings were required in the pedestals and valves to withstand 100°C temperatures. Special U-cup seals were required for the tie rods, piston bushing, and sleeve. Only carboxylized nitril (black) seals could withstand the 100°C temperatures, abrasion and wear, and 10 MPa pressures for extended use (over 6 tests of 1 month duration). Polymyte (viton, orange) U-cup seals were suitable for no more than 6 tests at 65°C. Molythane (urethane, yellow) U-cup seals were suitable for extended use at room temperature. The seals were specially ordered from Parker Seals, Salt Lake City, Utah through a local supplier, Kepco Sealing Supplies. Fluoromyte seals (fluoro-urethane) depolymerized (cracked) in the presence of even small quantities of water which occasionally contaminated the oil.

An active heating/passive cooling system was used to control temperatures in the HITEP cells. The temperature control system (TCS) is shown in Figure 3.4. It

consists of a programmable 'Tempstar' PID controller which powered two silicone band heaters attached to the exterior of the sleeve. Power was manually proportioned through a rheostat. An RTD temperature sensor on the specimen supplied the input signal to the controller and completed the feedback loop. A second RTD supplied an independent temperature measurement which was recorded by the data acquisition system. The digital controller display provided manual readings. Since cooling was not required for the program, it was not a control feature. The HITEP cells were insulated with custom designed split jackets.

Figure 3.5 shows the complete HITEP apparatus including the cell and data acquisition system, while Figure 3.6 shows a buffer specimen before consolidation with the lateral strain gage and RTD temperature probes.

### 3.2.3 Double-walled Apparatus

While the HITEP apparatuses were being built, an elevated temperature cell was improvised from a double-walled triaxial cell previously used by others for testing frozen specimens. Drainage was provided at the top and bottom of the specimen to a common pore pressure transducer and burette. Coarse porous stones and Whatman#54 filter paper were provided for drainage at the top and bottom of the specimens. Geotextile side drains were wound in a spiral around the specimen as in the HITEP tests. A single silicone membrane covered the specimens (type 5026 for T1210 and type 5050 for T1213).

A separate transducer was used to measure cell pressure. Back pressure was applied through a pressurized burette which measured volume change of the specimen. Antifreeze filled the inner and outer chambers of the cell. A sealed copper refrigerant coil surrounded the inner cell. Hot antifreeze was circulated through the coil using a 'Haake' temperature bath equipped with a 'Techne' model TE-8D



programmable circulating heater module. Cell pressure was supplied from compressed nitrogen bottles equipped with high pressure gas regulators. Back pressure was supplied from building air lines with low pressure regulators (less than 700 kPa).

A calibrated thermistor was fitted inside the cell and sent temperature signals to a Hewlett Packard digital multimeter. Neither of the two specimens tested was sheared because an extra loading frame was not available at the time. The maximum operating temperature was 65°C. All readings were manually recorded and entered into Lotus Version 1.0 spreadsheets for analysis and production of graphs.

### 3.2.4 Membrane Diffusion/Leakage Apparatuses

Three different apparatuses were used for measuring diffusion of oil and water across the silicone membranes. The first apparatus consisted of a standard low pressure triaxial cell filled with silicone oil instead of water. A porous silica dummy specimen was saturated with de-aired water and a single silicone membrane covered the specimen. A brass dummy specimen wrapped in Whatman #54 filter paper was also tested. Extra O-rings were used to assure a good membrane seal. Silicone grease could not be used on the pedestal or top cap, as recommended by Leroueil *et al.* (1988) because the silicone fluid leaked past it.

The second apparatus was similar to the first, but used a HITEP cell and a brass dummy specimen with geotextile side drainage. This was used to simulate the heat, pressure and potential leakage conditions of an actual buffer test.

Leakage tests were performed in the HITEP apparatus using the arrangement shown in Figure 3.7. This was used to test leakage of the membranes seals and O-rings.

The third apparatus was modified from the high pressure consolidation cell

designed by Oswell (1991). The cell is shown in Figure 3.8. Volume changes were measured using a burette and differential pressure transmitter (DPT). Pressures were applied to water on one side of the membrane and oil on the other side. The cell was heated using a silicone rubber heater band with power modulated manually using a rheostat. Temperature was measured inside the cell using a thermocouple sealed in a protective sheath. The reference junction was kept at room temperature. Pressures, temperature, and volume change were automatically recorded on a data acquisition system similar to the HITEP equipment. The cell was well insulated to maintain constant temperature. The membrane diffusion apparatus is shown in Figure 3.9.

The membrane used in the third apparatus was a circular piece cut from the standard silicone membrane. It was clamped using component 6 shown in Figure 3.8. This is similar to the concept used for testing semi-permeable membranes by commercial laboratories discussed by Crank and Park (1968).

### **3.3 Ancillary Equipment and Calibrations**

The equipment discussed in the following section was used in the HITEP apparatus. Instruments were calibrated for pressure and temperature, when applicable. The intent was to use equipment requiring the fewest corrections for pressure and temperature.

#### **3.3.1 LVDT**

Two different LVDT models were used: (1) HP DCDT1000 ( $\pm 1.00$  inch, 25 mm displacement) and (2) 'Transtek' Model 0244-0000. Both models had free displacement rods. The rods should not be bent or interchanged if the calibrations are to be maintained. The Transtek LVDT is a superior device. Specifications include: 6 to

30 VDC input; linearity= $\pm 0.5\%$  Full Scale (FS); and operating temperature= $-65^{\circ}\text{F}$  to  $250^{\circ}\text{F}$ .

Thirteen calibrations were made on five instruments at room temperature and elevated temperature. The LVDTs were calibrated against Mitutoyo and Lufkin vernier micrometers. The gain, or displacement (mm) versus output voltage (mV), decreased with elevated temperatures for both LVDT models. Temperature corrections in Table 3.1 were measured, but were in fact negligible for the HITEP tests because the LVDTs were mounted externally.

**Table 3.1: LVDT temperature dependency**

Model	Test Temp. ( $^{\circ}\text{C}$ )	$\Delta\text{Gain}/\Delta\text{T}$ (mm/V/ $^{\circ}\text{C}$ )	Input Voltage (VDC)
Transtek 0244-0000	26, 36	0.003	5
HP DCDT1000	26, 36, 94	0.005	5

Figure 3.10 shows calibration curves for the Transtek LVDT at  $26^{\circ}\text{C}$  and  $36^{\circ}\text{C}$ . Axial displacement of the buffer specimens during shear was checked against the load rate on the load frame and provided a good correlation.

### 3.3.2 Load Cells (LC)

'Interface' Model 1211 22 kN (5000 lb.) load cells were used in the HITEP cells. These were specially ordered with a vented case for high pressures, temperature compensation, and a teflon coated signal cable. Specifications included: non-linearity of  $0.05\%$  FS; hysteresis of  $0.02\%$  FS; non-repeatability of  $0.02\%$  FS; and temperature compensation to  $115^{\circ}\text{F}$ . The maximum operating temperature

is 200°F, but the manufacturer indicated safe operation at 212°F (Max Morton, personal communication).

No pressure compensation specifications were available, but the manufacturer indicated a safe operating pressure of 10 MPa. The load cell readings were monitored during HITEP test T1221 at 26°C. Figure 3.11 (a) shows a change of 10 N in the readings when the cell pressure is doubled from 2 to 4 MPa as shown in Figure 3.11(b). This is small compared to maximum specimen loads up to 1200 N.

Nineteen calibrations were performed on four different load cells at atmospheric pressure and temperatures from 26°C to 100°C. The calibrations at elevated temperature were done by submerging the load cell in a controlled temperature bath of silicone oil while loading. The load cells were calibrated using a 130 kN (30 kip) load frame or 45 kN (10 kip) proving ring. Figure 3.12 (a) shows that the 'zeroes' and 'gains' at elevated temperatures of 100°C and 26°C are the same. These calibrations were without a ball bearing attachment. Figure 3.12 (b) shows excellent repeatability at 100°C.

Load cell readings were usually taken during consolidation of the specimens in the HITEP cells. These readings provide a measure of the drift in the calibration 'zeroes' with time, temperature and pressure. The readings (N) typically increase during heating, sometimes as much as 800 N (LC# 44570). Factory specifications show zero shift of 0.0008% FS/°F, or 24 N at 46°C. The temperature at which these changes occur is not predictable. For tests at 100°C (LC# 44570) it occurs after temperature equilibrium is established, at constant pressure. Sometimes the change starts at 45°C. Thermal expansion of the ball bearing against the load cell is believed to be the cause. This effect is not important for this test program because the zero reading is taken at the beginning of shear at which

time the readings have stabilized.

The 'gain' has increased by as much as 0.3% of Factory Gain after a year of near continuous use at temperatures up to 100°C, while the 'zero' decreased by as much as 100 N (LC# 41373, and 44570).

In sum, because of the way tests were run, no corrections were needed for the load cell readings.

### 3.3.3 Pressure Transducers (PT)

'Microgage' Model P102 (2000 psi) pressure transducers were used in the triaxial equipment used to test buffer. These have an accuracy of 0.05% FS and compensated temperature range of 0°F to 212°F. Thirteen calibrations were performed on 5 transducers at temperatures from 26°C to 47°C and pressures up to 7.0 MPa. A 'Lucas Barnet' Model S8000 deadweight tester was purchased to calibrate the transducers. There was usually about a 1% difference between the factory specification and laboratory calibrations.

The variation in 'gain' between consecutive calibrations was of the order of 0.022% Factory Gain. The variation in the zeroes was 0.0134 mV. This is shown in Table 3.2.

Elevated temperature had the effect of reducing the gain and increasing the zero. This is reversible upon immediate cooling. A sample calibration is shown in Figure 3.13 (a).

The effect of time and temperature, that is continuous loading/unloading and heating/cooling cycles, is to increase the gain and decrease the zero. This statement is based on comparisons of calibrations at 26°C. Sample calibrations are shown in Figure 3.13 (b).

**Table 3.2: Summary of pressure transducer calibrations**

Variation in calibrations	Gain	Zero
Consecutive	$\Delta G/GFC$ (%) 0.022	$\Delta Z$ (mV) 0.013
Temperature	$\Delta G/GFC/\Delta T$ (%/°C) -0.003	$\Delta Z/\Delta T$ (mV/°C) 0.024
Time+Temp.	$\Delta G/GFC/\Delta t$ (%/Mo.) 0.036 to 0.117	$\Delta Z/\Delta t$ (mV/Mo) -0.318 to -0.661

NOTE: 1.  $\Delta G$ =Change in gain  
 2. GFC=Gain from Factory Calibration  
 3.  $\Delta T$ =Change in temperature  
 4.  $\Delta t$ =Change in time  
 5.  $\Delta Z$ =Change in zero

Continuous use at elevated temperature seems to have a larger effect on 'gain' and 'zero' than the temperature itself. For example, continuous use at 100°C for 1 month produces about the same magnitude of change in gain, but opposite in sign, as heating to 100°C. The former is not reversible, but the latter is reversible.

In a typical test with brass transducer housing and no insulation, the transducer reached only 47°C for a cell temperature of 100°C. With insulation the temperature reached up to 90°C. Most tests were run with insulation. Calculations have been done to account for thermal expansion of the water in the drainage lines and transducer housing during consolidation to determine the true volume change of the buffer and pore water. This is discussed in Chapter 6.

'Roctest' high pressure gas regulators were purchased to accurately control the nitrogen gas pressure used to provide cell pressure and back pressure.

### 3.3.4 Thermocouples (TC)

Since it was not feasible to circulate the fluid in the pressure cell, temperature gradients occurred in the cell due to non-uniform heat conductance through the cell walls, and convection in the cell fluid. An iron-constantan (J type) thermocouple was used to measure the difference in temperature between the top and bottom of the specimen. The thermocouple was accurate to  $\pm 0.1^\circ\text{C}$  and was also temperature compensated. The following equation can be used to fit results from the data acquisition system:

$$[3.1] \quad \Delta T(^{\circ}\text{C}) = 10 \cdot (\text{mV} - 179) / 34.5$$

Sources of error in temperature measurement were: self heating time lag and instrument settling time. These can lead to errors of 2.5% in the signal voltage which is a measure of differential temperature between two junctions in the thermocouple.

### 3.3.5 Resistance Thermal Devices (RTD)

Ceramic platinum 3-wire resistance thermal devices (RTD) have been used to measure the specimen temperature and room temperature. These were chosen as the most reliable device with large span ( $0^\circ - 500^\circ\text{C}$ ), good accuracy ( $\pm 0.1^\circ\text{C}$ ), and reasonable cost. They were small enough to measure local temperatures. In addition, they were compensated for lead wire resistance and self heating effects by using a Wheatstone bridge. This particular arrangement had a linear range of about  $100^\circ\text{C}$ . Self-heating error in water was  $0.006^\circ\text{C}/\text{milliWatt}$ , but in air the error was three orders higher, which gave an error of  $1.2^\circ\text{C}$

Considerable effort was required to keep all instruments reading within

$\pm 0.5^{\circ}\text{C}$  of the temperature measured by the Digital thermometer. Ten calibrations were done on 4 RTDs at temperatures of  $26^{\circ}\text{C}$  to  $110^{\circ}\text{C}$ . The following algorithm was written into the data acquisition software to convert the output signal from resistance to temperature:

$$[3.2] \quad T(^{\circ}\text{C}) = (\text{ohms} - 100) / \alpha$$

where  $\alpha$  was the characteristic of the RTD, typically 0.385. Figure 3.14 shows RTD calibrations against a 'Fluke' digital thermometer with thermistor probe.

For the wheatstone bridge arrangement, the following algorithm was used:

$$[3.3] \quad T(^{\circ}\text{C}) = (129.87 - 571.43 \cdot V) / (2.5 + V)$$

### 3.3.6 Volume Change Devices: VCT, DPT, Burettes

'Rosemount' Model 1151DP3E differential pressure transmitters (DPT) were used with back pressure burettes (Figure 3.2) almost exclusively in this program for measurement of volume changes. This arrangement makes use of the DPT accuracy to measure the change in height of the column of water in a burette. Figure 3.2 shows the DPT as device '1' and the burette as device '2'

The differential pressure transducer (DPT) used for volume change measurements was not insulated due to its remote location. Extensive calibrations were performed to assess its sensitivity to static and mean pressures. Theoretically, the DPT should be insensitive to applied pressure due to its diaphragm construction. In practice, readings should be corrected if a wide range of operating pressures and temperatures are used. Alternatively readings can be checked against a burette arranged in parallel with the DPT.

Twenty calibrations were performed on four DPTs for pressures up to 7.0 MPa. Calibrations at 0 and 1.0 MPa are compared in Figure 3.15 (a). The change in gain



and zero was less than 1.7%. A gain correction of  $\Delta G/\Delta p' = 1.638\%/MPa$  is recommended for DPT M85425, if large pressure changes are expected. Figure 3.15 (b) shows the signal processing used. Figure 3.15 (c) shows the observed pressure dependence in schematic form. Since most tests were run at constant back pressures of 1.0 MPa, no pressure corrections were applied to buffer volume change data

Pressure corrections are also a function of compressibility of the water, burette, and fittings. The back pressure burettes had an immediate volume change response of +0.09 ml from 0.0 to 3.5 MPa. The burettes with standard wall thickness have a burst pressure of 8.4 MPa, but a factor of safety of at least 2.5 should be used for safe operation of new burettes.

Repeatability and hysteresis of the gain in the volume change system was  $\pm 0.5\%$  of factory specifications.

The key to operating a volume change system is setting it up once using similar materials for all components and avoiding subsequent changes in the system. Periodic checks for leaks in fittings due to fatigue or differential thermal expansion are required.

### 3.3.7 Lateral Strain Gauge (LSG):

A strain-gauged spring steel loop was specially designed and built at the University of Manitoba for the HITEP cell to corroborate calculated shear strain data by direct measurement of the specimen diameter. The device was based on an earlier model described by El-Ruwayih (1976). A second generation device, similar in design (Yarechewski 1993) is shown in Figure 3.16. The influence of the stiffness of the device on specimen restraint still needs to be checked, particularly with increasing deformations, but is clearly small for the high density

buffer used in these tests. Account must also be taken of membrane compression, especially if the temperature or pressure are ramped.

Six calibrations were performed at room temperature and specimen diameters of 53mm to 61 mm. Calibration consisted of placing different sizes of gage blocks inside the LSG, but the process of removal and insertion introduced scatter in the data due to loading and unloading of the device. A typical calibration is shown in Figure 3.17. Diameters larger than about 61 mm resulted in permanent change in the calibrations.

The LSG works well for loading, but experiences hysteresis during unloading.

### 3.3.8 Temperature Control, Heaters, Insulation

Heating of the HITEP cell is accomplished using a programmable ramp and soak temperature controller, RTD temperature input, and two silicone rubber band heaters mounted externally at one-third and two-thirds of the sleeve height. A rheostat allows manual division of power between the two bands (Figure 3.4). A continuous power base heater element has been a late addition to provide more uniform heat distribution in the cell.

The controllers make use of three principles of control theory to regulate temperature: (1) proportional; (2) integral; and (3) differential control (PID). For proportional control, an arbitrary bandwidth encompasses the set-point temperature. One hundred percent of the total available heat output is applied if the control sensor indicates temperatures below the selected bandwidth, whereas zero power is supplied above the band. If temperatures are sensed within the bandwidth, a proportion of total heat output is applied according to the difference between the set-point and sensed temperatures.

An insulated case was designed to enclose the HITEP cell. Initially, no insulation was placed around the pressure transducers because it was hoped they would remain close to room temperature, simplifying temperature compensation. Insulation is now being tested in subsequent tests to (1) eliminate room temperature fluctuations, and (2) keep the transducers at temperatures closer to the specimen. Initially, no insulation was used at the cell base. However, temperature gradients of 3 °C between the top and bottom of the cell have prompted the use of a base heating coil and insulation.

### 3.3.9 Automatic Pressure Control System (PCS)

A computer controlled system for maintaining constant cell pressure, and for ramping cell pressures automatically was assembled by the author. The reason for using the system was to control temperature induced pressure fluctuations during overnight heating phases. The system used a feedback loop consisting of pressure transducers, solenoid valves, a special control card and a data acquisition system. Figure 3.18 shows the system in schematic form. Considerable effort was required to 'tune' the system, but pressures could be maintained within  $\pm 0.010$  MPa at 3.0 MPa static pressure. Later, suitable pressure relief valves were found by D.Yarechewski for this purpose and the original need for the PCS was removed.

Tests T1233 and T1234 were successfully run with the PCS at temperatures of 100°C with a cell pressure of 1.6 MPa. The apparatus worked well up to 5.0 MPa. At higher pressures, the solenoid valves would not open and close completely, which caused instability in reaching an equilibrium pressure, even when modulated with needle valves.

### 3.3.10 Load Frame

The HITEP cell was hoisted on to a 100kN load frame which was purchased for shearing the buffer specimens. Compliance of the load frame was negligible for buffer tests. The load frame had a range of axial displacement loading rates from 0.00005 mm/min to 4.00 mm/min.

### 3.3.11 Compaction Mold/Frame

An apparatus for forming specimens was developed by the author and the staff machinist. It consisted of a hydraulically operated static compaction frame and split mold with a 2 inch (50 mm) inside diameter. Figure 3.19 shows an isometric view of the apparatus. The purpose of this apparatus was to compact buffer specimens under static pressure and remove them with minimal disturbance. This provided a considerable improvement over extrusion from a thin walled tube as used by previous researchers.

Figure 3.20 shows the specimen compaction mold separate from the compaction frame.

## 3.4 Data Acquisition (D/A)

Data acquisition consists of the same transducers, multiplexer, digital voltmeter and computer used by previous researchers (see for example Graham *et al.* 1989a), but expanded to three banks of eight channels to give a total of twenty four channels. A simple program was written in BASIC to acquire the data from the transducer voltages. 'HP Instruments' software provided the interface with the digital multimeter, multiplexer (channel changer), instruments and user interface (screen and keyboard). This software is much simpler than that developed by Saadat

(1989), but does not automatically produce Lotus graphs. Different macros were used in separate Lotus spreadsheets to reduce data from the raw data files.

Rather than develop a fully automated high temperature triaxial system which alone would constitute doctoral research, the intent was to create a convenient, useable system; generate preliminary data; and develop a simple predictive constitutive model for dense buffer. Nine measurements are recorded in the prototype HITEP apparatus: (1) axial deformation; (2) axial load; (3) specimen volume change; (4) back pressure; (5) cell pressure; (6) specimen diameter; (7) specimen temperature; (8) temperature gradient across the specimen; (9) room temperature. Data from channel 9 are shared with tests run using the other cells.

Settling time for most instruments was about 0.1 sec, but as much as 1 second was required for some such as load cells, RTDs, and thermocouples. For the long-duration tests in this program, these settling times were perfectly acceptable. A high quality multimeter ( $\pm 0.00001V$ ) and power supply is necessary for good instrument performance

The first major source of reading error with the instruments was poor or broken electrical contacts at solder joints and connectors, particularly at the multiplexers. The contacts on the multiplexers had to be cleaned at 3 month intervals to ensure good performance. The second source of error was improperly shielded signal wires. Power cords should be isolated from all signal wires to avoid direct and inductive current interference. A third source of error was overheated fuses, relays, and circuit boards. Separate cooling fans are necessary for computers, temperature controllers, data acquisition systems, and power supplies.

Other sources of error and data loss were unexpected power failures, and

voltage fluctuations in the building.

### **3.5 Membranes**

A critical component of the equipment development for this project was the improved membranes needed to enclose the buffer specimens and seal them from the pressurized cell fluid at elevated temperatures. This section outlines the work that has been done in developing new membranes. A complete description of the manufacturing technology is included in a separate document "Membrane Technology For Elevated Temperatures", to be submitted for publication. A literature review was first undertaken to look for reliable current technology which would facilitate material selection. Equipment was then designed and manufactured to produce membranes which were subsequently tested for temperature stability, compatibility with the silicone cell fluid, pressure compliance, and tear resistance. Results from the compliance tests are included.

#### **3.5.1 Selection**

A review of current literature indicated two major problems: (1) little triaxial testing of soil had been undertaken at elevated temperatures and pressures and (2) only a few materials were suitable for the range of temperature, cell fluid, pore fluid, pressure, strength, and acceptable leakage rates that were to be used in the program. Details of the various membrane materials that have been investigated are given in Table 3.3.

**Table 3.3: Details of membrane materials that have been investigated.**

Membrane Material	Commercial Availability (preformed)	Continuous Service Temperature Rating	Comments
RTV Silicone (2 part) BJB Enterprises Dow Corning	Custom	260°C (5 days) 100°C (30 days)	Swells and depolymerizes in silicone oil above 200°C
Viton Rubber	Custom	>25°C in oil	Decomposes in H <sub>2</sub> O Expensive
Teflon	Sheet only	230°C	Stiff
Polythene wrap	Sheet only	-	Difficult to seal
Polyolefin (heat shrink)	Many sizes	135°C	Difficult to seal
Polyurethane	Custom	-	Pressure mould Expensive
Hypalon	Sheet only	-	
EPDM (40 Durometer)	Custom	175°C	Expensive
Copper	Sheet	>500°C	Difficult to seal 1.5% strain max.
Rubber Latex	Many sizes	<200° in salt water	
Latex Prophylactic	Wide availability	<100°C in silicone oil	

### 3.5.2 Manufacture

An extensive material selection program was undertaken to obtain a suitable type of rubber membrane to enclose the specimens. Conventional latex membranes disintegrate at temperatures of 100°C in silicone oil. Two grades of RTV silicone rubber (2 component), supplied by BJB Enterprises, were chosen: 5050 A/B (Shore A hardness 50) and 5026 A/B (Shore A hardness 26).

A special aluminum split mold was designed by the author. Figure 3.21 shows the design. The following molding procedure was developed to eliminate entrapped air during mixing of the components. Liquid rubber is poured into the mold and placed in a vacuum to remove most of the trapped air. (Air bubbles are a serious problem with membrane forming.) The plug is inserted into the mold before the rubber hardens. The top cap is bolted down and the mold is pressurized to compress remaining air bubbles. The membrane is removed after about one day and heat treated for one hour to cure the rubber.

An attempt to use urethane for a second generation membrane was less successful than silicone because of trapped air. Urethane would be more suitable because of its toughness, inertness, temperature stability and high density (low permeability). However, urethane is more difficult to cold patch than silicone.

### **3.5.3 Compliance: Extension Tests/ Rubber Dummy Tests (RD)**

#### **3.5.3.1 Membranes**

Preliminary tests were undertaken to evaluate the relative stiffnesses of latex, silicone, and urethane membranes. The stiffness of silicone membranes is less than the buffer, but it was necessary to quantify the effect of membrane confinement on the buffer strength. ASTM D4767-88 recommends a method based on 'hoop stress' theory and the work of Henkel and Gilbert (1952). However, ASTM D4767-88 does not make a distinction between the effects of compressive shell theory for no-buckling conditions and hoop stress theory as Henkel and Gilbert did. The ASTM standard does not explicitly account for decrease in membrane stiffness with strain, thus giving conservative values for membrane corrections. A comprehensive study by LaRochelle *et al.* (1988) gives methods for corrections in the buckling and



no-buckling condition. The former is applied to the lateral stress, but the latter is applied to the axial stress. The problem is complex and no definitive answer exists for membrane corrections. Temperature softening of the membranes is not considered here.

ASTM recommends corrections if the difference in deviator stress due to the strength of the membrane is greater than 5%. Calculations are based on the extension modulus of the rubber, obtained from a simple test in ASTM D4767-88. The extension modulus,  $E_m$ , may be thought of as a Young's modulus, and is determined by stretching bands of membrane 1 cm wide. The extension modulus decreases with strain. The actual  $E_m$  values used in this work were doubled for peak strength calculations, because the bands were strained 27% which is much more than caused by a specimen at peak strength. This will give a conservative estimate of the correction required.

Table 3.4 gives corrections  $\Delta q$  using both the ASTM method and LaRochelle's method. Tests T1228 and T1233 were chosen because they represent high strength and low strength specimens. The method of calculation is given in Appendix A. Clearly LaRochelle's corrections are more accurate than the ATSM recommendations, and give peak strength ( $q_p$ ) corrections of 0.80% at moderate confining stress and 4.4% at low confining stress. Larger corrections are indicated for end of test conditions,  $q_{tot}$ . ASTM indicated larger corrections than LaRochelle in all cases.

**Table 3.4 Membrane corrections: example calculations. Extension modulus,  $E_m$ , from ASTM D4767-88 on 1 cm. wide band of membrane. Membranes are 1.25 mm thick.**

LaRochelle <i>et al.</i> (1988)									
Test#	Memb.	$E_m$ (N/cm)	$\sigma'_c$ (MPa)	$q_p$ (MPa)	$\epsilon_{1p}$ (%)	$\Delta q_p/q_p$ (%)	$q_{eot}$ (MPa)	$\epsilon_{1eot}$ (%)	$\Delta q_{eot}/q_{eot}$ (%)
T1228	Y+B	18.3	2.2	1.60	2.58	0.80	1.48	7.0	1.40
T1233	B+B	22.2	0.6	0.56	4.40	4.40	0.52	10.8	5.76
ASTM D4767-88									
T1228	Y+B	-				1.07			2.90
T1233	B+B					6.33			15.54

NOTE: 1. Y=Yellow (type 5026 A/B) silicone membrane  
2. B=Blue (type 5050 A/B) silicone membrane

To further examine the question of membrane corrections, a series of ten uniaxial (unconfined) and triaxial shear tests were carried out on rubber dummy specimens. These were to simulate actual HITEP conditions and provide validation of the previous results. In addition they provide valuable information on the effects of side drains on specimen strength. Table 3.5 shows that geotextile side drains add no additional stiffness to the system. The largest correction of 0.068 MPa is for the highest confining pressure and represents approximately 6% of peak strength of a buffer specimen. The membrane corrections and stiffnesses in these tests agree well with the results from LaRochelle's theory.

**Table 3.5: Summary of membrane/side drain compliance tests using rubber dummy specimens. All tests at 26°C for loading condition only. Single membranes only**

Material	Test Type	Test#	q (MPa)	E (MPa)	p' (MPa)	v	$\epsilon_1$ (%)	$\Delta q$ (MPa)
RD	Uniaxial	TRDC20	2.64	2.06	0.0	0.55	12.8	-
RD+SM	Uniaxial	TRDC40	3.42	2.16	0.0	0.65	15.8	0.016
RD+SM+SD	Uniaxial	TRDC50	3.31	2.16	0.0	0.55	15.3	0.015
RD+SM+SD	Triaxial	TRDC80	2.58	2.32	0.6	0.50	11.1	0.029
RD+SM+SD	Triaxial	TRDC100	3.67	2.53	3.0	0.55	14.5	0.068
SM	Tear S.	F.S.	5.167	1.61	0.0	-	320.0	-

NOTE: 1. RD=rubber dummy  
 2. SM=Silicone membrane (type 5050 A/B)  
 3. SD=Side drain (geotextile)  
 4. Tear S.=Tear strength; F.S.=Factory Specifications

Figure 3.22 (a) shows the results of the rubber dummy tests. Readings were taken 'on the fly' in most tests and non-stop shearing was used. A different test procedure involving stop/start shearing with manual loading was used for TRDC9. Lower modulus result from the time lag in readings. The moduli of all the unconfined specimens were very similar, but less than the confined test. Figure 3.22 (b) shows the difference for two confined tests. It is apparent from this figure that confining pressure produces about the same change in specimen modulus as the two test methods. It may be inferred that confining pressure has only caused a slight increase in modulus of the membranes.

In conclusion, this work has shown that the effect of membrane modulus is generally less than 5% of peak strength. In view of the general variability of the results, no corrections need to be applied.

### 3.5.3.2 Geotextile Side Drains

ASTM D4767-88 has a correction for additional shearing resistance provided by side drains. However, it is not applicable to the HITEP tests because geotextile side drains were used and were placed in a spiral around the buffer specimens. Figure 3.22 (a) clearly shows that side drains add no additional modulus to the specimen/membrane system. Figure 3.23 shows typical drainage configurations for the buffer test program. The rubber dummy tests used the single drainage arrangement.

### 3.5.4 Diffusion Test Results

Three multi-stage tests were carried out by the author at 26°C, 65°C, and 100°C (MDAL1, MDAL2, MDAL3). The room temperature tests were successful and are discussed in Chapter 5. The tests at elevated temperature were not successful due to leakage. The apparatus was modified by Yarechewski (1993) for testing at elevated temperature. His test results are compared with theory in Chapter 6.

### 3.5.5 Strength: Test Results and Temperature Effects

First, the materials were soaked in silicone oil and water at 100°C to 110°C for durations up to 2 months at normal atmospheric pressure. Urethane, RTV silicone, polythene wrap, and buna rubber showed little or no degradation or loss of strength in oil. Latex rubber dissolved in oil and discolored in water. 5026 RTV softened in oil.

Latex, urethane, and silicone membranes were qualitatively tested for tear resistance. In some simple tests, tension was applied by hand to a notch cut in rubber coupons. Latex had the highest resistance at room temperature; 5026 RTV had

the lowest value; with 5050 RTV and urethane having intermediate values. Tear resistance of silicone rubber reduced after it was soaked in silicone oil at 110°C. Table 3.4 shows manufacturers specifications of room temperature properties of the candidate materials.

**Table 3.6: Manufacturer's specifications of room temperature properties of candidate materials.**

Material	Specific Weight	Hardness Shore A	Tensile Strength kPa	Elongation (%)	Tear Resistance
3-component Urethane	1.063	50	6000	350	-
2-component RTV 5026	1.07	23	5200	400	125
2-component RTV 5050	1.25	50	5200	2200	85

### 3.6 System Compliance

It was necessary to know the pressure-temperature-deformation response of the HITEP system for setting up the test program and analyzing buffer data.

#### 3.6.1 Triaxial Cell

##### 3.6.1.1 Pressure

Application of cell pressures of 10 MPa in Saadat's cell produced significant deformations. The tie rods stretched 0.5 mm and the sleeve diameter increased by 0.25 mm. These agree with theoretical calculations based on thick-walled cylinders. The HITEP cells had thicker walls and rods. Therefore smaller deformations can be expected.

### 3.6.1.2 Temperature

Thermal expansion of the HITEP cells during heating to 100°C produced volume changes in the system of approximately 1.5 litres. Most of the expansion was a contribution from the silicone oil.

### 3.6.2 Controller and System Thermal Inertia

As mentioned earlier, the temperature controllers use three process algorithms to regulate temperature: proportional, integral, and differential. It seemed advantageous to have all three functions in use in this test program, but even with the help of a technician familiar with these devices, a temperature overshoot of 5°C occurred in the first tests due to the large system thermal inertia. It took a minimum of 8 hours to heat to 65°C and 12 hours to heat to 100°C at full power output 300W. To overcome the overshoot, the power was cut for an hour when the current cell temperature was within 5°C of the setpoint temperature, then power was resumed. A colleague, D. Yarechewski, has recently discovered that only proportional control will provide a precise temperature cutoff at the target value.

### 3.6.3 Side Drains

#### 3.6.3.1 Pressure Effects on Efficiency

A study by the author and co-researchers (Oswell *et al.* 1989) has shown that Whatman #1 filter paper does not allow drainage of pore fluids above effective stresses of 1.0 MPa. Whatman #54 is effective up to 3.0 MPa. Geotextile is useful to at least 10 MPa. Mirafi #132 geotextile was chosen for its strength, low compressibility, high porosity and resistance to clogging. It experiences no degradation or mass loss when heated in air or oil at 110°C.

### 3.5.3.2 Specimen Confinement

As discussed earlier, rubber dummy tests indicate that side drains produce little or no effect on the strength of buffer specimens.

### 3.6.4 Compaction Frame and Mold

Measurements of the inside diameter of the split mold used for compaction have been recorded for 13 buffer specimens before ( $D_o$ ) and after ( $D_f$ ) the specimens were compacted, before removal. No compaction pressure was being applied to the specimens when the measurements were taken. The diameter  $D_o$  was 50.88mm. After a compaction gauge pressure  $P_g$  of 34.5 MPa (5000 psi) was removed from the specimen, the mold diameter,  $D_f$ , at the top was 51.91 mm. The gauge pressure of 34.5 MPa corresponds to a vertical pressure,  $\sigma_1$ , on the specimens of 24.8 MPa. The conversion factor  $\sigma_1/P_g$  is 0.72 (psi/psi) and assumes no frictional losses.

### 3.6.5 HITEP Leakage

Early in the HITEP test program, five membrane leakage tests (SML1-SML5) were conducted independently in a low pressure lucite triaxial cell at room temperature. These tests were designed to compare leakage rates of latex membranes with new technology silicone membranes. Leakage tests for the HITEP system and membranes will be discussed in Chapter 5. Four tests were performed: Leak#1, T1222, T1224, and T1231.

### 3.6.6 Burette-Water System: Pressure-Volume-Time Response

Figure 3.24 shows the response of the back pressure burettes to nitrogen gas pressure of 1.4 MPa. There is an immediate elastic compression of the water of 0.5 ml. The pressure was maintained to dissolve nitrogen in the de-aired water. Complete release of the pressure after 20 days, Figure 3.24 (a), shows an immediate elastic rebound followed by a time dependent recovery. Some gas bubbles appeared when the pressure was released. Figure 3.24 (b) shows little or no time dependent behavior, but the original volume is not recovered. The results seem to indicate that nitrogen dissolution may produce extraneous volume changes, but these are avoided in this program by keeping a nominal pressure on the buffer specimens at all times and measuring volume changes from a common reference point such as just after pressure application.

### 3.6.7 Thermal Stability of Components

A suite of tests was run early in the program to assess the thermal stability of side drain geotextile, membranes, O-rings, nylon tubing, and U-cup seals in air, water and silicone oil at 100°C. They performed well with a few exceptions: the nylon tubing became brittle in air and softened in oil; the buna O-rings hardened in air and oil; viton softened (reversibly) at high temperature; and only U-cup seals of carboxylized nitrile (black) survived intact for any length of time in oil. These are critical seals and are the only type that survive the test environment where water contamination of the cell fluid occurs.



### 3.6.8 Room Temperature Response of the HITEP System

Room temperature was monitored throughout the tests using the new equipment and data acquisition software developed for the high temperature tests. Cell temperature is inferred from room temperature. The temperature probe comprised a resistance thermal device (RTD) immersed in a small container of silicone oil. This arrangement (1) provided average values with time, (2) reduced self heating of the probes, and (3) eliminated background "noise" caused by local air currents.

Considering the level of activity in the laboratory, daily temperature fluctuations due to outside weather conditions and the occasional use of air conditioning, a reasonably constant room temperature of  $26^{\circ}\text{C} \pm 2^{\circ}\text{C}$  was maintained. The cell for these "ambient temperature" tests was not insulated although of course, the cells for the "elevated temperature" tests were.

Temperature readings monitored during HITEP tests showed a regular, near sinusoidal diurnal temperature response with time. In the summer months, maximum temperatures occurred around midnight and the minimum temperatures at noon. Less regular, smaller amplitude changes in temperature were observed during winter months. A primary concern with temperature control is during the undrained shear portion of the tests when pore pressure is being measured. A temperature change of  $3^{\circ}\text{C}$  will cause compliance of 200 kPa in the closed pore pressure measurement system under saturated conditions. No attempt has been made to correct the measurements in this series of tests. Measured cell pressures followed the room temperature changes exactly with little or no lag time. The pressure regulators used to control the cell pressure were reluctant to moderate increases in pressure inside the cell caused by temperature changes. Adequate cell insulation reduced the effects of room temperature changes to acceptable levels.

## CHAPTER 4 TEST PROCEDURES AND BUFFER PREPARATION

### 4.1 Introduction

This chapter discusses the buffer specimen compaction and installation procedures. The same basic procedures are used for both ambient temperature and elevated temperature tests, although the operational procedures for the HITEP cells are more complex. Generally it took a sixteen-hour day to install a specimen and reach 50°C. The 65°C and 100°C tests were generally left overnight to reach temperature equilibrium. The heating procedure and post test specimen removal procedures are discussed. Test procedures for the double-walled cell will not be discussed because only two tests (T1210, T1213) were performed in this cell.

### 4.2 Test Materials

The buffer tested in this program was a 50:50 mix by dry weight of quartz sand and bentonite. The sand was a blended mix with  $D_{10} = 0.2$  mm and  $D_{85} = 1.3$  mm. A sieve analysis of the blended sand is shown in Figure 4.1. The specification of the sand was reported by Gray, Cheung and Dixon (1984).

The bentonite was sodium-rich smectite commercially available from Avonlea Minerals Industries, Regina, Sask. Composition and mineralogy were reported by Dixon and Woodcock (1986) and Quigley (1984). The liquid limit was in the order of 225% to 250% with a plasticity index of about 200%. The grain size distributions in Figure 4.1 are similar to those determined by Dixon and Woodcock (1986).

After test T1220, a new bag of bentonite had to be opened, although it came from the same batch as the first bag. (Materials for the program were supplied by AECL Research.) Index parameters such as Atterberg limits were similar for the clay from each bag. For instance, the old bag of bentonite had a liquid limit,  $w_L$ , of 228% (tested by N. Piamsalee, Sept. 18, 1989:). The new bag had Atterberg

limits  $w_L = 222\%$ ,  $w_p = 36\%$  (tested by N. Piamsalee, June 11, 1990). The material properties of the bentonite are believed to be the same for both bags.

A new mix of sand, blended according to AECL specifications was also used after T1220 (mixed by N. Piamsalee, March 22, 1990). The gradation of the old and new mix are shown in Figure 4.1. Clearly, the mixes are very similar.

Distilled, de-aired water was used in the preparation of all specimens.

### **4.3 Specimen Preparation**

#### **4.3.1 Specimen Compaction**

Static compaction of buffer specimens in a cylindrical mold has been discussed by Sun (1986), Wan (1987), Yarechewski (1988), and Saadat (1989). They compacted buffer specimens in a thin-walled steel tube, and later extruded them using a hydraulic ram. Two uncertainties involved with this method were (1) the rigidity of the mold; and (2) the amount of shear deformation induced by the extrusion process. A split mold was designed to alleviate both of these concerns. The mold was rigid enough to handle the hydraulic compaction pressures of 24.8 MPa (5000 psi) used to achieve target densities of  $1.67 \text{ Mg/m}^3$ . This corresponds to full saturation at 95% Modified Proctor dry density.

Specimens were prepared according to the method developed by Yarechewski (1988). As indicated by Oswell (1991), this technique produced specimens of uniform density along the height of the specimen by compacting equal-mass lifts of the moist sand and bentonite mixture to carefully controlled thicknesses in the mold. As in Oswell's program, specimens for this program were overcompacted in the mold by 0.4 mm. Upon removal from the mold, this produced specimens with a final height closer to the 100 mm specification.

A thin film of multigrade lubricating oil was spread over the inner

surfaces of the mold to ease specimen removal. Only light pressure was required to remove the compacted specimen from the separated half of the split mold.

The control parameter used to achieve the specified density and high saturation was moisture content. The buffer for the first tests, up to T1219, was mixed at a moisture content of 22.75%. At the end of compaction the moisture content had dropped by approximately 0.5%. However, for the specified compaction height of 100 mm, and material quantities (164.5g of clay, 164.5g of sand, 74.8g water) the density was slightly less than required ( $1.65 \text{ Mg/m}^3$  compared with the target  $1.67 \text{ Mg/m}^3$ ). The mixing water content was therefore increased to 23% and the specified density of  $1.67 \text{ Mg/m}^3$  was reached in specimens after T1219. Significantly higher compaction pressures were required to achieve a final specimen height of 100 mm because larger material quantities were used (168.9g clay, 168.9g sand, 77.69g water). Apparently the buffer became fully saturated in the mold at the higher water content.

Statistical data for compaction density and moisture content of the specimens are given in Table 4.1. Test T1205 has been omitted in this statistical analysis because it was a low density specimen ( $\gamma_d = 1.5 \text{ Mg/m}^3$ ) corresponding to 85% ASTM Modified Proctor maximum dry density, as tested by earlier researchers. Details of individual tests are given in Appendix B.

**Table 4.1: Statistical data for Specimen Preparation**

Target $\gamma_d$ (Mg/m <sup>3</sup> )	Number of Specimens	Avg $\gamma_d$ (Mg/m <sup>3</sup> )	Std. Dev. (Mg/m <sup>3</sup> )	Avg $w_o$ (%)	Std. Dev. (%)	Avg $S_o$ (%)	Std. Dev. (%)
1.67	31	1.658	0.018	22.15	0.63	95.22	2.55

NOTE: 1. Avg=Average

2. Std. Dev. = standard deviation

3.  $w_o$  = initial moisture content

4.  $S_o$  = initial saturation

5.  $\gamma_d$  = dry density

The contact pressures applied to the specimens through the compaction ram were from about 4 MPa to a maximum of 29 MPa. The largest pressures were always required for the last layer compacted (lift 5). Friction between the buffer and the mold during the compaction process considerably reduced the actual pressure experienced by the buffer, especially at the bottom of the specimen as successive lifts were added. Stress release is also important since it affects the anisotropy of the specimen. The final contact pressures for individual specimens are summarized in Appendix C.

The specimens were slightly barreled after removal. The top and bottom were not completely flat, but instead had a convex shape which was most pronounced on the top. Details of the extent of the convexity are given in section 5.3.1.

#### 4.3.2 Specimen Drainage

In general, the same test techniques and equipment used by previous researchers (Saadat 1989, Wan 1987) were used for the ambient temperature tests in

this program (T1200 series of tests). However, two improvements were introduced: (1) geotextile side drainage strips, and (2) the addition of a transducer to measure pore water pressure at the base of the specimen, independent of the controlled back pressure applied at the top. This allowed more reliable pore water pressure measurement and interpretation of effective stresses (see also Oswell 1991). To reduce confusion, the term "side drainage" is used here instead of the more common "radial drainage". "Side drainage" indicates strips of drainage material applied externally on the outer circumference of the specimens. Side drains were placed in a spiral arrangement to reduce the influence on the specimen stiffness (Gens 1982). They extended from the top of the specimen to within 1 cm of the bottom of the specimen when pore pressure was measured at the bottom.

Instead of using two 0.635 mm thick latex membranes as in the earlier tests, a single 1.4 mm membrane was used in some tests to make specimen installation easier. Special care was taken to ensure that a good seal was obtained.

Concern over low levels of saturation in the porous stones during building-in led to tests where the moisture loss was measured under conditions simulating specimen installation. This was especially important for the top stone because it could not be flushed with water like the bottom stone. Measurements show that the stones remain about 75% saturated during installation. Application of the back pressure typically results in 1ml of water being pushed into the apparatus. This represents almost all of the water lost from the stones. Air pockets in the valves, lines, and cell base account for the balance of the volume change. Saturation levels were subsequently checked using the B-test described in section 4.4.

### 4.3.3 Specimen Installation

#### 4.3.3.1 Ambient Temperature Tests

Specimen installation and test start-up were carried out following broadly the methods developed by Wan (1987) and Saadat (1989). The introduction of back pressure measurement at the top of the specimens made installation more difficult and potential leakage had to be carefully monitored. An installation procedure developed in the University of Manitoba laboratories by Oswell (1991) and modified by the author was used. The procedure was as follows. (1) Porous stones, Whatman #54 filter paper disks, and drainage strips were saturated in de-aired, de-ionized water. (2) Filter paper disks were placed on top and bottom of the specimen; filter paper strips were placed in a spiral pattern on the outer circumference of the specimen. (3) Geotextile drainage strips were then placed over the paper strips and held in place at the top and bottom by rubber bands. (4) A single 1.4 mm thick latex membrane was placed around the specimen with the ends folded back. (5) The specimen was placed on a cell pedestal that had been flushed with de-aired water. The membrane was folded down and O-rings installed at the base. (6) A porous stone was placed on top of the specimen followed by the top cap. The membrane was folded up and O-rings applied. Drainage lines were pre-saturated and kept closed until the start of consolidation. (7) The cell was assembled and filled with cell fluid (silicone oil), then pressured for the start of consolidation.

The geotextile side drains could not be kept wetted and were placed around the specimen in an unsaturated condition.

Head (1986) recommends maintaining a minimum back pressure of 0.2 MPa to avoid dissolution of air in the water. A minimum back pressure of 1.0 MPa was used in all tests in this program.

Earlier procedures for saturating the top porous stone by flushing

introduced uncertainty in later volume change calculations because it allowed free swelling of the bentonite. This swelling was quite significant because of the relatively long assembly time; about four hours. Flushing was subsequently abandoned in favor of back pressuring to achieve saturation. Filter paper strips on the outside of the specimens were not used in tests after T1211. Instead, only geotextile strips were used because of their free draining capability and resistance to clogging. Keeping the geotextile strips saturated during installation was difficult.

Double latex membranes were used in the first ambient temperature tests. In ambient temperature tests after T1207, single latex membranes 1.40 mm thick were used. The procedure used for installing the top drainage lead in tests after T1207 prevented the use of double membranes. (Different procedures and equipment were needed for installing double drainage in tests conducted at elevated temperature). In all cases, a minimum of four O-rings were used to seal the ends of the membranes against the top cap and pedestal, two at the top and two at the pedestal. The types of membranes used in individual tests are given in Appendix D.

Specimens with top drainage lines were installed as described above, but the drain line was first connected to the back pressure source and top cap and pressure tested. Then the top cap was flushed with de-aired water and drainage was closed. The top cap was installed on the upper porous stone at the top of the specimen. The membrane was folded up and extra o-rings from the bottom of the specimen were rolled to the top to seal the membrane against the top cap. High density 1/8" polythene tubing (44 NSR) was used for the top drain line.



#### 4.3.3.2 HITEP Tests

The HITEP apparatus is considerably larger than a conventional triaxial cell and nine test parameters were measured instead of the five in a normal cell. A lengthy assembly procedure is required to operate the equipment successfully. The main steps for assembly are as follows. (1) Flush oil and contaminants from the cell base, pedestal and top cap with de-aired water, and remove excess water from the floor of the cell. (2) Place filter paper and side drainage on the specimen. (3) Place the lower porous stone on the pedestal and flush water from the pedestal, position the specimen, top porous stone and top cap. (4) Apply the inner membrane and O-rings at the top and bottom of the specimen. (5) Fit the outer membrane and O-rings. (6) Install the lateral strain gage, taking care to center it and avoid eccentricity. (7) Mount the temperature sensors. (8) Bring the load cell in contact with the specimen, and then back off 4mm. (9) Zero all instruments, check calibration factors and input voltages. Test the instruments individually to make sure they are reading correctly. Start the data acquisition program. (10) Photograph the specimen. (11) Lower the cell sleeve and bolt down. Fill the cell with silicone oil and install the axial deformation LVDT. (12) Install the cross beam of the load frame. (13) Apply the selected cell pressure, keeping the drainage connections closed. (14) Install the insulation jacket. (15) Program the temperature controller. (16) Record initial readings on the transducers and set time interval between readings. (17) Open the drainage connections and initiate the controller.

Double silicone membranes were used in all tests at elevated temperature, except T1210 and T1213. These tests were conducted in the double walled triaxial cell and there was room for only one membrane. Membrane types are given in Appendix D.

As in the ambient temperature tests, no silicone grease was applied to the top cap, pedestal, and membranes because it produced leaks. O-rings were placed similar to the ambient temperature tests, but the buna O-rings were only used once because they became permanently stretched at elevated temperature. Viton O-rings were used later because they were more resistant to temperature hardening.

Copper lines were used for top drainage lines in some tests at elevated temperature. This made specimen installation difficult. The specimen was installed as for tests with no top drain, except the top cap was flushed with de-aired water, then the top drain line was flushed with de-aired water and attached to the top cap. A good seal was obtained by tightening the line more with each test.

The time taken to install specimens carefully, including cell preparation and checking the data acquisition system is about eight hours. The tests that have been done so far use only set-point (internal) controller operation instead of programmed "ramp and soak" procedures to reach the setpoint temperature. A temperature overshoot measured as  $5^{\circ}\text{C}$  occurs when the test arrangement is properly tuned due to the thermal inertia of the system. Heating time is about 12 hours.

#### 4.4 Consolidation

Consolidation using the HITEP apparatus differed from that of the ambient temperature tests as follows. (1) Heating occurred during the initial day of consolidation. (2) Back pressure was applied at the base of the specimen. (3) Pore water pressure measurements (through the base of the specimen) were possible only during the shear phase of tests. (4) Full length side drains allowed drainage communication from top to bottom of the specimen (except in tests T1216 and T1219). There were a limited number of HITEP tests which measured pore pressure independently from the back pressure.

As in the previous ambient temperature tests and Saadat's program, consolidation readings were considered to start after the drainage leads were opened and to be complete when the volumetric strain rate was below 0.1%/day. Drainage leads were closed, the load cell response was checked. The load cell was brought into contact with the specimen and the load frame was turned on to commence the undrained shear portion of the test.

B-tests were performed near the end of consolidation before shearing. These tests were conducted using similar procedures to Saadat (1989).

#### 4.5 Heating Procedure

Three criteria were used for setting a protocol for heating the buffer specimens in the HITEP apparatus. The first criterion was a limitation in the power output of the controller which provided a maximum steady state heating rate of approximately 6°C/hour.

The second criterion was the ability to produce consistent repeatable heating rates. This was achieved by keeping the process variables on the controller constant throughout the test program. The process variables were set in the 'tune' mode, on or off line, and included the following: cycle time-60 seconds; proportional band-2%; resets per minute-0.01; and rate-0.2 minutes. These appear to be the optimum settings for the HITEP apparatus for a heating rate of 6°C/hour. Shorter cycle times lead to overheating of the controller output relay and circuit board.

A third criterion was the response of the buffer specimens. The duration of heating was arbitrary. The constant setpoint temperature  $T(^{\circ}\text{C})$  is reached within the first 12 hours of testing, while consolidation continued for periods between 2 weeks and 2 months. While this may not exactly model field conditions,

it provides a good first approximation of time-temperature pressure-volume change behavior. The HITEP tests will be referred to as 'isothermal' tests because following initial heating, during consolidation and shear, the specimens are kept at a constant temperature.

Variations in the heating rate apparently did not affect the final moisture content of the specimens. For example in tests T1232 and T1233, the heating rates were 1°C/hour (minimum) and 6°C/hour, respectively. The final moisture contents were the same.

In some cases the specimens were heated in increments because they could not be supervised over a full heating cycle. The strengths of the specimens after consolidation at constant elevated temperature apparently were not affected by heating rate at the start of consolidation. However, the time to reach the end-of-consolidation volumetric strain rate of 0.1%/day was reached in approximately 12 days for the 100°C specimens, compared to 20 days for the 65°C specimens.

Factory settings for the controller calibration can be changed in the 'calibration' mode using a special password, but factory settings were left unchanged for this test program.

#### **4.6 Undrained, Drained Shear**

Undrained and drained shear were conducted using procedures similar to Saadat (1989) and will not be discussed further here.

#### **4.7 Post-Test Procedure**

Specimen removal procedures were similar to installation procedures. To prevent ballooning of the membrane a minimum pressure of 700 kPa was kept on the

specimen until just before the cell sleeve was removed. All drainage valves were kept closed during disassembly. The specimen was removed in the hot condition to (1) maintain the specimen moisture content in the hot condition and (2) to avoid water absorption from the drainage stone and leads. Some cooling naturally occurred, but the greatest heat loss was during moisture determinations.

The specimen dried quickly at a rate approaching 0.1 g/min, so considerable care had to be taken to use standardized procedures when the final moisture contents were measured. The specimens were immediately weighed and measured, then covered with polythene wrap. The specimens were cut in five pieces of approximately the same length. A 25 mm diameter core was taken from each layer. Moisture contents were obtained for all ten pieces to check the variation of moisture along the specimen length and from inside to outside. The cores provided the most reliable final moisture content. Photographs were taken of the specimens to document shear failures.

Silicone oil was used as cell fluid for all tests except T1210, T1213 in which antifreeze was used instead. Determination of the true volume changes in specimens is not straightforward if leakage occurs past the O-ring seals or the membrane. The oil will impede drainage, but some oil is also adsorbed by the buffer. In tests where leakage occurred, oil collected on the outside of the specimen and in the top porous stone. This may have impeded drainage slightly.

As a precaution against impeded drainage through oil-contaminated stones, the following procedure was used for cleaning stones after each test: (1) Soak stones in lacquer thinner for 1 hour; (2) Air dry; (3) Wash and soak in soapy water for 1 day; (4) Rinse thoroughly in water in an ultrasound bath; and (5) De-air the stones. The drainage lines were flushed with de-aired water and oil was cleaned off the cell pedestal and top cap.

## CHAPTER 5 TEST RESULTS

### 5.1 Introduction

This chapter presents details of the triaxial testing program to investigate the temperature dependent stress-strain behavior of buffer using isothermal triaxial undrained shear tests with pore water pressure measurement. Buffer specimens were heated and consolidated simultaneously. Three temperatures were tested: 26°C, 65°C, and 100°C, with the target temperatures being reached within the first one to two days of consolidation. After the specimens reached an acceptably small volumetric strain rate, drainage was shut off and undrained shear testing was performed at constant elevated temperature. At the end of shear, the specimens were removed from the cell in their hot state to obtain representative moisture contents.

Results for 29 tests on buffer are discussed in relation to summary graphs. Two drained shear tests were also performed. The results of three compliance tests run on dummy specimens are briefly discussed. The results of cell fluid contamination tests (buffer mass loss tests) are presented, and leakage tests are discussed briefly.

### 5.2 Planning of the test program

The purpose of current research at the University of Manitoba is to quantify the behavior of a sand-bentonite (buffer) mixture at elevated temperatures (here chosen as 65°C and 100°C) and high hydrostatic pressures up to 10 MPa. This range of temperatures and pressures approximates the range of in-situ conditions in the proposed Canadian Nuclear Fuel Waste Management Program (CNFWMP). The objective of this research is to investigate the thermal dependence of representative parameters such as  $G$ ,  $E$ ,  $\lambda$ ,  $\phi'$ .

Results from the tests will be incorporated into idealized developments of constitutive models such as the elastic-plastic modified Cam clay model, or the hyperelastic model outlined by Saadat (1989). This will allow future construction and validation of a model capable of predicting deformation and strength of high density buffer at chosen pressures and temperatures. Validation of the model will be done by other researchers currently conducting tests on buffer at elevated temperatures along different stress paths such as constant  $p'$  (Yarechewski 1993), or with ramping temperatures (Tanaka).

Early in the research program, the author decided to undertake only isothermal (constant temperature) triaxial tests for his doctoral program. This allowed development of suitable equipment and testing technologies, without the additional complexities associated with testing at variable temperatures (Graham *et al.* 1990). The author's recent tests at elevated temperatures of 65°C and 100°C can be compared with similar tests done previously at ambient temperature (26°C). This permits examination of the effect of temperature on the stress-strain behavior of buffer. Results of this comparison will be discussed in a later section.

Table 5.1 shows a summary of the testing schedule. The buffer was first consolidated to one of 5 levels of effective stress: 0.6, 1.0, 1.5, 2.2, 3.0 MPa. Two additional tests at 7.0 and 9.0 MPa were run to delineate the strength envelope at high effective stresses. After consolidation was complete, (with volumetric strains less than 0.1%/day, as in previous reports), drainage from the specimens was closed, and the specimens were sheared (undrained) by increasing the axial stress until failure occurred. Pressure transducers attached to the cell base gave readings that allow calculations of the effective stresses in the specimens (Graham *et al.* 1991).

Table 5.1: Summary of test schedule for the HITEP apparatus

Temperature	Eff.Cons.Pres. (MPa)	Back Pressure (MPa)	Test Number	Notes
26°C (Ambient)	0.7	0.9	T1212	1,5a,12
	0.6	1.0	T1208	1,5b,11,12
	1.3	0.2	T1204	1,5b,11,12
	1.0	1.0 - 3.0	T1218,T1221	1,5a,12
	1.5	1.0	T1215	1,5a,12
	3.0	1.0	T1217	1,5a,12
	3.5	1.5	T1207	1,5a,12
65°C	0.6	1.0	T1216,T1225	1,13
	1.0	1.0	T1219,T1220	1,13
	1.4	1.0	T1205,T1209	1,13
	1.6	0.4	T1210,T1213	9,5b,5a
	1.5	1.0	T1224	1,4,5a,14
	2.2	1.0	T1214	1,13
	3.0	1.0	T1211,T1223	1,13
	1.0-3.0	1.5	T1222	1,2,3,13
	7.0	1.0	T1229	1,13
9.0	1.0	T1236	1,10,14	
100°C	0.5	1.1	T1232*	1,7,14
	0.6	1.0	T1231†,T1233,T1234*	1,4,7,14
	1.5	1.0	T1227#	1,5a,6,14
	2.2	1.0	T1228#,T1230	1,6,14
	3.0	1.0	T1226	1,8,5a,14
	9.0	1.0	T1235	1,14

## Notes:

1. Consolidated undrained triaxial test with pore pressure measurement
2. Cell pressure stepped in increments
3. Brass dummy specimen
4. †Aluminum dummy specimen
- 5a. Back pressure applied at top of specimen; pore pressure measured at base
- 5b. Back pressure applied at the base; pore pressure measured at top
6. #Membrane split; not sheared
7. \*Membrane ballooned; not sheared
8. Back pressure line collapsed; not sheared
9. Tested at 52°C using apparatus other than HITEP; not sheared
10. Test is in progress
11. CID(TXC)
12. Ambient temperature, high pressure triaxial apparatus
13. HITEP apparatus #1
14. HITEP apparatus #2



### 5.3 Test Results

The large volume of collected data prevents an in-depth treatment of each test in this thesis. Detailed data for tests completed up to the end of March 1990 (T1205 to T1219) were presented in a report to AECL (Graham *et al.*, 1990). Data for remaining tests (T1220 to T1235) were presented in a subsequent report to AECL (Graham *et al.* 1991). The final test T1236, and two drained tests, T1204 and T1208 are reported in a third report to AECL (Graham *et al.* 1992). A preliminary discussion of the results of all the tests is contained in the latter report. More complete discussion will follow later in this thesis.

Results from only a few representative tests will be discussed in the following section.

#### 5.3.1 Forming Specimens.

Earlier sections described forming of specimens by one-dimensional static compaction in a split mold. The contact pressures applied to the specimens through the compaction ram were from about 4 MPa to a maximum of 29 MPa. Friction between the buffer and the mold during compaction will considerably reduce the actual pressure experienced by the buffer, especially at the bottom of the specimen as later lifts are added. Stress release is also important since it affects the anisotropy of the specimen.

Measurements were taken on each triaxial specimen to assess axial and lateral rebound and 'bulging' after removal from the mold. Rebound is defined here as deformation arising between the stressed state in the mold and unstressed state after removal. Bulging is defined as the deviation from right cylindrical geometry (Figure 5.1). Lengths of the specimens were measured at both the centre and the edge of the ends, both while still in the mold, and after removal. Measurements were also taken of the diameters of the specimen at the middle and ends after

removal. The specimen diameter while still in the mold was assumed constant and equal to the internal diameter of the mold. Axial rebound is the difference between the lengths in the mold and after removal. The difference between the centre and edge lengths divided by the average length is a measure of axial bulging. Similarly, the average diameter of the specimen in the mold was subtracted from the average diameter after removal, and the result divided by the average specimen diameter to give the lateral rebound.

The specimens had typical values of axial rebound from +0.27% to +1.94%, averaging 1.15%, that is, a lengthening of 1.15% on removal from the mold. The lateral rebounds showed decreases in diameter of 0% to -0.59%, with an average value of -0.28%. The mechanism for the lateral compression on removal from the mold is unknown, but may be caused by relaxation of the specimen due to delayed elastic unloading of the mold (the diameter is measured in the mold without any vertical contact pressure), or by shear-induced pore water pressure redistribution. The lateral rebound reported here is not determined as rigorously as the axial value due to physical limitations. The specimen is not in the fully loaded state when the diameter is measured, but a method is suggested for the loaded case. Caliper measurements could not be taken of the mold inside diameter (top) while axial pressure is applied during each lift.

Inspection of the specimens after removal showed a slightly barrel shape (exaggerated in Fig.5.1), with mid-height diameter averaging 0.0mm to 0.11mm greater than the average end diameter. The lateral bulging averaged 0.22% of the specimen height. This may contribute to the initially non-linear load behavior shown in test T1230, and in most other tests to a lesser extent. Bulging occurred only at the top and sides of the specimen. It is not known why the bottom did not bulge significantly upon stress release.

### 5.3.2 Consolidation

Typical consolidation of buffer at room temperature and 1.0 MPa effective stress is shown by specimen T1221 in Figure 5.2 (a). Following the procedures of Saadat (1989), consolidation was considered complete when the volumetric strain rate was less than 0.1%/day. The pore water pressure (PWP), applied back pressure (BP), and applied cell pressure are shown in Figure 5.2 (b). The back pressure and cell pressure were increased in equal steps. The consolidation curve was unaffected by this procedure, indicating that the effective stress principle applies. Oswell (1991) found similar results at room temperature, Pore pressure was measured at the bottom of the specimen; back pressure was measured at the top. As in other tests in this program the pore pressure typically started below the back pressure and gradually reached an equilibrium value equal to the back pressure. Since these are independent measurements, pore pressures can be assumed equal along the specimen at the end of consolidation. No attempt was made to control room temperature, since the test temperature was positively controlled. This test was run during the summer months in which the building experienced the largest temperature fluctuations, and cyclic variations occurred on a daily basis. However, there is no evidence of this being reflected in the measured temperatures of the specimen. Room temperature changes have a second order effect on the volume changes of water in the burette used to measure specimen volume changes.

The effect of increasing the cell temperature while holding pressure constant is shown by specimen T1220 in Figure 5.3. The sudden changes in temperature tended to produce slight simultaneous increases in cell pressure and back pressure. Figure 5.3 (b) shows that the effective stress remains constant. However, the changes in the cell temperature are responsible for the volume changes shown by the arrows in the figure. The volume changes here are small (of the order

0.2 %), but clearly show temperature dependence. A family of consolidation curves can be interpreted from the results, as shown by the dotted lines in Figure 5.3 (a). Stepped temperature increases in Figure 5.3 (c) are responsible for the systematic specimen compression.

This test was generally well-behaved in spite of some control difficulties. The target temperature was initially overshoot by  $3^{\circ}\text{C}$ , and this is characteristic of the controller feedback response to the thermal inertia of the system. The drop in specimen temperature shown in Figure 5.3 (c) was caused by failure of a relay in the temperature controller. The gap in the temperature data was caused by a short circuit in the sensor lead. Both were repaired on day 3, and then the temperature was increased in a step-wise way. Another short circuit was repaired on day 6, and the controller retuned. Room temperature was moderated by switching on the air conditioning during summer months. Without control, the room temperature varied between  $25^{\circ}\text{C}$  around midnight and over  $30^{\circ}\text{C}$  around mid-day. Lateral strain gauge readings (not shown) have a trend similar to the volumetric strain. The temperature gradient reached a constant value of  $2.5^{\circ}\text{C}$ , over the length of the specimen.

In order to assess the volume change and pressure response of the HITEP apparatus at elevated temperature, a brass dummy specimen was tested in T1222, shown in Figure 5.4. Volume changes of less than 0.2% of a specimen volume occur due to temperature increases of  $60^{\circ}\text{C}$ . Volume changes less than 0.02% of the specimen volume occur due to pressure increases of 1.0 MPa. The system volume changes (0.003%/day) are second order compared to the buffer response.

Figure 5.5 (a) shows the response of the lateral strain gauge (LSG) in the same test. The initial increase in diameter was due to thermal expansion of the brass during heating. Temperature changes of  $5^{\circ}\text{C}$  produce changes in the diameter readings of 0.05mm. This is a direct effect on the instrument itself, but also

represents compression of the membrane in response to changes in cell pressure induced by temperature changes. Temperature gradients exist within the cell fluid. The difference in temperature of the brass dummy from top to bottom is shown in Figure 5.5 (b). The difference is  $1.0^{\circ}\text{C}$ , but larger differences occur with buffer specimens because they have lower thermal conductivities than brass. However, later introduction of the base heater element kept the temperature gradient over the length of the specimen below about  $0.2^{\circ}\text{C}/\text{cm}$ .

Specimen T1225 was tested at a lower effective pressure than T1220 and swelled more as a result. This is shown in Figure 5.6 (a). Volumetric straining and pore pressure equilibrium was established after 14 days. A B-test at day 6 gave a value of only 0.74 after 55 minutes perhaps indicating that the specimen was still trying to expand. A second B-test on day 21 gave a value of 1.0 after 40 minutes. The fluctuations in the cell pressure and back pressure are due to changes in cell temperature and room temperature. The gas pressure regulators are sensitive to changes in temperature and to building vibrations. They had to be periodically adjusted. A line failure caused loss of back pressure on day 13. The temperature difference was  $1.0^{\circ}\text{C}$  from top to bottom of the specimen. A voltage control problem is the suspected cause of erroneous lateral strain gauge readings in this test.

The response of the buffer at low effective stress, 0.6 MPa, and high temperature,  $100^{\circ}\text{C}$ , is shown for specimen T1233 in Figure 5.7. A large amount of swelling occurred as indicated in Figure 5.7 (a). A B-test was performed from day 9 to 11. Figure 5.7 (b) shows little or no change in pore water pressure during the B-test. Subsequent tests at end of consolidation gave B-values of 0.94 after 10 minutes. This was the first test to make use of the newly developed automatic pressure control system (PCS). No pressure 'spike' occurred in response to initial heating, in contrast with tests without this improvement. Temperature overshoot

has also been eliminated in this test as seen in Figure 5.7 (c).

Figure 5.8 shows a test run at high effective stress, 9.0 MPa, and high temperature, 100°C, (Specimen T1235). This specimen is highly compressive compared to T1233. This is due to four factors: (1) the high confining stress; (2) thermal expansion of water in the porous stones and drainage lines; (3) thermal expansion of water in the specimen; and (4) thermally induced consolidation. The latter three factors have been observed by other researchers for a variety of clays (Mitchell 1969, Green 1984, Hueckel and Baldi 1990).

Pore pressure response was measured independently of back pressure application in several tests at elevated temperature. Figure 5.9 shows this procedure for T1227. Initial heating leads to rapid pore pressure development, followed by dissipation once temperature equilibrium has been reached. This peak pore pressure development has not been seen in room temperature tests. The sudden increase in volumetric strain at day 6 was due to rupture of the membrane and contamination of the specimen with cell fluid. This is confirmed in two ways by the B-test run from day 11 to 12. First, the interpreted swelling pressure does not agree with Oswell's data (1990). Second, the back pressure rose rapidly when drainage was closed and approached the magnitude of the applied cell pressure.

Swelling pressure can be interpreted from leak tests at the end of consolidation if the seals are good and pore pressure equilibrium has been established. The tests are done by closing the drainage, and observing the burette leakage (volume change), and specimen leakage (pore pressure change). Two leak tests were run in a representative test, T1229, at the beginning and end of consolidation. The results are shown in Figure 5.10. Swelling pressure is interpreted from the latter leak-test as follows:

$$[5.1] \quad p_s' = CP - BP = 3.7 \text{ MPa}$$

Oswell (1991) produced a graph (Figure 4.8 in his thesis) of apparent effective

stress *versus* specific volume of clay for buffer. Using the final specific volume from T1229 and extrapolation from Oswell's graph, a swelling pressure of 4.0 MPa is obtained. Gray *et al.* (1985), and Dixon *et al.* (1991) summarized swelling pressure results from several different test methods, including those produced by Oswell. Dixon's own results from confined-swell tests give a swelling pressure of 3.3 MPa. This is further proof that the effective stress principle is valid for buffer at elevated temperature. A similar calculation was done for the first leak test done earlier on this specimen by back-calculating the current specific volume from the specimen's final specific volume and measured volume changes.

$$[5.2] \quad V_{cf} = V_{co} - \epsilon_v \cdot (1.037 + V_{co})$$

In this case the interpreted swelling pressure does not agree with results from Dixon and Oswell because pore pressure equilibrium had not been established at this stage in the test.

Figure 5.11 shows the response of the lateral strain gauge in T1229. The specimen diameter decreased approximately 1mm during consolidation. Using this and assuming a length decrease of 2 mm, the volume change is 8.0 ml which equals the measured volume change. The starting diameter of this specimen was approximately 55.9 mm including membrane thicknesses.

The results of tests T1204 to T1236 are summarized in Figure 5.12 as plots of clay specific volume versus logarithm of mean effective stress for the three temperatures used in this program. The moisture contents at the end of shear are used to calculate the specific volumes. Regression lines for 26°C, 65°C and 100°C data are shown. These are called hardening lines and have slope  $\lambda_c$ . They will be referred to later as  $\lambda$ -lines. There is fair evidence to support parallelism in the  $\lambda$ -lines and a trend of decreasing volume with increasing temperature. This supports preliminary results reported to AECL in 1990 (Graham *et al.* 1990) and agrees with research on other clays (Tidfors and Sällfors 1989, Eriksson 1989). As

in Saadat's program there is considerable scatter in the data. The proposed hardening laws for test data in the current program at 26°C, 65°C, and 100°C are as follows:

$$[5.3] \quad V_c^{26} = 3.102 - 0.278 \cdot \log(p'); \text{ S.D.} = 0.10; R^2 = 0.943$$

$$[5.4] \quad V_c^{65} = 3.050 - 0.278 \cdot \log(p'); \text{ S.D.} = 0.23; \text{ Fitted Line}$$

$$[5.5] \quad V_c^{100} = 2.950 - 0.278 \cdot \log(p'); \text{ S.D.} = 0.18; \text{ Fitted Line}$$

where  $p'$  is in units of kPa, S.D. is standard deviation and  $R^2$  is the square of the correlation coefficient. According to the definition of logarithms, the following is true:  $0.278 = 2.303 \cdot \lambda_c$ , from which  $\lambda_c = 0.121$ . From the definition of clay specific volume,  $\lambda_c = 2.037 \cdot \lambda$ . The regression line for the 65°C data was nearly parallel to that of the 26°C data, so for simplicity they have been assumed parallel. The regression for the 100°C data was not as good as the 26°C data because of scatter. A hardening line parallel to the 26°C was fitted. This expression is only approximate due to the small number of successful tests available. These equations revise the tentative equations previously reported (Graham *et al.* 1991). Clearly, the differences in specific volume between the hardening lines at the test temperatures are relatively small, less than 0.2.

Saadat's test data produced a greater slope for his hardening line ( $\lambda_c = 0.171$ ) than the 26°C hardening data in this test program ( $\lambda_c = 0.121$ ). The differences may be due to material variability and sensitivity to small differences in molding water content. The tests indicated by arrows experienced membrane or leakage problems. Their results have not been used in the regression analysis.

Where cell fluid contamination has occurred this will lead to an error in specific volume. No correction is used here, but will be discussed in the next chapter.

The HITEP triaxial cells are fitted with connections and pressure transducers for measuring pore water pressure at the base of the specimen, and for



applying back pressure or measuring pore water pressure at the top. At 100°C it proved impossible to measure pore water pressures reliably using the standard high pressure nylon tubing which softened and collapsed under high cell pressure (T1226). Pore water pressure changes were also affected by compressibility of the tubing as it responded to changes in the cell pressure. However, the same tubing performed well at 65°C (T1225). Substitution of copper tubing for the nylon tubing provided more reliable measurements, although some leakage was still experienced in the fittings and connections (Test 1227). It was necessary to wrap the copper tubing in a helix around the specimen. This made installation much more difficult. In later tests, it was decided to omit the top platen connections and simply not measure pore water pressures at the top of the specimen.

The second of the HITEP cells was fitted with a 36W heater element in the base of the cell designed for continuous operation during tests. The heater was added to reduce a vertical temperature gradient in the cell fluid that had been noted in tests in the first cell (for example Figure 5.11b). The following tests made use of this feature: T1224, T1227, T1228, and T1230-T1235. Using the heater, the maximum differential temperature  $\Delta T_{\max}^{\text{trans}}$  across the length of the specimen under transient conditions was from 1.4°C to 2.8°C with an average 2.0°C. The maximum steady state differential temperature  $\Delta T_{\max}^{\text{ss}}$  was from 1.2°C to 2.6°C with an average 1.8°C (7 tests). Without the base heater,  $\Delta T_{\max}^{\text{trans}}$  was typically 4°C to 5°C and  $\Delta T_{\max}^{\text{ss}}$  was 3.2°C. Tests T1225, T1226 lay outside the ranges given above. In these tests,  $\Delta T_{\max}$  was 1.6°C with the base heater turned off.

### 5.3.3 Undrained Shear Tests

This section presents results from the undrained shear portion of the CIU(TXC) test program on buffer at temperatures of 26°C, 65°C, and 100°C. All tests were run at an axial strain rate of 4mm/min. or 0.24%/hour. With this strain rate, shearing lasts 2 days. This is the same rate used by Saadat (1989). The influence of strain rate is discussed further in the following section.

Axial strains at the end of testing varied from 7% (T1228, T1207) to 16% (T1211). Most specimens were sheared to axial strains greater than 11%. The data have been plotted in the Figures for this section in terms of axial strain,  $\epsilon_1$ . It is worth noting that in these undrained (constant volume) tests,  $\epsilon_1$  is identical numerically to the shear strain  $\epsilon_s$ .

Critical state behavior can be approximated by the end-of-test behavior at the large strains that specimens were subjected to in this program. By definition, critical state strength is reached when the following relationships are true:

$$[5.6] \quad \frac{\partial u}{\partial \epsilon_s} = \frac{\partial p'}{\partial \epsilon_s} = \frac{\partial q}{\partial \epsilon_s} = \frac{\partial V}{\partial \epsilon_s} = 0$$

It relates to conditions when the microfabric of the soil has reached steady-state shearing conditions in terms of volume changes, but still contains a wide range of particle orientations. This will be discussed further in Chapter 7. Critical state strength is different from residual strength. The latter refers to the strength at very large strains, typically greater 20% , and is usually measured in direct shear tests after numerous load reversals. Failure at residual strength occurs along a thin shear zone where particles become preferentially oriented (Atkinson and Bransby 1978). Residual strength is not investigated in this thesis.

Three representative tests are described in detail, T1211, T1221, and T1233. T1211, a special test, was run at 65°C with 'stepped' strain rates to

illustrate the creep behavior of buffer at elevated temperature. To the author's knowledge, this test, T1211, is the first test of its kind performed on clay at elevated temperature.

Following the description of specimens T1211, T1221, and T1233, photographs of specimens T1209, T1219, T1229 and T1236 will be discussed. These show the appearance of specimens (1) before consolidation and (2) after shear. They provide some insight into the failure modes which occurred in the buffer.

A discussion of 22 of the 36 tests using comparative plots of data will follow. Tests have been grouped using two basic methods to compare results : (1) specimens at the same temperature; and (2) specimens at the same effective consolidation stress. The tests selected are not necessarily the best ones from the series, but were chosen to present results at representative values of mean effective stress,  $p'$ . Two tests (T1204 and T1208) have not been included in this section because they were sheared with drainage open.

The first test that will be discussed, test T1221, shows typical undrained shear behavior for buffer at 26°C, but also had independent pore pressure measurement at the top and bottom of the specimen. This is shown in Figure 5.13 (a) and (b). Pore pressures at the top and bottom differed by a maximum of 0.2 MPa (Figure 5.14 (a)). Pore pressure at the bottom of the specimen was always the higher value during shear, but the lower value during consolidation. This specimen swelled 4.4% during consolidation, and had the longest consolidation period, 75.8 days. It was consolidated to 1.0 MPa effective stress. This is below the swelling equilibrium pressure,  $p_s$  for buffer with  $V_c = 2.21$ , the final specific volume of this specimen T1221. The likely swelling pressure for this specific volume is between 2.0 MPa (Oswell 1991) and 2.3 MPa (Dixon *et al.* 1991). Specimen T1221 was initially compressive in shear in the elastic range, but became dilative long before peak strength was reached (Figure 5.13 (a), (b)). The specimen strain

softened slightly in shear (Figure 5.14 (b)). There appears to be a relationship between the room temperature, cell pressure and pore pressures for this test.

Specimen T1211 was tested at 65°C and consolidated at 3.0 MPa effective stress. This is the first test of its kind in which the shearing rate was changed systematically during shearing to investigate the rate dependence of shear strength at elevated temperature. It complements the tests done by Saadat (1989) at 26°C. Figure 5.15 (a) shows deviator stress versus axial strain with an initial shearing rate of 0.24%/hour up to 7.3% strain. The strain rate was then immediately decreased to 0.024%/hour and later increased to 2.4%/hour after 7.69% strain. Finally the strain rate was returned to its original value, 0.24%/hour. Dotted lines in the figure show the strain rate dependence of the deviator stress interpolated from different portions of the test. Increasing the standard shear rate an order of magnitude caused approximately 6% increase in deviator stress. This compares with a 9% increase for Belfast clay tested at room temperature and was reported by Graham *et al.* (1983). A reduction in shear rate of one order magnitude caused 6% decrease in deviator stress in buffer, related to peak deviator stress. The pore pressure change in response to shear rate can be seen in Figure 5.15 (b). More refined creep parameters can be obtained from the results, (Yin and Graham 1989) but the analysis is beyond the scope of this thesis.

Results from test T1233, Figure 5.16, are representative of shear behavior of buffer at 100°C. This specimen shows slight strain softening, Figure 5.16 (a), and initially compressive behavior, Figure 5.16 (b), which converts into a small tendency to expand (decreasing  $du$ ) at axial strains larger than about 1 %. A poor electrical contact caused erroneous temperature readings from the standard RTD's. Occurrences such as this make a strong case for acquiring readings from redundant instruments as shown by the symbols in Figure 5.16 (c). Notice that the readings from the RTD's are consistently higher than the true temperature by approximately

7°C.

'Bulging' modes of failure (rather than discrete failure planes) were typically observed in the buffer specimens. Figures 5.17 (a) and (b) show specimen T1219, tested at 65°C, before consolidation and after shear, respectively. The mottled appearance of the specimen is associated with dry densities less than 1.67 Mg/m<sup>3</sup>. The 5 horizontal bands define the individual layers produced during the compaction process. Earlier studies (Yarechewski 1988, Oswell 1991) have shown that the structure of the specimens (as reflected for example in water contents) is much more uniform than suggested by the visual appearance of these specimens. The two white bands, top and bottom are the rubber bands used to hold the side drains in place. The side drains and porous stones can be clearly seen in Figure 5.17 (a). Bulging occurred at the bottom of this specimen (Figure 5.17 (b)), but in other specimens it occurred at the top or in the middle. No systematic behavior has been observed. In each case, moisture contents were highest near the bulge. The lateral strain gage (LSG) has been moved to the top loading cap in Figure 5.17(b). The load cell is immediately above the LSG.

Figures 5.18 (a) and (b) show the appearance of specimen T1229 which was discussed earlier, before consolidation and after shear, respectively. This specimen had the highest compaction density, 1.70 Mg/m<sup>3</sup>. No mottling is apparent. As in most specimens bulging occurred with little or no rotation of the top cap. The ball bearing seat described in Chapter 3 allowed the top cap freedom to rotate but not translate, and generally prevented eccentric loading on the specimen. The ball bearing transmits only axial loads to the load cell.

In some of the specimens, for example T1209 shown in Figure 5.19 (a), a distinct irregular shear plane developed. The top cap rotated approximately 10°. Slight eccentricity developed at the bottom due to translation of the specimen relative to the pedestal. Figure 5.19 (b) shows a well behaved specimen, T1236,

having a compacted density of  $1.67 \text{ Mg/m}^3$  and tested at  $65^\circ\text{C}$ . Specimens tested at  $100^\circ\text{C}$  had a similar appearance. No photographs are available for the  $100^\circ\text{C}$  specimens.

A comparison of the 22 buffer tests will now be presented. In the overall test program, the buffer was consolidated to effective stresses of 0.6, 1.0, 1.6, 2.2, 3.0, 7.0, and 9.0 MPa. To determine the effect of elevated temperature on specimen behavior, composite plots of results from tests at each stress level have been produced. Only three sets of these plots will be discussed in the following text. The first set, in Figures 5.20 to Figure 5.22 shows the tests consolidated to 0.6 MPa effective stress (T1233, T1225, T1216, T1212). The specimens all had similar moisture contents, which varied by less than 1% from the top to bottom in any specimen. Failure occurred by 'bulging' (or occasionally with dominant slip planes, for example T1216). These observations relate only to failure at large strain (EOT). None of the specimens were eccentrically loaded. Bulging occurred in specimens where the local moisture content was highest. No oil contamination was visible in these tests. During test T1212, the internal load cell malfunctioned and an external load cell was added to the system to obtain readings of axial load. The deviator stress  $q$  was corrected (by subtracting an estimated 400 kPa) to account for piston friction. This correction still left the stress path at a higher value of  $p'$  than the other tests in  $q$  versus  $p'$  stress space.

There is a trend of reduced deviator stress with elevated temperature in Figure 5.20 (a). This is due to higher pore pressure generation at elevated temperature as shown in Figure 5.20 (b). This has been the overall general trend at each level of effective stress at which the buffer was tested. However, Figure 5.20 shows some exceptions to these general trends. Close inspection of Figures 5.20 (a) and (b) show that the  $100^\circ\text{C}$  test, T1233, has approximately the same peak deviator stress as the  $65^\circ\text{C}$  test, T1225. Moreover, pore pressure generation is not

consistent with the latter observation because the 26°C test, T1212 experienced similar pore pressures to the 100°C test, T1233. These discrepancies are due to the small differences in cell pressure shown in Figure 5.21.

Figure 5.20 (c) has been included to show the elastic parameter,  $m = \Delta u / \Delta p$ , for each test. Isotropic materials have  $m = 1.0$ , while anisotropic materials such as the buffer typically have compressive values of 1.5 to 2.0 indicating higher horizontal stiffnesses than vertical stiffnesses (Graham and Houlsby 1983). These specimens were all dilative in the later stages of shear. The two curves in Figure 5.20 (c) for T1225 are independent pore pressure measurements at the top and bottom of the specimen. All subsequent plots will simply show average pore pressures for tests where independent measurement have been taken. T1216 shows near-isotropic elastic behavior. Wan (1987) showed that when buffer is consolidated below its swelling equilibrium pressure (SEP) it expands, and its behavior in shear is isotropic. He also found anisotropic shear behavior for buffer tested above its SEP, which compressed during consolidation.

Figure 5.22 shows results from these tests plotted in  $q$  versus  $p'$  stress space. Saadat's regressed peak and end-of-test strength envelopes are also shown. Clearly, the author's end-of-test results at elevated temperature are close to Saadat's peak envelope. The stress paths are quite similar for each test. Specimen T1216 (65°C) shows a nearly vertical initial orientation in this plot, and this is characteristic of isotropic materials.

The second group of tests that will be discussed, in Figures 5.23 to 5.25, were consolidated to 1.6 MPa effective stress. This group was chosen because the stress level is intermediate. The tests at higher temperatures showed more strain softening, Figure 5.23 (a). However at large strains, they approached the end-of-test strengths for specimens tested at room temperature. Specimen T1227 has much higher strength than the others because it behaved like a drained test due to

a membrane rupture. A drained test gives a different peak strength than an undrained test because it follows a different path as it traverses the state boundary surface (SBS) (Atkinson and Bransby 1978). Furthermore, T1227 had the lowest final moisture content (17.2%) measured in this series and the fourth lowest of all the specimens tested. Specimen T1227 had the shortest duration for consolidation (12 days); T1209 had the longest (47 days), and this may explain the difference between these specimens. Specimen T1205 was compacted to a low density which would give a lower strength than the other test at 65°C, specimen T1209. Specimens T1209 and T1215 were compacted at the same density. Comparing the latter two tests at this level of effective stress, 1.6 MPa, it appears that elevated temperature causes an increase in deviator stress. However, this set of tests is difficult to compare for the reasons previously discussed. The other sets, at 1.0 and 2.2 MPa effective stress, clearly show decreased strength with elevated temperature.

The pore pressure changes in Figure 5.23 (b) are consistent with the preceding comments. Specimen T1227 developed a rapid increase in pore pressure and then continued at constant pore pressure. Specimen T1215 had higher pore pressures than T1209. Material anisotropy is evident from the values of  $m$ , approximately 1.5, in Figure 5.23 (c). Specimen T1205 was clearly the only compressive specimen, whereas T1209 was the most dilative specimen. (The  $m$  value for the drained test of T1227 is not useful in this discussion.)

As in the previous set of tests, at 0.6 MPa, the pressures and temperatures for these tests have been plotted together (Figure 5.24) to compare the level of control achieved in each test. Clearly, excellent control was achieved.

Figure 5.25 shows the strengths of each specimen in  $q$  versus  $p'$  stress space. It is clear that T1209 was tested at a higher mean effective stress than the comparable test (T1205) at the same temperature, and this would explain the



higher strength for the former.

The third set of tests to be compared, (at 3.0 MPa effective consolidation pressure) are shown in Figures 5.26 to Figure 5.28. Two tests were performed at 26°C, T1217 and T1207, and two tests were performed at 65°C, T1223 and T1211. The two room temperature specimens were compacted at slightly lower density, 1.64 Mg/m<sup>3</sup>, than the elevated temperature specimens, 1.67 Mg/m<sup>3</sup>. This would account for lower strengths in the room temperature specimens than the high temperature specimens, Figure 5.26 (a). Specimen T1217 had a higher final moisture content than the other specimens; T1223 had the lowest. In view of these test conditions the previous observation of decreased strength with elevated temperature still applies here. Specimen T1207 was consolidated for 66 days. This is much longer than the others, by a factor of four. It was the only specimen that was strongly strain softening in shear which may also explain the lower strength than in the other tests. This specimen also experienced some pressure control difficulties (it was one of the first tests at high pressure). On disassembly, specimen T1211 had a split in its inner membrane but serious leakage was not apparent.

Figure 5.26 (b) shows that pore pressure generation was similar for all the tests except T1207. Clearly, the specimens were all compressive as indicated by positive, continuously increasing pore pressure generation. The  $m$  values are now larger (1.33 to 2.85), in Figure 5.26 (c). This figure also indicates yielding of the specimens indicated by arrows.

Figure 5.27 and Figure 5.28 show that specimen T1207 was tested at higher cell pressure and effective stress than the other specimens, and so it should not be used in comparisons of strength. As in most of the tests at high effective stress the specimens experienced a drop in effective stress,  $p'$ , (0.2 MPa in this case), just after drainage was closed at the start of shearing.

A comparison of all of the available buffer triaxial shear data in this

program, T1205 to T1236, will now be discussed. Shear strengths at each test temperature will be discussed in turn in relation to Saadat's (1989) regressions for buffer at room temperature at peak deviator stress ( $q_p$ ) and end-of-test deviator stress ( $q_{eot}$ ). Figure 5.29 shows a summary of triaxial tests at 26°C. The peak shear strengths are well above the peak strength regression line from Saadat's data at low stress levels, from mean effective stress of 0.6 MPa to 1.6 MPa. For  $\sigma'_3$  of 3.0 MPa, the peak strength is within 0.10 MPa of Saadat's regression line. In most of the tests, the end-of-test shear strengths are above Saadat's peak strength regression by only 0.05 MPa. This verifies the trend of Saadat's end-of-test regression. Data from two tests, T1208 and T1212, have been corrected in this plot. In T1212, 0.4 MPa was subtracted from the deviator stress to account for piston friction as discussed earlier. This was only test where external load cell readings were used. In T1208, 0.4 MPa has been subtracted from the deviator stress to account for an error in the zero reading for the load cell.

Specimens sheared at 65°C are shown in Figure 5.30. This figure is for early specimens whose densities ( $1.64 \text{ Mg/m}^3$ ) tended to be a little lower than the target density ( $1.67 \text{ Mg/m}^3$ ). Four of the six tests have end-of-test shear strengths within 0.05 MPa of Saadat's end-of-test regression. The other two tests, T1214 and T1209 were well above Saadat's regression. Pressure control difficulties in T1214 have made interpretation of the true stress path difficult, and only low confidence can be placed in the peak and end-of-test strength values in this test. Peak strengths of four of the six tests were well above Saadat's regression peak strength. The other two tests, T1216 and T1205 were within 0.10 MPa of the regression. Both of these tests were tested below 1.5 MPa effective stress.

Specimens compacted at slightly higher densities of  $1.67 \text{ Mg/m}^3$  to  $1.70 \text{ Mg/m}^3$  and sheared at the same temperature of 65°C are shown in Figure 5.31. These 65°C results have been shown on a separate figures to (1) avoid confusion and (2)

illustrate differences in stress paths between these tests and tests compacted at slightly different densities. Specimens compacted to a higher density (Figure 5.31) show stress paths initially inclined to the left, whereas specimens compacted at lower density show near vertical stress paths. The former is typical of anisotropic materials, while the latter is typical of isotropic materials. The main observation from Figure 5.31 is that peak and end-of-test strengths are close to, but above Saadat's regressed strength envelopes at low effective stresses, less than 1.5 MPa. At greater mean effective stresses, the peak and end-of-test strengths are slightly below Saadat's regressions.

Specimens sheared at 100°C are shown in Figure 5.32. A high level of confidence is placed in three of these tests, T1233, T1235, and T1230. The other three tests experienced leakage (T1227, T1228), power failures (T1228), and cell pressure fluctuations. Specimens T1227 and T1228 were compacted to higher density, 1.68 Mg/m<sup>3</sup>, than the other specimens, 1.67 Mg/m<sup>3</sup>.

The data points for peak and end-of-test results for 26°C, 65°C and 100°C are shown in Figures 5.33 to Figure 5.35. Curves are fitted to the data for 65°C, and 100°C. Saadat's regression is used for 26°C data because the current test data fits it well for low to medium pressures (Saadat's program dealt exclusively with 26°C tests, and the author's limited number of tests at this temperature were confirmatory in nature.) Tests which experienced problems and in which a low degree of confidence is placed have not been included in the regressions.

Peak and end-of-test strength envelopes are shown separately in Figures 5.36 (a) and (b). Saadat's regression is again used for the 26°C data (Graham *et al.* 1989). The peak strength envelope at 65°C is approximately the same as Saadat's 26°C envelope, whereas the peak strength envelope at 100°C is well above Saadat's envelope. The end of test envelope at 65°C is approximately the same as Saadat's. The 100°C envelope lies well above Saadat's for effective stresses less

that about 8.0 MPa.

The regression equations for peak and end-of-test strength are as follows:

$$[5.7] \quad q_p^{100} = 6.672 \cdot (p')^{0.706}; \text{ S.D.}=953 \text{ kPa}; R^2=0.9786$$

$$[5.8] \quad q_p^{65} = 4.928 \cdot (p')^{0.719}; \text{ S.D.}=624 \text{ kPa}; R^2=0.9562$$

$$[5.9] \quad q_p^{26} = 2.590 \cdot (p')^{0.800}; R^2= 0.94 \text{ (Graham } et al. \text{ 1989)}$$

$$[5.10] \quad q_{cot}^{100} = 8.142 \cdot (p')^{0.674}; \text{ S.D.}=845 \text{ kPa}; R^2=0.9384$$

$$[5.11] \quad q_{cot}^{65} = 4.147 \cdot (p')^{0.733}; \text{ S.D.}=567 \text{ kPa}; R^2=0.9341$$

$$[5.12] \quad q_{cot}^{26} = 2.640 \cdot (p')^{0.790}; R^2= 0.88 \text{ (Graham } et al. \text{ 1989)}$$

These equations should be considered approximate for high effective stresses because of the small number of tests performed under these conditions, remembering that the main objective of the test program was to obtain data for low to medium pressures. Poor fit between the regressions and data points at high stress is the reason for the large values of standard deviation (S.D.). A previous report (Graham *et al.* 1991) showed that the specimens had effectively reached critical state at the end of the tests. "Critical state" will therefore be used interchangeably with "end-of-test" in the remainder of this thesis.

Figure 5.37 shows strength data at critical state plotted as  $V_c$  versus  $\log(p')$ . Linear regressions were performed on the data for each of the three temperatures. This produced critical state lines (CSL) with slopes slightly different from the hardening laws or normal consolidation lines (NCL) previously discussed. For simplicity, CSL lines with the same slope as the 26°C NCL have been fitted through the critical state data. The equations for the CSL's are:

$$[5.13] \quad V_c^{26C} = 3.102 - 0.278 \cdot \log(p'_{cs}); \text{ S.D.} = 0.12$$

$$[5.14] \quad V_c^{65C} = 3.020 - 0.278 \cdot \log(p'_{cs}); \text{ S.D.} = 0.15$$

$$[5.15] \quad V_c^{100C} = 2.930 - 0.278 \cdot \log(p'_{cs}); \text{ S.D.} = 0.23$$

These lines are again approximate, but represent a good qualitative description of the state boundary surface. Figure 5.38 shows these CSL lines together with the

NCL lines for 26°C, 65°C, and 100°C. Clearly, at each temperature the 'best fit' CSL line is close to the corresponding NCL. This may indicate a steep-sided state boundary surface at low stress ratios in  $q$ - $p'$ -space.

The data suggest that elevated temperatures produce state boundary surfaces with lower values of  $V_c$  for given values of  $p'$ . This is in agreement with findings from Hueckel and Baldi (1990) for Pontida silty clay which show a shrinking yield locus at elevated temperatures. However, it seems at first sight to be in conflict with the higher individual strengths observed in some buffer tests at elevated temperatures. Note however that specific volumes for a given consolidation pressure vary with temperature. This results in stress paths moving upwards to different locations on the appropriate state boundary surface. This question will be addressed further in Chapter 6.

A comparison of  $m$  values ( $m = \Delta u / \Delta p$ ) with results from Saadat (1989) and Wan (1987) is made in Figure 5.39. The increased temperatures in the current program appear to have produced a wider range of  $m$ -values.

#### 5.3.4 Drained Shear Tests

Two tests, T1204 and T1208 were sheared with drainage open at an axial strain rate of 0.0077 %/hour. Pore water pressure was measured independently of back pressure in these tests. In T1204, back pressure was applied at the bottom of the specimen, and pore water pressure was measured at the top. The measuring locations were reversed in T1208 since it was thought this would provide more reliable pore pressure measurements. Specimen T1204 was a special test because the deviator stress was completely unloaded, then reloaded just before peak shear strength was reached. This is shown in Figure 5.40 (a). The axial strain rate,  $\dot{\epsilon}_1$ , was changed to 0.02 %/hour during unloading and reloading to shorten the test time. Figures 5.40 (b) and (c) show the corresponding pore water pressures and volumetric

strains, respectively. Figure 5.41 (a) shows the drained stress path in  $q$ - $p'$  stress space. The pressure control during shear is shown in Figure 5.41 (b).

Data from tests T1204 and T1208 are summarized in Tables 5.2 to 5.5. The axial strains for test T1208 are somewhat approximate. A power failure near the beginning of the test caused some uncertainty regarding the true strain values. Table 5.2 shows drained shear results for tests T1204 and T1208 at peak deviator stress. Table 5.3 shows normalized drained shear test results at peak deviator stress. These values were calculated from Table 5.2. Table 5.4 shows drained shear results at end-of-test. Table 5.5 presents the end-of-test data in normalized form.

**Table 5.2: Summary of drained shear test results at peak deviator stress.**

Specimen Number	Temp. (°C)	$\sigma'_{cons}$ <sup>1</sup> (MPa)	$\epsilon_{1f}$ (%)	$\epsilon_v^7$ (%)	$q_f$ (MPa)	$p'_f$ (MPa)	$q_f/p'_f$	$u_f^2$ (MPa)	$\Delta u_f$ (MPa)	$A_f^3$	$m$
T1204 <sup>4,5</sup>	26	1.3	2.54	-0.55	1.02	1.60	0.64	0.14	0.02	0.02	0.06
T1208 <sup>4,6</sup>	26	0.6	8.12	-	0.93	0.85	1.10	0.89	-0.14	-0.15	-0.92

NOTE: 1.  $\sigma'_{cons}$  = cell pressure - back pressure

2.  $u_f = (u_{top} + u_{bot})/2$

3.  $A_f = \Delta u_f / \Delta q_f$  (plastic range);  $B = 1.0$ ;  $m = \Delta u / \Delta p$  (elastic range during shear)

4. CID triaxial tests. Axial strain rate,  $\dot{\epsilon}_1 = 0.0077$  %/hour

5. Unload/Reload cycle performed at 2.6% strain; specimen near peak strength. Axial strain rate,  $\dot{\epsilon}_1 = 0.020$  %/hour

6. Volume change readings not available during drained shear

7. Volumetric strain for shear portion only (not including consolidation)

**Table 5.3: Summary of normalized drained shear test results at peak deviator stress**

Specimen Number	Temp. (°C)	$\sigma'_{cons}$ (MPa)	$\epsilon_{1f}$ (%)	$q_f/\sigma'_{cons}$	$q_f/p'_f$	$\Delta u_f/\sigma'_{cons}$	Test Type	Spec.
T1204	26	1.3	2.54	0.78	0.64	0.02	CID[TXC]	buffer
T1208	26	0.6	8.12	1.55	1.10	-.23	CID[TXC]	buffer

NOTE: 1.  $\sigma'_{cons}$  = cell pressure - back pressure

2.  $u_f = (u_{top} + u_{bot})/2$

**Table 5.4: Summary of drained shear test results at end-of-test**

Specimen Number	Temp. (°C)	$\sigma'_{cons}$ (MPa)	$\epsilon_1$ (%)	$\epsilon_v$ (%)	$q_{eot}$ (MPa)	$p'_{eot}$ (MPa)	$q/p_{eot}$	$u_{eot}^2$ (MPa)	$\Delta u_{eot}$ (MPa)	$A_{eot}^3$
T1204	26	1.3	-	-	-	-	-	-	-	-
T1208	26	0.6	11.7	-	0.91	0.85	1.07	0.91	-.12	-.13

NOTE: 1.  $\sigma'_{cons}$  = cell pressure - back pressure

2.  $u_{eot} = (u_{top} + u_{bot})/2$

3.  $A_{eot} = \Delta u_{eot} / \Delta q_{eot}$  (plastic range)

**Table 5.5: Summary of normalized drained shear test results at end-of-test**

Specimen Number	Temp. (°C)	$\sigma'_{cons}$ (MPa)	$\epsilon_{leot}$ (%)	$q/\sigma'_{cons}$	$q/p'_{eot}$	$\Delta u/\sigma'_{cons}$	Test Type	Specimen
T1204	26	1.3	-	-	-	-	CID(TXC)	buffer
T1208	26	0.6	11.7	1.52	1.07	-0.20	CID(TXC)	buffer

NOTE: 1.  $\sigma'_{cons}$  = cell pressure - back pressure

2.  $u_{eot} = (u_{top} + u_{bot})/2$

3.  $A_{eot} = \Delta u_{eot} / \Delta q_{eot}$  (plastic range)

### 5.3.5 Buffer Mass Loss Tests (BML)

A suite of four buffer mass loss tests (OB-ML1, OB-ML2, OB-ML3, OB-ML4) was undertaken to examine how the duration of drying affected the measured water contents, and to determine if contamination by silicone oil would affect the measured values. The tests were done on compacted and granular (uncompacted) buffer at temperatures of 110°C and 26°C using an oven for the high temperature tests, and a desiccator for the room temperature tests. The purpose of these tests was to evaluate the effect of membrane leaks on measured values of moisture content under the likely operating conditions during the HITEP test program. The conditions (temperature, soil moisture, oil content, humidity, and time) used in these mass loss tests represent a worst case scenario in which buffer could become contaminated with oil because the membrane breached, or under even worse circumstances, because the cell seal failed and loss of oil and membrane allowed excessive evaporation rates. The amount of oil contamination brought into the test arrangement from the very lightly oiled compaction mold is considered small relative to the amounts that would come from leaking membranes, and will be



neglected.

Mass losses with time were recorded for: (1) a compacted buffer specimen and oil at 110°C; (2) granular buffer and oil at 110°C; (3) granular buffer at 110°C; and (4) granular buffer and oil at 26°C. Silicone oil cell fluid was used as the contaminant. The procedures for the four tests in this series have been described previously (Graham *et al.* 1991)

The results from the mass loss tests will now be discussed (in an order different from that in which they were performed). Test OB-ML3 on uncontaminated buffer showed that oven drying at 110°C resulted in constant mass after 24 hours.

Test OB-ML1 consisted of oven-drying a standard triaxial specimen of buffer (with filter paper and side drains still attached) at 110°C until a constant mass was reached. To this was added 10% oil by weight (normalized to the dry mass of the buffer), and the specimen was returned to the oven. The total mass was then recorded daily for approximately 50 days. It can be seen from Figure 5.42 that addition of the oil caused an increase in mass loss which attenuated with time. That is, the water content of the contaminated specimen appeared to continue decreasing below the value for the uncontaminated specimen. The average rate of mass loss was 0.1%/day during the period of the test. It is probably due to displacement of structural water in the clay matrix (Dixon 1991) since the interstitial and adsorbed water has likely been driven off at a temperature of 110°C.

In order to assess possible reactions between system components, a flask of oil, a flask of oil and filter paper, and filter paper were dried in the oven at the same time as OB-ML1. None of these tests showed mass loss or signs of reaction. The results are also shown in Figure 5.42 along with the results from the contaminated buffer specimen. The mass loss (%) was normalized by dividing the

individual mass change by the buffer dry mass.

Results from test OB-ML4 suggest that when compared with the results of the test OB-ML1 that the compaction level (or density) of the specimen has negligible effect on the rate of mass loss.

Since the effect of temperature on mass loss was unknown, test OB-ML2 was undertaken. An increase in drying rate was observed, but the average rate remained at about 0.25%/day. The buffer had not reached moisture content equilibrium, so the effects of the oil are unclear.

Results from the tests indicate that unsaturated buffer undergoes a long term (5 weeks) mass loss at the rate of about 0.1%/day after the addition of 10% silicone oil. The behavior has been observed for periods up to 5 weeks, and some information suggests that it may be independent of temperature.

If specimens from the main series of triaxial tests are exposed to oil contamination for the periods of 3 to 4 weeks required for most tests, then it is possible that mass losses of up to 3% could occur. This would affect the measurements of water content and specific volume, and hence the quality of estimates of consolidation behavior, including the swelling equilibrium line. However, the levels of contamination would have to be high, of the order 10% of buffer dry weight.

Careful examination of the water contents measured from triaxial specimens showed no sign of this mass loss phenomenon. Visual inspection of specimens after testing found in most cases, only trace amounts of silicone oil on the porous stones, filter paper, and side drains. This implies two things: (1) the oven dried moisture contents are reliable; and (2) the specimens in the main test series were not significantly contaminated.

### 5.3.6 Leakage and Membrane Diffusion

Latex membranes were used initially by Saadat (1989) for tests at room temperatures. However, these proved unsuitable for tests at elevated temperature, and the new silicone membranes described in section 3.5 had to be developed. A combination of soft (yellow) and medium (blue) outer silicone membranes was used at first (T1205). After Test T1229, double blue membranes were used as standard procedure.

Early in the test program (before T1209) five membrane leakage tests were undertaken at room temperature (SML1-SML5) to compare leakage rates of new technology silicone membranes with results from previous research (F. Saadat, 1989) for latex membranes. The apparatus consisted of a standard lucite triaxial cell with cell pressure and pore pressure transducers mounted in the base. A porous dummy specimen or a solid brass dummy specimens was wrapped in #54 filter paper and covered with a single yellow membrane (type 5026 A/B) 1.25 mm. thick. The effective confining stress was 1.0 MPa. Two cell fluids were used: silicone oil (CSL 500cP.) and water. Representative leakage rates are shown in Table 5.6

**Table 5.6: Summary of membrane leakage results from a low pressure triaxial cell at 1.0 MPa effective stress using full size silicone membrane 1.2 mm thick.**

Test No.	B.P. (MPa)	p' (MPa)	$\dot{\epsilon}_v^1$ (%/day)	T (°C)	t (day)	Test <sup>2</sup> Type	Membrane Type
SML3 <sup>3</sup>	0.5	1.0	0.10	26	5	Leak(TXC)	Sil 5050
SML4 <sup>4</sup>	0.5	1.0	0.02	26	40	Leak(TXC)	Sil 5050

NOTE: 1. Volumetric strain rate,  $\dot{\epsilon}_v$ , based on 200 cc specimen. A Single membrane used; lucite pedestal and top cap  
 2. Leak(TXC) = leakage test under isotropic stress conditions  
 3. Silicone oil cell fluid  
 4. De-aired water used as cell fluid

Further leakage tests have since been undertaken using the HITEP triaxial cells with brass and aluminum dummy specimens to evaluate the capabilities of the membranes and sealing rings at elevated temperatures (T1222, T1224, T1231). Two membranes were used. These were then compared with results from similar tests done by Saadat (1989) at room temperature using double latex membranes with three thicknesses, namely 0.36mm, 0.64mm, and 1.27mm. Saadat recorded leakage rates of 0.002%/day to 0.025%/day at 1.2MPa and 3.0MPa effective stress for double 0.64mm membranes. Leakage rates of similar magnitude were obtained for 1.27mm membranes for back pressures up to 7.0 MPa. This leakage rate can be considered satisfactory when it is remembered that consolidation has been assumed to be finished when the volumetric strain rate drops below 0.1%/day. Figure 5.43 shows the low leakage rates of 0.006%/day over 32 days that were obtained for silicone membranes at 65°C and 3.0MPa effective stress (T1222). (The 'specimen' in this test was brass, so any measured volume change originates in leakage through the membranes or past the pedestal seals.) A similar trend in volume change was observed by Yarechewski (1993) and more recently by Tanaka using an improved pedestal design.

Test T1231 was performed at 100°C and 0.6MPa. Leakage rates were in this case approximately 0.03%/day after 5 days. Previous calibrations showed that the fittings and lines leaked 0.006%/day. The consensus appears to be that leakage rates are less than one half the long term consolidation rate.

At elevated temperatures Buna O-rings in the cell pedestal had to be replaced with viton O-rings due to splitting and increased leakage (0.21%/day). Tests T1224, T1226, T1227, T1228, T1230, T1231-T1236 were later run in HITEP cell #2 using Viton O-rings appear to seal as well as fresh buna-N rings.

A leakage test (Leak#1) was performed to measure leakage of newly installed viton O-rings (replacing buna-N O-rings) in the pedestal of HITEP cell #1. The

test results in Figure 5.44 shows a leakage rate of 0.05ml/day (0.025%/day for 200 cc specimen) at 2.0 MPa effective stress with drainage open. This drops to 0.02ml/day when drainage is closed, the difference being associated with additional leakage of the burette and fittings. When later repeated at 7.0 MPa effective stress, the same leakage rate was measured, showing that this leakage is independent of pressure. However, the increase in pressure did reduce leakage to 0.03ml/day under drained conditions. This is believed to be the result of O-ring compression.

Leroueil *et al.* (1988) performed leakage tests in a slightly modified triaxial cell by using latex membranes 0.3mm thick x 50mm diameter x 100mm high with different cell fluids (de-aired water, glycerin, castor oil, liquid paraffin, silicone oil). They measured rates of 0.04 ml/week (silicone oil) to 1.45 ml/week (for glycerin). This is equivalent to a range of 0.003%/day to 0.104%/day, of the same order as rates achieved in the present tests at the University of Manitoba. Glycerin was not recommended because its presence actually increased the diffusion rate due to its hydrophilic nature. They recommended using silicone oil and a film of silicone grease to seal the ends of the membrane. This grease caused excessive leakage in the present tests.

Membrane diffusion tests will now be discussed. The author conducted calibration and diffusion tests on small pieces of membrane in a diffusion apparatus at 26°C. The results are tentative because the small membrane size required testing close to the accuracy of the apparatus. Table 5.7 summarizes the diffusion results at room temperature. The net diffusion or rate of flux,  $(\dot{\epsilon}_v)_{Net}$ , is the difference of the measured rate of volume change and the system compliance.

**Table 5.7: Summary of membrane diffusion results from the diffusion apparatus<sup>1,2</sup> at 0.6 MPa, 3.0 MPa, 9.0 MPa effective stress. Membrane diffusion area has been multiplied by 20 to give the equivalent area of a triaxial membrane.**

Test No. (Diff/System)	B.P. (MPa)	p' (MPa)	$(\dot{\epsilon}_v)_{Net}^3$ (%/day)	T (°C)	t (day)	Test <sup>4</sup> Type	Membrane Type
MD1-1/MDAL2-B1.0		0.6	0.16	26	4.0	Diff(TXC)	Sil 5050
MD1-2/MDAL2-C1.0		3.0	-0.25	26	4.0	Diff(TXC)	"
MD1-3/MDAL2-E1.0		9.0	0.02	26	4.0	Diff(TXC)	"

NOTE: 1. Single O-Ring used in pedestal of apparatus

2. Membrane clamped with aluminum ring

$$3. (\dot{\epsilon}_v)_{Net} = \frac{100}{200} \left[ (\Delta\dot{V})_{Diffusion} - (\Delta\dot{V})_{System} \right]; \text{ equivalent specimen volume} = 200\text{cc}$$

4. Diff(TXC) = diffusion test under isotropic compressive stress

Appendix E contains summary graphs and tables of the diffusion and leakage tests and a more complete description of the calculations.

Figure 5.45 (a) summarizes the diffusion test results of Yarechewski (1993) and the author. The tests were all run in a similar diffusion apparatus. Yarechewski (1993) conducted diffusion tests at elevated temperatures (65°C, 100°C) on full size silicone membranes in an improved version of the diffusion apparatus. A trend of greater diffusion with higher effective stress and temperature is observed. A different trend is observed for leakage tests in triaxial cells, Figure 5.45 (b). The cell fluid, membrane and specimen type are indicated in the legend as "Sil/Sil/Dummy" where Sil refers to silicone. Silicone membranes appear to have higher leakage rates than latex membranes at 26°C. Silicone membranes appear to have higher leakage rates at lower effective stress than at higher

effective stress. The different trend observed in Figure 5.45 (b) may be due to differences in the test apparatus. Another explanation is differences between the processes of leakage and diffusion.

The diffusion rates shown in Figure 5.45(a) are for a single silicone membrane. These rates will be checked with theory in Chapter 6. The leakage rates shown in Figure 5.45 (b) are for double silicone membranes. It is believed that the diffusion rates are about the same magnitude as the leakage rates.

Saadat (1989) checked additional pore pressure build-up due to membrane leakage at 3.3 MPa confining stress using a brass dummy specimen and two 0.64 mm thick latex membranes. He measured an average gain in pore water pressure of only 20 kPa/day which indicated excellent sealing. The current test program has examined this behavior at 100°C using two silicone membranes over geotextile side drains and a brass dummy specimen (T1231). The pressure rise was again only 20 kPa/day over a period of 13 days.

Swell tests were performed on silicone membranes in the current program. Membranes were immersed in silicone oil at elevated temperature. The results in Figure 5.46 (a) and (b) show that the membranes may absorb up to 12% oil after 30 days and the membrane circumference may increase 0.76 mm.

### **5.3.7 Membrane/Side Drain Restraint**

Corrections to specimen strength from membrane restraint were discussed in general in Chapter 3. Some representative tests are discussed here. Figures 5.47 (a) and (b) show results from an undrained shear test on a rubber dummy specimen with a single membrane and standard side drains. Clearly, the dummy behaves in a linear manner but hysteresis is present. The stress path is near vertical at the beginning (Figure 5.48). A lateral strain gage provided extra data to test the condition of zero volume change. Figure 5.49 (a) shows a discrepancy between the

measured and calculated lateral strain. This may be due to anisotropy or incomplete saturation of the rubber. Figure 5.49 (b) shows a Poisson's ratio slightly greater than 0.5.

For comparison, an unconfined test on the rubber dummy specimen is shown in Figure 5.50. Near linear elastic behavior was observed with a small amount of hysteresis in Figure 5.50 (a). The dummy showed classical barrel deformation. The stress path was at 3:1 in  $q$  vs.  $p'$  stress space in Figure 5.50 (b). Figures 5.51 (a) and (b) shows the lateral strain and Poisson's ratio. Clearly, these were similar to those of the undrained test. In general, these results suggest behavior close to linear isotropic elasticity, which is to be expected from rubber. They therefore support the validity of the measuring systems that have been used.

#### 5.4 Preliminary Discussion of Results

Choosing the correct strain rate is crucial to measuring representative pore water pressures in drained and undrained shear tests. Sufficient time must be allowed for equalization of pore pressures inside the specimen, otherwise the computed effective angle of friction will be in error. The chosen strain rate of 0.004 mm/min meets the criterion for pore pressure equilibrium set by Bishop and Gibson (1966).

Elevated temperatures do not appear to affect the time required for pore pressure equilibrium. Results by Mitchell and Campanella (1968) show that creep of clay in sustained loading tests occurs at an increased rate at elevated temperature, but pore water pressures remain constant after initial temperature or load application.

Figures 5.3 (a) and (b) showed initial compression in specimen T1220 during consolidation when the temperature was increased, and that this was subsequently followed by swelling following successive temperature steps. This shows that 1.0



MPa consolidation pressure is lower than the swelling equilibrium pressure for 26°C, 42°C, 60°C, and 65°C. Another way of thinking of these data is that the swelling equilibrium pressure decreases with temperature if the specific volume stays constant. The observed behavior which produces larger compressions at higher temperatures is consistent with findings from the literature, for example, Mitchell 1969; Green 1984; Eriksson 1989; Tidfors and Sällfors 1989; Hueckel and Pellegrini 1991.

The results shown in this thesis represent the first triaxial tests carried out at the University of Manitoba at elevated temperature. In spite of recurring equipment problems the quality of the data is equivalent to that in other programs. The level of control achieved at the target temperatures is as good or better than that achieved by Green (1984), and the tests were run at pressures an order of magnitude higher than Green's tests. There is less scatter in these data than in Green's data. The quality of data from later tests in this program is as good as that reported by Hueckel and Baldi (1990).

#### 5.4.1 Failure Patterns in Buffer Specimens

In general, clays exhibit systematic behavior at large strains which can be explained by the modified Cam clay model. A key assumption in the model is elliptical yield loci (Roscoe and Burland, 1968) that expand with plastic strain hardening. The yield loci are shown in Figure 5.52 (a) in  $q$ - $p'$  stress space and in Figure 5.52 (b) in  $V_c$ - $\ln(p')$  space. By definition, normally consolidated (NC) and lightly over consolidated (L-O/C) specimens have current mean effective stress,  $p'_o$  greater than  $p'_c/2$  (Wood, 1990), where  $p'_c$  is the isotropic effective preconsolidation pressure. (The ratio  $R = p'_c/p'_o$ , the isotropic overconsolidation ratio, is used here to describe overconsolidation. It has different values from the traditional overconsolidation ratio  $OCR = \sigma'_{zc}/\sigma'_{zo}$ ). In  $V$ - $p'$  space, stress

paths for NC and L-OC specimens during shearing lie between the NCL and CSL. In undrained shear these specimens are compressive (pore water pressures increase), that is, ductile non-strain softening; tend to bulge; and have high ' $A_f$ ' values (greater than 0.33) (Atkinson and Bransby, 1977).

Heavily over-consolidated specimens (H-OC) have  $p'_o$  less than  $p'_c/2$ . In  $V$ - $p'$  space the stress path at the start of shearing is on the left (dry) side of the CSL. In undrained shear these specimens are dilative (pore pressures decrease), they strain soften (deviator stress,  $q$  decreases), they exhibit "brittle" stress-strain behavior (as opposed to ductile behavior), they develop distinct shear planes, and have low ' $A_f$ ' values ( $<0.33$ ) (Atkinson and Bransby, 1977, Wood, 1990). Typical variation of  $A_f$  values with  $R$  for Weald clay (Wood 1990) is shown in Figure 5.52(c).

#### 5.4.1.1 Bulging of Specimens during Shear

In the following discussion it is necessary to differentiate L-OC from H-OC states for tests in the current program. That is, it is necessary to determine the relationship between  $p'_{cons}$  and  $p'_c/2$ . This can be estimated (a) from the swelling equilibrium pressure (SEP) as the ratio  $SEP/p'_o$ , (b) from stress path directions in  $q$ - $p'$  stress space and (c) from the position of the consolidation state relative to the critical state line (CSL) in  $v_c$ - $\ln(p')$  space. A swelling equilibrium pressure (SEP) of 2.2 MPa ( $\gamma_d = 1.67 \text{ Mg/m}^3$ ;  $V_{co} = 2.251$ ) has been interpreted from swell tests at 26°C by Oswell (1991). Dixon *et al.* (1986) suggests a somewhat lower SEP, about 1.7 MPa. As mentioned earlier, it is assumed here that the swelling equilibrium line (SEL) coincides with the normal consolidation line (NCL). In  $q$ - $p'$  stress space, the stress path of H-OC specimens during shearing is towards increasing  $p'$ . In contrast, L-OC and NC specimens near failure have stress paths towards decreasing  $p'$ . Using this understanding, and examining Figure 5.30, it is

apparent that  $p'_c/2$  is approximately 1.4 MPa. This means that  $p'_c$  is higher than the SEP, which for the purposes of discussion, can be taken to be in the range 1.7 MPa to 2.2 MPa.

Bulging failures are usually associated with NC behavior in clay. The most common failure mode observed in this test program has been of the bulging type. This is true of specimens tested in the current program in a normally consolidated state, that is, in specimens where the consolidation pressure was higher than the swelling equilibrium pressure. Bulging also occurred in L-OC and H-OC specimens at 26°C, 65°C and 100°C (T1212, T1233 at  $p' = 0.6$  MPa; T1218, T1219, T1221 at  $p' = 1.0$  MPa; T1205, T1215 at  $p' = 1.6$  MPa). The mode of failure associated with bulging (as opposed to the development of discrete failure planes) appears to be independent of temperature.

However, some cases of brittle behavior have been observed in a small number of specimens tested elevated temperature. Distinct shear planes were observed in the three specimens T1209, T1216, and T1227 which were tested at 65°C, 65°C, and 100°C, respectively. Figure 5.53 shows the failure modes in these specimens, and also the ductile specimen T1205, which were all tested at pressure close to the SEP. At first sight, it might appear that strain softening, distinct shear plane failure, brittle behavior, and stronger specimens are all associated with higher temperatures. However, this is not the case at all consolidation pressures. Actually, specific volume at the end of consolidation and its relationship to the SEL is the governing factor. The specific volume seems to dominate specimen strength at most consolidation pressures regardless of temperature. By definition, T1216 is H-OC ( $R=3.6$ ) but T1209 and T1227 are L-OC ( $R=1.4$ ). Specimen T1216 failed in a ductile, slightly strain softening manner. Specimen T1209 failed in a brittle, distinctly strain softening manner. Specimen T1227 experienced effective stresses of 0.5 MPa at the top (due to cell fluid leak)

and 2.4 MPa at the bottom. The low effective stress would lead to brittle failure. In fact, the specimen followed a drained stress path in  $p'$ - $q$  stress space and failed in a brittle, strain softening mode. Clearly, behavior of specimen T1216, tested at elevated temperature is atypical for H-OC clay at room temperature.

Pore water pressures are measured by transducers attached to the cell base at a short distance from the specimen, and strains are numerically averaged from axial and lateral deformations. Atkinson and Bransby (1977), and Wood (1990) point out that under these conditions it is not possible to measure the stresses and strains at the failure plane. This implies that the state boundary surface from a complete testing program is a generalized model, and may not represent true material behavior in the plane of failure in H-OC specimens. In some programs, pore pressures have been measured internally or locally (Baldi *et al.* 1988, Hight 1982). Strains have been measured locally to obtain more representative results for clays (Baldi *et al.* 1988, Tatsuoka 1988, Symes and Burland 1984), but an improved Cam clay model is still not available. Similarly, bulging failures in the NC range present difficulties in determining truly representative stress and strain measurements. Barreling failures are more a function of the test arrangements than material property. Frictionless (greased) end platens have been used with success to obtain uniformly deformed specimens, but the effective strength parameters were the same as for specimens with a length to diameter ratio of 2 tested between ordinary platens (Barden and McDermott 1965). The additional difficulties in measuring pore pressures are apparently not worth the additional effort. More recent practice involves measurement of lateral strains at several locations and numerical averaging of measurements.

A third type of failure occurred in T1225, T1220, and T1214. All three of these specimens were tested at the same temperature (65°C), but at different pressures (0.6 MPa to 2.2 MPa). The failure mode was characterized by a horizontal

band of wrinkles at the middle of the specimen and bulging at one end. The wrinkles are interpreted as multiple slip lines. The mechanism of failure invoked is unknown. It is unlikely that this is a phenomenon that is purely related to temperature.

#### 5.4.1.2 Shear Strain Softening

A small amount of strain softening occurred in all L-OC and NC specimens sheared at 26°C, 65°C, and 100°C. No specimens strain hardened in shear at failure. The strain softening was generally less than 15% of the peak strength. This behavior is not strongly related to temperature, since it was also observed by Saadat (1989) at room temperature for both low and high density buffer (1.5 Mg/m<sup>3</sup> and 1.67 Mg/m<sup>3</sup>, respectively). Strain softening in the NC range is not inherent in the Cam clay model, but is seen in plastic clays.

Shear strain softening in the NC range in plastic clays can be related to the  $\eta_c = q_c/p'_c$  stress ratio. For example, specimens consolidated anisotropically (1-dimensionally) and loaded along stress paths of high stress ratio exhibit significant strain softening (Noonan 1980, Li 1983, Lau 1986). In contrast, isotropically consolidated specimens exhibit no strain softening (Li 1983, Sun 1986, Noonan 1980). This behavior is true of remolded natural clay (Li 1983), reconstituted illite subjected to stress release disturbance (Lau, 1986), low density ( $\gamma_d = 1.5 \text{ Mg/m}^3$ ) buffer (Sun 1986), and natural clay (Noonan 1980, Lew 1981).

Oswell (1991) performed stress controlled tests (incremental and constant rate of stress) on low and high density buffer. Strain softening is not observable in these types of test. However, he found that an adjusted Cam clay model fits the buffer behavior. Buffer has a state boundary surface and an approximately elliptical yield locus. In spite its high volume change capacity, it appears to

behave like many 'ordinary' soils. It exhibits limited elastic anisotropy and the flow rule may be non-associated. Thus the model is relevant, but additional work should be incorporated to allow it to handle strain softening in the NC range of stresses.

Different mechanisms are believed to be responsible for strain softening at low and high effective stresses. At low effective stresses (that is, in the O/C range) specimens are more isotropic than NC specimens because they have been allowed to swell under isotropic total stress. (Wan, 1988 found that specimens that swelled prior to shearing exhibited isotropic behavior in the early stages of undrained strain controlled triaxial compression. Specimens that compressed prior to shearing exhibited anisotropic behavior. The implication is that swelling tends to remove anisotropy.)

At low stresses, the microstructure of clay particles induced by compaction is preserved, and specimens tend to dilate as the particles move relative to each other along planes of weakness (eventually coalescing into shear planes) during the application of deviatoric load. At the same time, the pore water pressures are decreasing. In the process, a new micro-structure is developed locally, and water is attracted to the failure plane during dilation from neighboring regions. Due to the low hydraulic conductivity of buffer and rate of shear, pore pressures may not be fully equilibrated at the end of testing. In contrast, dense well graded materials like tills tend to dilate and work harden strongly in the O/C range of stresses during shear. As deformations are applied, resistance to shear builds locally due to changes in microstructure on a global level. When water can no longer be attracted quickly enough into a region of high dilatancy, then adjacent areas are relatively stronger than the dilatant region, and barrel shaped failures are observed.

At high effective stresses (in the NC range of behavior), the anisotropic

specimen fabric caused by the 1-dimensional compaction process is dominant and is better preserved than at low effective stresses (O/C range). Oswell (1991) found that buffer anisotropy was different from that measured in undisturbed Winnipeg clay. Buffer was stiffer in the vertical direction than the horizontal direction, whereas natural Winnipeg clay was 1.8 times stiffer in the horizontal direction than the vertical direction (Graham and Houlsby 1983). The greater vertical stiffness in the buffer is due to compaction with zero lateral strains in a rigid mold. Bulging failures in buffer appear to be principally associated with slight strain softening in the NC stress range.

It is also probable that differences in micro-structure may account for changes in the position of the NCL in V-p' space and that this may have some relation to softening

In summary, shear strain softening of buffer specimens in the normal consolidation stress range has to do with the anisotropic fabric generated during compaction.

## CHAPTER 6 FACTORS AFFECTING INTERPRETATION OF DATA

### 6.1 Introduction

At the start of the test program it became apparent that some factors affecting the volume change and final moisture content of buffer should be investigated. This chapter discusses the following factors.

Cell fluid (silicone oil) contamination affects the mass balance of buffer at room temperature and oven drying temperatures (110°C), and this can influence the measured moisture content.

Two different methods are available to calculate the average moisture content of several pieces of the same specimen. Two different answers are sometimes obtained from these methods. Although the differences are small numerically, the philosophical question of 'Which should be used?' should be answered.

The high temperature of the buffer specimens at the end of testing leads to rapid surface drying rates when exposed to the room temperature environment. A critical review of moisture determination procedures was required to obtain representative moisture contents. Moisture contents measured from the entire specimens are compared with values for only the core of the specimens.

The thermal volume change of the water contained in the buffer specimens is calculated in a simplified way to predict what the final specific volume of the buffer should be. This value is compared with the specific volume calculated from measured final moisture contents.



## 6.2 Final Moisture Content of Buffer

### 6.2.1 Average Moisture Content

According to standard room temperature procedures used at the University of Manitoba, the end-of-test buffer specimens were cut into 10 pieces to determine variation of moisture content throughout the specimens, and obtain an average final moisture content. The specimen was cut into 10 pieces by slicing into 5 layers and taking cores from each layer. Figure 6.1 shows the method. Two methods can then be used to calculate the moisture content:

$$[6.1] \quad \text{Average M/C} = \left[ \frac{\sum_1^n (\text{M/C Pieces})}{n} \right]$$

$$[6.2] \quad \text{Average M/C} = \left[ \frac{\sum_1^n (\text{wt. water in piece})}{\sum_1^n (\text{wt. dry soil piece})} \right]$$

These values can then be used to calculate the final clay specific volume,  $V_{cf} = 1+w \cdot G_s$ , where  $w$  is the moisture content and  $G_s$  is the specific gravity of the mineral solids. Values of  $V_{cf}$  calculated using the two methods are shown in columns 3 and 5 in Table 6.1 (given in the next section). The values are shown to the second decimal place, and the differences are small (less than 0.02). However, the differences become larger at lower moisture contents. The question of which method should be used appears to be a philosophical one and in literature the issue is not addressed; rather an arbitrary choice is made. ASTM 4318 (Liquid Limit, Plastic Limit, and Plasticity Index of Soils) specifies the average of moisture contents from three plastic limit specimens. Modern laboratories such as the one at AECL, Pinawa use this method (Dixon, 1992). For the sake of continuity, this is the approach used at the University of Manitoba.

### 6.2.2 Mass Loss

Buffer that has been contaminated with cell fluid loses mass at a steady rate after the first day of oven drying at 110°C. (Uncontaminated buffer and oil individually maintain constant mass at 110°C) Chapter 5 contains the results of a suite of tests performed to quantify this phenomenon. The addition of 10% oil (by weight) caused a steady mass loss (0.1%/day) under continued heating after the buffer had been dried for the normal 1 day period. It is not known how long this phenomenon will continue but tests were performed up to 50 days with no apparent change in rate of mass loss. The behavior was observed for compacted and uncompact (granular) buffer at 110°C (oven dried) and 26°C (desiccated at room temperature). The mass loss may introduce some error into the final moisture content (and hence the calculation of specific volume) if the triaxial specimen has adsorbed oil through leakage over the duration of consolidation. This will be examined in the following text.

It is thought that the oil reacts chemically or physically with the clay-water system or simply displaces bound water in the diffuse layer and/or Stern layer. Active clays provide a siloxane adsorption surface which interacts most strongly with solvent ions or molecules just small enough to fit into the voids created by the crystal lattice (Grim 1953). Silicone oil is a polysiloxane (polymer). It is probable that the oil eventually bonds to the existing mineral flake, thereby displacing other layers of adsorbed water.

It has been suggested that the pH of the diffuse water layer decreases as the particle surface is approached in a solution of pH equilibrium (Iwata *et al.* 1988; Yoshida and Iwata 1970). If this is the case, then it is possible that silicone oil may react with the clay-water system and/or be chemically decomposed. Buffer has a corrosive effect on brass, aluminum and iron. This may be a result of acidity of the pore water or the cation exchange capacity of the clay.

The rate of heating and temperature level also affects the mass loss (among other things) of clays (Grim 1953, Gillott 1987). Rate effects appear to be related mostly to mineralogical transformation and structural water breakdown (Gillott 1987) at very high temperatures (200 to 1000°C). These temperatures are higher than in this program, but the results indicate that water exists in stable forms (unbound, bound/diffuse, structural/ hydroxyl) up to various temperatures.

Figure 6.2 (Lambe 1951) shows different moisture contents at different drying temperatures for several natural (marine) clays. Clearly, it is important to maintain constant oven temperature for moisture determinations. Notice however, that silica (Ottawa sand) maintains constant moisture content (hence mass) at the measured temperature range of 40 to 200°C.

A corrected moisture content was calculated for buffer by first determining the final weight of dry solids (uncontaminated), then using mass loss recorded during the first day of oven drying to obtain a corrected final specific volume,  $V_{cf}^{OC}$ . For all practical purposes, the unbound (bulk) water is driven off within 24 hours at 110°C (Dixon 1992). The relationship used to calculate the weight of dry solids (no oil contamination) is as follows:

$$[6.3] \quad \left[ \frac{\text{Sum dry soil (no oil)}}{\text{Sum final wt. (wet)}} \right]_{\text{pieces}} = \left[ \frac{\text{initial wt. (dry)}}{\text{final wt. (wet)}} \right]_{\text{intact}}$$

where 'pieces' refers to the weight of either the full 10 pieces of specimen, or of 5 core pieces. The numerator applies to uncontaminated buffer, while the denominator refers to contaminated buffer. The sum of weights is discussed in the following section. The corrected moisture content,  $w_f^{OC}$ , is obtained as follows:

$$[6.3a] \quad w_f^{OC} = \frac{\text{mass loss (1 day)}}{\text{sum dry soil (no oil)}} = \frac{w_w}{w_s}$$

The corrected specific volume,  $V_{cf}^{OC}$ , is calculated as follows:

$$[6.3b] \quad V_{cf}^{OC} = 1 + 5.5 \frac{w_f^{OC}}{S_f}$$

where  $S_f$  is the degree of saturation of buffer at the end of the test.

In the current test program, deformations induced by stress and deformation have been lumped together by heating during the consolidation stage (drainage open). The final moisture content of the specimens provides the most reliable means of calculating the true specific volume at the end of the test. Room temperature values are used as reference. The final specific volume of the specimen is calculated as follows:

$$[6.4] \quad V_{cf} = 1 + 5.5w_f/S_f; \quad S_f = 1.0$$

where  $V_{cf}$  is the final clay specific volume,  $w_f$  is the final water content at the end of the test, and  $S_f$  is the saturation at the end of the test

The difference between the corrected and uncorrected specific volume is as follows:

$$[6.5] \quad \Delta V_{cf}^{OC} = V_{cf}^{OC} - V_{cf}$$

where  $\Delta V_{cf}^{OC}$  is the specific volume correction for oil contamination (see Table 6.1).

Table 6.1 lists the values of specific volume calculated from the corrected and uncorrected moisture contents. Column 4 gives the corrected specific volume for 10 pieces per specimen. The average correction,  $(\Delta V_{cf}^{OC})_{Avg}$  (column 6) is small (0.02). The results are plotted in Figure 6.3. There is a maximum scatter in the data the order of 0.07, but the correction appears to be most heavily populated in the range 0 to 0.03. Values shown are rounded up to the second decimal. There is no apparent relationship between the value of the correction  $\Delta V_{cf}$  and the temperature at which the tests were performed.

Table 6.1 Final clay specific volume with and without correction for oil contamination.

Test	Temp. T(°C)	Avg m/c	Avg weight (10 pieces)			Avg weight (core)		
		V <sub>cf</sub>	V <sub>cf</sub> <sup>OC</sup>	V <sub>cf</sub>	ΔV <sub>cf</sub> <sup>OC</sup>	V <sub>cf</sub> <sup>OC</sup>	V <sub>cf</sub>	ΔV <sub>cf</sub> <sup>OC</sup>
T1204	26	2.22	2.24	2.23	0.02	2.22	2.19	0.02
T1205	65	2.28	2.21	2.27	-0.06	2.25	2.32	-0.07
T1207	26	2.12	2.20	2.14	0.06	2.14	2.08	0.06
T1208	26	2.37	2.41	2.38	0.03	2.38	2.35	0.03
T1209	65	2.10	2.11	2.10	0.01	2.09	2.08	0.02
T1210	63	1.66	1.72	1.66	0.07	1.75	1.68	0.07 *
T1211	65	2.14	2.16	2.14	0.02	2.15	2.13	0.02
T1212	26	2.34	2.36	2.35	0.01	2.34	2.32	0.02
T1213	52	1.83	1.87	1.83	0.04	1.86	1.82	0.04
T1214	65	2.07	2.08	2.07	0.02	2.11	2.10	0.01
T1215	26	2.21		2.22	N/A		2.20	N/A
T1216	62	2.34	2.36	2.35	0.02	2.36	2.34	0.02
T1217	24	2.16	2.18	2.17	0.01	2.16	2.14	0.01
T1218	27	2.26	2.29	2.28	0.02	2.26	2.24	0.02
T1219	63	2.17		2.17	N/A		2.19	N/A
T1220	65	2.17	2.18	2.16	0.02	2.21	2.20	0.01
T1221	26	2.22	2.24	2.22	0.02	2.22	2.20	0.02
T1223	65	2.10	2.10	2.09	0.00	2.13	2.09	0.04
T1225	65	2.28	2.30	2.28	0.02	2.31	2.28	0.02
T1226	100	1.97	1.97	1.97	0.01	2.03	1.97	0.06 *
T1227	100	1.95	1.95	1.95	0.00	2.01	1.95	0.06 *
T1228	100	1.97	1.98	1.97	0.01	2.01	1.97	0.04
T1229	65	2.00	2.05	2.00	0.05	2.07	2.00	0.07
T1230	100	2.04	2.04	2.04	0.00	2.09	2.04	0.04
T1232	100	2.33	2.32	2.30	0.01	2.34	2.30	0.04 #
T1233	100	2.32	2.33	2.32	0.01	2.34	2.32	0.02
T1234	100	2.66	2.70	2.66	0.04	2.64	2.66	-0.01 #
T1235	100	1.90	1.88	1.85	0.02	1.92	1.85	0.06
T1236	65	1.92	1.92	1.92	0.01	1.94	1.94	0.00
				Avg =	0.02		Avg =	0.03

NOTE:1. V<sub>cf</sub><sup>OC</sup> = Final clay specific volume corrected for oil contamination

2. \* Membrane leakage

3. # Membrane ballooned

If the buffer is uncontaminated then  $\Delta V_{cf}^{OC}$  is zero, while contaminated buffer is expected to have  $\Delta V_{cf}^{OC} > 0$ . The specific volume of most specimens increased with the correction. The implication from Table 6.1 is that most of the specimens were contaminated. However, residual oil in the drainage lines may account for some of the contamination rather than membrane leakage.

The correction  $\Delta V_{cf}^{OC}$  was also calculated using only the core pieces of the specimens (Table 6.1 ; column 9). A slightly larger correction,  $(\Delta V_{cf}^{OC})_{Avg}$ , (0.03) was obtained than for the entire specimen. The magnitude of scatter in the data is the same as before, but not concentrated in any range.

Uncorrected specific volumes are plotted against log effective stress in Figure 6.4. In this Figure, (which was also presented earlier in Figure 5.12), the specific volume was determined using only the core pieces of buffer specimens because they provide more consistent data. The corrected and uncorrected specific volumes are shown in Figure 6.5. The differences are not large. T1213 was not included in the results because a different test apparatus and cell fluid (antifreeze) was used. Excluding T1213 provides a better regression.

The correction,  $\Delta V_{cf}^{OC}$  is small (maximum 0.06) even for tests such as specimen T1226 in which leakage had been observed for over 10 days. It is believed that the saturated conditions and high effective stresses imposed during testing may mitigate the mass loss phenomenon.

The combined test results in Figures 6.3, 6.4 and 6.5 indicate that (1) oil contamination is essentially independent of temperature (up to 100°C), but is a complex phenomenon, (2) the test data and contamination correction are independent of test equipment, (3) the quality of data improved later in the test series, (4) the correction for oil contamination is small (0.02 to 0.03), and (5) there is a gradient in moisture content and oil contamination between the outer surface and center of the specimens. The correction does not improve the overall fit of the

data to a linear regression in  $V_{cf}$  versus  $\log p'$  space. It is worth remembering that in the most favorable of circumstances the repeatability of moisture content determinations is about  $\pm 0.1$  to  $0.2\%$  (Head 1986) and this corresponds to a change in specific volume of  $\pm 0.01$ . For all practical purposes it appears that the correction for oil contamination,  $\Delta V_{cf}^{OC}$  is unnecessary.

### 6.2.3 Drying Gradients

Examination should be given to the choice of pieces used to determine the final moisture content. The standard practice has been to use all 10 pieces. This may not be prudent because the final elevated temperature of the specimens during removal causes excessive drying of the buffer during post test handling. Pieces taken from the core of the specimen may be the only ones representative of the true moisture content (and hence specific volume of the specimens while still in the test cell). The buffer moisture contents have been calculated using all 10 pieces, and only the core 5 pieces. The results have been reported in Table 6.1. There is a small difference between the two methods for uncorrected specific volume (compare columns 5 and 8), but a larger, more random difference for the corrected specific volume (columns 4 and 7). This is believed to be a result of drying gradients set up after the specimens are removed from the test cell.

It is of passing interest that montmorillonite clays when subjected for long periods of time to substantially uniform moisture conditions, develop hydration characteristics of considerable stability (Grim 1953). If the hydration is changed, the stability may be abruptly and completely lost. A high swelling bentonite sample carefully collected to preserve its natural hydration can be placed in water without any slaking, even when moderately stirred. However, if such a bentonite is dried only a very small amount, it will slake and swell immediately when placed in water. This indicates that drying will upset any

equilibrium set up during a given test and may influence the distribution of both water and oil (if any) throughout the specimen.

### 6.3 Thermal Volume Change

In the current test program there are two ways to determine the final specific volume of buffer,  $V_{cf}$ . The first and most reliable way is to calculate  $V_{cf}$  from the final moisture content. The second way of calculating  $V_{cf}$  is by taking account of the volumetric strains observed and applying appropriate corrections to the initial specific volume,  $V_{co}$ . A correction must be applied to the measured volume change for apparatus compliance, thermal expansion of the pore water and mineral solids. Three methods (in order of increasing complexity) are investigated for estimating thermal volume changes. These methods account for (a) thermal expansion of pore water and system compliance (b) thermal expansion of pore water, pore voids, and system compliance; and (c) all of the previous, plus thermally induced compression of the soil skeleton. A new definition of specimen volume change is required. Mass balance is proposed as a better way of quantifying the state of volume of buffer undergoing thermal changes. A new coefficient,  $\beta_{st}$ , is investigated to characterize the volume change due to thermal and mechanical skeletal deformation using thermo-elasto-plastic theory.

Many confusing terms have been used in the literature to describe the state of water contained in clay. Terms such as bound, unbound, adsorbed, firmly adsorbed, bulk, interstitial, interlamellar, structural, double layer, diffuse, surface, and Stern water are a few examples of the terms used to classify different types or phases of water contained in active clay. These were discussed in detail in Chapter 2. Figure 6.6 shows the types of water most likely present in low density bentonite (structural water is not shown).

The following convention will be used throughout this thesis. Three basic



types of water exist in dense clays and clay gels: (1) unbound; (2) bound; and (3) structural. The first type of water, unbound water, is contained mainly in the largest of the pore spaces in the clay matrix and is driven off first at elevated temperature. It is also known as bulk or interstitial water. The second type of water, bound water, interacts with the clay minerals through hydrogen bonds, van der Waals forces, osmotic pressures, ionic bonds, and concentration gradients (chemical, physical, electrical, thermal). It exists as (a) diffuse double layer water, and (b) Stern water.

The second type of water, bound water, is likely the most abundant water in dense buffer (Dixon and Gray 1990, Hueckel *et al.* 1991). It is reasonable to assume that bound water dominates the compressive and shear properties of dense buffer for the range of temperatures used in this test program, 26°C to 100°C. Physical properties of bound water in dense buffer, such as coefficient of thermal expansion, density, and structure, are not known with certainty (Hueckel *et al.* 1991). No attempt is made here to differentiate the properties of the types of water for quantitative prediction of buffer response to drained heating.

The third type of water, structural water (not shown in Figure 6.6) is water that makes up the crystalline lattice of hydrated clay minerals such as montmorillonite.

In the following paragraphs, thermal volume changes in clay are interpreted in terms of micromechanical studies by other researchers. No definitive statement can be made regarding absolute values of thermal expansion of bound water, unbound water and structural water in buffer. It is known that fluid pressure in the bound water close to the particle surface of montmorillonite is extremely high; as much as several thousands of atmospheres (Bailey, 1965). Tests on Boom clay by Hueckel (1991) suggest that the surface water (in the Stern layer, for instance) is in a highly stressed state and undergoes thermal expansion during heating due to

increase in entropy.

The interlamellar water in Na-montmorillonite constitutes more than 90% of the total water content at dry densities exceeding  $1.60 \text{ Mg/m}^3$  (Pusch, 1990). The maximum number of interlamellar hydrates (water layers) is 3, which means that a fully expanded state of the mineral stacks is theoretically obtained at around  $1.8 \text{ Mg/m}^3$  saturated unit weight ( $1.30 \text{ Mg/m}^3$  dry density). It is believed that there are 3 to 5 mineral flakes in a stack. Interlamellar water forms an ordered medium in or through which interparticle forces are established and transferred (Graham *et al.* 1992). Interlamellar water is a dynamic adsorption phase and has a density between  $1.00$  and  $1.05 \text{ Mg/m}^3$  (Pusch, 1990). Some experimental and theoretical results suggest higher densities of  $1.2$  to  $1.4$  (Hueckel, 1991, Yong and Warkentin, 1975), which is about the clay density of the buffer. Pusch assumes that the first hydrate layer (0-hydrate) is insensitive to temperatures below  $100^\circ\text{C}$  and pressures of  $100 \text{ MPa}$ . The coefficient of thermal expansion for Na-montmorillonite is less than  $3.9 \times 10^{-5} \text{ 1/}^\circ\text{K}$  from  $25^\circ\text{C}$  to  $400^\circ\text{C}$  (McKinstry, 1965). This is 2 orders of magnitude smaller than bulk water according to Gray and Cheung (Baldi, *et al.*, 1990a). Low's modified DLVO model suggests that bound water exists in one of two forms; as a mixture of polymer like molecules in a regular arrangement with a distribution of voids within; or as a continuum of molecules with a regular orientation like a crystalline material. The surface water undergoes thermal expansion of the same order as bulk water but remains bonded to the clay surface above  $200^\circ\text{C}$ .

### 6.3.1 Method 1: Pore Water and System Compliance

#### 6.3.1.1 Back Calculation

As a simple approximation, thermal expansion of the water held by the buffer was calculated by applying the coefficient of expansion of bulk water,  $\beta_w$ , to the entire mass of water that was initially mixed with the dry buffer. The calculated volume changes are given in Table 6.2 for individual tests.

**Table 6.2: Final clay specific volume of buffer corrected for thermal expansion of bulk water and apparatus water (drain line, porous stone, and transducer housing).**

Test	Corrected Final Specific Volume									
	Forward Calculation					Back Calculation				
	T (°C)	V <sub>cf</sub> (S=1)	V <sub>co</sub> (S=1)	ε <sub>v</sub> <sup>TA</sup> (%)	V <sub>cf</sub> <sup>TA</sup>	ΔV <sub>cf</sub> <sup>TA</sup>	V <sub>cf</sub> (S=1)	ε <sub>v</sub> <sup>TB</sup> (%)	V <sub>cf</sub> <sup>TB</sup>	ΔV <sub>cf</sub> <sup>TB</sup>
T1204	26	2.221	2.238	-0.38	2.250	-0.029	2.221	0.00	2.221	0.000
T1205	65	2.282	2.551	2.02	2.478	-0.196	2.282	1.42	2.329	-0.047
T1207	26	2.122	2.293	3.00	2.193	-0.071	2.122	0.00	2.122	0.000
T1208	26	2.369	2.150	-7.50	2.388	-0.019	2.369	0.00	2.369	0.000
T1209	65	2.100	2.221	2.18	2.150	-0.050	2.100	1.67	2.152	-0.052
T1211	65	2.139	2.188	4.18	2.053	0.086	2.139	1.60	2.190	-0.051
T1212	26	2.342	2.249	-4.38	2.392	-0.050	2.342	0.00	2.342	0.000
T1213	52	1.825	2.293	4.74	2.135	-0.310	1.825	1.15	1.858	-0.033
T1214	65	2.073	2.238	2.74	2.148	-0.075	2.073	1.65	2.124	-0.051
T1215	26	2.210	2.183	-2.67	2.268	-0.058	2.210	0.00	2.210	0.000
T1216	62	2.342	2.249	-6.31	2.456	-0.114	2.342	1.55	2.394	-0.052
T1217	24	2.161	2.205	0.75	2.180	-0.019	2.161	0.09	2.158	0.003
T1218	27	2.265	2.199	-4.28	2.338	-0.073	2.265	0.04	2.266	-0.001
T1219	63	2.172	2.227	-5.17	2.395	-0.223	2.172	1.60	2.223	-0.051
T1220	65	2.172	2.172	-2.57	2.254	-0.082	2.172	1.71	2.227	-0.055
T1221	26	2.216	2.232	-4.40	2.376	-0.160	2.216	0.00	2.216	0.000
T1223	65	2.095	2.210	1.69	2.155	-0.060	2.095	1.70	2.148	-0.053
T1225	65	2.282	2.227	-3.79	2.350	-0.068	2.282	1.71	2.339	-0.057
T1226	100	1.968	2.293	-3.82	2.420	-0.452	1.968	3.24	2.065	-0.097
T1227	100	1.946	2.199	0.32	2.189	-0.243	1.946	3.23	2.042	-0.096
T1228	100	1.968	2.194	0.13	2.189	-0.221	1.968	3.27	2.066	-0.098
T1229	65	2.001	2.177	5.61	1.997	0.004	2.001	1.97	2.061	-0.060
T1230	100	2.045	2.221	-1.65	2.275	-0.230	2.045	3.22	2.144	-0.099
T1232	100	2.326	2.216	-0.74	2.240	0.086	2.326	3.16	2.432	-0.106
T1233	100	2.320	2.238	-17.52	2.812	-0.492	2.320	3.20	2.427	-0.107
T1234	100	2.656	2.199	-13.92	2.650	0.006	2.656	3.09	2.770	-0.114
T1235	100	1.895	2.206	1.39	2.161	-0.266	1.895	3.13	1.987	-0.092
T1236	65	1.916	2.196	4.77	2.042	-0.126	1.916	1.65	1.965	-0.049
					AVG	-0.125			AVG	-0.050

NOTE: 1. Specific Volumes based on average moisture method.

$$2. \Delta V_{cf}^{TA} = V_{cf} - V_{cf}^{TA}$$

$$\Delta V_{cf}^{TB} = V_{cf} - V_{cf}^{TB}$$

The final clay specific volume after cooling to 26°C,  $V_{cf}^{26}$ , is back calculated from the measured final clay specific volumes,  $V_{cf}^{65}$ [meas], and  $V_{cf}^{100}$ [meas] using the theoretical volume changes  $\epsilon_v^{65}$ , and  $\epsilon_v^{100}$  (for thermal expansion of the water). The back calculated specific volume  $V_{cf}^{26}$  is shown as  $V_{cf}^{TB}$  in Table 6.2. The difference between the measured  $V_{cf}$  and  $V_{cf}^{TB}$  is also shown. The following equation is used for 65°C data:

$$[6.6] \quad V_{cf}^{26} = V_{cf}^{65}[\text{meas}] + \frac{\epsilon_v^{65}}{100} \cdot \left[ 1.037 + V_{cf}^{65}[\text{meas}] \right]$$

where

$$[6.7] \quad \epsilon_v^{65} = \left[ \frac{\Delta V_w^{65}}{V_t} \right] \cdot 100 = \epsilon_v^{TB} \text{ (Table 6.2)}$$

$$[6.8] \quad \Delta V_w^{65} = V_w \cdot \beta_w \cdot \Delta T = 0.001162 \cdot (T-26) \cdot V_w$$

where  $V_{cf}^{65}$ [meas] is the final clay specific volume calculated from the final moisture content. The assumed volume strain (%) produced by thermal expansion of bulk water is  $\epsilon_v^{65}$ . The corresponding volume change is  $\Delta V_w^{65}$ . The initial total volume of the specimen is  $V_t$ , the volume of water initially added to the buffer is  $V_w$ , and  $\beta_w$  is the coefficient of thermal volumetric expansion of water as a function of temperature. The derivation of  $\beta_w$  is given later in this chapter. Equation [6.6] is the same form of equation used to calculate the final specific volume from the initial specific volume using volume changes recorded during consolidation. An equation similar to equation [6.6] is used for 100°C data. No correction for system compliance is required for this calculation. All volume changes are referenced to specimen behavior, thus thermal expansion of pore water leads to expulsion of water into the drainage burettes, and this translates to specimen compression and a positive volume change.

Figure 6.7 shows two regression lines from back calculations. The back

calculation of  $V_{CF}^{26}$  from 65°C data is labelled  $V_{CF}^{65}(\text{Corrected})$  and the back calculation of  $V_{CF}^{26}$  from 100°C data is labelled  $V_{CF}^{100}(\text{Corrected})$ . These two regression lines (solid lines) are close to the regression line for  $V_{CF}^{26}[\text{Meas}]$ . This implies that the dominant thermal effect is thermal expansion of the pore water in a manner similar to the behavior of bulk water.

Clearly, this is a good first approximation, but additional factors are involved. The specific volumes measured from the final moisture content for tests at 26°C, 65°C and 100°C are shown for comparison ( $V_{CF}^{26}[\text{Meas}]$ ,  $V_{CF}^{65}[\text{Meas}]$ ,  $V_{CF}^{100}[\text{Meas}]$ ). One data point for the 100°C data has been excluded from the regression (shown by the arrow). Cheung (1991) suggests that at high density, the buffer contains no bulk water. The expulsion of water during heating of buffer may come from liberation of bound water. This is clearly one aspect of dehydration.

The final clay specific volume is used in the calculations because it has been generally found more reliable than a forward calculation using the initial clay specific volume and specimen volume change (see for example Graham *et al.* 1991).

### 6.3.1.2 Forward Calculation

The final specific volume at elevated temperature was also calculated for 65°C and 100°C taking account of thermal expansion of water and the system compliance. The forward calculation from the initial specific volume was as follows:

$$[6.9] \quad V_{CF}^{65}[\text{Corrected}] = V_{CO}[\text{Meas}] - \frac{\epsilon_V^C}{100} \cdot \left[ 1.037 + V_{CO}[\text{Meas}] \right]$$

where

$$[6.10] \quad \epsilon_V^C = \epsilon_V^{65}[\text{Meas}] - \frac{100}{V_i} \left[ \Delta V_W^{65}[\text{Calc}] + \Delta V_W^{TR}[\text{Calc}] \right] = \epsilon_V^{TA} \text{ (Table 6.2)}$$

$$[6.11] \quad \Delta V_W^{65}[\text{Calc}] = \left[ V_W^{BS} + V_W^{PS} \right] \cdot [T-26] \cdot \beta_W^{65}$$

$$[6.12] \quad \Delta V_W^{TR}[\text{Calc}] = V_W^{TR} \left( T_{TR} - 26 \right) \cdot \beta_W^{65}$$

$$[6.13] \quad \beta_W^{65} = 0.001162 \text{ (1/}^\circ\text{C)}$$

where  $V_{CF}^{65}[\text{Corrected}]$  is the prediction of  $V_{CF}^{26}[\text{Meas}]$  using elevated temperature data. These are given in Table 6.2 as  $V_{CF}^{TA}$  and  $V_{cf}$ . The initial specific volume of the heated specimens measured before the start of the test is  $V_{CO}[\text{Meas}]$ . The corrected volumetric strain during the test is  $\epsilon_V^C$ . The volumetric strain of the buffer specimen measured at the end of consolidation at elevated temperature is  $\epsilon_V^{65}[\text{Meas}]$ . The total volume of the specimen at the start of the test is  $V_t$ . The estimated volumetric thermal expansion of water in the buffer and porous stones caused by heating from 26°C to 65°C is  $\Delta V_W^{65}[\text{Calc}]$ . The estimated volumetric thermal expansion of the water in the pore pressure transducer is  $\Delta V_W^{TR}[\text{Calc}]$ .  $V_W^{BS}$  and  $V_W^{PS}$  are the volumes of water in the buffer and porous stones, respectively. Temperature of the buffer is  $T$ , and  $\beta_W^{65}$  is the volumetric thermal expansion coefficient for bulk water for the temperature range 26°C to 65°C. The volume of water in the transducer is  $V_W^{TR}$ , and  $T_{TR}$  is the temperature of the transducer.

Thermal expansion of water in the drainage lines and/or specimen leads to expulsion of water which is interpreted as specimen compression, according to equation [6.10]. As an approximation, the expansion of water in the line connecting the transducer housing to the DPT is ignored. This is justified because the line is uninsulated and contains a relatively small volume of water. In most tests the transducer housing temperature was lower than the HITEP cell. The transducer, porous stones and drain line contained 20.5 ml of water compared to 77 ml in the buffer.

The calculated values of thermal volumetric system compliance have been compared with calibration tests using dummy specimens. The results are given in

Appendix F (Tables F1 and F2) and discussed in detail. Good agreement was found between the calculated and measured volume changes. The discrepancies are small compared to the total volume of water in the buffer.

Figure 6.8 shows regressions for  $V_{CF}^{65}$ [Corrected] and  $V_{CF}^{100}$ [Corrected] which are estimates of the final specific volume of the elevated temperature specimens corrected to a common temperature of 26°C. The regressions are compared with the regressions for measured final specific volumes at 26°C, 65°C and 100°C. If thermal expansion of the water in the system and buffer are the only factors involved, then the corrected specific volume regressions for 65°C and 100°C data should coincide with the regression for the measured 26°C data. Figure 6.8 suggests that thermal expansion is more complicated than assumed in this calculation.

The results of the forward calculation are summarized in Table 6.2. where  $V_{CF}^{65}$ [Corrected] is shown as  $V_{cf}^{TA}$ . The difference between  $V_{cf}$  and  $V_{cf}^{TA}$  is  $\Delta V_{cf}^{TA}$ . There is moderate agreement between the correction,  $\Delta V_{cf}^{TA}$  for the forward calculation and  $\Delta V_{cf}^{TB}$  the correction for the back calculation for tests at 65°C.

"Forward" calculations result in more scatter within the data and produces a poorer trend in temperature correlations than the back calculation method. This is not surprising because this approach also produced more scatter in the results for  $V_{cf}$  calculated from the volume change recorded during consolidation. This method has provided no useful information and has since been abandoned.

This discussion shows that thermal expansion of the bulk water alone can account for most of the thermally induced volume changes experienced by the buffer. A similar conclusion was reached by Gray, Dixon and Cheung in a report to the Commissione delle Comunita' Europee (CEC) (Baldi, *et al*, 1990a, 1990b). Their results pertained to dry densities ranging from 0.21 to 1.09 Mg/m<sup>3</sup>. The coefficient of thermal expansion of the pore water approaches that of bulk water at



higher densities.

Clearly other factors such as thermal expansion of the clay and sand particles, and skeleton deformation are at work. The former are believed to be small relative to bulk water.

Without performing drained heating-cooling tests, it is not possible to determine the reversibility of the process. Grim (1953) points out that as long as some water exists in the interlayer regions, Na montmorillonite can be rehydrated, but the process is irreversible at temperatures typically above 400°C. It is likely that the process is reversible at 100°C.

### 6.3.2 Method 2: Pore Water, Pore Void, and System Compliance

#### 6.3.2.1 Forward Calculation

This section discusses a hypothetical case. The measured final specific volumes of buffer specimens,  $V_{CF}^{26}[\text{Meas}]$ , tested at 26°C have been used with suitable thermal expansion coefficients for specimen water and voids (under drained conditions) to predict the final specific volumes,  $V_{CF}^{65}[\text{Predicted}]$  and  $V_{CF}^{100}[\text{Predicted}]$  of heated specimens. The predicted values are compared with regressions for measured values,  $V_{CF}^{65}[\text{Meas}]$  and  $V_{CF}^{100}[\text{Meas}]$ , in Figure 6.9. If the values agree, then thermal volume changes are due to expansion of the bulk water and soil voids. Otherwise, other factors such as skeletal volume changes are involved. Clearly, there is good agreement for the 65°C tests, but less agreement for the 100°C tests. There must be considerably larger skeletal changes at 100°C than 65°C. Other factors could include the mode of skeletal/void volume changes, and behavior of bound water which is different from bulk water. The equations used to predict the specific volumes are as follows:

$$[6.14] \quad V_{CF}^{65}[\text{Predicted}] = V_{CF}^{26}[\text{Meas}] - \frac{\epsilon_v^{65}}{100} \cdot \left[ 1.037 + V_{CF}^{26}[\text{Meas}] \right]$$

$$[6.15] \quad \epsilon_v^{65} = 100 \cdot \Delta V^{65} / V_t$$

$$[6.16] \quad \Delta V^{65} = \beta_w^{65} V_w \Delta T + \beta_s^{65} [V_t - V_s] \Delta T$$

where  $\epsilon_v^{65}$  is the estimated strain due to thermal expansion of the pore water and voids. The corresponding volume change is  $\Delta V^{65}$ .  $V_w$ ,  $V_t$ , and  $V_s$  are volumes of the pore water, total specimen volume and volume of mineral solids, respectively.  $\beta_w^{65}$  and  $\beta_s^{65}$  are the volumetric thermal expansion coefficients for the pore water and mineral solids for the temperature range  $\Delta T$ . In this case  $\Delta T$  is from 26°C to 65°C. These calculations are for drained conditions. For undrained conditions, equation [6.16] indicates thermal expansion of pore water should be equal and opposite to void volume changes.

### 6.3.3 Method 3: Skeletal Thermal Volume Change

The problem of predicting volume changes due to thermally induced skeletal volume changes using only test results from the current test program is indeterminate. However, it is possible to calculate and verify a thermal expansion coefficient for skeletal volume changes,  $\beta_{st}$ . Two variations of this coefficient are discussed: (1) for mechanical plus thermal effects and (2) for thermal effects alone. These coefficients can be used to predict skeletal volume changes in a set of ramped temperature tests.

#### 6.3.3.1 $\beta_{st}$ (mechanical + thermal compression)

Mitchell (1969, 1976) and Hueckel (1987) observed that volume change occurs in triaxial tests during drained heating due to thermal expansion of the specimen constituents, soil skeleton, and apparatus including drain lines and water. Differential thermal expansion of the specimen pore water and soil solids may lead to deformation of the soil skeleton and the fabric may be permanently altered.

As a first approach, mechanical and thermal components of plastic deformation are described by the expansion coefficient  $\beta_{st}$  in this section.

To obtain  $\beta_{st}$ , it is necessary to determine the coefficient of thermal expansion for bulk water,  $\beta_w$ , pore water,  $\beta_{cw}$ , and clay minerals,  $\beta_s$ . This is discussed in the paragraphs that follow:

Baldi *et al.* (1990a, 1990b) reported constant-volume, and dilatometer triaxial tests on quartz, kaolinite, illite and montmorillonite to determine the coefficient of thermal expansion for pore water in clay,  $\beta_{cw}$ . The following expression was used for the constant volume tests:

$$[6.17] \quad \Delta V_{DR} = (V_s \beta_s + V_w \beta_{cw}) \Delta T + \Delta V_{app}$$

where  $\Delta V_{DR}$  is the volume of fluid drained from the specimen,  $V_s$  is the volume mineral solids,  $V_w$  is the volume of water,  $\Delta V_{app}$  is the thermal volume change of the apparatus,  $\beta_s$  and  $\beta_{cw}$  are the coefficient of thermal expansion for mineral solids and pore water, respectively, and  $\Delta T$  is the change in temperature. The tests showed that the thermal expansion of pore water in low-density montmorillonite was less than pure water, but approached the pure water value at a clay density of  $1.0 \text{ Mg/m}^3$  (The clay density in the buffer is about  $1.2 \text{ Mg/m}^3$ ). Figure 6.10 shows their results. The tests were carried out at an effective stress of 2.5 MPa, a pressure which is applicable to the range of pressures in the current test program. Much higher clay density was used in the current program, but in fact this supports the use of Baldi's expansion coefficient  $\beta_{cw}$ .

Baldi *et al.* (1991) showed that  $\beta_{cw}$  is two orders of magnitude larger than  $\beta_s$ . There are uncertainties in the Volume of solids (calculated from specific gravity of solids),  $\beta_s$ , and  $\beta_{cw}$ , but these are minor. The author checked the values used by Baldi *et al.* (1991) for  $\beta_w$  and  $\beta_s$  and found them to be correct. Calculations are shown and discussed in Appendix F. For practical purposes,  $\beta_{cw}$  for the dense buffer in this program can be taken as equal to  $\beta_w$  for pure water.

The specific volume for pure water is temperature dependent, but as shown in Figure 6.11, the variation is negligibly small considering the other uncertainties in the data. The coefficient of thermal expansion for pure water and its variation with temperature and pressure was calculated by the author using data from standard steam tables as shown in Appendix F. Figure 6.12 (a) and (b) show the pressure dependency at pure water at 65°C and 100°C as calculated by the author. The pressure dependency of  $\beta_s$  is even smaller as discussed in Appendix F.

The temperature dependency of  $\beta_w$  and  $\beta_s$  was also calculated by the author from standard steam tables and literature as discussed in Appendix F. The dependency of  $\beta_w$  on temperature from these calculations is significant:

$$[6.18] \quad \left[ \frac{\partial \beta_w}{\partial T} \right]_{0.1 \text{ MPa}} = 6.20 \times 10^{-6} \text{ (1/}^\circ\text{C/}^\circ\text{C)}$$

$$[6.19] \quad \left[ \frac{\partial \beta_w}{\partial T} \right]_{2.5 \text{ MPa}} = 6.14 \times 10^{-6} \text{ (1/}^\circ\text{C/}^\circ\text{C)}$$

$$[6.20] \quad \left[ \frac{\partial \beta_w}{\partial T} \right]_{10 \text{ MPa}} = 5.82 \times 10^{-6} \text{ (1/}^\circ\text{C/}^\circ\text{C)}$$

The dependency of  $\beta_s$  on temperature is approximately an order of magnitude smaller than that of  $\beta_w$ .

The coefficients of thermal expansion for the three types of water in clay, mentioned previously, are not known (Hueckel *et al.* 1991), but for dense buffer only the coefficients of thermal expansion for structural water,  $\beta_{sw}$ , and interlamellar water,  $\beta_i$  are important. No attempt is made here to determine  $\beta_{sw}$  or  $\beta_i$ .

Mitchell (1976), Green (1984), Agar (1984), and Kosar (1989) used generic expressions to account for thermal expansion of the soil skeleton and compression due to particle rearrangement in marine clay, shale and oil sand. Neglecting Kosar's term for bitumen, the volume of fluid drained ( $\Delta V_d$ ) from a soil specimen under a temperature change  $\Delta T$  can be calculated as follows:

$$[6.21] \quad (\Delta V_d)_{\Delta T} = \beta_w V_w \Delta T - \beta_s (V_t - V_s) \Delta T - \beta_{st} V_t \Delta T$$

where  $V_t$  is the volume of specimen,  $V_w$  is the volume of water,  $\beta_s$  and  $\beta_{st}$  are the coefficient of thermal expansion for the minerals and particle structure, respectively. The thermal expansion coefficient for water,  $\beta_w$ , is the same as Baldi's coefficient  $\beta_{cw}$ . The term  $(V_t - V_s)$  is the volume of voids. The second term on the right hand side of equation [6.21] is the thermal expansion of the voids and the third term is for particle rearrangement. Subtracting the apparatus compliance,  $(\Delta V_{app})_{\Delta T}$  from the right hand side (RHS) of equation [6.21] gives the following:

$$[6.22] \quad (\Delta V_d)_{\Delta T} - (\Delta V_{app})_{\Delta T} = \beta_w V_w \Delta T - \beta_s (V_t - V_s) \Delta T - \beta_{st} V_t \Delta T$$

where  $V_t$  is the volume of the specimen,  $\beta_s$  is the coefficient of thermal expansion for the solids. Volume changes start after the confining and back pressure are applied, therefore mechanical compliance for the apparatus is eliminated. Since the volume of fluid drained  $(\Delta V_d)_{\Delta T}$  is measured in the current tests, the apparatus compliance is known, and the remaining parameters can be estimated; it is possible to calculate  $\beta_{st}$  for each test. It will be shown later that the left hand side (LHS) of equation [6.22] is equivalent to the vertical distance between the NCL's for different temperatures in  $V_c - \ln(p')$  space. However, as a first approximation for the current tests  $(\Delta V_d)_{\Delta T}$  will be the total fluid drained from the specimen due to both temperature application and consolidation at room temperature. Later, another term will be added to equation [6.22] to allow calculation of thermal volume change separately. Table 6.3 contains the parameters used in the calculation of equation [6.22].

Table 6.3: Calculation of thermal expansion coefficient,  $\beta_{st}$  for 65°C and 100°C

Test	$(\Delta V_d)_{\Delta T}$ (cc)	$\beta_w$ (1/°C) $\times 10^{-6}$	$\beta_s$ (1/°C) $\times 10^{-6}$	$\Delta T$ (°C)	$V_w$ (cc)	$V_s$ (cc)	$\Delta V_{app}$ (cc)	$\beta_{st}^{65}$ (1/°C) $\times 10^{-6}$	$\beta_{st}^{100}$ (1/°C) $\times 10^{-6}$
T1204									
T1205	8.26	923	39	40	77.80	126.67	0.76	548	
T1206									
T1207									
T1208									
T1209	8.53	923	39	40	74.80	121.85	0.76	638	
T1210									
T1211	12.35	923	39	40	74.80	121.85	0.76	1118	
T1212									
T1213	12.39	923	39	40	74.80	121.85	0.76	1125	
T1214	9.65	923	39	40	74.80	121.85	0.76	774	
T1215									
T1216	-8.87	923	39	40	74.80	121.85	0.76	-1521	
T1217									
T1218									
T1219	-6.46	923	39	40	74.80	121.85	0.76	-1220	
T1220	-0.96	923	39	40	78.00	125.63	0.76	-549	
T1221									
T1222									
T1223	7.82	923	39	40	78.00	125.63	0.76	525	
T1224									
T1225	-3.38	923	39	40	78.00	125.63	0.76	-846	
T1226	0.53	1162	39	75	78.00	125.63	1.79		-280
T1227	8.93	1162	39	75	78.00	125.63	1.79		271
T1228	8.57	1162	39	75	78.00	125.63	1.79		248
T1229	16.15	923	39	40	74.80	121.85	0.76	1579	
T1230	4.90	1162	39	75	78.00	125.63	1.79		7
T1231									
T1232	6.64	1162	39	75	78.00	125.63	1.79		121
T1233	-27.68	1162	39	75	78.00	125.63	1.79		-2111
T1234	-20.43	1162	39	75	78.00	125.63	1.79		-1645
T1235	11.28	1162	39	75	78.00	125.63	1.79		410
T1236	13.95	923	39	40	78.00	125.63	0.76	1279	

Values of  $\beta_{st}$  are shown in Figure 6.13. The following curves have been fitted to the data:

$$[6.23] \quad \beta_{st}^{65C} = -322 \times 10^{-6} + 1005 \times 10^{-6} \ln(p'); \quad R^2 = 0.8359;$$

$$[6.24] \quad \beta_{st}^{100C} = -636 \times 10^{-6} + 593 \times 10^{-6} \ln(p'); \quad R^2 = 0.6112;$$

The principal conclusions are that (1) the soil skeleton does experience thermal deformation due to particle rearrangement (2)  $\beta_{st}$  is pressure dependent (3)  $\beta_{st}$  is temperature dependent and (4)  $\beta_{st}$  is of the same magnitude as  $\beta_w$ . Since  $\beta_{st}$  consists of both mechanical and thermal deformation components, the first three findings are not surprising. These calculations are the first to quantify the thermal response of the skeleton. The related testing performed by Yarechewski (1992) where consolidation is completed in two stages, first mechanical then thermal, is better suited to this type of analysis.

### 6.3.3.2 $\beta_{st}$ (Thermal compression)

The following approach is suggested for separating mechanical and thermal skeletal deformations in order to calculate  $\beta_{st}$  for thermal compression. A fourth term must be added to the right hand side of equation [6.22] as follows:

$$[6.25] \quad (\Delta V_d)_{\Delta T} - (\Delta V_{app})_{\Delta T} = \beta_w V_w \Delta T - \beta_s (V_t - V_s) \Delta T - \beta_{st} V_t \Delta T + \Delta V_d$$

where  $\Delta V_d$  is the average consolidation volume change at room temperature at a given consolidation pressure. This equation, unlike equation [6.22], is a more complete application of Kosar's equation [6.21] which considers volume changes due to changes in temperature.

The following calculation is used to estimate  $\Delta V_d$ . As shown previously:

$$[6.26] \quad V_{cf} = V_{co} - \epsilon_v (1.037 + V_{co})$$

and knowing the NCL at 26°C from a regression of buffer data:

$$[6.27] \quad V_{cf} = 3.102 - 0.278 \cdot \log(p')$$

and knowing that  $V_{co} = 2.252$ ,  $V_o = 202$  cc for saturation,  $S = 1$ , and  $\gamma_d = 1.67$

Mg/m<sup>3</sup>, it can be shown from equation [6.25] and equation [6.27] that at room temperature:

$$[6.28] \quad \Delta V_d = 17.074 \cdot \log(p') - 52.204$$

where  $p'$  is in MPa. Equation [6.28] is substituted into equation [6.25] to calculate  $\beta_{st}$  using a forward calculation.

The values of  $\beta_{st}$  are shown for forward and back calculations in Figure 6.14 (a) and (b). Clearly the dependency of  $\beta_{st}$  on pressure has been essentially eliminated. The forward and back calculations agree for the 100°C data, but not for the 65°C data. Table 6.4 gives average values of  $\beta_{st}$  calculated for all the data. The skeletal thermal expansion coefficient is of the same order as the volumetric thermal expansion coefficient for bulk water, but of opposite sign. In a typical high density specimen, the volume ratio of water to solids is approximately 62%, assuming bulk water and saturated conditions. Therefore, according to equation [6.25], volumetric thermal compression of the skeleton represents a substantial portion of the measured volume change and is offset by thermal expansion of water at 100°C. The behavior at 65°C is more complicated.

**Table 6.4: Summary of thermal expansion coefficients for buffer  
(average values)**

Temperature (°C)	$\beta_{cw} \times 10^{-6}$ (1/°C)	$\beta_s \times 10^{-6}$ (1/°C)	$\beta_{st} \times 10^{-6}$ (1/°C)
65	923	39	-65
100	1162	39	-1572



### 6.3.4 Discussion of Thermal Expansion Calculations

The relatively simple calculations used in Methods 1 and 2 provide good predictions of thermal deformation at 65°C as shown in Figures 6.6 and 6.8. However the predictions for 100°C are not as good. The implication may be that the pore water has thermal expansion characteristics similar to bulk water up to 65°C, but more complex behavior at 100°C. The temperature dependent NCLs from measured final moisture contents have been used as a reference. It was shown in Chapter 5 in the summary graph, Figure 5.12 that on average, drained heating from 26 to 65°C and from 26°C to 100°C caused reductions in specific volume of 0.05 and 0.15, respectively.

Method 3 provided a detailed analysis of the thermal skeletal deformation. Equations [6.22] and [6.25] which were used to determine the skeletal thermal expansion coefficient,  $\beta_{st}$ , can also be interpreted in terms of thermo-elasto-plasticity which was discussed in Chapter 2.

The stress dependent elastic strain component,  $\epsilon_v^{se}$ , is derived in the following text. From equation [6.26] it can be shown that:

$$[6.29] \quad \epsilon_v = \left[ \frac{V_{co} - V_{cf}}{1.037 + V_{co}} \right] = \left[ \frac{\Delta V_c}{1.037 + V_{co}} \right]$$

and from elasto-plastic soil mechanics

$$[6.30] \quad \Delta V_c = \left[ \Gamma - \kappa \cdot \ln(p_1') \right] - \left[ \Gamma - \kappa \cdot \ln(p_2') \right] = \kappa \cdot \ln \left[ \frac{p_2'}{p_1'} \right]$$

Combining [6.29] and [6.30] gives

$$[6.31] \quad \epsilon_v^{se} = \frac{\kappa \cdot \ln \left[ \frac{p_2'}{p_1'} \right]}{1.037 + V_{co}}$$

Similarly for the stress dependent plastic volumetric strain:

$$[6.32] \quad \epsilon_v^{sp} = \frac{\lambda \cdot \ln \left[ \frac{p_2'}{p_1'} \right]}{1.037 + V_{co}}$$

Combining [6.31] and [6.32]

$$[6.33] \quad \left[ \epsilon_v^{se} + \epsilon_v^{sp} \right] = \left[ \lambda + \kappa \right] \cdot \left[ \frac{\ln \left[ \frac{p_2'}{p_1'} \right]}{1.037 + V_{co}} \right]$$

The thermo-elastic strain component,  $\epsilon_v^{te}$ , is defined using Mitchell's parameters.

This is described in detail in Appendix G:

$$[6.34] \quad \Delta V^{te} = \beta_w V_w \Delta T - \beta_s (V_t - V_s) \Delta T$$

from which

$$[6.35] \quad \epsilon_v^{te} = \frac{\Delta V^{te}}{V_o} = \frac{1}{V_o} \left[ \beta_w V_w \Delta T - \beta_s (V_t - V_s) \Delta T \right]$$

The thermo-plastic strain component,  $\epsilon_v^{tp}$ , is also defined using Mitchell's parameters in terms of the thermally induced particle movements (skeletal deformation)

$$[6.36] \quad \epsilon_v^{tp} = \frac{\Delta V^{tp}}{V_o} = \frac{1}{V_o} \left[ -\beta_{st} V_t \Delta T \right]$$

The thermo-elasto-plastic strain component,  $(\epsilon_v^{te} + \epsilon_v^{tp})$  is:

$$[6.37] \quad \left[ \epsilon_v^{te} + \epsilon_v^{tp} \right] = \frac{1}{V_o} \left[ \beta_w V_w \Delta T - \beta_s (V_t - V_s) \Delta T - \beta_{st} V_t \Delta T \right]$$

Combining equations [6.33] and [6.37] gives the following:

$$[6.38] \quad \left[ \epsilon_v^{se} + \epsilon_v^{sp} \right] + \left[ \epsilon_v^{te} + \epsilon_v^{tp} \right] = \left[ \lambda + \kappa \right] \cdot \left[ \frac{\ln \left[ \frac{p_2'}{p_1'} \right]}{1.037 + V_{co}} \right] + \frac{1}{V_o} \left[ \beta_w V_w \Delta T - \beta_s (V_t - V_s) \Delta T - \beta_{st} V_t \Delta T \right]$$

To the author's knowledge, equation [6.38] is a new simple approach to defining thermo-mechanical strains, and does not appear in literature. Here the author is using strain behavior of the clay to form part of a macroscopic model which will be

discussed in chapter 8. Hueckel and Pellegrini (1991) describe strains in a more complex way using plastic potentials, yield functions, and advanced mathematics. They build their thermo-mechanical model using Cam clay, thermoplasticity theory for the soil skeleton, and non-linear thermoelasticity for the pore water pressure response. They then use their model to predict strains and pore pressures during undrained heating of clay. The general effects of temperature on strains and stresses in their model appears consistent with the concepts used in this model. Figure 6.15 shows the components of equation [6.38] graphically. Thermo-elastic strains are defined in terms of a heating/cooling cycle.

In practice, due to the type of data in the current test program, a variation of this equation has been used for data analysis as discussed in Appendix G. The concepts of component strains are idealized in Figure 6.15. Deformation due to heating is essentially complete after 24 hours (path 1-2). Mechanical deformation continues for 2 to 3 weeks (path 2-3). In reality, the specimen consolidation follows a non-linear path between 1-2'-3 and 1-2-3. A controlled path using pressure and temperature ramping is currently being investigated by others (Graham *et al* 1992). A stress path similar to 1-2'-3 has been investigated by Yarechewski (1993). A program comprising ramped temperature tests in addition to the current test program would be required to verify equation [6.38].

There is still some controversy in the scientific community regarding the types of water present, its structure in the various phases, its density and coefficient of thermal expansion. In spite of these uncertainties, some observations can be made from current test results and results from previous research. It would appear that most of the volume change observed in dense Na-montmorillonite ( $1.67 \text{ Mg/m}^3$  dry density) during heating is associated with expulsion of 1 or 2 hydrate layers from interlamellar water to interstices at temperatures up to  $100^\circ\text{C}$  due to thermal expansion of the surface water. It is

likely that the expelled water also undergoes thermal expansion. The net result is collapse of the water 'shell' (interlamellar spacing) , increase in the pore size and increased hydraulic conductivity. Above 100°C Stern water (surface water) and structural water become involved in the process of dehydration.

The discussion above relates to drained conditions during heating. According to Pusch (1990) the interlamellar spacing increases during undrained heating as pore water is forced by osmotic potentials into the interlamellar regions.

Montmorillonite-water systems at medium to high densities are probably dominated by surface and interlamellar water (Baldi *et al* 1990a). Surface water is defined here as the first two molecular layers of water on the clay particle.

#### 6.4 Membrane Diffusion

In order to assess the true volume change of buffer specimens due to expulsion of water, it was necessary to estimate the amount of diffusion of oil and/or water across the silicone membranes (polymeric elastomer). Experimental details were given in sections 3.2.4 and 3.5.4. The first approach was to set up a triaxial environment similar to the actual test pressure and temperature conditions using a flat coupon of silicone membrane with a surface area of about 20 cm<sup>2</sup>. This produced ambiguous results because the apparatus was limited by the accuracy of the equipment used to measure diffusion rates across the small coupon area. The second approach was to test with brass dummy specimen and membrane identical in size and configuration to actual buffer triaxial specimens. The latter tests were performed by Yarechewski and will be included in his thesis (Yarechewski 1993). The tests produced net diffusion rates of 0.16 to 0.60 ml/day inward towards the specimen. A third approach was a simple theoretical prediction of outward diffusion of specimen water. This provided a relative basis of comparison for assessing the need for

corrections to specimen volume changes.

#### 6.4.1 Theory and Calculations

The following is a discussion of the third approach. Basic theory and a more complete discussion of diffusion is given in Appendix H. Eight factors influencing diffusion are considered, but calculations include only the most important factors (the first, fifth, and seventh factors). These factors are: (1) driving potential of vapour pressures on either side of the membrane; (2) the effect of temperature; and (3) thickness of the membrane. It should be appreciated that the diffusion process is a complicated one, and the presence of not one, but two diffusants (water and silicone oil) adds complexity. Simplifying assumptions were made as necessary without invalidating the prediction.

Consider a simple system where only water diffuses through a silicone rubber membrane from the void spaces of the specimen towards the silicone oil used as cell fluid. The water is adsorbed on the inner surface and diffuses through the membrane as vapour and is desorbed on the outer surface in a condensed form (H. Gesser, personal communication). The driving potential is provided by differential vapour pressures across the membrane. Vapour pressure on the inside varies with temperature, applied back pressure, and solution chemistry, but is independent of applied effective stress. Values of vapour pressure are given at standard temperature (0°C) and pressure (75 cm Hg) (STP) up to 1 atm. by Perry *et al.*(1984).

For systems where gas diffuses through a membrane, the vapour pressure on each side is often known but the concentrations are not known. If there is a linear relationship between the external vapour pressure and the corresponding concentration just within the surface of the sheet (i.e. the sorption isotherm is linear) then:

$$[6.39] \quad C = S \cdot p$$

where  $C$  is the concentration of the diffusing substance (g diffusant/ml polymer),  $S$  is the solubility coefficient of the membrane with diffusant, and  $p$  is the driving vapour pressure (cm Hg). It can be shown that

$$[6.40] \quad F = P_r \cdot \frac{dp}{dx}$$

where  $F$  is the rate of diffusion (flow rate) per unit area,  $P_r$  is the permeability, and  $x$  is the space coordinate measured normal to the section from which:

$$[6.41] \quad P_r = D \cdot S \left[ \frac{\text{cc gas (STP) cm (thick)}}{\text{cm}^2(\text{memb}) \cdot \text{sec} \cdot \text{cm Hg} (\Delta p)} \right]$$

$P_r$  is the permeability in units given here as  $\text{cm}^2/(\text{sec} \cdot \text{cm Hg})$ ,  $D$  is the diffusion coefficient ( $\text{cm}^2/\text{sec}$ ) and  $S$  is the solubility coefficient ( $\text{ml(RTP)}/\text{ml} \cdot \text{cm Hg}$ ), RTP is room temperature and pressure, and STP is standard temperature and pressure. It is important to distinguish the vapour pressure,  $p$ , from the ambient pressure in the liquid phase. Clearly, the rate of diffusion is a function of diffusivity and solubility.

The rate of diffusion is calculated by using published values of  $P_r$  as follows:

$$[6.42] \quad Q = 75 P_r \cdot \frac{dp}{dx} \cdot A$$

where  $Q$  is the flow rate of vapour (ml/day) for silicone rubber and water vapour as diffusant,  $dp/dx$  is the water vapour pressure gradient across the membrane; and  $A$  is the area of the membrane. The constant 75 is used to convert units of cm Hg. to units of atm. The ideal gas law is used to calculate the volume of liquid equivalent to the volume of water vapour calculated from equation 6.42. The liquid values are reported in Table 6.5.

The membranes used in this program are polydimethylsiloxane. With 25% silica filler, the published permeability to water vapour of this type of polymer is  $3600 \times 10^{-9} \text{ cm}/(\text{sec} \cdot \text{cm Hg})$  at RTP (Robb 1965). Crank and Park (1968) give values of  $4300 \times 10^{-9}$  at  $35^\circ\text{C}$ , and  $3280 \times 10^{-9}$  at  $65^\circ\text{C}$  at STP. kPa.). Using  $P_r = 3600 \times 10^{-9}$ , the diffusion of water (liquid) over a period of one month was 0.007

ml at 26°C (vapour pressure = 0.0332 atm.); 0.34 ml at 65°C (vapour pressure = 0.247 atm.); and 5.04 ml at 100°C (vapour pressure = 1.0 atm.). The diffusion of water increases by 3 orders of magnitude by increasing the temperature from 26°C to 100°C.

The effect of back pressure on the vapour pressure of pore water at the surface of a specimen is small compared to temperature effects. The Clausius-Clapeyron equation (Mortimer 1975) shows that a pressure increase in the liquid phase causes a pressure increase in the vapour phase. Equation 6.40 therefore implies that the diffusion rate also increases. For the current study, the Clausius-Clapeyron equation in Appendix H (equation H2) is used to account for the effect of back pressure of 1.0 MPa (10 atm). The vapour pressure,  $p$ , increased 2.5% at 26°C and increased 17.4% at 100°C. Therefore, the diffusion rates also increase by these amounts. Note that the theory used here assumes vapour pressure of the silicone oil does not influence vapour pressure of the pore water. This is consistent with Dalton's law of ideal gases. Mixture theory of gases indicates that this may be a second order effect.

#### 6.4.2 Measured Diffusion

We will now examine data from the laboratory tests described in Chapter 5. A high pressure triaxial consolidation cell was modified to measure diffusion in an environment equivalent to the buffer triaxial test. A full sized dummy specimen was used. An oil-membrane-water interface was provided with a confining stress on the outside and a constant back pressure of 1.0 MPa on the inside. The following results in Table 6.5 for two temperatures were obtained by Yarechewski (unpublished). The data are also shown in Figure 6.16. Theoretical rates of water diffusion and measured net diffusion rates are plotted with the same sign for comparison purposes.

**Table 6.5:** Diffusion rates (tangent) of silicone oil and water across silicone membranes (Yarechewski unpublished). The system is oil-membrane-water. One membrane (polydimethylsiloxane) 1.2 mm thick was used for all the results reported. The nominal surface area of the membrane was 178 cm<sup>2</sup>.

Temp. T(°C)	Effective Stress p'(MPa)	Meas.Flux <sup>1</sup> Net <sup>3</sup> (ml/day)	Predicted Flux <sup>2</sup> Water (ml/day)	Comments
26	0.6	0.08	-0.017	Steady state
26	1.5	0.22	"	Average
26	3.0	0.26	"	duration
26	6.0	0.30	"	3 days
26	9.0	0.30	"	
65	0.6	0.16	-0.922	
65	1.5	0.40	"	
65	3.0	0.60	"	
100	-	-	-14.70	

NOTE: 1. Positive strains are compressive. This implies net diffusion towards the inside of the membrane. Net diffusion includes oil and water  
 2. For water only; oil diffusion not included.  
 3. Net flux is measured as the tangent to the graph of volume change versus time.

It is evident from the measured diffusion rates that the process of diffusion is pressure and temperature dependent. There appears to be a logarithmic relationship between the net diffusion rate of water and oil, and ambient pressure pore water. A logarithmic curve has been fitted to the measured data in Figure 6.16. This is considerably different than theory predicts for the relationship between diffusion rate of water and ambient pressure in the water. The relationship of diffusion with temperature is not entirely clear because only two temperatures are reported. On average, the net diffusion rate from the experiments may be expressed as:

$$[6.43] \quad \dot{\epsilon}_v^{PT} = (0.2963 + 0.2727 \cdot \ln p') \left[ \frac{\Delta T}{39} \cdot \frac{1}{2} \right] \quad ; 26^\circ\text{C} < T < 65^\circ\text{C} \quad ; R^2 = 0.9996$$



where  $p'$  is in MPa and  $\Delta T$  is in  $^{\circ}\text{C}$ .

A comparison of observed and theoretical predictions of diffusion are made in the following concluding remarks. The observed net diffusion rate in our diffusion apparatus using the dummy specimen was 0.16 to 0.60 ml/day inwards towards the specimen at  $65^{\circ}\text{C}$  for effective stresses from 0.6 to 3.0 MPa, respectively. This equals an apparent volume change of 5 to 18 ml (2.5% to 9.0%) in one month. Diffusion of oil in towards the specimen and diffusion of water outward towards the cell fluid can not be separated in these tests. Theory predicts an outwards diffusion rate of water of  $-0.922$  ml/day at  $65^{\circ}\text{C}$ , independent of effective stress. Theory can not be used to predict the diffusion of oil inward because the permeability,  $P_r$ , of the rubber to silicone oil is not known and cannot be measured using equipment from the current test program.

The observed net inwards diffusion rate at  $26^{\circ}\text{C}$  was 0.08 to 0.24 ml/day at effective stresses of 0.6 to 3.0 MPa, respectively. Theory could only be used to predict diffusion rate of water, and a value of  $-0.92$  ml/day (outward) was obtained.

The measured diffusion rates are for net diffusion and offer no insight into the relative diffusion rates of water and oil, or interaction between the fluids. However, if the predicted diffusion rate of water is assumed correct, then the cross diffusion of oil toward the specimen must be of the same order of magnitude as the outward diffusion of water. This can be shown from Table 6.5 in which the measured net flux of fluids must equal the sum of the predicted flux of water and the unknown flux of oil. Predictions above  $65^{\circ}\text{C}$  appear to be an order of magnitude too high. Triaxial tests on buffer specimens show much smaller volume strain rates at  $100^{\circ}\text{C}$ . It is believed that actual diffusion rates of water at  $100^{\circ}\text{C}$  are approximately an order of magnitude less than those summarized in Table 6.5.

The measured net diffusion rate at steady state is of the same order as the end-of-consolidation strain rate criterion assumed to be 0.1% per day. The observed diffusion rates reached steady state in 3 days, which is much longer time than theory would suggest for water vapour diffusion. In actual buffer tests two membranes are used, and therefore diffusion rates should take much longer to reach steady state than indicated here.

The theory and assumptions in the previous paragraphs account for the effects of changes in back pressure, but not effective stress across the membrane. Robb (1965) reported permeability to  $\text{CO}_2$  is constant within  $\pm 10\%$  for changes in differential pressure from 0.2 to 500 psi (1.4 to 3500 kPa). Similarly, it is possible that changes in effective stress produce only small changes in permeability of the membranes to water vapour.

As stated earlier, the most important factors have been used to predict diffusion of water through the membranes. Two other factors, not discussed in Appendix H, may be of some importance, but are difficult to quantify: (1) affinity of silicone for water; and (2) affinity of buffer for silicone oil. The second of these factors was examined in section 5.3.5 and 6.2.2 in terms of mass balance, but has not been examined in terms of partial pressures.

Earlier, three chemistry based approaches to obtaining diffusion rates of the oil-membrane-water system were discussed. A fourth approach would be to cover a container of water with a membrane leaving an air space for vapour pressure to equilibrate and place it in a desiccator or drying chamber. The weight of the container could be recorded with time to give the diffusion rate. In a second container silicone oil could be placed on top of a membrane covering the same amount of air and water. Comparing results, the relative influence of the silicone oil on net diffusion could be determined. This would involve considerably more work and has not yet been undertaken.

## 6.5 Side Drain Restraint and Membrane Modulus

### 6.5.1 Side Drain Restraint

The use of full length geotextile side drain strips in a spiral arrangement as shown in Figure 3.23 with ends overlapping the porous stones at each end of the buffer specimen does not directly affect the strength of the buffer specimens. Figure 6.17 shows peak and end-of-test data at 65°C for specimens with full length side drainage. Regressions using these data are essentially the same as for the whole data set which included tests with other drainage configurations. This implies that there is no significant effect of drainage configuration on the observed strengths of specimens in the current program. The side drain length had no effect on the strength of specimens tested at 26°C. It is possible that strength was indirectly affected to a small extent by impeded drainage. The partial length drains apparently are not as efficient at transporting pore water to or from the specimens as the full length drains. The result is that swelling, for instance, takes longer with the partial length drains.

### 6.5.2 Membrane Modulus

The membrane modulus relative to the specimen modulus can be an important consideration in analysis of test data at large strains ( $\epsilon_1 > 15\%$ ) and for thick membranes ( $t > 2$  mm). The modulus of elasticity of membranes increases nonlinearly with membrane thickness. The relationship is complicated because the membrane acts (1) in a compressive shell mode when specimen axial strain is small (1%) and (2) in a hoop stress mode when specimen axial strains are large. In addition, the membrane thickness changes with specimen axial strain. ASTM D4767-1988 outlines a test method for determining the Extension modulus of membranes. This is equivalent to Young's modulus.

In the current test program as discussed in Chapter 5, the membrane influence is small ( $<5\% q_{peak}$ ). Calculations of the extension modulus for silicone membranes are contained in Appendix A. Young's modulus for buffer specimens, membranes and the rubber dummy specimens (Chapter 5) are compared in Table 6.6. Clearly, the buffer specimens in the current program are an order of magnitude stiffer than the membranes. It will be shown that the psuedo-elastic moduli (first loading) of buffer increases with temperature. The modulus of the membranes decreases when temperature increases. Therefore the effect of elevated temperature is to reduce the influence of membrane modulus on specimen strength.

**Table 6.6: Comparison of Young's modulus for buffer, membranes and rubber dummy specimens**

Item	$\gamma_d$ (Mg/m <sup>3</sup> )	$E_{50}$ (MPa)	Comments
Buffer spec.	1.67	65.7	$p'_c=3.0$ MPa (Oswell 1991)
RTV 5050 Memb.	-	2.0	current program
RTV 5026 Memb.	-	1.3	"
Rubber Dummy	-	2.8	"

NOTE: 1.  $E_{50}$  refers to tangent modulus at 50% of peak strength. This criterion not applicable to rubber. Extension tests were used to determine Young's modulus for the membranes.

2.  $E_{50} = 3G_{50}$  for undrained conditions.

## CHAPTER 7.0 SYNTHESIS OF DATA

### 7.1 Introduction

Chapter 6.0 discussed the parameters which influence the data presented earlier in Chapter 5. This chapter synthesizes the data from Chapter 5, and interprets them in terms of pore water pressure parameters and critical state behavior with particular attention being given to the additional variable of temperature. Critical state behavior of a pelagic clay, tested by Green (1984) at low effective stress and elevated temperature (4°C, 40°C, 100°C, and 200°C), is compared with measured results for buffer. Green's pelagic clay data have not previously been interpreted using critical state concepts.

### 7.2 Pore Pressure Parameters

This section discusses the pore water pressure response of buffer at different temperatures in terms of the pore pressure parameters ( $a$ ,  $b$ ,  $m$ ,  $n$ ,  $A$ ,  $n^*$ ) and two different constitutive models: (1) an empirical curve fitted model based loosely on elasto-plastic theory and (2) a linear anisotropic elastic model. The traditional definitions for pore pressure parameters are discussed in this section and a new pore pressure parameter,  $n^*$  is defined and discussed in relation to the classical parameters.

#### 7.2.1 Definition of Parameters

Two related pore pressure parameters,  $m$  and  $n$  are defined as follows:

$$[7.1] \quad m = \Delta u / \Delta p$$

$$[7.2] \quad n = -\Delta p' / \Delta q$$

where, in general, pore water changes are produced by changes in both mean total stress  $\Delta p$  and deviator stress  $\Delta q$ . These definitions are not new. They are similar to the classical pore pressure parameters, 'B' and 'A', described by Skempton (1954), Lambe and Whitman (1969), [7.2a] and referred to as 'b' and 'a' by Wood (1990) [7.2b]

$$[7.2a] \quad \Delta u = B \left[ \Delta \sigma_3 + A(\Delta \sigma_1 - \Delta \sigma_3) \right]$$

$$[7.2b] \quad \Delta u = b \left[ \delta p + a \delta q \right]$$

In triaxial tests,  $\Delta \sigma_3 = \Delta p$ , and  $\Delta q = (\Delta \sigma_1 - \Delta \sigma_3)$ , so rearranging [7.2a] gives

$$[7.2c] \quad \Delta u = B \left[ \Delta p + \left[ \frac{3A-1}{3} \right] \Delta q \right]$$

The parameter  $m$  is equal to  $b$  (and  $B$ ), and parameter  $n$  is equal to  $-a$  (and  $-A$ ) for two special cases: (1)  $\Delta \sigma_1 = \Delta \sigma_3$ , isotropic consolidation, and (2)  $\Delta \sigma_3 = 0$  and  $B = 1$ , in standard CIU and CID triaxial shear. Four definitions of  $a$  from current literature (Wood 1990) will be discussed in the following section. From now on, parameter  $A$  will be used to refer to the classical shear dilatancy parameter (Skempton 1954):

$$[7.3] \quad A = \Delta u / \Delta q = \Delta u / \Delta \sigma_1$$

Equation [7.3] is applicable to standard CIU and CID triaxial shear tests where  $\Delta \sigma_3 = 0$  and  $B = 1$ . The parameters are mostly not constant, but depend on combinations of stress level, strain level and fabric. The subscripts Y, F, CS refer respectively to the specimen stress states at Yield, Failure and Critical State.

## 7.2.2 Graphical and Physical interpretation

Figures 7.1 (a) and (b) shows graphical interpretations of  $m$  and  $n$ . In Figure 7.1 (a), elastic isotropic undrained (EIU) behavior is shown by a slope of  $m$

= 1. An  $m$ -value greater than 1.0 in Figure 7.1 (a) indicates elastic anisotropic undrained (EAU) behavior in which the horizontal stiffness is greater than the vertical stiffness (Graham and Houlsby 1983). A typical stress path for an anisotropic compressive specimen is shown schematically by line 0-1-2-3. Yielding occurs at point 1, which ends the linear portion of the path. The slope  $m$  of the linear portion is characteristic of initial elastic behavior in most specimens. After this point, there is a distinct change in slope of the path and significant shear deformations and pore pressures develop in the specimen as it moves towards peak strength (failure). Point 2 represents stresses at peak strength. The specimen may move on to a different point 3 at critical state.

The pore pressure changes at yield stress were interpreted graphically from figures such as Figure 5.20 and 5.23 in Chapter 5. These figures show specimens consolidated to similar effective stresses. In general, specimens consolidated at higher temperatures generated larger excess pore pressures during shear. Pore pressure changes at peak stress and critical state are more precise than those at yield because they were interpreted from spreadsheets of the measured data.

Line 0-4-5-6 in Figure 7.1 (a) shows a typical stress path for an anisotropic dilative specimen. Yielding occurs at point 4, peak failure at point 5 and critical state at point 6. These are identified by distinct changes in slope of the stress path. Values of  $m$  for compressive and dilative specimens are usually similar. No obvious changes in slope of  $\Delta u$  versus  $\Delta p$  diagrams can be used to identify peak stress in dilative specimens. These graphical techniques are not applicable to specimens which develop distinct shear planes because it is not possible to measure pore pressures at the shear zone with standard tests. In these cases, the pore pressure in the shear zone is different than the average pore pressure in the specimen.

Values of  $m$  vary with temperature and stress level. Values of  $m$  were previously reported by Graham *et al.* 1989, 1990, 1991. A synthesis of these data in Figure 7.2 shows linear variation of  $m$  with consolidation pressure,  $p'_{\text{cons}}$  and decreasing  $m$  values with increased temperature. A tendency towards more isotropic behavior ( $m \approx 1.0$ ) is apparent at elevated temperature. Data from low and high density specimens from Saadat (1989) are also shown for 26°C. Linear regressions are used for comparing the data, but are tentative for the 65°C data because of scatter. Figure 7.3 shows  $m$  plotted against volumetric strains at the end of consolidation. Compressive specimens have higher  $m$  values which show more strongly anisotropic behavior. Swelling specimens show more isotropic behavior.

In general,  $n$  is inversely proportional to the slope (cotangent) of the line joining the beginning of shear to the failure point. Figure 7.1 (b) shows the same specimens discussed in Figure 7.1 (a), but now shown in  $q$ - $p'$  stress space. Path 0-1-2-3 again represents a compressive specimen. A dilative specimen is shown by path 0-4-5-6. Yielding occurs at point 4, peak stress at point 5 and critical state at point 6. The initial slope of these lines 0-1 and 0-4 are similar and are typical of both compressive and dilative anisotropic specimens. A vertical line would represent an isotropic elastic stress path, indicated earlier by  $m = 1$ . The parameter  $n = -\delta p' / \delta q$  is only defined for test stages after yielding. It may be thought of as a measure of the pore pressures generated during shear, and shear-induced anisotropy. Thus, in contrast with  $m$ ,  $n$  is stress path and test type dependent. It will be shown later that values of  $n$  at peak and critical state depend on temperature and stress level.

The value of ' $n$ ' is referenced to the isotropic elastic state by setting  $n=0$  on a vertical line in  $q$ - $p'$  space. That is, changes in  $n$  measure changes in the slope  $-\delta q / \delta p'$  to the vertical. Figure 7.4 (a) shows the variation in  $\Delta p'$  in  $q$ - $p'$



stress space for a dilative anisotropic undrained specimen. Figure 7.4 (b) shows the variation in  $\Delta u$  in  $q$ - $p'$  stress space for a specimen. A new parameter  $n^*$  will be defined later which is referenced to the initial slopes of these effective stress paths.

Values of  $n$  vary with temperature and stress level in a non-linear way. Figure 7.5 shows  $n_Y$  versus  $p'_{cons}$ . A graphical description of  $n_Y$  is shown by the inset figure. The value of  $n_Y$  is not strongly stress dependent, but there is temperature dependence. This means the material elasticity is temperature dependent. At low pressures and higher temperatures the buffer is more isotropic ( $n=0$ ). Figure 7.6 shows  $n_f$  versus  $p'_{cons}$ . A graphical description of  $n_f$  is shown by the inset figure. The value of  $n_f$  is strongly stress level dependent and slightly temperature dependent. The regression lines show a reversal in temperature dependent effect at approximately 2.5 MPa effective stress. This is close to the swelling equilibrium pressure of buffer at a dry density  $\gamma_d = 1.67 \text{ Mg/m}^3$ .

Figure 7.7 shows values of  $A_f (= \Delta u_f / \Delta q_f \text{ at peak stress})$  plotted against consolidation pressure,  $p'_{cons}$ . These values have been reported previously (Graham *et al.* 1989, 1990). The dependency of  $A_f$  on stress level is strong. Regression lines for each test temperature are shown as solid lines. These are approximate at high effective stresses. Logarithmic relationships seemed to fit the data best. The regressions were good for most temperatures. Some scatter is present in the 65°C and 100°C data, but it is much less than in Saadat's 26°C data. Temperature dependency is slight. A change in temperature dependent behavior occurs at a consolidation pressure of approximately 2.5 MPa. Below this pressure, higher temperature produces higher  $A_f$ . Above this pressure, the relationship is reversed. Regression lines for Saadat's low density and high density specimens are shown in

dashed lines for comparison . As expected, his high density data fit the current data better than do his low density data.

Figure 7.8 shows values of  $A_f$  against volumetric strain,  $\epsilon_v$ , at the end-of-consolidation (EOC). Swelling specimens have  $A_f$  values lower than those measured in compressive specimens. Similar findings were reported by Wan (1987) and Saadat (1989). Regressions are shown for Saadat's data at 26°C, but his data had more scatter than the current data. Tentative interpretation of temperature effects are shown by the fitted lines for 26°C, 65°C and 100°C. The trend is towards lower  $A_f$  values in compressive specimens at elevated temperatures.

Figure 7.9 shows values of  $A_{cot}$  versus consolidation pressure. An envelope is drawn to generalize the behavior. No systematic behavior is observed with respect to temperature. Figure 7.10 shows the same envelope, but now with data points corresponding to peak failure. Clearly, the individual test data at peak and critical state are different. However, the general trend for all the data is the same for both peak failure and critical states.

Figure 7.11 shows  $A_{cot}$  versus  $\epsilon_v$ . Bounding lines indicate general behavior. Once again, swelling specimens show lower A-values.

At failure, normally consolidated soils have positive a-values, close to unity. Overconsolidated soils have smaller, or indeed negative a-values. Large values of 'a' indicate a strong anisotropy. During plastic deformation, 'a' describes the pore pressures generated from the soil's tendency towards plastic shear deformation.

### 7.2.3 Pore Pressure Equation (Curve Fit Model)

The pore pressure results presented in previous sections have been described in terms of empirical relationships. These relationships may be used

informally in a type of curve-fit model which is loosely based on elasto-plastic theory. A pore pressure equation can be written in various ways, but the following equation is used here:

$$[7.4] \quad \Delta u = \Delta u^e + \Delta u^p$$

where  $\Delta u^e$  and  $\Delta u^p$  are the excess pore pressures due to elastic and plastic strains, respectively. They are defined as follows:

$$[7.5] \quad \Delta u^e = m\Delta p$$

$$[7.6] \quad \Delta u^p = n\Delta q$$

Wood (1990) developed an expression for  $n$ , at failure, from elasto-plasticity, but he called it  $a_f$ .

$$[7.7] \quad a_f = \frac{\left[ \frac{n_p}{r} \right]^{-\Lambda} - 1}{M}$$

where  $n_p$  is the isotropic over-consolidation ratio as shown in Figure 7.12. Parameter  $r$  is the distance between the NCL and CSL in  $V_c - \ln(p')$  compression space along an unload-reload line. The value  $r$  defines the separation of the normal consolidation line (NCL) and critical state line (CSL) along an unload-reload line (URL) in  $V_c - \ln(p')$  space as shown in Figure 7.12

$$[7.8] \quad r = \frac{p'_c}{p'_{cs}}$$

The parameters  $a_f$ ,  $M$ , and  $\Lambda$  are measured from the current test program for buffer. Therefore, it is possible to determine  $n_p$  and  $r$  using an appropriate assumption.

The parameters are defined as follows:

$$[7.9] \quad n_p = \frac{p'_c}{p'_i}$$

This  $n_p$  is not the same as the pore pressure parameter  $n$  described earlier. The preconsolidation pressure,  $p'_c$ , is different than the consolidation pressure  $p'_{cons}$ .

Here  $p'_i$  is equal to  $p'_{cons}$ . It is not known *a priori* if  $p'_{cons}$  equals the swelling equilibrium pressure,  $p'_s$ . This issue will be addressed later. The hardening parameter,  $\Lambda$ , is defined as

$$[7.10] \quad \Lambda = \frac{\lambda - \kappa}{\lambda}$$

and  $M$  is the slope of the critical state line in  $q$ - $p'$  stress space. For normally consolidated specimens,  $a_f$  reduces to:

$$[7.11] \quad a_f = \frac{\left(\frac{1}{r}\right)^{-\Lambda} - 1}{M}$$

From Oswell (1991) and Saadat (1989),  $\lambda = 0.084$  and  $\kappa = 0.022$ . Therefore,  $\Lambda = 0.74$ . An average value of  $M$  from the current program is 0.5. For dense buffer ( $\gamma_d = 1.67 \text{ Mg/m}^3$ ), Equation [7.11] then becomes:

$$[7.12] \quad a_f = \frac{\left(\frac{1}{r}\right)^{-0.74} - 1}{2}$$

Predictions for values of  $a_f$  have been calculated using  $r$  values of 2.0 and 1.5 and are shown in Table 7.1. The value of  $r = 2.0$  comes from assuming an elliptical yield locus as for example, would be done in the Cam clay model. The value of  $r = 1.5$  has been determined from Oswell's data. Since  $M$ -values vary with preconsolidation pressure, a group of Oswell's tests with similar preconsolidation pressures (between 1.5 and 2.0 MPa) were selected. These had yield stress ratios,  $q_Y/p'_Y$  of 0.45 to 0.65, and  $r$  values between 1.28 and 2.14. The average  $r$ -value was 1.57 and average ' $M$ ' was 0.53. Among this group of tests, four had yield stress ratios of 0.55. The average ' $M$ ' from the four tests was 0.62 and the average  $r$  was 1.52. Clearly, this implies a non-elliptical yield locus similar to that described by Oswell (1991), though the basic ideas of Cam clay modeling will still hold.

**Table 7.1: Comparison of values for  $n_f$  and  $a_f$**

	$n_p$	$p'_{Cons}$ (MPa)	$q_y/p'_y$	$M$	$\Lambda$	$r$	$a_f = -n_f$	Comments
<u>Calculated</u>								
Equation 7.7	1.0	-	-	0.62	0.74	2.0	1.08	Ellipse
"	1.0	-	-	0.62	0.74	1.5	0.56	Non-Ellipse
"	1.5	-	-	0.62	0.74	1.5	0.0	Non-Ellipse
<u>Measured</u>								
Oswell (1991)	-	1.54	0.53	0.62	-	1.52	-	avg 4 tests
Figure 7.6 ( $n_f$ )	-	1.54	-	-	-	-	0.0	26°C

Table 7.1 shows that the assumption of  $n_p=1$  is wrong for both elliptical and non-elliptical yield loci, because  $n_f$  calculated from equation 7.2 disagrees so strongly with the  $n_f$  from the current results. Note that an isotropic overconsolidation ratio,  $n_p$  of 1.5 gives the correct value of  $a_f$  for a preconsolidation pressure of 1.5 MPa. This suggests that for the current test program  $r \neq 1$ . In other words swelling equilibrium has not been reached and the hardening lines in Figure 5.12 do not correspond completely to swelling equilibrium.

A theoretical derivation for 'a' from the Cam clay elastic-plastic model has been described by Wood (1990):

$$[7.13] \quad a = \frac{2(\lambda - \kappa)\eta}{\lambda(M^2 + \eta^2) - 2(\lambda - \kappa)\eta^2}$$

Here Wood assumed an elliptical yield locus and a straight critical state envelope in  $q$ - $p'$  stress space. Equation [7.13] reduces to the following for critical state conditions, that is when  $\eta = M$ :

$$[7.14] \quad a = \frac{\lambda - \kappa}{\kappa M}$$

When values for  $\lambda$  and  $\kappa$  from the buffer are substituted into equation [7.14], values of  $a$  are obtained which are an order of magnitude larger than from Equation [7.7]. Clearly, one or more assumptions used in equation [7.13] such as an elliptical yield locus or a straight critical state line are invalid for buffer. As a result, equation [7.14] is not suitable for the current data.

#### 7.2.4 Pore Pressure Equation (Pseudo-Elastic Model)

A more rigorous model is available for the case of a linear anisotropic elastic material. A constitutive relationship was developed for a cross-anisotropic material by Graham and Houlsby (1983):

$$[7.15] \quad \begin{Bmatrix} \delta p' \\ \delta q \end{Bmatrix} = \begin{bmatrix} K^* & J \\ J & 3G^* \end{bmatrix} \begin{Bmatrix} \delta \epsilon_p \\ \delta \epsilon_q \end{Bmatrix}$$

which can be written in compliance form:

$$[7.16] \quad \begin{Bmatrix} \delta \epsilon_p \\ \delta \epsilon_q \end{Bmatrix} = \frac{1}{D} \begin{bmatrix} 3G^* & -J \\ -J & K^* \end{bmatrix} \begin{Bmatrix} \delta p' \\ \delta q \end{Bmatrix}$$

For an undrained test:

$$[7.17] \quad \delta \epsilon_p = 0 = \frac{1}{D} \left[ 3G^* \delta p' - J \delta q \right]$$

from which

$$[7.18] \quad \frac{\delta p'}{\delta q} = \frac{J}{3G^*}$$

where  $J$  is a cross coupling modulus between (1) deviatoric stress and volumetric strain and (2) mean stress and deviatoric strains (Graham and Houlsby 1983).  $G$  is the shear modulus. For isotropic elastic soil,  $a=J=0$ . It should be noted that ' $a$ ' is not a constant, but varies with plasticity, stress history, and elasticity (Atkinson and Bransby 1978). Equation 7.18 is similar to the definition of  $n$  originally described by equation 7.2, except for the change of sign. Therefore:

$$[7.19] \quad n = \frac{-\delta p'}{\delta q} = \frac{-J}{3G^*}$$

Oswell gives values for  $J$  and  $G^*$ . These are given in Table 7.2 with the calculated values of  $n_Y$  from equation [7.19], also called ' $a$ ' by Wood (1990).

**Table 7.2: Values of  $n_Y$  for isotropic and anisotropic elastic soils (after Oswell 1991)**

	Isotropic	Anisotropic
$J/p'_c$	-	10.1
$3G^*/p'_c$	21.9	23.4
$K^*/p'_c$	31.5	27.2
$n_Y$	0	0.43

Note: 1.  $G^*$  and  $K^*$  are modified shear and bulk moduli which contain an anisotropy parameter,  $\alpha$ . When  $\alpha$  is 1.0 then the modified moduli reduce to the classical shear and bulk moduli

The value of  $n_Y$  given by equation [7.19] is independent of preconsolidation pressure,  $p'_c$ , whereas the value of  $a_f$  given by equation [7.7] is pressure dependent. Clearly,  $n_Y$  and  $a_f$  by these definitions are not equivalent.

### 7.2.5 Pore Pressure Parameter $n^*$

Up until now the value of  $n$  has been referenced to the elastic isotropic undrained case where  $n = -\delta p'/\delta q = 0$ . We need a more general expression for  $n$ , and will use here the initial slope of the stress path in  $q$ - $p'$  stress space as the reference. Figure 7.13 (a) and (b) will be used to derive the expression. The reference line is  $O$ - $A$  in Figure 7.13 (a). The total stress path is  $O$ - $D$ . The specimen yields at  $Y$ , fails at  $C$  and reaches critical state at  $G$ . The change in pore pressure at failure,  $\Delta u_f$ , is  $C$ - $D$ . The distance  $A$ - $D$  represents the total pore pressure at failure,  $u_f$ , that is, the difference between a fictitious anisotropic elastic state at the failure stress and the total stress path. This may be written:

$$[7.20] \quad \overline{AD} = \Delta p_f \cdot m$$

where  $\overline{AD}$  represents distance  $A$  to  $D$  in Figure 7.13. The distance  $A$ - $B$  is obtained from Figure 7.13 (b). The distance  $E$ - $F$  represents the difference in pore pressure between anisotropic and isotropic states and may be written:

$$[7.21] \quad EF = (m-1)\Delta p$$

However, this also represents  $A$ - $B$  in Figure 7.13 (a). A new parameter  $n^*$  will be defined as follows:

$$[7.22] \quad n^* = \frac{-\overline{AC}}{\overline{OB}} = \frac{-\overline{AD} + \overline{CD}}{\overline{OB}}$$

This reduces to the following



$$[7.23] \quad n^* = A_f - m/3$$

This expression can also be derived algebraically from the pore pressure equations in [7.2] where:

$$[7.24] \quad n^* = \frac{\Delta u - m\Delta p}{\Delta q} = A - m/3$$

Equation [7.24] is a general equation for  $n^*$ . For the special case of  $m = 1$ , that is an isotropic specimen in which the behavior was such that  $n = -\Delta p'/\Delta q = 0$ .

$$[7.25] \quad n^* = a = -J/3G^*.$$

For the special case of  $m = 2$

$$[7.26] \quad n^* = a - 1/3 = -(J/3G^* + 1/3)$$

In compressive normally consolidated specimens  $A_f$  is approximately 1.0,  $m$  is approximately 1.5 and  $n^*$  is then 0.5. This is close to the value of  $n$  calculated from equation [7.25]. For lightly overconsolidated specimens,  $A_f$  is approximately 0.3,  $m$  is approximately 1.5 and  $n^*$  is then -0.2. This is close to the value of  $n$  for an isotropic material. Clearly,  $n^*$  described by equation [7.24] provides a link between a pseudo-elastic soil model, equation [7.16], and the pore pressure equation [7.2a].

### 7.2.6 Discussion

Pore pressure parameters have useful applications for instance, in determining yielding and long term settlement in embankments. Estimation of the settlement that accompanies the dissipation of excess pore pressures requires a measure of the soil stiffness to associate with the changes in effective stress. A plausible approach is that of Skempton and Bjerrum (1957). They propose that changes in total stresses should be calculated from an elastic analysis, and excess pore pressures should be calculated from the total stress changes using a pore pressure equation (Atkinson and Bransby 1978, Wood 1990)

$$[7.27] \quad \Delta u = b(\Delta p + a\Delta q)$$

There are two flaws in the logic of this approach. On the one hand, the pore pressure parameter  $a$  is not a soil constant. Its value depends on the stress history of the soil and the imposed stress changes. On the other hand, the settlement that occurs during dissipation of excess pore pressures is not the result of one-dimensional deformation of the soil, as would be implied for example by taking values of the compressibility,  $m_v$ , from oedometer tests (Wood 1990). An alternate approach is to use the Cam clay model to estimate the pore pressures that are generated when the soil is loaded without drainage. The advantage of this model is that it is not restricted to a single value of  $m_v$ . It can be used to estimate pore pressures and strains incrementally.

The current research has identified specific dependence of pore pressure parameters not only on current stress, and stress path, but also on temperature and stress history. More importantly, the elasticity of the buffer is temperature dependent. This is consistent with the additional compression with elevated temperatures presented in Chapter 5. Chapter 8 will show that the elastic moduli  $K$ ,  $G$  and  $E$  also change with temperature. The graphical techniques for determining 'm' in this chapter will be used in Chapter 8 to determine the yield stresses from undrained triaxial tests. This procedure gives information not normally available from undrained tests

### **7.3 Critical State Data**

#### **7.3.1 Buffer**

Critical state of a given specimen, as used in the simple elasto-plastic model, Cam clay, is the ultimate condition in which plastic shearing could continue without changes in volume or effective stresses (Wood 1990). This condition of

perfect plasticity can be expressed as:

$$[7.28] \quad \frac{\partial p'}{\partial \epsilon_s} = \frac{\partial q}{\partial \epsilon_s} = \frac{\partial v}{\partial \epsilon_s} = \frac{\partial u}{\partial \epsilon_s} = 0$$

Arrival at this condition may require very large strains. Conditions in triaxial tests may not permit sample uniformity to be retained to these large deformations, and critical states may not actually be attained (Wood 1990). Average values and standard deviations of the rates of change of mean stress, deviator stress, and pore water pressure measured at the end of the current tests are presented in Table 7.3:

**Table 7.3: Summary of critical state differentials**

		$\frac{\partial p'}{\partial \epsilon_s \cdot p'_{\text{cons}}}$	$\frac{\partial q}{\partial \epsilon_s \cdot p'_{\text{cons}}}$
Average	65°C	0.0083	0.0026
Std.Dev.	65°C	0.0061	0.0018
Average	100°C	0.0095	0.0059
Std.Dev.	100°C	0.0088	0.0032

The statistical analysis of the critical state differentials shows that the 65°C tests were closer to critical state conditions than the 100°C tests. The comparative differences were largest for normalized deviator stress, not pore pressure as might have been expected. This seems to indicate a weak link between strain softening and dissipation of excess pore pressures during undrained shear at elevated temperature. It must be remembered that these values are quite small. This indicates that the specimens have essentially reached critical state

conditions.

### 7.3.2 Synthesis of Other Research

This section discusses the consolidation and critical state behavior of pelagic clay tested by Green (1984) at 4°C, 20°C, 40°C, 100°C, and 200°C. Green tested two marine clays, a montmorillonitic-illitic clay (Glomar Samples) and illitic clay (Challenger samples) in undisturbed and disturbed states. Only her undisturbed test results for the illitic clay will be discussed here. The specimens she tested were 68% clay with a natural moisture content of 111% and Atterberg limits of  $w_L = 88\%$  and  $w_p = 41\%$ . Her triaxial data have been replotted here in a way that has not been done before.

Green performed undrained and drained triaxial tests at low effective stresses (29, 100 kPa) and high back pressures (1.0 MPa) to simulate deep marine conditions. Figure 7.14 (a) shows her critical state strengths in  $q$ - $p'$  stress space for undrained tests for five test temperatures. Linear regressions are shown only for the 4°C and 100°C results for comparison with buffer results. The regressions are as follows:

$$[7.29] \quad q_{cs}^{100^\circ\text{C}} = 11.285 + 1.354(p'); \quad R^2 = 0.9986$$

$$[7.30] \quad q_{cs}^{4^\circ\text{C}} = 4.490 + 1.233(p'); \quad R^2 = 0.9927$$

The clay has very high  $\phi'$  values, 33.5° at 100°C and 30.8° at 4°C. The  $\phi'$  values were calculated using the Cam clay model as follows:

$$[7.31] \quad \sin\phi' = 3M/(6+M)$$

The  $M$  values, 1.35 at 100°C and 1.23 at 4°C, are large compared to values of 0.5-0.65 usually encountered in buffer and most natural clays although high values like these have also been measured by Japanese researchers in tests on marine clays. At low effective stresses in triaxial stress space, clay strengths are

bounded by a 'zero tension cut-off' as described by the Cam clay model (Schofield and Wroth 1968). At these low stresses very high  $q/p'$  stress ratios can be obtained. This could explain Green's results. The main observation from Figure 7.14 is that temperature has a small, but measurable effect on the 'critical state envelope' of a natural marine clay. That is, the critical state line is higher for 100°C samples than 4°C samples. This has also been observed for buffer. At 200°C, Green's specimens show a unique behavior which may be related to thermal disturbance of the fabric or chemical bonds not seen at lower temperatures.

Figure 7.14 (b) shows the same test results from Figure 7.14 (a), but now plotted in specific volume versus log mean effective stress space. Regressions are shown for the 4°C and 100°C critical state data. These indicate reasonably unique lines for each temperature, though it appears that the lines are not parallel. Note however that the range of stresses (15 kPa - 50 kPa) is very low and may be affecting the results. Other work discussed in Chapter 2 (Tidfors and Sällfors 1989) suggests that parallel behavior could be expected. The buffer data presented in this thesis shows stronger parallelism of the critical state lines in  $V_c - \log(p')$  space. There is more scatter in Green's data than in the buffer data. Regressions for the normal consolidation lines for the tests are shown as dotted lines with the following equations:

$$[7.32] \quad V^{4^\circ\text{C}} = 4.211 - 0.626 \cdot \log(p'); R^2 = 0.8603$$

$$[7.33] \quad V^{100^\circ\text{C}} = 3.919 - 0.579 \cdot \log(p'); R^2 = 0.9412$$

The lines are almost parallel and have distinctly lower specific volumes at elevated temperatures. The slope of these normal consolidation lines is approximately parallel to the average slope of the critical state lines suggesting once more that the non-parallelism of the critical state lines is caused by scatter of the data, or low stresses, rather than some inherent property. The main

conclusion from this new examination of Green's data is that a critical state model modified to take account of temperature dependence is applicable to both a natural marine clay, and a sand-clay mixture such as buffer.

A slightly better regression for Green's critical state data in q-p' space is obtained using a power law fit. This is shown in Figure 7.15. As noted earlier, some of this curvature may represent the "zero tension" cut-off at low stresses. The regressions for the power law curves in Figure 7.15 are:

$$[7.34] \quad q_{cs}^{100^{\circ}\text{C}} = 3.327(p')^{0.821}; R^2 = 0.9953$$

$$[7.35] \quad q_{cs}^{4^{\circ}\text{C}} = 1.995(p')^{0.895}; R^2 = 0.9961$$

These are similar in principal to the curves shown for buffer in Figure 5.36.

Green plotted her test data in s-t space, where  $s' = (\sigma'_1 + \sigma'_3)/2$ ,  $t = (\sigma'_1 - \sigma'_3)/2$ . Figure 7.16 shows data from her Figure 17, replotted in the more useful q-p' stress space used throughout this thesis. She did not include all of the available data in the her figure. Linear critical state envelopes are shown in Figure 7.16 as solid lines with slope 'M'. Peak envelopes are shown as dotted lines with slope 'n'. Specimens at low temperatures consolidated to 29 kPa and 98 kPa respectively, behave like lightly overconsolidated strain-softening clay. However, at 100°C and 200°C, the samples strain soften in a way only seen in heavily overconsolidated clays. That is, higher temperatures led to increased brittleness, exhibited as more highly overconsolidated behavior. The specimens tested at 200°C had distinct failure planes, strain softened with further shearing, and developed large pore pressures due to a tendency to volumetric creep strains. Specimens tested at 100°C failed by bulging, did not strain soften and had smaller pore pressure build-up due to creep strains. The marked softening in this clay may represent a thermally sensitive collapse structure at low effective stresses. There is no evidence of this behavior in tests reported in earlier chapters and it

does not appear to apply to buffer. Green's specimens were tested with saline pore fluid. Perhaps the 200°C temperatures caused dissolution of existing cementation or formation of new bonds in the presence of salts. These specimens are the only ones seen in the literature which were tested at elevated temperature with a saline pore fluid.

Green also investigated the effects of cooling the specimens. The specimens were initially consolidated to an effective stress of 98.1 kPa and a temperature of 200°C. Following consolidation, the specimen was cooled to 100°C, allowing drainage after the temperature had stabilized. This produced a decrease in the rate of secondary compression and essentially no change in the volumetric strain from that already achieved prior to the cooling. The peak strength was typical for 200°C specimens at comparable effective stress. In the cycled (heated, then cooled) specimens, strain softening behavior was not observed, there was no distinct failure plane, and the pore pressures due to secondary effects were very small. The stress path had the appearance of a lightly overconsolidated clay. The specimens tested at 200°C had inclined initial stress paths indicating considerable anisotropy. In contrast, the samples tested at lower temperatures showed vertical stress paths indicating near isotropic behavior. This confirms similar behavior seen in buffer.

#### 7.4 Discussion of Critical State Results

A comparison of the critical state results from buffer and pelagic clay shows that temperature has similar effects on the strength and volume change characteristics of both clays. This is significant considering the differences in these clays. Buffer was tested with deionized water and contains 50% montmorillonite, a highly active mineral known for its swelling characteristics and interaction of particles through diffuse double layer forces. The pelagic clay contains illitic minerals and mineral salts which would tend to collapse diffuse double layers. A similar mechanical response from both clays indicates that elevated temperatures lead to predictable mechanical responses for diverse types of clays.



## CHAPTER 8 MODELING AND DISCUSSION

### 8.1 Introduction

This chapter will discuss two models of thermal behavior for buffer: (1) Isothermal-pseudo-elastic and (2) Isothermal-elasto-plastic. These models are not complete, but will provide a preliminary framework for understanding the effect of elevated temperature on the behavior of buffer. Other types of triaxial tests, for example, CID, constant stress ratio- $\eta$ , and constant- $p'$  triaxial tests are required to verify the models. This testing is beyond the scope of the research described in this thesis. Most attention will be focused on the thermo-elasto-plastic model. A brief discussion will follow in which the major findings in the thesis will be discussed in relation to the hypotheses proposed in Chapter 1

The major findings from Chapter 5 and 7 will be used to provide a basis for the two isothermal models presented in this chapter. Additional analysis of buffer behavior will be discussed in section 8.3. This will lend support for conceptual details such as temperature dependency of elastic moduli, yield loci, critical state behavior, and hardening laws. Observed behavior of other clays at elevated temperature, (outlined in Chapter 2), will be compared with behavior of buffer in relation to the proposed models. Normalization techniques used for example by Wood (1990), and Atkinson and Bransby (1977) to analyze London clay, Weald clay, Vienna Clay, and Chattohochee sand for shear behavior will be employed in sections 8.3.2 and 8.3.3. to confirm temperature dependence of strength envelopes and yield loci of buffer.

### 8.2 Isothermal-Pseudo-Elastic Model

In this section a linear elastic model with temperature and pressure dependent elastic moduli is discussed. The model is a simpler version of the one

discussed in Chapter 7 and is suitable only for the early stages of testing. The constitutive equation [7.15], developed by Graham and Houlsby (1983) for a cross-anisotropic material, is repeated here for convenience:

$$[8.1] \quad \begin{Bmatrix} \delta p' \\ \delta q \end{Bmatrix} = \begin{bmatrix} K^* & J \\ J & 3G^* \end{bmatrix} \begin{Bmatrix} \delta \epsilon_v \\ \delta \epsilon_s \end{Bmatrix}$$

where  $J$  is a cross coupling modulus between (1) deviatoric stress and volumetric strain and (2) mean stress and deviatoric strains. The parameter  $G^*$  is a modified shear modulus and  $K^*$  is a modified bulk modulus. Incremental volumetric and shear strains are  $\delta \epsilon_v$  and  $\delta \epsilon_s$ , respectively. The pore pressure response of dense buffer, discussed in Chapter 7, showed anisotropic behavior at mean effective stresses above approximately 2.0 MPa. At lower stresses more isotropic behavior was apparent. The model discussed here will be isotropic, that is,  $J=0$ . Pseudo-elastic secant moduli from first time loading will be used.

This model is not as sophisticated as the hyperelastic and hypoelastic models discussed in Chapter 2. The latter models are non-linear elastic models which model large strain behavior incrementally. The hyperelastic model is the more restrictive and satisfies energy conservation. The hypoelastic model uses stress level dependent tangent moduli and is path dependent. The current model is restricted to small deformations (less than 1% strain), and is path independent.

### 8.2.1 Isothermal Pseudo-Elastic Moduli (First Loading)

The method of obtaining the moduli will be discussed next. Graham and Houlsby used a least squares technique to obtain elastic moduli which required results from triaxial tests with at least two significantly different effective stress paths such as constant stress ratio- $q/p'$  and constant- $p'$ . Only one type of

test (that is the compression test), undrained triaxial, was performed in the current program, and so the least squares technique could not be used. The moduli determined here are pseudo-elastic because they are determined from first loading in which both elastic and plastic strains occur. From each test, it is possible to obtain only two related pseudo-elastic moduli,  $G_{50}$  and  $E_{50}$ , plus the Poisson's ratio. The moduli are taken as secant values between the start of the test and 50% of peak deviator strength,  $q_{50}$ . Figure 8.1 shows the graphical technique used to obtain  $G_{50}$ . Since the tests were undrained, ( $\nu = 0.5$ ), values of  $E_{50}$  were calculated from  $G_{50}$  as follows:

$$[8.2] \quad E_{50} = 3G_{50}$$

It can also be shown that the shear modulus is the same whether the results are interpreted from total stresses or effective stresses ( $q=q'$ ).

$$[8.3] \quad G_{50} = G_u = G'$$

where  $G_u$  is the undrained shear modulus and  $G'$  is the drained shear modulus. A small correction to the initial strain was required in Figure 8.1 to account for seating of the load ram. The choice of 50% peak strength is a common practice for design of earth works, and ensures, for example, that deformations are small in embankments and retained earth structures which are designed with an adequate safety margin. Table 8.1 contains values of  $G_{50}$  determined from each test. These are normalized with respect to the consolidation pressure,  $p'_{cons}$ , in order to allow comparisons of tests. As in Oswell's test program (Oswell 1991) there was some variation in the normalized shear moduli. (He performed 'stress probe' tests at different effective stress ratios ( $q/p'$ ), and all his work was at constant ambient temperature.) The variation may be a result of non-equilibrium of pore pressures at the beginning of shear, small differences in specimen density, or pressure dependence.

**Table 8.1: Undrained secant modulus,  $G_{50}$ , and  $v_p$  from CI $\bar{U}$ (TXC) tests on buffer at 26°C, 65°C, and 100°C. Poisson's ratio,  $v_p$ , at peak deviator stress shown for tests with Lateral Strain Gauge (LSG) readings**

Test	Temp (°C)	$p'_{cons}$ (MPa)	$3G_{50}^1$ (MPa)	$3G_{50}/p'_{cons}$	$v_p$	Comments
T1204	26	1.3	-	-		Drained Shear
T1205 <sup>2</sup>	65	1.5	42	28	0.47	
T1206			-	-		No Test
T1207	26	3.5	222	63		
T1208	26	0.6	-	-		Drained Shear
T1209 <sup>2</sup>	65	1.4	200	143	0.38	
T1210	63	1.6	-	-		DW Cell (no shear)
T1211 <sup>2,3</sup>	65	2.9	222	77	0.33	
T1212	26	0.6	48	79		
T1213	52	1.6	-	-		DW Cell (no shear)
T1214 <sup>2</sup>	65	2.2	210	96	0.30	
T1215	26	1.5	114	76		
T1216 <sup>2</sup>	62	0.6	74	123	0.35	
T1217	24	3.0	182	61		
T1218	27	1.0	57	57		
T1219 <sup>2</sup>	63	1.0	80	80	0.30	
T1220 <sup>2</sup>	65	1.0	80	80	0.44	
T1221	26	1.0	77	77		
T1222	65	3.0	-	-		Dummy Specimen
T1223 <sup>2</sup>	65	3.0	125	42	0.48	
T1224	65	1.5	-	-		Dummy Specimen
T1225 <sup>2</sup>	65	0.6	74	123	0.47	
T1226	100	3.0	-	-		Leak (not sheared)
T1227	100	1.5	200	133		
T1228 <sup>4</sup>	100	2.2	285	130		
T1229 <sup>2</sup>	65	7.0	69	10	0.44	
T1230	100	2.2	167	76		
T1231	100	0.6	-	-		Dummy Specimen
T1232	100	0.5	-	-		Ballooned (not sheared)

Table 8.1: (Continued)

Test	Temp (°C)	$p'_{\text{cons}}$ (MPa)	$3G_{50}^1$ (MPa)	$3G_{50}/p'_{\text{cons}}$	$v_p$	Comments
T1233	100	0.6	30	51		
T1234	100	0.6	-	-		Ballooned (not sheared)
T1235	100	9.0	100	11		
T1236	65	9.3	87	9		

- NOTE: 1. Secant moduli obtained graphically from  $q$ - $\epsilon_s$  figures at 50% of Peak Deviator stress,  $q_p$ .
2. Lateral Strain Gage (LSG) measurements taken
  3. Variable strain rate and Relaxation test
  4. Unload/Reload test performed

Table 8.2 shows a statistical analysis of the shear moduli presented in Table 8.1. A more useful analysis is provided in Table 8.3 where the average and standard deviation of the modulus values are calculated for each temperature. However, higher test temperatures give higher modulus values. Higher temperatures also produced a large standard deviation in the values. In three tests at elevated temperature, T1229, T1235, and T1236, the shear moduli were an order of magnitude lower than the average value for all the tests. As shown in Table 8.3, the removal of these test values increased the average value for the shear modulus at elevated temperature and reduced the standard deviation to approximately 33% of the average value at elevated temperature. Based on these results, there is an increase in the undrained secant shear modulus,  $G_{50}$ , of 29% at 65°C, and 41% at 100°C.

**Table 8.2** Statistical analysis of shear (secant) modulus,  $G_{50}$ , and Young's modulus,  $E_{50}$ , at 50% of peak deviator stress,  $q_{50}$ , for buffer at 26°C, 65°C, and 100°C. All tests averaged together.

	$G_{50}/p'_{cons}$	$E_{50}/p'_{cons}$
<u>22 Tests:</u>		
Average	24.59	73.86
Std.Dev.	12.98	38.92

NOTE: 1. Method of obtaining the secant shear modulus is shown in Figure 8.1

**Table 8.3** Statistical analysis of shear (secant) modulus,  $G_{50}$  and Young's modulus  $E_{50}$  at 50% of peak deviator stress for buffer program at 26°C, 65°C, and 100°C.

	$G_{50}/p'_{cons}$			$E_{50}/p'_{cons}$			Comments
	26°C	65°C	100°C	26°C	65°C	100°C	
<u>22 Tests:</u>							
Average	22.83	24.64	26.60	68.83	73.73	80.20	
Std.Dev.	2.91	14.90	15.34	8.73	44.30	46.75	
<u>Remove 3 Tests:</u>							
Average	22.83	29.44	32.25	68.83	88.00	97.50	
Std.Dev.	2.91	12.01	11.61	8.73	35.75	35.15	
<u>Oswell (1991):</u>							
Isotropic	21.9	-	-				Average
Anisotropic	23.4	-	-				LSM <sup>2</sup>

NOTE: 1. Three tests, T1229, T1235, and T1236 were removed from the statistical analysis because they had much lower moduli than the other tests.  
2. LSM = Least squares method

The isotropic pseudo-elastic moduli obtained by Oswell (1991) from first loading of drained stress controlled tests are also shown in Table 8.3. The moduli from the current program are higher than Oswell's isotropic values, but lower than his anisotropic moduli. From theory of elasticity, the drained shear modulus should equal the undrained shear modulus.

The shear modulus depends on both temperature and consolidation pressure in the current test program. This is best seen in Figures 8.2, 8.3 and 8.4. The normalized shear modulus,  $G_{50}/p'_{cons}$ , is plotted against consolidation pressure,  $p'_{cons}$ , in Figure 8.2. Tentative regression lines are as follows:

$$[8.4] \quad G_{50}^{26^{\circ}\text{C}} = 25.508 - 1.434(p'_{cons}); \text{ S.D.} = 3.1; R^2 = 0.5359$$

$$[8.5] \quad G_{50}^{65^{\circ}\text{C}} = 35.952 - 4.099(p'_{cons}); \text{ S.D.} = 15.4; R^2 = 0.7489$$

$$[8.6] \quad G_{50}^{100^{\circ}\text{C}} = 47.468 - 4.912(p'_{cons}); \text{ S.D.} = 19.1; R^2 = 0.9075$$

These regressions are tentative because of the lack of data points at high pressure. The current data at 26°C have less scatter than Saadat's data. The regression is poor because of the limited range of pressures. Using a semi log regression equation produced approximately 2% improvement in the regression coefficient  $R^2$  for elevated temperature data.

Figure 8.3 shows the shear modulus plotted against temperature. The regression lines show that temperature has its largest effect on shear modulus at consolidation pressures of 0.6 MPa. The shear modulus is insensitive to temperature at effective pressures above 1.0 MPa. Figure 8.4 shows a semi log plot of shear modulus against consolidation pressure.

Poisson's ratio was determined from axial and lateral deformation readings in the following tests: T1205, T1209, T1211, T1214, T1216, T1219, T1220, T1222, T1223, T1225 and T1229. The  $v_p$ -values shown in Table 8.1 are taken as the secant from 0 to peak deviator stress,  $q_p$ . The strains were obtained by subtracting initial deformation readings at the start of shearing from the deformation reading

at peak stress, and dividing by the initial diameter or length, as appropriate. Poisson's ratio is assumed to be 0.5 for the other undrained tests for which no lateral deformation readings are available. Figure 8.5 (a) shows the deformation readings from specimen T1205 compared with a rubber dummy specimen, TRDC9, tested in undrained triaxial compression. In this figure, measured lateral strain  $\epsilon_3[\text{Meas}]$  is compared with the theoretical lateral strain,  $\epsilon_3[\text{calc}]$  derived from measurements of axial and volume strains ( $\epsilon_3[\text{calc}] = 0.5(\epsilon_v - \epsilon_1)$ ) which assumes that the specimen remains cylindrical as it is compressed. The average slope for each test is 1.14. A slope of 1.0 defines perfect agreement between theory and measurement. The two specimens were tested at different effective stresses and temperatures, yet similar results were obtained.

Figure 8.5 (b) shows the variation of Poisson's ratio,  $\nu$ , with axial strain,  $\epsilon_1$ , for specimens T1205 and TRDC9. For an isotropic elastic material with no volume change, Poisson's ratio is 0.5. The theoretical value  $\nu = 0.5$  for constant volume, undrained shearing is reached near peak strength for the buffer specimen, T1205. The rubber dummy specimen, TRDC9, had no peak strength, but continued to accept higher loads with strain. However, both specimens showed a 'barrelling' type of deformation at large strains. The observed behavior is not truly isotropic elastic, but is nearly so. Both materials behave in a similar way.

It is difficult to determine Poisson's ratio reliably below axial strains of about 1.0% because of instrument sensitivity and initial seating. At 1.0% strain in typical buffer specimens, the stress is more than  $0.5q_p$ , the point at which we want to know Poisson's ratio,  $\nu_{50}$ . Figure 8.5(b) shows  $\nu_{50} \cong 0.2$  for buffer at about  $q_p/2$ . This is consistent with readings in other buffer specimens elevated temperature and the suite of 10 rubber dummy tests at 26°C. This indicates the problem is not heat induced.

Creep compliance of the membranes has a negligible effect on the strain



readings. Using results from a compliance test on a metal dummy specimen (Leak#1), it can be shown that compression of the membranes by the lateral strain gauge is as follows:

$$[8.7] \quad \Delta\epsilon_3 = +12.3 \times 10^{-6} \text{ \%/day}$$

where the initial specimen diameter,  $D_0$ , is 50.80 mm. For the current program the rate of strain,  $\dot{\epsilon}_1$ , is 5.76%/day and shear lasts 2 days. The creep deformation will be very small. A larger component of elastic deformation of the membrane will result from increased pressure on the buffer specimen by the strain gauge during shear. However, this deformation will also be small compared to the specimen deformation.

Table 8.4 shows Poisson's ratio,  $\nu_{50}$  and  $\nu_p$  obtained from two different lateral strain gauges (LSG#1, LSG#2). Thermal stability of LSG#1 got worse with successive tests at elevated temperature. Therefore, only the first test for this gauge is reported. The improved gauge (welded continuous loop construction), LSG#2, did not have this problem. All the results are reported for this gauge. Not much confidence is placed in the values of  $\nu_{50}$ , except for tests T1223 and T1225. Few values of Poisson's ratio have been reported in the literature, and none for buffer.

**Table 8.4** Poisson' ratio,  $\nu$ , at 50% of peak deviator stress,  $q_{50}$ , and peak deviator stress,  $q_p$ . Selected results are shown for the prototype lateral strain gauge (LSG#1). All results are shown for the modified version (LSG #2).

Test	T (°C)	$p'_{\text{cons}}$ (MPa)	$\nu_{50}$	$\nu_p$	Comments
<u>Prototype (LSG#1):</u>					
T1205	65	1.5	0.17	0.47	Uncorrected <sup>1</sup>
T1205	65	1.5	0.21	0.48	Corrected <sup>2</sup>
<u>Modified (LSG#2):</u>					
T1220	65	1.0	0.15	0.44	Uncorrected
T1223	65	3.0	0.40	0.48	"
T1225	65	0.6	0.41	0.47	"
T1229	65	7.0	0.22	0.44	"

NOTE: 1. Secant values of strains taken, starting at  $q = 0$

$$(\epsilon_{1,3} = 0 \text{ at } q = 0)$$

2. Secant values of strains taken, starting at  $q = 0.25q_{25}$

$$(\epsilon_{1,3} = 0 \text{ at } q = 0.25q_p) \text{ to avoid 'noise' in the initial readings}$$

As mentioned earlier, initial values of Poisson's ratio at axial strains,  $\epsilon_1$ , less than 1.0% are not reliable. An improved method of calculating  $\nu$  has been developed. It arbitrarily assumes zero strains at  $0.25q_p$  and calculates values of Poisson's ratio from this new zero. This method eliminates the instrument 'noise' at the beginning of shear. More reliable values of  $\nu_{50}$  are obtained. Figure 8.6 (a) and (b) shows this method of calculating  $\nu$ . The new  $\nu$ -values are compared with the original  $\nu$ -values in Figure 8.6(b). Table 8.5 also shows the new (corrected) values. This method can be used to obtain average  $\nu$ -values over smaller stress increments as shown in Table 8.4:

**Table 8.5** Average values of Poisson's ratio,  $\nu$ , for deviatoric stress ranges:  $0.25-0.50q_p$ ,  $0.25-0.75q_p$ , and  $0.25-1.0q_p$ .

Test	$0.25q_p$	$0.50q_p$	$0.75q_p$	$q_p$	$V_{25-50}$	$V_{25-75}$	$V_{25-p}$
T1205	0.157	0.315	0.472	0.630	0.21	0.38	0.48

NOTE: 1.  $0.25 - 0.75q_p$  implies measurements in the stress range  $0.25q_p - 0.75q_p$ .  
 2.  $q_p$  measured in MPa

The pseudo-elastic bulk modulus,  $K'$ , and plastic bulk modulus,  $K^P$ , will now be discussed. The  $K'$ -modulus is defined in elastic theory as follows (Wood 1991):

$$[8.8] \quad K' = \delta p' / \delta \epsilon_v$$

It is normally calculated from drained incremental isotropic compression tests. For undrained tests,  $K'$ , is undefined because the volume change is zero. Therefore it is not possible to obtain  $K'$  from the current test program. However, it is possible to obtain a plastic bulk modulus,  $K^P$ , using the hardening laws developed in Figure 5.12. By definition:

$$[8.9] \quad V = V_\lambda - \lambda \ln(p')$$

where  $V$  is specific volume,  $V_\lambda$  is the specific volume at an effective stress of 1 kPa, and  $\lambda$  is the slope of the hardening lines. This can be written in incremental form as follows:

$$[8.10] \quad \delta V = -\lambda \delta p' / p'$$

By definition

$$[8.11] \quad \delta \epsilon_v = -\delta V / V$$

Combining equations [8.10] and [8.11]:

$$[8.12] \quad \delta \epsilon_v = \lambda \delta p' / V p'$$

Comparing this with equation [8.1] it is apparent that

$$[8.13] \quad K^P = V_{p'}/\lambda$$

Substituting this into equation [8.9]:

$$[8.14] \quad K^P = \left[ V_{\lambda}/\lambda - \ln(p') \right] p'; \quad (K^P \text{ and } p' \text{ in kPa})$$

The  $K^P$ -modulus for dense buffer at 26°C, 65°C and 100°C is characterized by equation [8.14] with different  $V_{\lambda}/\lambda$ -constants for each temperature. The constants are given in Table 8.6. The value of  $\lambda$  obtained in Chapter 5 was  $\lambda = 0.121$ .

**Table 8.6** Plastic bulk modulus,  $K^P$ , for dense buffer at 26°C, 65°C, and 100°C calculated from equation [8.14]. A  $\lambda$ -value of 0.121 is assumed for each temperature

T (°C)	$V_{\lambda}$	$V_{\lambda}/\lambda$	$K^P$ (kPa)
26	3.102	25.63	$\left[ 25.63 - \ln(p') \right] p'$
65	3.050	25.21	$\left[ 25.21 - \ln(p') \right] p'$
100	2.950	24.38	$\left[ 24.38 - \ln(p') \right] p'$

### 8.2.2 Isothermal Elastic Moduli (Unload/Reload)

From the unload/reload portions of test T1228, it is possible to obtain elastic shear moduli,  $G^e$ , for unloading and reloading of dense buffer. Such values are known to be higher than values calculated from the beginning of testing since they do not include "bedding in" strains between the specimen and the end platens. Figure 8.7 shows a semi-graphical method for calculating  $G^e$ . The first unload-reload cycle occurred in T1228 just before peak stress. The initial unload portion involving a drop in stress of approximately 300 kPa, was done by "relaxation". That is, load readings were taken while the load ram was held

stationary. After this, the specimen was unloaded at an axial strain rate,  $\dot{\epsilon}_1 = 1.0\%/day$  to a deviator stress of about 600 kPa. This was followed by reloading at  $\dot{\epsilon}_1 = 5.76\%/day$ . Secant moduli were obtained using the initial final points of each stage of the cycle. In the case of reloading, the final point is when the stress reaches the previous maximum stress. The second unload reload cycle was done at the end of the test. Unexpected strain readings were obtained during reloading, and no reload modulus has been reported for this second cycle.

Table 8.7 contains the  $G^e$ -moduli from Test T1228. These values are compared with similar unload-reload moduli calculated by Oswell (1991) from constant stress ratio- $q/p'$  tests and Saadat's undrained tests. The unload moduli from T1228 are approximately three times Saadat's average value. Note that specimen T1228 was tested at a higher temperature,  $100^\circ C$ , than Saadat's specimens, but at approximately the same density and pressure. The reason for the high modulus value is not known, but may be due to high strain rates used in the current program. The effect of temperature on the pseudo-elastic moduli, discussed in the previous section, was much less than observed in these tests where there is a 300% difference with the hotter specimens again showing higher stiffness. The  $G^e$ -reload modulus from T1228 is approximately equal to  $G^e$ -unload moduli from Oswell and Saadat's results. Note that Oswell's specimens had lower density (about  $1.51 \text{ Mg/m}^3$  compared with  $1.67 \text{ Mg/m}^3$  in the present program), and were tested at lower effective stresses.

**Table 8.7 Isotropic elastic moduli from isothermal unload/reload buffer data at 26°C and 100°C**

Test	T (°C)	$p'_{cons}$ (MPa)	$\gamma_d$ (Mg/m <sup>3</sup> )	$\dot{\epsilon}_1$ (%/day)	Unload $3G/p'_{cons}$	Reload $3G/p'_{cons}$	Comments
<u>Current Program:</u>							
T1228 $q_p$	100	2.2	1.69	(1.00)	318	-	Undrained S.C. <sup>1</sup>
				5.76	-	159	Undrained S.C. <sup>1</sup>
T1228 $q_{EOT}$	100	2.2	1.69	(5.76)	280	-	Undrained S.C.
<u>Oswell (1991):</u>							
T1120	26	0.5	1.47	0.35	60	-	$dq/dp' = 3.3$ S.C.
T1121	26	0.5	1.50	0.30	148	-	$dq/dp' = 1.2$ S.C.
T1139 <sup>2</sup>	26	0.5	1.49	Incr	68	-	$dq/dp' = 0.4$ S.C.
<u>Saadat (1989):</u>							
T927 1 <sup>st</sup>	26	1.5	1.66	0.24	59	-	Undrained S.C.
T927 2 <sup>nd</sup>	26	1.5	1.66	0.24	65	-	Undrained S.C.
T931	26	3.0	1.66	-	143	-	Undrained S.C.

NOTE:1. S.C. indicates "strain controlled"

2. T1139 was sheared after swelling at OCR = 2.75

3. Unloading Rate,  $\dot{\epsilon}_1$ , shown in brackets

### 8.3 Isothermal-Elasto-Plastic Model

Specific elements of an isothermal elasto-plastic model will be addressed in the following sections, such as shrinking yield loci, and temperature dependent hardening laws and critical states.

The proposed model assumes behavior at constant temperature because this was the condition of testing in the program. To verify generality of the model for non-isothermal conditions would require a set of 'ramped' temperature tests where the temperature is increased and decreased at constant or varying effective stress. This is beyond the scope of the current work, but is being examined in the

following doctoral program of N. Tanaka.

### 8.3.1 Curved Critical State (CS) Envelope

Analysis of the undrained shear results from the current test program at 26°C indicates that the critical line in  $q$ - $p'$  stress space is curved over the full range of applied stresses, 0.6 to 10.0 MPa. This was shown in Figure 5.36. A power law regression seems to fit the data best. Similar curvature was observed for tests at by Saadat (1989) for a similar range of stress and by Oswell (1991) for stresses up to 3.5 MPa, the highest stress in his program. Note that these tests included a variety of stress paths, such as Oswell's stress probe tests at different stress ratios,  $\eta$ .

When Saadat and Oswell discussed Cam clay modeling, they assumed a straight critical state line in  $q$ - $p'$  stress space. Clearly, use of the standard Cam clay model in this way is a simplification of observed behavior. The observed curvature of the critical state line should not be confused with a Hvorslev surface. The latter is a locus of peak stress states above the critical state line obtained from drained or undrained tests on clay at high values of overconsolidation ratio (greater than 2 for idealized isotropic Cam clay).

Curvature of the critical state line appears to be more strongly developed than usual in buffer, perhaps because of the high range of pressures in these tests. It does not appear to occur in London clay, Weald clay and Vienna clay, discussed by Wood (1990) and Atkinson and Bransby (1978). Nor is it apparent in undisturbed, softened, or freeze/thawed Winnipeg clay as discussed by Graham and Au (1984). These clays were tested at low effective stresses, typically less than 1.0 MPa pressure. On the other hand, curvature of the critical state line in  $q$ - $p'$  stress space is most noticeable in buffer at low effective stresses.

Curvature has been observed for buffer compacted at different densities.

Low density buffer ( $\gamma_d = 1.3$  to  $1.5 \text{ Mg/m}^3$ ) tested by Wan (1987) and Oswell (1991), and high density buffer ( $\gamma_d = 1.67 \text{ Mg/m}^3$ ) tested by Saadat (1989) and Oswell (1991) all show similar curved critical state behavior in  $q$ - $p'$  stress space. Note that Wan's specimens were formed at densities corresponding to swelling equilibrium. His specimens apparently had a different fabric than Saadat's. The main point being made here is that curvature of the critical state line in  $q$ - $p'$  stress space is a real material response in buffer and has been observed in tests with various stress states, fabrics, and densities.

Note that the assumption of a straight critical state line (CSL) in  $q$ - $p'$  stress space does not imply a straight line for the CSL in  $V$ - $\ln(p')$  compression space for real soils. The aspects of behavior can be reached independently. In the Cam clay model, the CSL is straight both in  $q$ - $p'$  stress space and in  $V$ - $\ln(p')$  compression space.

A key element in the critical state behavior, the consolidation behavior, has not been discussed in detail, although test data were presented in Chapter 5. In the modified Cam clay model, a logarithmic relationship is assumed between clay specific volume density and effective stress during first loading along the Normal Consolidation Line (NCL) under isotropic and one-dimensional compression. In  $V_c$ - $\ln(p')$  compression space, the CSL and NCL are parallel and separated by a distance of  $\ln 2$  along unload-reload paths. This arises from a complementary assumption of elliptical yield loci in  $q$ - $p'$  stress space. However, Oswell (1991) showed that yield loci for buffer are not elliptical and the current program has shown that at  $26^\circ\text{C}$  the CSL and NCL are nearly coincident in  $V_c$ - $\ln(p')$  compression space (Figure 5.38). Further, the NCL and CSL for buffer at  $26^\circ\text{C}$  in  $V_c$ - $\ln(p')$  compression space are assumed linear for purposes of simplification. In fact, however, the data show a trend of decreasing slope at higher stresses. An important result of this is that the stress ratio,  $M$  in  $q$ , $p'$ - space at critical



state changes with stress level. The friction angle  $\phi'$  would also change with stress level if the relation  $\sin\phi' = 3M/(6+M)$  still holds. It would therefore require a much more complicated model than Cam clay to incorporate the non-linearity observed in buffer. Modeling of this kind is beyond the scope of this thesis, but some implications of such a model will be discussed briefly.

The undrained shear strength of clay at critical state may be derived from the Cam clay model. Wood (1990) writes the relationship as follows:

$$[8.15] \quad q_f = Mp'_i \left[ \frac{n_p}{r} \right]^\Lambda$$

where  $n_p$  is the isotropic overconsolidation ratio (equation [8.16]),  $r$  is the separation of the CSL and NCL along unload/reload lines (equation [8.17]), and  $\Lambda$  is a hardening parameter defined in (equation [8.18]):

$$[8.16] \quad n_p = \frac{p'_o}{p'_i}$$

$$[8.17] \quad r = \frac{p'_o}{p'_{cs}}$$

$$[8.18] \quad \Lambda = \frac{\lambda - \kappa}{\lambda}$$

For NC clay  $p'_i = p'_o$  which is the same as the preconsolidation pressure,  $p'_c$  and equation 8.15 can be written as:

$$[8.19] \quad q_f = \frac{M}{p'_c, \Lambda-1} \left[ p'_{cs} \right]^\Lambda$$

where  $p'$  is in kPa. Equation 8.19 is in a form similar to the regression equation obtained by Saadat (1989) for buffer at critical state:

$$[5.12] \quad q_{eot} = 2.64(p')^{0.79}$$

Saadat gave a value of  $\Lambda = 0.74$ . It is likely a coincidence that this is close to the index 0.79 in equation [5.12]. Certainly equation [5.12] is not equal to equation 8.19 for the Cam clay model because  $M$  is a constant and  $p'_c$  is a variable

making the term  $M/p_c^{\Lambda-1}$  also a variable. However, in a non-linear CS model, mentioned earlier,  $M$  is variable and equation [5.12] may be equal to equation [8.19]. If  $\kappa$  is a constant then  $\Lambda$  will also be constant. A forthcoming MSc. program by T. Crilly will examine the dependency of  $\kappa$  on temperature.

### 8.3.2 Isothermal Curved CS Envelopes

In this section, the additional variable of elevated temperature will be discussed in relation to the critical state concepts discussed in the previous section. The curvature of the critical state line in  $q$ - $p'$  stress space is more pronounced at 100°C than at 26°C, especially at stresses less than approximately 2.0 MPa (Figure 5.36). This has important implications regarding the plastic and elastic behavior of buffer. The existence of separate peak strength envelopes for tests at different temperatures, shown in Figure 5.36 (a), was the first clear evidence of individual Hvorslev surfaces for each temperature. This will be discussed in the next section in detail. The existence of separate critical state envelopes, shown in Figure 5.36 (b), was the first evidence of what can be thought of as individual state boundary surfaces (overconsolidated strength envelopes) for each temperature. This will also be discussed in the following text with the use of three normalization methods. First however, the implications of a curved CSL in  $q$ - $p'$  stress space will be addressed in more detail.

Changes in the curvature of the critical state envelope with temperature can be linked to changes in the elasticity of buffer with temperature. It was shown in Chapter 5 that the critical state envelopes in  $q$ - $p'$  stress space for the current test program are:

$$[5.10] \quad q_{\text{cot}}^{100} = 8.142 \cdot (p')^{0.674}$$

$$[5.11] \quad q_{\text{cot}}^{65} = 4.147 \cdot (p')^{0.733}$$

$$[5.12] \quad q_{\text{cot}}^{26} = 2.64 \cdot (p')^{0.79}$$

These regressions are generalized for NC soil as:

$$[8.20] \quad q_{\text{eot}} = A \left[ p'_{\text{eot}} \right]^B$$

which is similar in form to equation 8.19. For now, assume that  $A$  is equal to  $M/(p'_c)^{\Lambda-1} = M/(p'_c)^{\kappa/\lambda}$ , the index  $B$  is equal to the hardening parameter  $\Lambda = (\lambda - \kappa)/\lambda = 1 - \kappa/\lambda$ , and  $\kappa/\lambda = 0.15$ . If  $A$  is constant and heating causes  $p'_c$  to decrease an order of magnitude from 5.0 MPa to 0.5 MPa, then  $(p'_c)^{0.15}$  would decrease 41%. This means  $M$  would have to increase by a proportionate amount for  $A$  to remain constant. If  $p'_c$  is assumed constant, but  $\kappa/\lambda$  increases with temperature ( $\lambda$  is assumed constant), then  $M$  must decrease. It was shown in Chapter 2 (Eriksson 1989) that when sulphide rich clays are heated,  $\kappa$  increases and  $p'_c$  decreases ( $\lambda$  is constant). The point being made is that the proposed model indicates changes in  $M$ ,  $p'_c$ , and  $\kappa$  with changes in temperature and the changes are consistent with the observed behavior of sulphide rich clay.

Equation 8.19 has implications for the changes in psuedo-elastic parameters with temperature. Assume that the constitutive equation for isotropic elastic behavior is valid:

$$[8.1] \quad \begin{Bmatrix} \delta p' \\ \delta q \end{Bmatrix} = \begin{bmatrix} K' & 0 \\ 0 & 3G' \end{bmatrix} \begin{Bmatrix} \delta \epsilon_p \\ \delta \epsilon_q \end{Bmatrix}$$

This relationship holds for the Cam clay model, and so:

$$[8.21] \quad K' = Vp'/\kappa$$

(This equation is similar in form to equation 8.13). Inspection of equations 5.10 to 5.12 shows that  $B = \Lambda$  decreases with increasing temperature. For the proposed model it is assumed that 8.21 is valid, and  $\kappa$  is constant with stress level but may vary with temperature. (The former requirement can be relaxed later if necessary).

For a given stress level, drained heating would cause a reduction in  $V$  and an increase in  $\kappa$ . This means the modulus  $K'$  would decrease with an increase in temperature. This agrees with the trend observed for values of  $K^P$  in Table 8.6 which were obtained from equation 8.14. On the other hand the normalized pseudo-elastic modulus  $G_{50}/p'_{cons}$  discussed previously increased with increases in temperature.

It has been assumed that  $\Lambda = B$  is constant when temperature is constant. This means  $\kappa/\lambda$  is constant, but  $\kappa$  and  $\lambda$  may change with pressure by proportionate amounts. The implication is that if curvature of the  $\lambda$ -lines occurs then there is also curvature of the  $\kappa$ -lines.

It was mentioned earlier that a non-linear critical state model requires  $M$  to vary with stress level, and this is evident in the buffer data (equations 5.10 to 5.12). A previous paragraph showed that  $M$  varies with temperature at a given stress level. Assume for the moment that the NCL and CSL for buffer coincide in  $V-\ln(p')$  compression space for each temperature, that is, that the yield loci are non-elliptical). Assume also that the buffer is normally consolidated. From the hardening laws in Figure 5.12 it is possible to determine  $p'_c$  at each temperature for specific stress levels. It is then possible to calculate  $M$  and  $\kappa$  for each temperature at specific stress levels using equation 8.19. Note that for buffer at any stress level  $\lambda$  is approximately constant with temperature. Table 8.8 shows the results for a stress level corresponding to assumed normal consolidation at the compaction specific volume of 2.252 ( $\gamma_d = 1.67 \text{ Mg/m}^3$  and  $w_o = 22.75\%$ ).

**Table 8.8** Calculation of  $M$  and  $\kappa$  at 26°C, 65°C, and 100°C for a specific volume of 2.252 ( $\gamma_d = 1.67 \text{ Mg/m}^3$  and  $w_o = 22.75 \%$ ). Assume: (1)  $\kappa$  is constant with stress level (2) the buffer is normally consolidated and (3) that the NCL and CSL coincide in  $V\text{-ln}(p')$  compression space.

Temp. (°C)	$\Lambda$	A	$p'_c$ (kPa)	$\lambda$	M	$\phi'$ (°)	$\kappa$
26	0.790	2.640	1143	0.121	0.60	15.8	0.025
65	0.733	4.147	743	0.121	0.71	18.5	0.032
100	0.674	8.142	324	0.121	1.24	30.9	0.039

The  $M$  and  $\phi'$  values for 100°C seem very large, but it should be noted that this corresponds to  $p'_c$  of only 324 kPa, where the curvature of the peak strength envelope is quite marked. Note that these may not be true values for buffer because not all the assumptions made earlier have been verified. The importance of the data in Table 8.8 is that it supports the idea of a non-linear critical state model which is temperature dependent. What is perhaps more important is that it suggests a linkage between the undrained strength envelope and the drained consolidation parameters  $\kappa$  and  $\lambda$ . This ability to synthesize behavior from different soil parameters suggests that the model itself must be quite powerful and inclusive.

The data in Table 8.8 are consistent with observed trends in behavior. An assumption of coincident NCL AND CSL was made earlier to model buffer behavior. This possibility will be discussed later in relationship to swelling equilibrium and stress history of the specimens.

A mathematical model for characterizing critical state behavior of buffer will now be discussed. The model will be compared with the data in normalized

stress space,  $q/p'-V_\lambda$ . The parameter  $V_\lambda$ , previously defined by equation 8.9, is shown in Figure 8.8 (a).

$$[8.9] \quad V = V_\lambda - \lambda \cdot \ln(p')$$

This space is often used to characterize the state boundary surface (SBS) of sands (Atkinson and Bransby 1978), but also clays (Wood 1990). The image in this space shows important graphical relationships by providing a two dimensional projection of the three dimensional SBS. In Figure 8.8 (a) a state boundary surface is shown, in part, by four elliptical yield loci in  $q,p'$  stress space. A line of constant stress ratio  $\eta$  intersects these yield loci (YL) at points 1,2,3, and 4. The YL are shown in Figure 8.8 (b) as unload-reload lines (URL). The projection of points 1,2,3, and 4 onto the plane located at  $p' = 1$  gives a single value of  $V_\lambda$ . Values of  $V_\lambda$  provide a graphical view of the SBS similar to section A-A, in the direction of arrow B. The common practice is to plot  $q/p'$  versus  $V_\lambda$  as shown in Figure 8.8 (c). The  $q/p', V_\lambda$ -projection makes the SBS appear as a line instead of a surface.

Figure 8.8 (c) shows the SBS surface of an idealized clay in  $q/p'-V_\lambda$  space. Point N represents the isotropic NCL and point C represents the CSL with an  $\eta$ -value of  $M$  and a  $V_\lambda$ -value of  $\Gamma$ . Drained and undrained shear tests on lightly overconsolidated isotropic clay originate from point P in Figure 8.8 (c). Similarly, shear tests on heavily overconsolidated isotropic clay originate from point R. The different starting points result in significantly different shear behavior. From point P the clay yields at points F and Q on the Roscoe surface, shown as line N-F-Q-C, and fails at critical state, point C. From point R the clay reaches peak strength at points S and G on the Hvorslev surface, and strain softens to critical state, point C. Anisotropic clay would have initial stress paths inclined to the left of vertical (not shown).

Figure 8.9 (a) shows an idealized critical state line for buffer at constant temperature in  $q-p'$  stress space. The CSL is shown in compression space

in Figure 8.9 (b). For this modeling exercise, straight parallel lines are assumed for the CSL and NCL in  $V_c$ - $\ln(p')$  compression space. Projection of the idealized SBS in  $q/p'$ - $V_\lambda$  space, Figure 8.9 (c) shows a line for the CSL from point 8 to point 14, rather than a single point. This arises from the apparent change in shape of the yield loci (ellipses) with pressure  $p'$ . The importance of this will be seen when buffer data is examined. An expression has been derived for the stress ratio,  $M$ , where:

$$[8.22] \quad M = f(V_\lambda)$$

From the definition of  $V_\lambda$ , equation 8.9:

$$[8.23] \quad \ln(p'_{cs}) = \left[ (V_\lambda)_{cs} - V_{cs} \right] / \lambda$$

and from equation 8.20:

$$[8.24] \quad \ln(q_{cs}) = \ln(A) + B \cdot \ln(p'_{cs})$$

Substitution of equation 8.23 into equation 8.24 gives

$$[8.25] \quad q_{cs} = \exp \left[ \ln(A) + \frac{B}{\lambda} \left[ (V_\lambda)_{cs} - V_{cs} \right] \right]$$

But

$$[8.25] \quad M = q_{cs} / p'_{cs} = \frac{1}{p'_{cs}} \exp \left[ \ln(A) + \frac{B}{\lambda} \left[ (V_\lambda)_{cs} - V_{cs} \right] \right]$$

The general equation for the critical state line in compression space is as follows:

$$[8.26] \quad V_{cs} = \Gamma - \lambda \cdot \ln(p'_{cs})$$

which is rearranged

$$[8.27] \quad p'_{cs} = \exp \left[ \frac{\Gamma - V_{cs}}{\lambda} \right]$$

Combining equations 8.27 and 8.25 gives

$$[8.28] \quad M = \exp \left[ \ln(A) + \frac{B}{\lambda} \left[ (V_\lambda)_{cs} - V_{cs} \right] - \frac{1}{\lambda} \left[ \Gamma - V_{cs} \right] \right]$$

which can be simplified to

$$[8.29] \quad M = A \cdot \exp \left[ \frac{B}{\lambda} \left[ (V_{\lambda})_{cs} - V_{cs} \right] + \frac{1}{\lambda} \left[ V_{cs} - \Gamma \right] \right]$$

Values of specific volume,  $V_{cs}$ , must be chosen to calculate values of  $M$  corresponding to values of  $V_{\lambda}$ . To model the compaction density and range of stresses in the current program, values of  $V_{cs}$  of 2.4, 2.2, and 2.0 are chosen. For 26°C  $A$  is 2.64 and  $B$  is 0.79. The computed values of  $M$  for 26°C from equation 8.29 are shown in Figure 8.10. (This is the same stress space that was used in Figure 8.8 (c).) The solid line shows  $M$  values for a specific volume  $V_{cs}$  of 2.2, close to the compaction density. Curve  $C_1$ - $CS_1$  is an interpretation of the average stress path to critical state. Also shown are the peak data values and average critical state (CS) values for 26°C, 65°C and 100°C. Critical state values show a similar distribution to the peak values. For a range of specific volumes of 2.4 to 2.0 there is a variation in  $M$  values from point 1 to point 3 at 26°C. This line segment represents the critical state line for the range of stresses in the current program. It does not coincide with the average critical state value,  $CS_1$ , for 26°C, but it does show that there is a range of values of  $M$  in this graphical projection of the SBS. This suggests that the dispersion of the data points may not be due to scatter alone.

Referring again to equation [8.29], if  $(V_{\lambda})_{cs} = \Gamma$ , then:

$$[8.30] \quad M = A \cdot \exp \left[ \frac{1}{\lambda} (B-1) (\Gamma - V_{cs}) \right]$$

If  $\kappa=0$ , that is,  $\Lambda = 1 = (\lambda - \kappa)/\lambda$  then  $B=1$ . This indicates that  $\kappa$  decreases to a value of zero at  $p'_{cs} = 1$ . This seems unlikely for real soil. It is more likely that  $\Gamma = V_{cs}$ . This simply refers to the specific volume at very low critical state stress. Then equation 8.30 becomes:

$$[8.31] \quad M = A$$



This implies a limiting critical state stress ratio at very low stress levels,  $p' = 1$  kPa.

It was mentioned earlier that the yield loci in Figure 8.9 (a) apparently change shape with pressure,  $p'$ . It is possible that the shapes have not actually changed, but the angle of the projected image has changed. This would imply that the  $\kappa$ -lines in  $V_c \ln(p')$ -space are not parallel with each other but change slope with successively lower specific volumes.

The first of three normalization methods has been used in Figure 8.10 to analyze data from tests at different isothermal temperatures. All values of  $V_\lambda$  shown in Figure 8.10 have been calculated from a single NCL from the regression of the 26°C data. Individual values of  $q$  for peak state (open symbols) and average values for critical state (dark symbols) have been normalized by the corresponding  $p'$  values. This is the first method of normalization.

The value of equation [8.29] is apparent when elevated temperatures are considered. Values of  $A$  and  $B$  corresponding to 26°C 65°C and 100°C have been used in equation 8.29 and the computed values of  $M$  are plotted as separate curves for each temperature in Figure 8.11. The same specific volume,  $V_{cs} = 2.2$  was used for each curve. The proposed curves do not fit the average critical state data points well, but they do show an expected trend in the critical state values with increasing temperature from left to right. The poor fit of the curves may be the result of simplifying assumptions made earlier such as constant  $\lambda$ , and parallelism of the CSL and NCL. As mentioned earlier,  $\lambda$  may decrease with increased effective stress. This also indicates that the thermo-elastic-plastic model being proposed may have to be restricted to a limited range of pressures where the compression line is reasonably linear.

Graphical methods will be now used to define the relationship of the critical state lines to state boundary surfaces for different temperatures. Figure

8.12 shows average values of  $V_\lambda$  at an expanded scale. For 26°C data average data points are shown for consolidation ( $C_1$ ), yield ( $Y_1$ ), peak strength ( $P_1$ ), and critical state ( $CS_1$ ). A curve is drawn through the peak and critical state data points as an interpretation of the SBS. Here the buffer is interpreted as overconsolidated because the estimated preconsolidation pressure at point O is larger than the average consolidation pressure, point  $C_1$ . A similar procedure is used for elevated temperature data and general similarity of curves is assumed. It will be shown in following sections that this is a reasonable assumption.

Figure 8.13 shows individual points for the critical state data at 26°C, 65°C, and 100°C. The average values of critical state for each temperature are also shown as bold symbols. The variation in data values required use of an averaging technique to show trends in the data.

A second method of normalization will now be used. It requires the use of equivalent pressure,  $p'_e$ , and  $V_\lambda$  for each value of  $q$ . The definition of equivalent pressure is shown in Figure 8.14 (a). The data point to be normalized is on an unload/reload line (URL). The isotropic normal consolidation line is used here as the reference for normalization, but other lines (such as the CSL) could also be used. Later a third method of normalization which uses the normalized stress space in Figure 8.14 (b) will be discussed.

Figure 8.15 shows average values of  $q$  normalized to  $p'_e$ . Here, the 26°C NCL is used as the reference line for all the data. Clearly, normalized stress ratios are lower at elevated temperature, but the average specific volumes are also lower for the data shown. Note that two different normalization techniques,  $V_\lambda$  space and equivalent pressure,  $p'_e$ , have been used in this Figure. These are normally used separately as  $q/p'_e$  versus  $p'/p'_e$ , or  $q/p'$  versus  $V_\lambda$  (Atkinson and Bransby 1978, Wood 1990). A combined method which has not been attempted before is justified for this program in order to characterize multiple state boundary surfaces.

Individual critical state data points have normalized in Figure 8.16 using the same technique as in Figure 8.15. Three separate lines can be drawn through the data for different temperatures. These lines show a similar trend to critical state equation [8.29], modeled in Figure 8.10. This supports the idea of geometrically similar critical state lines at different temperatures.

A third method of normalization is used to normalize critical state data in Figure 8.17. This technique, used by Wood (1990) and Atkinson and Bransby (1978) mostly for clays, has been adapted to the current program. Figure 8.14 (b) showed the Hvorslev surface and Roscoe surface in  $q/p'_c$  versus  $p'/p'_c$  stress space. Drained and undrained stress paths are also shown. The values of both  $q$  and  $p'$  in Figure 8.17 are normalized to  $(p'_c)^{cons, 26^\circ C}$  which is the equivalent pressure with reference to the  $26^\circ C$  normal consolidation line ( $26^\circ C$  NCL). Average values for each temperature are shown by the filled symbols. Note that the all data plots near a single straight line with a slope of  $M = 0.63$ . A common slope is expected when all the data is normalized to a common reference line. This supports the idea of geometrically similar Hvorslev surfaces at different temperatures.

Considerable effort has gone into defining the critical state behavior of buffer at different temperatures and developing a descriptive model using normalization techniques. There are two reasons for the effort: (a) the critical state behavior of buffer is a significant departure from Cam clay; and (2) it is hoped that behavior of buffer can be generalized. Generalized critical state behavior will be summarized in section 8.3.6.

### 8.3.3 Isothermal Peak Strength and Hvorslev Surfaces

Earlier, an isotropic constitutive model was used to model pseudo-elastic behavior of buffer. However, buffer has an anisotropic stress history. That is, it was subjected to one-dimensional compaction during specimen formation. It was

then consolidated under different isotropic stresses and allowed to swell or compress. Wood (1990) suggests that clays have 'memory' of such processes and that yield loci from one-dimensional compression processes are retained but modified under subsequent isotropic compression. In Chapter 5 (section 5.4.1) it was observed that in the current program some strain softening occurred in many tests. No strain hardening has been observed in undrained tests on buffer. This indicates that the specimens behaved in an overconsolidated manner.

In the Cam clay model, an associated flow rule is assumed, which means that the yield loci and plastic potential coincide. Strain softening in Cam clay is modeled as a transition from elastic or pre-yield conditions to dilative plastic behavior. Peak strengths in undrained tests represent the condition of yielding, and the Hvorslev surface is the trace of the yield loci in the heavily overconsolidated stress range in  $q$ - $p'$  stress space. For the moment, this will be assumed for buffer. It will be shown that the Hvorslev surface is temperature dependent. Later it will also be shown that the Hvorslev surface is actually a rupture locus quite distinct from the yield locus bounding linear 'first loading' behavior.

The equivalent pressure normalization method (Figure 8.14) is used in this discussion to provide new information about peak strength behavior at elevated temperature and to allow comparison of the current buffer data with that of Oswell (1990). The data in Figure 8.18 are the average of all the peak strength data in the current program. The arrows starting from average consolidation pressures at each temperature, show the initial direction of the stress paths. Hvorslev and Roscoe surfaces have been interpreted from individual data points and plotted here. Oswell's yield locus is shown as a solid line. A rupture surface is shown as the dotted line and joins the yield locus near the top. Oswell interpreted the rupture locus as secondary yielding. In order to compare the current data with Oswell's

rupture locus, all data have been normalized using equivalent pressure with Oswell's swelling equilibrium line (SEL) as the reference line. (The SEL was obtained from Oswell's buffer specimen T99). There appears to be similarity between the 26°C Hvorslev surface from the current program and Oswell's rupture locus. Note that Oswell used drained triaxial constant stress ratio tests which follow different stress paths than the undrained tests used in the current program.

In the current program, it was noticed that individual peak strengths and critical state strengths were lower at elevated temperature, even though the strength envelopes were higher (Figure 5.36). As shown previously, specimens consolidated at elevated temperature also have lower specific volumes. Figures 8.19 (a) and (b) show four different tests for which this was true. One explanation for this behavior is the development of larger positive pore water pressures in the elevated temperature specimens, which causes them to reach the state boundary surface at lower deviator stresses than specimens tested at lower temperature. Higher positive pore water pressures at elevated temperatures were also evident in Figures 5.20 and 5.22. A full understanding of this behavior cannot be obtained simply by testing specimens at the same pressure. Alternatively, tests could be run at the same specific volume, but the current program was not designed on this basis, and in any case it is difficult to control. As a compromise the data can be analyzed as done in the previous section, using  $V_\lambda$  space which shows the combined effects of pressure and specimen density.

Hueckel and Baldi (1990) found similar behavior during drained triaxial tests on Pontida silty clay, shown in Figure 2.8. The lower strengths at elevated temperature are associated with a tendency to more ductile strength behavior and compressive straining.

By coincidence, several tests in the current program were consolidated to approximately the same specific volume before shearing. The specific volumes of

interest are 2.32, 2.25, 2.15, 2.05, and 1.95. These provide a range of densities above and below the compaction density of 2.252. In all cases the peak deviator stress and mean effective stress were lower at higher temperatures. Figure 5.22 shows specimens T1216 and T1233 which were consolidated at nearly the same effective stress. This clearly shows lower peak and critical state strengths at 100°C than at 65°C. Comparison of shear results from specimen T1214 and T1230 confirms this behavior. Each specimen was consolidated to a specific volume of approximately 2.05, which is lower than the compaction density.

As mentioned earlier in connection with Figure 8.18 which showed average values, the Hvorslev surfaces for each test temperature have been interpreted from individual data points. These are shown in Figure 8.20 in terms of  $(p'/p_e^{SEL})^{26^\circ\text{C}}$  versus  $q/(p_e^{SEL})^{26^\circ\text{C}}$  and in Figure 8.21 in  $q/p'$  versus  $V_\lambda$  space. In these figures, the 26°C NCL from the current test program has been used as the reference line as indicated by  $(V_\lambda^{cons})^{26^\circ\text{C}}$ . The average data points at 26°C ( $P_1$ ), 65°C ( $P_2$ ), and 100°C ( $P_3$ ) are not shown. Figure 8.21 suggests that the peak stress ratio  $q/p'$  is 10% higher at 100°C than at 26°C.

Two main conclusions may be drawn: (1) the peak stress ratio  $q/p'_p$  is higher at elevated temperature; and (2) the peak deviator strength is lower at elevated temperature.

### 8.3.4 Isothermal Yield Loci

Using triaxial shear tests with different incremental stress ratios  $\Delta q/\Delta p'$  Oswell (1991) showed that the buffer behaves anisotropically in the elastic stress range. It was suggested in Chapter 5 that anisotropic behavior of clay may also be induced by the stress path chosen for testing. Strain softening occurs in natural clays in the lightly overconsolidated stress range when sheared at large stress ratios  $q/p'$ . These observations and the data presented in earlier chapters,

suggest that buffer specimens behave in an anisotropic overconsolidated manner. The observed pore water pressure behavior discussed in Chapter 7, also indicates that the anisotropic elastic behavior is temperature dependent.

Figure 8.20 suggested that the yield locus of buffer 'shrinks' at elevated temperature. Tests were not conducted in the current program to prove this, but examination of normalized data (Figure 8.18, 8.20) confirms this conclusion and will be discussed later. Hueckel and Baldi (1990) observed similar behavior in Pontida silty clay and Boom clay and call it 'thermal softening'. This was discussed in Chapter 2 and defined in Figures 2.16 (b) and (c). At constant pressure, the yield locus actually remains the same size, but plastic compressive straining occurs during heating and moves the yield locus to a lower position in  $V-\ln(p')$  compression space. The corollary is that at constant specific volume, the yield locus at elevated temperature is smaller than a room temperature yield locus. Hueckel and Baldi (1990) conducted drained triaxial shear tests along the same effective stress path but at different temperatures. These were shown in Figures 2.8, 2.9 and 2.24. Two different levels of overconsolidation ratio were tested, 5.0 and 12.5. Similar trends were observed in each. Note that heating normally consolidated specimens under constant drained isotropic stress produces a normally consolidated specimen at elevated temperature because a new, state boundary surface is created.

Hueckel *et al.* (1987) showed that undrained heating can bring an overconsolidated soil to a yield condition and eventually to failure. The implication is that the state boundary surface has 'shrunk' until the Roscoe surface comes into contact with the current position in stress. Continued shrinking, then brings the stress state to failure.

To understand yielding in buffer at elevated temperature, it is necessary to return to the concepts of early yield and rupture loci discussed in the previous

section. Early yield was recognized in Winnipeg clay by Graham and Au (1984), but was not well understood. Baldi *et al* (1990) observed a phenomenon similar to early yield in Boom clay. They observed early linearity followed by non-linearity in deviatoric stress and pore pressure response prior to failure. They used a two parameter yielding model to predict stresses during a simulated heat experiment. Oswell (1991) used the idea of early yielding to explain the plastic straining which occurred before the Hvorslev surface was reached in his overconsolidated specimens ( $OCR = 1.5$ ). His yield and rupture loci are shown in Figure 8.22 together with his individual data points. In order to compare data from the current test program with Oswell's early yield locus, it was necessary to normalize to Oswell's swelling equilibrium line from his test T99. Figure 8.23 shows the normalized average data from the current program and Oswell's yield locus. Yield loci are drawn through the current average data at 26°C, 65°C and 100°C. The shape of the loci is assumed to be similar to Oswell's, and it is clear that the size decreases at elevated temperature. This is also apparent in  $V_\lambda$  space as shown in previous figures (Figures 8.18, 8.20).

Normalization of buffer data in  $q/p'_c$  versus  $p'/p'_c$  stress space will be discussed now. The yield loci have been drawn differently in Figure 8.24 than in Figure 8.23. In Figure 8.24, the yield loci are normalized to the 26°C NCL from the current program and the specimens are assumed to be normally consolidated. In fact, the specimens may not have fully reached swelling equilibrium, especially when tested at low effective stresses. Therefore they may behave in an overconsolidated way. The yield loci may actually be of similar shape to Oswell's, but this can not be proven with the data available. Individual data points for the 65°C tests are shown in Figure 8.25, but do not help much in interpreting the shape of the yield locus.

A useful technique for determining shape of the yield loci is shown in



Figure 8.26. Here, individual stress paths, consisting of the consolidation point, early yield point, peak stress point and critical state point, are plotted for five tests at 100°C. The yield points from four of the tests match the proposed yield locus which is approximately elliptical. The low pressure test T1233 does not match the yield locus. Specimens at lower effective stresses probably take longer to reach swelling equilibrium and may not be representative of early yield.

The pseudo-elastic moduli  $E_{50}$  and  $G_{50}$ , discussed in section 8.2.1, were obtained from stress ranges that are within the range of early yield. However, because the moduli are for first loading, they are not truly representative of early yield elasticity. The elastic modulus  $G^\circ$  discussed in section 8.2.2 may be more representative of early yield elasticity. The value  $3G/p'_c = 159$  for reloading, shown in Table 8.7, is similar to values reported by Oswell (1991).

There are two factors which may contribute to the apparent overconsolidated behavior of buffer specimens during undrained shear. One factor is the stress history carried over from the compaction process in which the soil is taken through a process of confined, one-dimensional loading and unloading, then subjected to isotropic stresses which may leave it in an overconsolidated state. It has been customary in work coming from the University of Manitoba (for example Wan 1987, Saadat 1989, Oswell 1991) to assume that samples consolidated at low effective stresses would expand to a swelling equilibrium line (SEL) indistinguishable from the normal consolidation line (NCL). The evidence for this is inconclusive, but the differences between the two lines are thought to be small (Oswell 1991). The second factor is the possibility that some specimens, particularly at low effective stresses, may not have reached swelling equilibrium and therefore may behave in an overconsolidated way. This is consistent with buffer test results from Sun (1986). Oswell (1991) noted that specimens with early yield had three things in common: (1) they swelled; (2) they had steep stress paths in  $q, p'$ -space, and (3) they had been

tested at low stresses. Oswell used the concept of viscoplastic swelling to model their tendency toward swelling equilibrium. Implicit in his work is the assumption that buffer specimens would achieve swelling equilibrium. Clearly, the behavior of buffer is more complex than the time independent thermo-elasto-plastic model used by Hueckel and Baldi (1990). A more complicated model than proposed here will be required to incorporate these time dependent swelling effects.

Five main conclusions can be made regarding yielding in buffer. The first is that early yielding, interpreted from non-linear pore pressure response, is a real phenomenon at 26°C, 65°C and 100°C. A method similar to that proposed by Baldi *et al* (1990) has been used in Chapter 7 for obtaining these yield stresses from undrained tests. The second conclusion is that buffer specimens show anisotropic elastic behavior at 26°C, 65°C and 100°C. As discussed in Chapter 7, pore pressure response of specimens at 100°C indicates more anisotropy than specimens at 26°C. The third conclusion is that the magnitude of elastic moduli increases with temperature. The fourth conclusion is that the yield locus 'shrinks' during drained and undrained heating. The fifth conclusion is that buffer specimens behave like lightly-overconsolidated clay at low stresses and may not be at swelling equilibrium.

### 8.3.5 Isothermal Hardening Laws

Regressions for isothermal hardening laws were presented in Chapter 5 and will not be repeated here. This section considers ideas concerning shrinking yield loci during drained and undrained heating from the point of view of a thermo-elasto-plastic model. Two simple cases will be considered: (1) drained heating and (2) undrained heating. The former applies to testing in the current program.

In Chapter 6, equation 6.38 defined coefficients of thermal expansion of

the pore water, apparatus, and soil skeleton which can be used to account for thermal volume changes observed in buffer. The general equation is based on the following relationship:

$$[8.32] \quad \epsilon_v = \epsilon_v^{Te} + \epsilon_v^{Tp} + \epsilon_v^{se} + \epsilon_v^{sp}$$

where  $\epsilon_v$  is the total volume strain, T denotes the thermal component of strain, s denotes the stress induced strain, e denotes elastic strains and p denotes plastic strains. This equation will be used in the following discussion

In Figure 8.27(a), the effects of drained heating during application of isotropic stress,  $p'$ , are idealized for normally consolidated clay. Starting from  $p_c^{26^\circ\text{C}}$ , point A, heating causes plastic volume straining to point B which is  $p'_{c100}$ . The yield locus has remained the same size in compression space, but is smaller relative to a  $26^\circ\text{C}$  specimen on the same unload/reload line B'-B-C. In contrast with what was shown in section 8.3.2, the slope  $\kappa$  of the unload-reload lines in this figure have been assumed independent of temperature. The specimen is normally consolidated because the stress point is still on the normal consolidation line for  $100^\circ\text{C}$ . Unloading at  $100^\circ\text{C}$  moves the stress point to C. Cooling moves the stress point to D, on to a new  $20^\circ\text{C}$  unload/reload line. The components of strain are:  $\epsilon_v^{Te} = \overline{EB}$ ;  $\epsilon_v^{Tp} = \overline{AE}$ ;  $\epsilon_v^{se} = \overline{CF}$ . Note that no stress induced plastic strains were introduced, but plastic straining has occurred. The  $20^\circ\text{C}$  preconsolidation pressure has moved from point A to point G. Thus a specimen which was normally consolidated at A and B, would be overconsolidated at E after a heating/cooling cycle at constant pressure. Note also that no plastic strains occurred during cooling. This cannot be verified from the current program, but has been verified for Pontida silty clay, and Boom clay by Hueckel and Baldi (1990), and for pelagic clay by Green (1984) although she did not frame her data in elastic-plastic terms. Figure 8.27(b) shows a similar loading cycle, but for overconsolidated clay. The cycle is: heating = A-B; loading = B-C-D; unloading = D-E; cooling = E-F. The

stress path for the consolidation phase of the CIU(TXC) tests in the current program would start at a point such as A and proceed to point D along a curvilinear path during the heating/consolidation stage. This assumes consolidation pressures higher than the swelling pressure of the buffer. Isothermal undrained shearing would start at D and move left along a constant volume line to critical state.

Figure 8.28 (a) shows the effects of undrained (constant volume) heating for the model under constant isotropic total stress. The heating/cooling cycle is as follows: Heat = A-B; Cool = B-D. Since no drainage is allowed  $\epsilon_v = 0$ , and therefore:

$$[8.33] \quad \epsilon_v^{Te} + \epsilon_v^{Tp} = -(\epsilon_v^{se} + \epsilon_v^{sp})$$

Note that the specimen after cooling to D is left in an overconsolidated state relative to the 26°C NCL. This is because plastic strains do not occur during cooling (Hueckel and Baldi 1990). No volume change has been allowed, so no plastic strains have occurred, but if drainage were allowed immediately after cooling and  $p'_c$  reestablished, compression would occur to point E. Heating tends to produce redistribution of water from its bound state to free water state. In the case of active clays, time may be required to reverse the process (visco-plastic swelling).

This cycle has not been verified experimentally for buffer. It forms a core part of the current doctoral program being undertaken by Tanaka. Analogous behavior has been observed in other clays. For example, Campanella and Mitchell (1968) found that two cycles of undrained heating/cooling of kaolinite from 40°F to 160°F and back to 40°F caused hysteresis in the pore pressure response, pore pressures to increase slightly, and a length decrease of 0.072%. Similar behavior was observed for illite. Henkel and Sowa (1963) showed a 10% increase in pore pressures after 3 cycles of undrained heating/cooling of Weald clay. Pore pressure non-equilibrium does not account for the hysteresis (Mitchell 1977), but it would result in net compression of the clay if drainage were allowed. Green (1984) did

similar tests on pelagic clay, except she did not cool her specimens. The excess pore pressures generated during heating caused net compression when drainage was opened at elevated temperature. Yarechewski (1993) has shown that drained heating of buffer following mechanical consolidation results in additional compression.

Figure 8.28(b) shows similar undrained heating for initially overconsolidated clay. The net effect at D is to produce a more heavily overconsolidated specimen than at A. For buffer it is likely that with enough time, a specimen would swell again to reach equilibrium at a normally consolidated state if drainage was again allowed after heating/cooling cycles. It will be left to other researchers to verify this prediction. Isothermal undrained shear would bring the specimens to failure along a constant volume section of the state boundary surface.

### 8.3.6 State Boundary Surfaces

The state boundary surface in  $q, p', V_c$ -space is defined by the elements previously discussed, namely the hardening law, critical state line, Hvorslev surface and Roscoe surface. Not included here is the question of the zero tension cut-off. The thermo-elastic-plastic model proposed here also includes an early yield criterion, and assumes a non-associative flow rule. Governing equations will not be discussed in detail in this thesis, but regressions of buffer data have produced isothermal stress-strain-temperature relationships which could be used to form governing equations. It is considered more important in this first presentation of these ideas to air them qualitatively. Later researchers can design and perform the experiments needed to confirm the model.

The two main differences between the proposed model and Cam clay are: (1) the critical state stress ratio ( $q/p'$ ) is pressure and temperature dependent and (2) early yielding is included. Visco-plastic swelling and a pressure dependent

hardening law may be thought of as addenda to the proposed model. Note that Cam clay assumes the onset of yielding is coincident with (1) onset of irreversibility; (2) onset of dilatancy; and (3) onset of softening. Baldi *et al* (1990) have written governing equations for a complex model which decouples these three processes from yielding. Their model uses a double hardening law and dilatancy onset loci which are separate from the classical critical state loci. A similar approach may be required to model buffer behavior, but developing the mathematics for such a model is beyond the scope of this thesis.

The model proposed for the current program makes use of multiple, nested state boundary surfaces similar to the model proposed by Hueckel and Borsetto (1990). Figure 8.29 (a) shows the state boundary surface derived from Hueckel and Borsetto's tests at room temperature. Figure 8.29(b) shows the state boundary surfaces with variable thermo-plastic volumetric strains,  $\epsilon_V^{Tp}$ , and temperature change  $\Delta T$ . Figure 8.29(c) shows the effect of temperature on a yield surface assuming constant thermo-plastic strains, that is, the thermo-elastic process.

If multiple state boundary surfaces are geometrically similar then they should form a single surface with a unique CSL if normalized to one temperature. In addition, stress paths to failure should in this case coincide. To demonstrate the latter, three tests with different consolidation pressures have been selected and plotted in normalized  $q/p'$  stress space in Figure 8.30. All data from the start of shear up to peak stress have been normalized to equivalent pressures which were calculated using separate loci of peak strength for each temperature. The critical state data was normalized using the critical state locus for each temperature. Therefore there is actually a discontinuity between peak data and critical state data. The normalization has brought the stress paths closely together, within the scatter normally encountered in these tests. The 26°C and 65°C critical state data plotted close to a unique CSL, but the 100°C test further

away from the CSL.

A simplification of the model is shown in Figure 8.31(a). Here, averages of the three temperatures have been normalized to the 26°C NCL rather than to their temperature dependent NCL's. It is assumed that the state boundary surfaces at each temperature pass through the consolidation points  $C_1$ ,  $C_2$ ,  $C_3$ . Constant volume sections of the state boundary surfaces are shown as ellipses. The aspect ratio of the major and minor axis is interpreted on the basis of the 100°C data. Clearly, the peak data points for 26°C and 65°C data do not coincide with the interpreted constant volume sections. The discrepancy is due in part to a few tests which had unusually high values and increased the average values reported here. There are two other possible causes of the poor data fit: (1) the constant volume sections are asymmetric in shape or (2) the points  $C_1$ ,  $C_2$ ,  $C_3$  do not represent the preconsolidation pressures which must form part of the state boundary surface. Figure 8.31 (b) shows the constant volume sections in compression space.

Similarity of the state boundary surfaces can be shown by Figure 8.32. Here, the average data values have been normalized to the consolidation line for their own specific temperature. This has brought the peak, critical state and yield points close together. Figure 8.33 shows the data normalized to the swelling equilibrium pressures  $S_1$ ,  $S_2$ ,  $S_3$  for each temperature. A state boundary surface has been interpreted passing through the swelling equilibrium lines (SEL). Note that the horizontal scale has been expanded by a factor of two compared to Figure 8.32.

A new technique has been developed in the preceding section for estimating the swelling equilibrium pressure based on swelling tests at 26°C and hardening laws at elevated temperature. Figure 8.34 shows the SEL interpreted from Oswell's test T99 and the hardening laws from the current program. The hardening laws may be considered as pseudo-unload/reload lines. These have been idealized in Figure

8.35 (a). A pivot point is identified where the 26°C SEL and NCL intersect. Pivot points for 65°C and 100°C are below this point. The hardening lines are rotated upwards parallel to the SEL to form SEL's at 65°C and 100°C. The swelling pressures at 65°C and 100°C are interpreted from the intersection of the SEL's and the constant volume section through the 26°C pivot point ( $V_c = 2.138$ ). Swelling equilibrium pressures for the compaction specific volume ( $V_c = 2.252$ ) are interpreted in Figure 8.35 (b). This interpretation of the state boundary surface would add more complexity to the isothermal elasto-plastic model described in earlier paragraphs of this section. The hardening laws are no longer parallel to the SEL's and would appear as lines instead of points in stress space normalized to the SEL's.

The model proposed in this chapter is based on averaged behavior and supports a hypothesis of lower strengths in individual tests at elevated temperature even though the peak strength envelope may be higher. Figures 8.19 (a) and (b) showed lower strengths at elevated temperature than at ambient temperature. Figure 8.23 shows average behavior of the buffer specimens and supports this conclusion. Note that in this case all data have been normalized to the same 26°C SEL using equivalent pressure.

The result in the previous paragraph may seem in conflict with the summary graphs of critical state envelopes shown in Figure 5.36. However, when comparing strengths there are two bases of comparison: (1) effective stress; and (2) specific volume. The first basis has been discussed. The importance of the second was apparent from Figure 5.53 where higher strength was noted at elevated temperature than ambient temperature. This was due to lower specific volume at elevated temperature than at ambient temperature. If two specimens with the same final specific volume are sheared undrained at different temperatures then the specimen at the higher temperature will have the lower strength.



Wood (1990) has shown mathematically that the critical state parameter  $\Gamma$  is strongly related to the liquid limit,  $w_L$ , and plasticity index,  $I_p$ . The latter two parameters are the variables which define Casagrande's soil classification chart. It was shown in Chapter 2 that heating of clay causes data points on Casagrande's chart to move down the A-line (Youssef and Ramli 1961). Leaching of salts from clay has a similar effect (Mitchell 1977). These observations imply that heating or leaching processes may make active clays behave at critical state like lower plasticity clays. Clays of lower plasticity also tend to have smaller  $\lambda$  values (Wood 1990). This deserves further study, but has not been incorporated into figures such as Figure 5.12. Trends in the peak strength envelopes of buffer with temperature and pressure are similar to the observed trends at critical state.

#### 8.4 Concluding Remarks

Elements of two models for behavior of buffer at elevated temperature have been discussed. The first model, an isothermal pseudo-elastic model showed that pseudo-elastic moduli and elastic moduli increase with temperature. A constitutive relationship was proposed for non-linear elasticity

The second model proposed is an isothermal elasto-plastic model. It is based on the concepts of multiple state boundary surfaces, a curved critical state line in  $q$ - $p'$  stress space, and early yield loci. The latter implies a non-associated flow rule although this has not been examined in detail. It was shown that the behavior of buffer at end-of-consolidation, yield, peak stress and critical state is temperature dependent.

It is appreciated that many of the ideas presented in this chapter are tentative and supported only by limited data. However the ideas provide insight into buffer behavior which is not otherwise understandable, and indicate approaches for further research.

## CHAPTER 9 REVIEW, CONCLUSIONS AND SUGGESTED RESEARCH

### 9.1 Discussion

After an initial outline of the thesis in Chapter 1, the strength and volume change behavior of different clay minerals and some natural clays at elevated temperature were discussed in Chapter 2. These clays displayed similar volume change behavior to what has been observed in buffer. The strength behavior is broadly similar, but differs at critical state and peak strength in some cases (Green 1984).

Chapter 3 described three high temperature high pressure (HITEP) triaxial apparatus that have been developed by the author for testing buffer in undrained shear. Special materials (seals, membranes) and instruments were required for the apparatus to withstand prolonged use at pressures up to 10 MPa, temperatures up to 100°C and exposure to water. Pressure transducers, load cells, displacement transducers and lateral strain gauges were all susceptible to temperature effects, and required careful calibration.

Chapter 4 described new procedures developed by the author for testing buffer at elevated temperature.

A detailed description of the observed behavior of buffer at elevated temperature was given in Chapter 5. This will not be repeated here, but a general observation regarding the effect of temperature can be made. The behavior of buffer at elevated temperature is governed by similar laws of mechanical response as at room temperature, with some minor changes that were discussed in detail in Chapters 7 and 8.

Some important factors that affect the interpretation of buffer behavior at elevated temperature are the compaction stress history, the extent to which swelling equilibrium has been attained, diffusion of fluids through the membranes,

and thermal expansion of the mineral components and test apparatus (Chapter 6). Coefficients of thermal expansion for the apparatus, soil pore water, soil skeleton have been determined based on theory developed by Mitchell (1977), Agar (1984), Green (1984) and Kosar (1989).

Chapter 7 showed how pore pressure response of the buffer at elevated temperature during undrained shear indicates anisotropic behavior. The anisotropy is more pronounced than at room temperature. Critical state behavior of buffer at elevated temperature is broadly similar to clays such as pelagic clay and Boom clay tested by other researchers.

Chapter 8 discussed two isothermal models of behavior for buffer. A simple macroscopic (isothermal pseudo-elastic) model was discussed in section 8.2. It showed that pseudo-elastic moduli  $E_{50}$  and  $G_{50}$  are temperature and stress level dependent. The moduli increase with temperature. The elastic modulus  $G^c$  from unloading at 65°C was approximately 3 times the magnitude of elastic moduli determined by Oswell (1991) at room temperature. Buffer shows larger pore pressure generation at elevated temperature (section 8.2.1) during yielding and through to failure.

The following conclusions can be made regarding the second model proposed (isothermal elastic-plastic) which can be used for much larger strain changes than the simpler pseudo-elastic model. A complete mathematical description has been considered beyond the scope of the thesis which is restricted to qualitative and phenomenological use of the model. Due to the inherent difficulty in clearly presenting the data and state boundary surfaces in three dimensions, no such drawing has been shown. In any case, the experiments in this thesis were not designed for such a study. Instead a generic representation has been used from Hueckel and Baldi (1990) in Figure 8.29. Two important modifications to their model have been introduced in this thesis: (1) a non-linear CSL line in  $q$ - $p'$  space;

and (2) 'early yield' loci below each SBS.

How general is the proposed model? That is, how does it compare with data from other clays? The main elements of the model seem general to many types of clay, but specific aspects have been incorporated for specialized features of buffer behavior. The concept of multiple state boundary surfaces (SBS) is supported by data from Green (1984) for pelagic clay and from Hueckel and Baldi (1990) for Pontida silty clay and Boom clay. The effects of temperature on peak strength (section 8.3.3) and critical state strength (section 8.3.2) are supported by data from Green (1984) and Hueckel and Baldi (1990), Mitchell and Campanella (1968), and Kosar (1989). Inherent in the concept of multiple SBS's is the idea of shrinking yield loci with increased temperature. This is related to the family of hardening lines and decreasing preconsolidation pressure noted by Campanella and Mitchell (1968), and Mitchell (1977), Eriksson (1990), Sällfors and Tidfors (1990). The idea of increased softening at elevated temperature is supported by Green (1984). Reduced critical state and peak strength at elevated temperature in individual tests is supported by drained tests of Hueckel and Baldi (1990). Early yield has been noted by Graham and Au (1984), Baldi *et al.* (1990), Oswell (1991). The curved CSL in  $q$ - $p'$  space is seen in other clays but is particularly well defined in buffer and perhaps montmorillonite. Examination of the way the curvature changes with temperature suggests that the slopes  $\kappa$  of unload/reload lines must also vary with temperature. The concept of SEL is applicable to montmorillonites, but not to less active clays. To summarize this model of behavior it can be said that elevated temperature tends to increase the density of buffer under drained conditions. Grim (1969) observed regarding montmorillonites that the effect of elevated temperature on material behavior is similar to increasing the water content. (That is, the SBS is smaller at elevated temperature.)

The mechanical behavior of buffer is difficult to characterize because of its swelling properties and the high activity of one constituent, the mineral montmorillonite. Its behavior depends heavily on its microfabric (Wan 1987). It shows highly non-linear stress-strain behavior, and is stress level dependent (Saadat 1989). The behavior in terms of effective stress at the microscopic level in terms of interparticle attractions/repulsions is difficult to define. Buffer has a non-associative flow rule and yields well before failure is reached (Oswell 1991). Its strength and compressive behavior is time and rate dependent (Yin 1990). Data from the current program shows that these characteristics of buffer are also applicable at elevated temperature. A single model covering all these aspects of behavior has not yet been produced, but several elements of behavior have been reproduced in two models presented in the thesis which deal specifically with isothermal behavior of buffer

How do these models compare with the models used by other researchers? The models in this thesis have not been fully verified with test data. Constant  $p'$  tests carried out by Yarechewski (1993) at the same time as the author's program support the concept of temperature dependent strength and hardening lines.

## 9.2 Conclusions

### Major Conclusions

1. Two of the three hypotheses posed in Chapter 1 have been proved in the current program. The third hypothesis has been discussed by another researcher (Yarechewski 1993).
  - (a) Buffer responds to elevated temperature in a way similar to medium plasticity clays (sections 2.2.3, 2.2.4, 2.2.5, 2.2.10, 8.3.4, 8.3.5)
  - (b) The concept of effective stress applies to buffer at elevated temperature (section 2.2.8, and Yarechewski 1993)
  - (c) A simple macroscopic model can be used to describe the compression and shear response of buffer to temperature (section 8.2)
2. Elements of a more complex isothermal elasto-plastic model have been proposed to characterize volumetric behavior during heating and shear behavior at peak and critical state. This model shows the following.
  - (a) Behavior of buffer at elevated temperature can be characterized by a separate state boundary surface (SBS) for each temperature. At elevated temperatures the SBS's are smaller than at room temperature (section 8.3.6).
  - (b) Peak and critical state envelopes (lines) are curved in  $q$ - $p'$  stress space. The stress ratio,  $M$ , at critical state is pressure dependent. This contrasts with the Cam clay model which assumes constant  $M$ . (section 8.3.1).
  - (c) The peak and critical state envelopes (lines) are higher at elevated temperature than at room temperature (section 8.3.2, 8.3.3).
  - (d) Peak and critical state strengths for specimens at the same specific volume or same pressure are lower at elevated temperature than at room temperature (sections 8.3.2, 8.3.3, 8.3.6).

- (e) Larger pore water pressures are generated at elevated temperature starting at the beginning of undrained shear through to critical state than at room temperature. This results in lower strengths even though the strength envelopes are higher (sections 8.3.2, 8.3.3).
- (f) buffer specimens in the current program strain soften in shear, and do not strain harden. For effective stresses over 1.6 MPa, specimens at elevated temperature strain soften more than specimens at room temperature (section 8.3.3).
- (g) The pore pressure response of buffer indicates anisotropy at room temperature and elevated temperature. Buffer behaves more anisotropically at 100°C than at 26°C (Chapter 7).
- (h) Separate and parallel hardening lines exist in  $V-\ln(p')$  space at elevated temperature (section 8.3.5) with higher temperatures leading to lower specific volumes at a given pressure. Similarly, separate critical state lines exist for each temperature. The critical state lines nearly coincide in  $V-\ln(p')$  space with the hardening lines for each temperature (Chapter 5). Linear regressions were used to model consolidation and shear data even though they show slight non-linearity.
- (i) The 'early yield' noted by Oswell (1991) for buffer at room temperature has been confirmed at elevated temperature. This implies a non-associated flow rule at elevated temperature (section 8.3.4).
- (j) Yield loci shrink during drained and undrained heating of buffer. This is consistent with the concept of multiple state boundary surfaces. (section 8.3.6).
- (k) Pseudo-elastic moduli increase in magnitude with elevated temperature (section 8.2), that is, the buffer appears to get stiffer.

- (l) buffer specimens in the current program apparently had not completely reached swelling equilibrium (section 8.3.6).
  - (m) A new technique has been developed for estimating the swelling equilibrium pressure at elevated temperature (section 8.3.6).
  - (n) A new technique has been used for estimating the yield stresses of buffer at elevated temperature from undrained shear tests (Chapter 7).
  - (o) Normalization of data using  $V_\lambda$  space or equivalent pressure is necessary to define the state boundary surfaces at different temperatures. Due to scatter in the data and the complex behavior of buffer it is necessary to average the data in order to clearly see trends in behavior for different temperatures (section 8.3.3).
3. A new pore pressure parameter  $n^*$  based on the classical parameters A and B has been defined for buffer (Chapter 7).
  4. Coefficients of thermal expansion for the apparatus, pore water, soil solids and soil skeleton have been developed (Chapter 7). During drained heating, buffer pore water expands, but the soil skeleton compresses.
  5. Strength of buffer is time rate dependent at room temperature (Yin 1990) and at elevated temperature (see for example test T1211).



**Minor Conclusions:**

1. Three high temperature and pressure (HITEP) triaxial apparatuses have been designed, built, calibrated and used for conducting CIU(TXC) tests on buffer (Chapter 3).
2. Internal load cells, pressure transducers, lvdt's, temperature probes, and lateral strain gauges have been successfully used for testing buffer at elevated temperatures of 65°C and 100°C (Chapter 3 and 4). Most instruments have temperature dependent zeroes and gain factors. Some instruments such as pressure transducers and load cells are pressure dependent. Most instruments show a shift in gain and zero with prolonged use at elevated temperatures.
3. Technology for producing custom sized silicone membranes has been developed as a part of this program. Leakage and diffusion tests were conducted as calibrations and during actual buffer tests (Chapter 3 and 5).
4. Diffusion of oil and water occurs across the silicone membranes used in the current program at a rate similar to the long term consolidation rate of buffer (section 5.3.6, 6.4).
5. Use of pressurized burettes and differential pressure transmitters (DPT) has allowed automatic acquisition of volume change data (Chapter 3).
6. Three data acquisition systems were developed for the HITEP apparatus. In addition, a programmable pressure control system (PCS) was developed for controlling pressure build-up during heating (Chapter 3).
7. Room temperature control of  $\pm 1^\circ\text{C}$  is a minimum criterion for obtaining consistent results.

### 9.3 Suggested Research

1. A more complete mathematical model should be developed to describe all aspects of heating/cooling/loading/unloading.
2. To verify the proposed isothermal models it is suggested that ramped temperature and pressure tests be performed on buffer.
3. Stress probe tests at elevated temperature would provide new data regarding the shape of yield loci.
4. Triaxial shear tests should be conducted on isotropically normally consolidated buffer or montmorillonite to compare with the results of compacted specimens. This may help better define the complex state of overconsolidation in compacted specimens. Alternatively, illite could be used and would reach pore pressure equilibrium sooner than buffer.
5. Tests should be conducted at the same final specific volume at different temperatures to confirm peak strength and critical state behavior.
6. Better membranes should be investigated which will minimize the interaction with cell fluid and reduce the amount of diffusion of both pore water and cell fluid.
7. Further testing should assure that room temperature control is  $\pm 1^\circ\text{C}$ . Control of specimen temperature must be better.

Many of these latter topics are currently being investigated by N. Tanaka and T. Crilly.

## REFERENCES

- Agar, J., 1984, "Geotechnical Behavior of Oil Sands at Elevated Temperatures and Pressures.", PhD Thesis, University of Alberta, Edmonton, Alberta
- Agar, J., Morgenstern, N.R., Scott, J.D., 1986, "Thermal expansion and pore pressure generation in oil sands", Canadian Geotechnical Journal, Vol 23, No 3, 327-333
- Agar, J., Morgenstern, N.R., Scott, J.D., 1987, "Shear Strength and Stress Strain Behavior of Athabasca Oil Sand at elevated Temperatures and Pressures", Canadian Geotechnical Journal, Vol 24, No 1, 1-10
- Atabek, R., Lajudie, A., Lechelle, J., Pusch, R., 1990, "Pilot field experiment with canister-embedding clay under simulated repository conditions", Engineering Geology, Vol 28, No 3, 291-303
- Atkinson, J.H., Bransby, P.L., 1978, "The Mechanics of Soils: An Introduction to Critical State Soil Mechanics", McGraw-Hill Book Company (UK) Limited
- Bailey, W.A., 1965, "The effects of salt on the consolidation behavior of saturated remolded clays", Contact Report No. 3-101: Phase Report No 3, U.S. ARMY MATERIAL COMMAND
- Balasubramonian, B.I., 1972, "Swelling of Compaction Shale", PhD. Thesis, Department of Civil Engineering, University of Alberta
- Baldi, G., Hight, D.W., Thomas, G.E., 1988, "STATE-OF-THE-ART PAPER: A Reevaluation of Conventional Triaxial Test Methods", Advanced Triaxial Testing of Soil and Rock, ASTM STP 977, R.T. Donaghe, R.C. Chaney and M.L. Silver (Eds), Philadelphia, 219-263
- Baldi, G., Hueckel, T., Pellegrini, R., 1988, "Thermal volume changes of the mineral-water system in low-porosity clay soils", Canadian Geotechnical Journal, Vol. 25, 807-825
- Baldi, G, Hueckel, T, Peano, A, Pellegrini, R, 1990a, "Developments in modelling of thermo-hydro-geomechanical behaviour of Boom clay and clay based Buffer materials", Vol. I, submitted to Commissione delle Comunita' Europee by ISMES, Progetto ASP-4361, Doc. n. RAT-DMM-149
- Baldi, G, Hueckel, T, Peano, A, Pellegrini, R, 1990b, "Further check and development of the thermo-hydro-geomechanical model for Boom clay and clay based Buffer materials with an emphasis on the thermo-mechanics of water-solid systems", Vol II, submitted to Commissione delle Comunita' Europee by ISMES, Progetto ASP-4361, Doc. n. RAT-DMM-149
- Barbour, S.L., Fredlund, D.G., 1989, "Mechanisms of osmotic flow and volume change in clay soils", Canadian Geotechnical Journal, Vol 26, No 4, 1989, 551-562

- Barden, L., McDermott, J.W., 1965, "The Use of Free Ends in Triaxial Testing of Clays", *Journal of the Soil Mechanics and Foundations Division, ASCE*, Vol. 91, No. SM6
- Biot, M.A., 1941, "General theory of three dimensional consolidation", *J.Appl.Phys.*, 12, 155-164
- Bird, G.W., 1982, "Hydrothermal stability of potential clay-based buffer materials: a review", *Atomic Energy of Canada Technical Report TR-199*
- Bird, G.W., Cameron, D.J., 1982, "Vault sealing research for The Canadian Nuclear Fuel Waste Management Program", *Atomic Energy of Canada Ltd. Technical Report TR-145*.
- Bishop, A.W. and Henkel, D.J. 1962, "The measurement of soil properties in the triaxial test", *Edward Arnold Ltd., London, England*.
- Bjerrum, L., 1967, "Engineering Geology of Norwegian Normally Consolidated Marine Clays as Related to Settlements of Buildings", 7th Rankine Lecture, *Geotechnique* 17, 81-118
- Booker, J.R., Smith, D.W., 1989 "Behavior of a Heat Source in a Fully Coupled Saturated Thermoelastic Soil", *Numerical Models in Geomechanics, Numog III*, Editors S. Pietruszczak, G.N. Pande, 399-406
- Booker, J.R., Savvidou, C., 1985 "Consolidation around a point heat source", *International Journal for Numerical and Analytical Methods in Geomechanics*, Vol. 9, 173-184
- Börgesson, L., Broc, D., Plas, F., 1990, "Mechanical Properties of Dense Ca-Smectite Clay", *Engineering Geology*, 28, 419-429
- Bowen, R.M., 1980, "Incompressible porous media models by the use of theory of mixtures", *Int. J. Eng. Sci.*, 18, 1129-1148
- Britto, A.M., Savvidou, C., Maddocks, D.V., Gunn, M.J., Booker, J.R., 1989, "Numerical and centrifuge modeling of coupled heat flow and consolidation around hot cylinders buried in clay", *Geotechnique*, 39, no 1, 13-25
- Brodsky, N.S., Getting, I.C., Spetzler, H., 1985, "An Experimental and Theoretical Approach to Rock Deformation at Elevated Temperature and Pressure", *ASTM STP 869*, H.J. Pincus, E.R. Hoskins, Editors, *American Society for Testing and Materials*, Philadelphia, pp.37-54
- Campanella, R.G., Mitchell, J.K., 1968, "Influence of temperature variations on soil behavior", *Proceedings of ASCE Journal of Soil Mechanics and Foundations Division*, SM3, 709-734
- Chan, L.G., Rivard, P.J., 1963, "The effect of test techniques on the shear strength of Western Canadian clays", *ASTM STP 361*, Ottawa

- Chandrasekharan, E.C., Boominathan, S., Sadayan, E., Setty, K.R., 1969, "Influence of Heat Treatment on the Pulverization and Stabilization of Characteristics of Typical Tropical Soils", HRB Spec.Rept.103
- Chattopadhyay, P.K., 1972, "Residual Shear Strength of Some Pure Clay Minerals", PhD Thesis, Department of Civil Engineering, University of Alberta
- Cheung, S.C.H., Gray, M.N., Dixon, D.A., 1986, "Hydraulic and Ionic Diffusion Properties of Bentonite-Sand Buffer Materials", Proc.Inter.Symp. on Coupled Processes Affecting the Performance of a Nuclear Waste Repository, Lawrence Berkeley Laboratories, Berkeley, CA, 393-407
- Claesson, P.M, Kjellander, R., Stenius, P., Christenson, H.K., 1986, "Direct measurement of temperature dependent interactions between non-ionic surfactant layers", J.Chem.Soc., Faraday Trans. I, 82, 2735-2746
- Clementz, D.M., Low, P.F, 1976, "Thermal expansion of interlayer water in clay systems: I. Effect of water content", In M.Kerker (ed), Colloid Interface Sci., Vol 3, 485-502
- Couture, R.A., 1985, "Steam Rapidly Reduces the Swelling Capacity of Bentonite", Nature, 318, 50-52
- Crank, J., Park, G.S.(Editors), 1968, "Diffusion in Polymers", Academic Press, London
- Crooks, J.H.A., Graham, J., 1976, "Geotechnical properties of Belfast estuarine deposits", Geotechnique, Vol 24, No 2, 293-316
- Davidson, B., 1988 (Personal Communication) University of Waterloo, Ontario
- Demars, K.R., Charles, R.D., 1981, "Soil Volume changes induced by temperature cycling", Canadian Geotechnical Journal, 19, 188-194
- Derjaguin, B.V., Karasev, V.V., Khromova, E.N., 1986, "Thermal expansion of water in fine pores", J.Colloid and Interface Sci., 9(11), 586-587
- Derjaguin, B.V., Zorin, Z.M., Churaev, N.V., Shishin, V.A., 1977, "Examination of Thin Layers of Liquids on Various Solid Substrates", in Wetting, Spreading and Adhesion, Academic Press, NY, 201-236
- Dixon, D.A., Cheung, S.C.H., Gray, M.N., Davidson, B.C., 1987, "The Hydraulic Conductivity of Dense Clay Soils", 40th Can.Geotech.Conf., Regina, Saskatchewan, p389-396
- Dixon, D.A., Gray, M.N., 1985, "The Engineering Properties of Buffer Material", Technical Report TR-350, Fuel Waste Technology Branch, WNRE, Pinawa, Manitoba

- Dixon, D.A., Wan, A.W.L., Graham, J., Kjartanson, B.H., 1991, "Assessing Pressure-Volume Equilibrium in Bentonite-Based Materials", 44th Canadian Geotechnical Conference, Calgary, Alberta, Paper No. 61
- Dixon, D.A., Woodcock, D.R., 1986, "Physical and Engineering Properties of Candidate Buffer Materials", Technical Record TR-352, AECL, Pinawa, Manitoba
- Dixon, D.A., 1991, (Personal Communication)
- El-Ruwayih, A.A., 1976, Technical Note: "Design manufacture and performance of a lateral strain device", *Geotechnique*, vol 26, 215-216
- Eriksson, L.G., 1989, "Temperature effects on consolidation properties of Sulphide clays", *Proceedings of the 12th International Conference on Soil Mechanics and Foundation Engineering*, Rio de Janeiro, Vol. 3, 2087-2090
- Fernandez, F., Quigley, R.M., 1985, "Hydraulic conductivity of natural clays permeated with simple liquid hydrocarbons", *Canadian Geotechnical Journal*, 22, pp 205-214
- Gens, A, 1982, "Stress-strain and strength characteristics of a low plastic clay", PhD Thesis, Department of Civil Engineering, Imperial College of Science and Technology, University of London, London, U.K.
- Gillott, J.E., 1987, "Clay in Engineering Geology: Developments in Geotechnical Engineering", 41, Elsevier Science Publishers B.V., Amsterdam
- Graham, J., Au, V.C.S., 1984, "Effects of freeze-thaw and softening on a natural clay at low stresses", *Can.Geotech.Journal*, 22, 69-78
- Graham, J., Housby, G.T., 1983, "Anisotropic elasticity in a natural plastic clay", *Geotechnique*, 33, No.2, 165-180
- Graham, J., Crooks, J.H.A., Bell, A.L., 1984, "Time effects on the stress-strain behavior of natural soft clays": DISCUSSION, *Geotechnique*, Vol 34, No 3, 433-444
- Graham, J., Saadat, F., Gray, M.N., Dixon, D.A., Zhang, Q-Y., 1989, "Strength and Volume Change behavior of a Sand-Bentonite Mixture", *Canadian Geotechnical Journal*, Vol. 26, No 2, 292-305
- Graham, J., Saadat, F., Lingnau, B.E., Yin, J.-H., Oswell, J.M., Azizi, F., 1989, "Constitutive Modelling of Sand-Bentonite Buffer (RBM)", Progress Report-Contract WS-27J-62961, Department of Civil Engineering, University of Manitoba, Winnipeg, Manitoba
- Graham, J., Yin, J.-H., Oswell, J.M., Lingnau, B.E., 1990, "Constitutive Modelling of Sand-Bentonite Buffer (RBM)", Final Report-Contract WS-27J-62961, Department of Civil Engineering, University of Manitoba, Winnipeg, Manitoba

- Graham, J., Lingnau, B.E., Yarechewski, D.S., Tanaka, N., 1991, "Thermo-Elastic-Plastic Modelling of Sand-Bentonite Buffer for Use in Underground Disposal of Nuclear Fuel Waste", Progress Report on Contract No. WS-30J-79981, Department of Civil Engineering, University of Manitoba, Winnipeg, Manitoba
- Graham, J., Oswell, J.M., Gray, M.N., 1992, "The effective stress concept in saturated sand-clay buffer", *Can. Geotech.J.*, Vol. 29, No. 6, 1033-1043
- Gray, M.N., Cheung, S., Dixon, D.A., 1984, "The influences of sand content on swelling developed by statically compacted Na-bentonite.", Atomic Energy of Canada Ltd. Report AECL-7825
- Gray, M.N., Cheung, S., Dixon, D.A., 1985, "Swelling pressures of compacted bentonite/sand mixtures", *Mat.Res.Soc.Symp.Proc.*, Vol 44, p523-530
- Green, S.L., 1984, "The behavior of deep ocean sediments in response to thermo-mechanical loading", PhD Thesis, University of California, Berkeley
- Grim, R.E., 1953, "Clay Mineralogy", McGraw-Hill Book Company Inc., N.Y.
- Güven, N., 1990, "Longevity of Bentonite as Buffer Material in a Nuclear-Waste Repository", *Eng.Geol.*, 28, 233-247
- Head, K.H. 1986, "Manual of soil laboratory testing, Volume 3, Effective stress tests", Pentech Press, London, England.
- Henkel, D.J., Gilbert, G.D., 1952, "The effect of the rubber membrane on the measured triaxial compression strength of clay samples", *Geotechnique*, Vol 3, p20-29
- Henkel, D.J., Sowa, V.A., 1963, "Discussion", *Laboratory Testing of Soils*, A.S.T.M. Spec. Tech. Pub. No.361
- Heuze, F.E., 1983, "High Temperature mechanical, physical, and thermal properties of granitic rocks-A review", *Int.J.Rock Mech. and Mining Sci.*, 20(1), 3-10
- Hight, D.W., 1982, "A Simple Piezometer Probe for the Routine Measurement of Pore Pressure in Triaxial Tests on Saturated Soils", *Technical Note, Geotechnique*, Vol. 32, No. 4, 396-401
- Houston, S.L., Houston, W.N., Williams, N.D., 1985, "Thermo-Mechanical Behavior of Seafloor Sediments", *Journal of Geotechnical Engineering* Vol 3,no 2, 1249-1263
- Hueckel, T., Baldi, G., 1990, "Thermoplasticity of Saturated Clays: Experimental Constitutive Study", *ASCE Journal of Geotechnical Engineering*, Vol. 116, No. 12, 1778-1797

- Hueckel, T., Borsetto, M., 1990, "Thermoplasticity of Saturated Soils and Shales: constitutive Equations", ASCE Journal of Geotechnical Engineering, Vol, 116, No. 12, 1765-1777
- Hueckel, T., Borsetto, M., Peano, A., 1987a, "A Study of Thermo-Plastic-Hydraulic Coupling in Clays Applied to Nuclear Waste Disposal", Proceedings of the 2nd International Conference on Constitutive Laws for Engineering Materials, Tucson, Arizona, 213-235
- Hueckel, T., Borsetto, M., Peano, A., 1987b, "Modeling of Coupled Thermo-Elastoplastic-Hydraulic Response Of Clays Subjected to Nuclear Waste Heat", Numerical Methods for Transient and Coupled Problems, Editors R.W. Lewis, E. Hinton, P. Bettess, B.A. Schrefler, John Wiley and Sons Ltd.
- Hueckel, T., Pellegrini, R., 1989, "Modeling of Thermal Failure of Saturated Clays", Numerical Models in Geomechanics, NUMOG III, S.Pietruszczak, G.N.Pande (ed), Niagara Falls, Pub. Elsevier Applied Science
- Hueckel, T., 1991, "On the Nature of Water-Mineral Interaction in Saturated Clays (including effects of environmental loads)", International Workshop on Stress Partitioning in Engineered Clay Barriers, Duke University, Durham, NC, USA
- Hueckel, T., Borsetto, M., Peano, A., 1987a, "A study of Thermo-Plastic-Hydraulic Coupling in Clays Applied to Nuclear Waste Disposal", Proceedings 2nd Int.Conf.Constitutive Laws for Eng.Materials, Tucson, Arizona, 311-327
- Hueckel, T., and Pellegrini, R., 1991, "Modeling of Thermal Failure of Saturated Clays", Numerical Models in Geomechanics, Numog III, Edited by S. Pietruszczak, G.N. Pande, Niagara Falls, Elsevier Applied Science, 81-90
- Hueckel, T., Pellegrini, R., 1991, "Effective Stress and Water Pressure in Saturated Clays During Heating-Cooling Cycles", Workshop on Stress Partitioning in Engineered clay barriers, Duke University, Durham NC
- Hueckel, T., Pellegrini, R., 1991b, "Thermoplastic Modeling of Undrained Failure of Saturated Clay Due to Heating", Soils and Foundations, Japanese Society of Soil Mechanics and Foundation Engineering, Vol 31, NO 3,
- Inoue, A., Kohyama, N., Kitagawa, R., Watanabe, T., 1987, "Chemical and morphological evidence for the conversion of smectite to illite", Clays Clay Miner., 35, 111-120
- Inoue, A., Velde, B., Mennier, A., Touchard, G., 1988, "Mechanism of illite formation during smectite-to-illite conversion in a hydrothermal system", Am. Mineral., 73, 1325-1334
- Israelachvili, J.N., Pashlay, R.M., 1983, "Molecular layering of water at surfaces and origin of repulsive hydration forces", Nature, 306, Nov, 249-250



- Iwata, S., Tabuchi, T., Warkentin, B.P., 1988, "Soil-Water Interactions: Mechanisms and Applications", Marcel Dekker, Inc., N.Y.
- Kay, B.D., Low, P.F., 1975, "Heats of Compression of Clay-Water Mixtures", Clays and Clay Minerals, vol 23, 266-271
- Khitarov, N.I., Pugin, V.A, 1966, "Behavior of montmorillonite under elevated temperatures and pressures", Geochem. Int., 3(4), 621-628
- Kolymbas, D, Wu, W, 1989, Technical Note: "A Device for Lateral Strain Measurement in Triaxial Tests with Unsaturated Specimens", ASTM Geotechnical Testing Journal, GTJODJ, vol 12, No 3, 227-229
- Kosar, K.M., 1989, "Geotechnical Behavior of Oil Sands and Related Strata", PhD. Thesis, University of Alberta
- Kovalenko, A.D., 1969, "Thermoelasticity: Basic Theory and Applications", Wolters-Noordhoff Publishing Groningen, Netherlands
- La Rochelle, P., Leroueil, S., Trak, B., Leroux, L., Tavenas, F., 1988, "Observational Approach to Membrane and Area Corrections in Triaxial Tests", Advanced Triaxial Testing of Soil and Rock, ASTM STP 977, R.T. Donaghe, R.C. Chaney, M.L. Silver (Editors), p 715-731
- Laguros, G.L., 1969, "Effect of Temperature on some Engineering Properties of Clay Soils", Proceedings of the International Conference on Effects of Temperature and Heat on Engineering Behavior of Soils, Washington, DC, HRB Special Report 103, 267-272
- Lambe, T.W., 1951, Soil Testing for Engineers: Series on soil Engineering, John Wiley and Sons, N.Y., 165 pp
- Lau, S.L-K, 1986, "Effects of Stress Release Disturbance on the Shear Behavior of Simulated Offshore Clays Subjected to Drained Storage", MSc. Thesis, Department of Civil Engineering, University of Manitoba
- Lee, E.H., 1970, "Thermo-Elastic-Plastic Analysis at Finite Strain", International Union of Theoretical and Applied Mechanics Thermoelasticity Symposium, June 25-28, 1968, East Kilbride, Edited by B.A. Boley, Springer-Verlag, N.Y.
- Lee, E.H., Germaine, P., 1974, "Elastic-plastic theory at finite strain", Problems of Plasticity, International symposium on foundations of plasticity, Sept, 1972, Edited by A. Sawczuk, Noordhoff International Publishing, Netherlands
- Leroueil, S., Tavenas, F., La Rochelle, P., Tremblay, M., 1988, "Influence of Filter Paper and Leakage on Triaxial Testing", Advanced Triaxial Testing of Soil and Rock, ASTM STP 977, R.T. Donaghe, R.C. Chaney, M.L. Silver (Editors), p 189-201

- Lew, K.V., 1981, "Yielding Criteria and Limit-State in a Winnipeg Clay", MSc. Thesis, Department of Civil Engineering, University of Manitoba
- Li, E.C-C, 1983, "A Geotechnical Study of Remolded Winnipeg Clay", MSc. Thesis, Department of Civil Engineering, University of Manitoba
- Low, P.F, 1979, "Nature and Properties of Water in Montmorillonite-Water Systems", *Soil Sci.Soc.Am.J.*, Vol 43(5), 651-658
- Low, P.F., 1976, "Viscosity of interlayer water in montmorillonite", *Soil Sci.Soc.Am.J.*, Vol 40, 500-505
- Low, P.F., 1980, "The Swelling of Clay: II Montmorillonites", *Soil Sci.Soc.Am.J.*, Vol 44, No 4, 667-676
- McCall, D.W., Anderson, E.A., Huggins, C.M., March 1961, *J.Chem. Phys.*, 34, No. 3, 804,
- McKinstry, H.A., 1965, "Thermal expansion of clay minerals", *American Mineralogist*, 50, 212-222
- McConnachie, I., 1974, "Fabric changes in consolidated kaolin", *Geotechnique*, 24, No 2, 207-222
- McTigue, D.F., 1986, "Thermoelastic Response of fluid-saturated porous rock", *J.Geophys.Res.*, 91(139), 9533-9542
- Mesri, G., Olson, R.E., 1971, "Consolidation Characteristics of Montmorillonite", *Geotechnique*, 21, No 4, 341-352
- Mitchell, J.K., 1969, "Temperature Effects on the Engineering Properties and Behavior of Soils", *Proceedings of the International Conference on Effects of Temperature and Heat on Engineering Behavior of Soils*, Washington, DC, HRB Special Report 103, 9-28
- Mitchell, J.K., Campanella, R.G., 1963, "Creep Studies on Saturated Clays", *ASTM STP 361*, Ottawa, 91-110
- Mitchell, J.K., 1976, "Fundamentals of Soil Behavior", T.W.Lambe, R.V.Whitman (ed), John Wiley and Sons Inc., N.Y.
- Mohamed, A.M.O., Yong, R.N., Xu, D.A., Cheung, S.C.H., 1990, "Application of an identification technique to evaluate diffusion parameters in a coupled flow", *Proc. of the IASTED International symposium on Modelling, Simulation and Optimisation*, 103-106
- Mortimer, 1975, "Chemistry; A conceptual Approach", 3rd Ed., D. Van Nostrand Company, N.Y.

- Murayama, S., 1969, "Effect of Temperature on Elasticity of Clays", Proceedings of the International Conference on Effects of Temperature and Heat on Engineering Behavior of Soils, Washington, DC, HRB Special Report 103, 194-203
- Noble, C.A., Demirel, T., 1969, "Effect of Temperature on Strength Behaviour of Cohesive Soil", Proceedings of the International Conference on Effects of Temperature and Heat on Engineering Behavior of Soils, Washington, DC, HRB Special Report 103, 204-218
- Noonan, M.L., 1980, "Limit State Studies in Winnipeg Clays", MSc.Thesis, Department of Civil Engineering, University of Manitoba
- Nowinski, J.L., 1978, "Theory of thermoelasticity with applications", Sijthoff and Noordhoff International Publishers, Alphen aan den Rijn
- Oliphant, J.L., Low, P.F., 1983, "Isothermal Compressibility of Water Mixed with Na-Saturated Montmorillonite", J.Colloid and Interface Science, vol 95, No 1, 45-50
- Oscarson, D.W., Dixon, D.A., Gray, M.N., 1988, "Clay Longevity studies for the Canadian Nuclear Fuel Waste Management Program", Workshop on Artificial Clay Barriers for High Level Radioactive Waste Repositories, Lund, Sweden,
- Oscarson, D.W., Dixon, D.A., 1989, "The effect of steam on montmorillonite", Applied Clay Science, 4, 279-292
- Oscarson, D.W., Dixon, D.A., Gray, M.N, 1990, "Swelling Capacity and permeability of an unprocessed and a processed bentonitic clay", Eng.Geol., 28, 281-289
- Oscarson, D.W., Dixon, D.A., 1990a, "Effect of heating unsaturated bentonite on the swelling and hydraulic properties of subsequently saturated clay", Proceedings of the Annual Conference and 1st Biennial Environmental Specialty Conference of the Canadian Society of Civil Engineering, Hamilton, Ontario II-1, Construction, 312-322
- Oswell, J.M. 1991, "Elastic Plastic Behavior of a Sand-Bentonite Mixture", PhD Thesis, University of Manitoba, Department of Civil Engineering
- Oswell, J.M., Graham, J., Lingnau, B.E., King, M.W., 1991, "Use of Side Drains in Triaxial Testing at Moderate to High Pressures", ASTM Geotechnical Testing Journal, GTJODJ, Vol 14, No 3, 315-319
- Oswell, J.M., Lingnau, B.E., Osiowy, K.B.P., Graham, J., 1989, "Discussion on 'Automatic Volume Change and Pressure Measurement Devices for Triaxial Testing of Soils' by Poul V. Lade", ASTM Geotechnical Testing Journal, GTJODJ, Vol 12, No 4, 325-326
- Perry, R.H., Green, D.W., Maloney J.O. (Editors), 1984, "Perry's Chemical Engineer's Handbook", 6th Ed, McGraw-Hill BookCo.,N.Y.

- Phillips, A., 1970, "Yield Surfaces of Pure Aluminum at Elevated Temperatures", International Union of Theoretical and Applied Mechanics Thermoelasticity Symposium, June 25-28, 1968, East Kilbride, Edited by B.A. Boley, Springer-Verlag, N.Y.
- Plum, R.L., Esrig, M.I., 1969, "Some Temperature Effects on Soil Compressibility and Pore Water Pressure", Proceedings of the International Conference on Effects of Temperature and Heat on Engineering Behavior of Soils, Washington, DC, HRB Special Report 103, 9-28
- Post, J.L., 1989, Moisture Content and Density of Smectites, Geotechnical Testing Journal GTJODJ, Vol. 12, No. 3, Sept, pp 217-221
- Pusch, R., Güven, N., 1990, "Electron microscope examination of hydrothermally treated bentonite clay", Eng.Geol., 28, 303-314
- Pusch, R., Karnland, O., Hokmark, H., 1991, "The Nature of Expanding Clays as Exemplified by the Multifaced Smectite Mineral Montmorillonite", Workshop on Stress Partitioning in Engineered Clay Barriers, Duke University, Durham, NC, May, 1991, 1-23
- Quigley, R.M., 1984, "Quantitative mineralogy and preliminary porewater chemistry of candidate buffer and backfill materials for a nuclear fuel waste disposal vault", Atomic Energy of Canada Ltd. Report AECL-7827
- Radhakrishna, H.S., 1982, "Evaluation of the thermal properties of buffer materials for a deep underground nuclear waste disposal vault", Atomic Energy of Canada Ltd. Technical Report TR-183
- Radhakrishna, H.S., Chan, H.T., Crawford, A.M., Lau, K.C., 1989, "Thermal and physical properties of candidate buffer-backfill materials for a nuclear fuel waste disposal vault", Canadian Geotechnical Journal 26, 629-639
- Ravina, I., Low, P.F., 1972, "Relation between swelling, water properties and b-dimension in montmorillonite-water systems", Clays and Clay Minerals, Vol 20, 109-123
- Robb, W.L., 1965, "Thin Silicone Membranes-Their permeation properties and some applications", Report No. 65-C-031, Oct., General Electric Research and Development Center, Schenectady, N.Y.
- Roscoe, K.H., Schofield, A.N., and Wroth, C.P., 1958, "On the yielding of soils", Geotechnique, No.8, p22-52
- Roscoe, K.H., Burland, J.B., 1968, "On the generalised stress-strain behaviour of 'wet' clay", Engineering Plasticity (J. Heyman and F.A. Leckie, eds), Cambridge University Press, Cambridge
- Rowe, P.W., 1972, "The relevance of Soil Fabric to Site Investigation Practice", Geotechnique, Vol 22, No 2, 195-300

- Van Olphen, H., 1963, "Clay Colloid Chemistry For Clay Technologists, Geologists, and Soil Scientists", Interscience Publishers Div of John Wiley and Sons, N.Y.
- Viani, B.E., Low, P.F., Roth, C.B., 1983, "Direct Measurement of the Relation between Interlayer Force and Interlayer Distance in the Swelling of Montmorillonite", *J. Colloid and Interface Sci.*, Vol 96, no 1,
- Wan, A.W.-L., 1987, "Compaction and Strength characteristics of sand-clay buffer material formed at swelling pressure-water content equilibrium", MSc. Thesis, University of Manitoba, Department of Civil Engineering,
- Wan, R.G., Chan, D.H., Kosar, K.M., 1991, "A constitutive model for the effective stress-strain behaviour of oil sands", *The Journal of Canadian Petroleum Technology*, Vol 30, No.4, 89-98
- Wawersik., E.W.R., 1985, "Steady State Creep Rates and Activation Parameters for Rock Salt", ASTM STP 869, H.J. Pincus, E.R. Hoskins, Editors, American Society for Testing and Materials, Philadelphia, pp.72-92
- Williams, N.D., 1982, "The effects of elevated temperature on the engineering properties of seafloor sediments", PhD. Thesis, University of California, Berkeley
- Wood, D.M., 1990, "Soil Behaviour and Critical State Soil Mechanics", Cambridge University Press, Cambridge
- Wroth, C.P., Houlsby, G.T., 1985, "Soil mechanics - Property characterization and analysis procedures", ICSMFE, San Francisco
- Xu, D.M., Mohamed, A.M.O., Yong, R.N., Cheung, S.C.H., 1990, "Evaluation of thermal conductivity of backfill material", Scientific Basis for Nuclear Waste Management, Proc. Materials Research Society Meeting, Boston, MA, USA
- Yarechewski, D.S., 1988, "Quality control tests for making sand-bentonite specimens for nuclear waste containment studies", BSc Thesis, University of Manitoba, Department of Civil Engineering
- Yarechewski, D.S., 1993, "Constant Mean Effective Stress Tests on Sand Bentonite Specimens at Elevated Temperature", MSc. Thesis, Department of Civil Engineering, University of Manitoba
- Yin, J.-H., 1990, "Constitutive Modeling Of Time-Dependent Stress-Strain Behavior of Soils", PhD Thesis, University of Manitoba, Department of Civil Engineering
- Yin, J.-H., Graham, J., 1989, "Viscous-elastic-plastic modelling of one-dimensional time-dependent behavior of clays", *Can. Geotech. J.*, Vol 26, p199-209

- Yin, J-H., Graham, J., Saadat, F., Azizi, F., 1989, "Constitutive modelling of soil behaviour using three modulus hypoelasticity", Proceedings, 12th ICSMFE, Rio de Janeiro, A.A. Balkema, pp143-147
- Yong, R.N., Warkentin, B.P., 1975, "Soil Properties and Behaviour: Developments in Geotechnical Engineering 5", Elsevier Scientific Publishing Company, N.Y.
- Yong, R.N., Xu, D.A., 1988, "An identification for evaluation of phenomenological coefficients in coupled flow in unsaturated soils", Journal of Numerical and Analytical Methods in Geomechanics 12, 283-299
- Yoshida, T, Iwata, S., 1970, "Consideration on pH of soil solution", Proc. Jap. Soil Sci. Soc. Conf., (Japanese)
- Youssef, M.S, Ramli, A.H, 1961, "Temperature Changes and their Effects on some Physical Properties of Soils", Proceedings of the 5th Int. Conf. Soil Mech. Found. Eng., Vol 1